

RIGID BARRIER WITH A GABION CUSHION SUBJECTED TO BOULDER IMPACT

Pethati Mudiyanseelage Don Jude Shalitha Perera

<https://orcid.org/0000-0003-1432-8851>



Prof. Nelson Lam

Dr. Mahdi Miri Disfani

Submitted in fulfilment of the requirements for the degree of
Doctor of Philosophy

Department of Infrastructure Engineering
Faculty of Engineering
University of Melbourne

2019

Keywords

Rockfall, Structural impact, Impact, Concrete barrier, Gabion, Cushioning effect, Rockfall protection, Rockfall protection structures, Disaster management, Disaster prevention, Energy absorption

Abstract

Protection against rockfalls occurring alongside landslides contribute to the major part of the disaster management budget in many countries like Switzerland, Japan and Hongkong. Protective structures are usually built over disaster trajectories to safeguard lives and properties. Reinforced concrete barriers that are fitted with gabions are one common form of installations to provide the protection. Few experimental investigations involving impact testings of a rigid reinforced concrete barrier which was fitted with a gabion cushion cover have been reported in the literature. But these investigations were limited to studying the localised actions of impact. The change of structural response behaviour of the barrier as a whole by the presence of a cushion layer is typically not within the scope of the reported investigations. Design methodologies that have been developed are typically limited to overly simplified calculations based on applying an equivalent static force to the barrier. To fill this knowledge gap full-scale pendulum tests have been conducted by the authors on a barrier that was fitted with a gabion cushion layer. The structural response behaviour of the barrier, contact force and tensile strains in the longitudinal reinforcement were of interests. Results recorded from the tests were compared with results from control experiments which were without the protection of any cushion materials. The introduction of a layer of cushion is shown to be able to have the deflection demand on the structure reduced by more than 70% when the amount of energy delivered by the impact is kept constant. An analytical procedure employing the Hunt and Crossley contact model, Swiss code model and two-degrees-of-freedom (2DOF) system modelling technique is presented for evaluating the flexural response demand behaviour of the cushioned barrier. The proposed analytical procedure is shown to be able to predict the reduced deflection demand with a reasonable degree of conservatism. At the end of the thesis, a simple hand calculation procedure featuring the use of design charts is presented for engineering applications. The procedure is illustrated by a worked example which is based on a realistic rockfall scenario.

Table of Contents

Keywords	i
Abstract.....	ii
Table of Contents	iii
List of Figures	vi
List of Tables	xi
List of Abbreviations	xii
Statement of Original Authorship.....	xv
Acknowledgements.....	xvi
Chapter 1: Introduction	1
1.1 Background.....	1
1.2 Research objectives	5
1.3 Thesis outline.....	6
Chapter 2: Literature Review	9
2.1 Characterisation of gabion.....	10
2.1.1 Test on full-scale gabion	11
2.2 Rockfall protection structures	13
2.3 Reinforced concrete barriers.....	14
2.4 Structural behaviour of an RC barrier under impact loads	14
2.4.1 Local Structural Behavior.....	14
2.4.2 Global Structural Behavior.....	15
2.4.3 Hard Impact vs Soft Impact.....	15
2.5 Material behaviour of an RC barrier under impact loads	16
2.6 Function of the cushion layer	17
2.7 Force-based design	17
2.7.1 Hertz impact equation	17
2.7.2 Modified Hertz equation.....	18
2.7.3 Model developed by Labiouse, Descoedres [14].....	19
2.7.4 Japanese code model	20
2.7.5 Swiss code model	21
2.7.6 Limitations of forced based design.....	22
2.8 Displacement based design.....	25
2.8.1 Empirical model	25
2.8.2 Eurocode 1 model.....	26
2.8.3 Limitations of displacement-based design	26
2.9 Analysis of the impact taking into account energy partitioning	27
2.10 Prediction of localised effects of impulse.....	31
2.10.1 Spring connected lumped mass models.....	31
2.10.2 Estimating the contact force	33
2.11 Analytical models	40

2.12	Numerical models	45
2.12.1	Finite element modelling (FEM)	45
2.12.2	Discrete element modelling (DEM).....	46
2.13	Experimental studies	49
2.13.1	Vertical Impact experiments	49
2.13.2	Horizontal Impact tests	53
2.14	Summary, research gap and proposed study	55
Chapter 3: Behaviour of the Gabion Cushion Layer under Impact Load ...		57
3.1	Force distribution through granular cushion layer	57
3.2	Small scale drop test	58
3.2.1	Stress distribution in cushion layer	61
3.2.2	Contact force models for gabion cushion	64
3.2.3	Multiple strikes on the same cushion.....	69
3.3	Applying the Swiss code model for horizontal impact by a boulder	73
Chapter 4: Large Scale Experimental Studies		75
4.1	Specimen.....	76
4.2	Impactor objects	78
4.3	Cushioning materials.....	79
4.3.1	Particle properties	80
4.3.2	Gabion properties.....	82
4.4	Instrumentation	87
4.4.1	Strain gauges.....	90
4.4.2	Linear variable differential transformers (LVDTs)	92
4.4.3	Laser sensors.....	93
4.4.4	Accelerometers	95
4.4.5	High-speed camera (HSC).....	96
4.5	Experimental set-up and procedures	96
4.5.1	General Set-up	96
4.6	Test series.....	98
4.6.1	Test Series A: Pre-yield bending tests (without cushion).....	98
4.6.2	Test Series B: Gabion cushion with different fill materials.....	99
4.6.3	Test Series C: Gabion cushion with different thicknesses.....	101
4.7	Test results and analysis.....	104
4.7.1	Cushioning effect of the gabion layer.....	104
4.7.2	Contact force.....	106
4.7.3	Permanent indentations of the cushion layer	111
4.7.4	Deflection of the wall	117
4.7.5	Strain.....	127
Chapter 5: Analytical Modelling of Cushioned Impact.....		135
5.1	Non-linear viscoelastic model.....	135
5.2	2DOF model for cushioned impact	136
5.3	Calibration of parameters.....	136
5.3.1	Calibration of COR.....	137
5.3.2	Calibration of p	138
5.3.3	Calculation of the mass of structure (m_2).....	139
5.3.4	Calculation of the stiffness of structure (k_2)	140

5.3.5	Calibration of the stiffness of cushion (<i>kn</i>)	141
5.4	Calculation of the stiffness of cushion (<i>kn</i>) based on contact force model	144
5.5	Wall deflection simulated by 2DOF model comparisons	147
5.6	Estimation of tensile reinforcement strain	149
Chapter 6:	Simplified Design Approach.....	153
6.1	Development of a closed form solution.....	153
6.2	Development of the design chart	156
6.3	Results comparison using simplified model	160
Chapter 7:	Industrial Application.....	165
7.1	Force from debris flow	165
7.2	Calculation of bending performance of the wall for combined actions.....	166
7.3	Design for localised damage.....	168
7.4	Design steps	170
7.5	Worked example 1	171
Chapter 8:	Conclusions	177
8.1	Summary and conclusions	177
8.1.1	Chapter 2	177
8.1.2	Chapter 3	178
8.1.3	Chapter 4	179
8.1.4	Chapter 5	180
8.1.5	Chapter 6	180
8.1.6	Chapter 7	181
8.2	Limitations and recommendations.....	181
Bibliography	183
Appendices	195

List of Figures

Figure 1.1 Vulnerability of a rockfall impact (Fushi town's Liuliao village)	1
Figure 2.1 Unconfined compression test in Ref. [31]	12
Figure 2.2 Stress-strain relationship of gabion cushion as reported in Ref. [31].....	12
Figure 2.3 Comparison of energy absorption capacities and cost of construction per meter for different rockfall protection systems (After Yoshida [33]).....	13
Figure 2.4 – Strain rate for different loading periods [48]	16
Figure 2.5 – Force distribution through the cushion layer Japan Road Association [59].....	21
Figure 2.6 – Force distribution through cushion layer ASTRA [61]	22
Figure 2.7 – Schematic diagram showing contact force, inertial force and reaction force.....	23
Figure 2.8 Diagrams demonstrating the difference of contact force and reaction force in (a) hard impact scenario (b) soft impact scenario.....	24
Figure 2.9 – Reinforcement layout in Zhan, Wang [65]	25
Figure 2.10 Concrete responses to impact action: (a) penetration, (b) cone cracking, (c) spalling, (d) cracks on (i) proximal face and (ii) distal face, (e) scabbing, (f) perforation, and (g) overall target structure response [67]	26
Figure 2.11 – Experimental setup for cantilever lumped mass	30
Figure 2.12 – Force displacement diagram for (a) perfectly plastic system (b) elastoplastic system.....	30
Figure 2.13 – Hard impact of a rigid body on a lightweight target.....	31
Figure 2.14 – Impact on elastic half-space.....	32
Figure 2.15 – Linear elastic 2DOF model.....	32
Figure 2.16 – Linear viscoelastic 2DOF model	33
Figure 2.17 – Schematic diagram of Hertz theory	34
Figure 2.18 Non-linear Elastic model	36
Figure 2.19 Kelvin-Voigt model	36
Figure 2.20 (a) Bourrier, Gotteland [26] model and b. Schellenberg [47] model.....	41
Figure 2.21 – Single degree of freedom system used by Schellenberg and Vogel [77]	42
Figure 2.22 – Multi degree of freedom system used by Bourrier, Gotteland [26].....	42
Figure 2.23 –Three degree of freedom model used by di Prisco and Vecchiotti [98].....	43
Figure 2.24 – Different FEM model used by researchers [104, 105].....	46

Figure 2.25 – Schematic representation of sphere-sphere interaction in LS-DYNA	47
Figure 2.26 – DEM Geo-cell model by [110]	48
Figure 2.27 - Load-cell arrangement in Schellenberg, Volkwein [16]	52
Figure 2.28 – Experimental arrangement used by Calvetti [22]	53
Figure 2.29 – Horizontal impact experimental arrangements	53
Figure 3.1 Experimental arrangement	60
Figure 3.2 Steel plates	60
Figure 3.3 Experimental setup	60
Figure 3.4 Stress distribution	61
Figure 3.5 Volume of the particles under impact loading (0.5m)	62
Figure 3.6 Stress distribution at concrete surface	63
Figure 3.7 Stress-strain diagram of 100mm cubical gabion box	66
Figure 3.8 Contact force time history for small scale drop test	66
Figure 3.9 Comparison of Eq. 3.2 to Eq 3.5 with peak contact force of small-scale drop test	67
Figure 3.10 Particle size distribution curves for soil cushions reported in Ref. [33]	68
Figure 3.11 Multiple impact 1 m drop height on gravel filled cushion	69
Figure 3.12 Multiple impact contact force factor for different impact conditions	70
Figure 3.13 Statistical analysis of contact force factor	70
Figure 3.14 Comparison of contact force results with calculated values	72
Figure 3.15 Horizontal impact test setup	73
Figure 3.16 Comparison of experimental results with Swiss code equation (Eq. (3.2)) and modified Swiss code equation (Eq. (3.6))	74
Figure 4.1 Reinforced concrete specimen	77
Figure 4.2 Photograph of reinforced concrete specimens	78
Figure 4.3 Torpedo shaped impactor objects	79
Figure 4.4 Image analyses	81
Figure 4.5 Particle size distribution curves	81
Figure 4.6 Dimensions of wire net and production of gabion box	83
Figure 4.7 Photographs showing samples of gabions	83
Figure 4.8 Static test setup	84
Figure 4.9 Stress-strain diagram	85
Figure 4.10 Sample calculation of modulus of elasticity (500 mm – 4)	86
Figure 4.11 Front view (tensile side) of specimen showing instrumentations	87

Figure 4.12 Rear view (compressive side) of the specimen showing instrumentations	88
Figure 4.13 Side view of specimen showing instrumentations	88
Figure 4.14 Front view (tensile side) of specimen showing instrumentations	89
Figure 4.15 Rear view (compressive side) of the specimen showing instrumentations	89
Figure 4.16 Front and rear view of reinforcement showing instrumentations	90
Figure 4.17 Photographs of strain gauges on reinforcement bar -specimen 1	91
Figure 4.18 Photographs of strain gauges on reinforcement bar - specimen 2	91
Figure 4.19 Photograph of a strain gauge on concrete surface – specimen 2	92
Figure 4.20 Photograph of LVDTs at the front of the wall.....	93
Figure 4.21 Photographs showing laser sensors attached to the timber frame	94
Figure 4.22 Photographs showing calibration.....	94
Figure 4.23 Photographs showing the accelerometer sensor attached to 280 kg impactor	95
Figure 4.24 Drawing showing overview of test set up.....	97
Figure 4.25 Photograph showing overview of test set up	97
Figure 4.26 Sketch illustrating fixed base wall.....	98
Figure 4.27 Position of protective steel plate	99
Figure 4.28 Typical set-up of cushion protective layer.....	100
Figure 4.29 Front view of specimen with cushion layer prior to Test B1-1 and Test B3-1.....	100
Figure 4.30 Typical set-up of cushion protective layer.....	102
Figure 4.31 Test setup for gabion cages with different thicknesses.....	102
Figure 4.32 Schematic diagram.....	104
Figure 4.33 Sample screen captures of HSC for Test A1	104
Figure 4.34 Sample screen captures of HSC for Test B1-1	105
Figure 4.35 Contact force time-history from Test Series A.....	106
Figure 4.36 Contact force time-history from Test Series B	107
Figure 4.37 Contact force time-history from Test Series C	109
Figure 4.38 Variation of peak contact force with cushion thickness	110
Figure 4.39 Variation of peak contact force with cushion ME	111
Figure 4.40 Permanent indentation after each strike on same cushion layer-Test Series B	112
Figure 4.41 Permanent indentation after each strike on same cushion layer-Test Series C	113

Figure 4.42 Damage to the gabion cushion following the impact – Test Series B.....	114
Figure 4.43 Damage to the gabion cushion following the impact – Test Series C.....	116
Figure 4.44 Effect of the permanent indentation with the gabion cage strength	117
Figure 4.45 Deflection time-histories recorded at top centreline of wall from Test Series A.....	117
Figure 4.46 Deflection time-histories recorded at top centreline of wall from Test Series B.....	119
Figure 4.47 Deflection time-histories recorded at top centreline of wall from Test Series C.....	120
Figure 4.48 Maximum deflection values recorded from Test Series A.....	122
Figure 4.49 Maximum deflection values recorded from Test Series B.....	123
Figure 4.50 Maximum deflection values recorded from Test Series C.....	125
Figure 4.51 Maximum wall deflection for comparison between Test Series A and B (with cushion and without cushion).....	126
Figure 4.52 Variation of peak deflection with cushion thickness.....	127
Figure 4.53 Variation of peak deflection with cushion ME	127
Figure 4.54 Reinforcement strain over the length of the wall.....	128
Figure 4.55 Maximum reinforcement strain recorded along wall length.....	128
Figure 4.56 Concrete strain profiles on the compressive side of the wall (on concrete surface) at the wall centreline.....	129
Figure 4.57 Concrete strain at base of wall taken across its length.....	129
Figure 4.58 – Strain diagram.....	132
Figure 4.59 Crack profile observed following Test Series B.....	132
Figure 5.1 2DOF spring mass system utilising Hunt and Crossley Model.....	136
Figure 5.2 Force distribution in structure and 2DOF simplification.....	137
Figure 5.3 Sensitivity analysis of COR : Test B1-2 (m = 280 kg H = 1.4 m & t = 500mm (FG/CG)).....	138
Figure 5.4 Force displacement diagram for different analytical models.....	139
Figure 5.5 Sensitivity to change in the value of p : Test B1-2 (m = 280 kg H = 1.4 m & t = 500mm (FG/CG)).....	139
Figure 5.6 Calculation of cushion volume under load.....	140
Figure 5.7 2DOF model calibration.....	142
Figure 5.8 Calibrated kn values for Test Series B.....	142
Figure 5.9 Calibrated kn values for Test Series C.....	143
Figure 5.10 Comparison of stiffness of the frontal spring (kn) under different cushion strengths.....	143

Figure 5.11 Comparison of stiffness of the frontal spring (<i>kn</i>) with different cushion thicknesses	144
Figure 5.12 Comparison of peak contact forces – Test Series B	146
Figure 5.13 Comparison of peak contact forces – Test Series C	146
Figure 5.14 2DOF model – contact force diagram.....	147
Figure 5.15 Deflection time histories of the wall.....	148
Figure 5.16 Maximum deflection of the wall – Test Series B	148
Figure 5.17 Maximum deflection of the wall – Test Series C	149
Figure 5.18 Comparison of peak tensile reinforcement strain	150
Figure 5.19 Comparison of peak tensile reinforcement strain	150
Figure 6.1 Design chart for determine the γ factor	160
Figure 6.2 Comparison of <i>kn</i> calibrated, calculated using 2DOF model and calculated using Eq. (6.7) for Test Series B.....	161
Figure 6.3 Comparison of <i>kn</i> calibrated, calculated using 2DOF model and calculated using Eq. (6.7) for Test Series C.....	161
Figure 6.4 Deflection of the wall comparison.....	162
Figure 6.5 Deflection of the wall comparison.....	162
Figure 6.6 Strain comparison for Test Series B	163
Figure 6.7 Strain comparison for Test Series C	163
Figure 7.1 Punching shear failure of a flat slab panel.....	168
Figure 7.2 Punching shear failure of a boulder impact	169
Figure 7.3 Dimensions of rigid barrier	172

List of Tables

Table 2.1 Hexagonal mesh gabion cages	10
Table 2.2 Square mesh gabion cages	11
Table 2.3 Shapes of impactors	51
Table 3.1 Geotechnical properties of cushion materials reported in Ref. [33]	68
Table 3.2 Range of parameters used to develop Swiss code	68
Table 4.1 In-situ material properties of reinforcing bars and concrete	77
Table 4.2 Impactor object dimensions	79
Table 4.3 Results from image analyses of gabion materials	81
Table 4.4 Modulus of elasticity values	86
Table 4.5 Impact conditions for all test series.....	103
Table 5.1 Modulus of elasticity values for multiple impact.....	145
Table 6.1 Calculations for development of the design chart.....	157
Table 6.2 Calculations showing effects of varying ν_0	159
Table 7.1 Punching shear capacity calculated from Test series D.....	169
Table 7.2 Design data for rigid barrier	171
Table 7.3 Reinforcement details	171

List of Abbreviations

SI units of kilograms (kg), metres (m), seconds (s), pascals (Pa), newtons (N) and joule (J) are used in this thesis, unless noted otherwise. Except where specifically noted, the notation adopted in this thesis has the following meanings:

a	=	Radius of the contact surface
A_d	=	Static equivalent force (Swiss code)
A_{st}	=	Cross-sectional area of tensile reinforcement in an RC section
A_p	=	Perimeter area of the particle
AR	=	Aspect ratio
b	=	Diameter of the column
B	=	Width of beam/length of wall
COR	=	Coefficient of restitution
C	=	Ductility modification factor
C_{ME}	=	Consolidated Swiss code constant
$C_{f,n}$	=	Contact force factor for n^{th} impact
D	=	Diameter of the impacting rock (Japanese code)
Dl	=	Damping coefficient of a linear damper
Dn	=	Damping coefficient of a non-linear damper
d	=	Effective depth, depth of the slab panel in Section 7.2
e	=	Thickness of the gabion cushion
E	=	Young's modulus
E_b	=	Elastic modulus of boulder
E_B	=	Elastic modulus of barrier
E_d	=	Energy generated by debris flow
F	=	Quasi-static force
F_d	=	Lateral force generated by debris flow
F_c	=	Contact force
F_{max}	=	Maximum contact force
F_p	=	Point force acting on the column
F_u	=	Ultimate force
F_y	=	Yield force
f'_c	=	Maximum characteristic compressive cylinder stress of concrete
f_u	=	Ultimate stress of reinforcement
f_y	=	Yield stress of reinforcement
g	=	Gravitational acceleration (9.81 ms^{-1})
H	=	Drop height of the impactor
h	=	Height of target structure
h_d	=	Debris thickness
h_i	=	Vertical distance between point of impact and axis of rotation

I	=	Second moment of area
I_{cr}	=	Cracked second moment of area
K_c	=	Kwan factor
KE_0	=	Kinetic energy imposed by impactor
KE_1	=	Kinetic energy carried by the rebounding impactor
KE_2	=	Kinetic energy transferred to target
k	=	Flexural stiffness of target
k_{cr}	=	Cracked flexural stiffness of an RC element
k_l	=	Stiffness of the frontal linear spring in a two degree of freedom spring connected lumped mass system
k_n	=	Stiffness of the frontal non-linear spring in a two degree of freedom spring connected lumped mass system
k_1	=	Stiffness of the 1 st spring
k_2	=	Stiffness of the 2 nd spring
L	=	Span length of wall
L_{eff}	=	Effective length of wall
m, m_1	=	Mass of the impactor
m, m_b	=	Mass of impactor
m_2	=	Mass of the target
m_{gabion}	=	Mass of the gabion cushion
m_{wall}	=	Mass of the wall
M_E	=	Elastic modulus of the soil layer / gabion cushion
M_u	=	Ultimate moment
M_y	=	Yield moment
p	=	Exponent characterising non-linearity of the frontal spring in a two degree of freedom spring connected lumped mass system, taken as 1.5 in Hertz model
p_0	=	Max pressure under Hertz theory of elastic contact
P	=	Perimeter of the particle
q	=	Non-linear exponent for the unloading phase of the contact
r, r_b	=	Radius of boulder
r_1	=	Radius of the force transmitted area
R	=	Radius of the impactor
SE_2	=	Strain energy absorbed by target
T	=	Thickness of the cushion layer (Japanese code)
T_m	=	Natural period of the frontal spring
T_{m_2}	=	Natural period of the rear spring
v	=	Velocity of the impactor
v_0, v_b	=	Incident velocity of impactor
W	=	Wight of the impactor
α	=	Factor describing conditions of re-bounce
β	=	Mass reduction factor
β_d	=	Angle between the frontal face of the barrier and the direction of movement of the debris

δ	=	Indentation of impactor into surface of target (linear)
δ_p	=	Permanent deformation
δ_{max}	=	Maximum indentation at the end of compression phase
δ^p	=	Indentation of impactor into surface of target (non-linear)
$\dot{\delta}$	=	Velocity of indentation
$\dot{\delta}_0$	=	Relative velocity between two colliding objects at initial contact
Δ	=	Maximum deflection/displacement of target following an impact action
Δ_b	=	Deflection of wall when struck by boulder
Δ_d	=	Deflection prior to being subjected to the impact action from a fallen boulder
Δ_y	=	Yield deflection at the top of the wall
Δ_{yi}	=	Deflection of stem wall at yield limit
ε_s	=	Maximum tensile strain of reinforcement
ε_{sy}	=	Yield strain of reinforcement
ϕ	=	Curvature
ϕ_y	=	Yield curvature
φ_k	=	Internal friction angle of particles
γ	=	Deflection reduction factor for the selected cushion properties
λ	=	Target's generalised mass to impactor's mass
λ_2	=	Target's generalised mass and gabion cushion mass to impactor's mass
λ_c	=	Lambda constant
μ_b	=	Poisson ratio of boulder
μ_B	=	Poisson ratio of barrier
ρ	=	Density of the gabion cushion
ρ_d	=	Density of debris flow
ν	=	Poisson's ratio

Statement of Original Authorship

This is to certify that:

- I. This dissertation comprises only my original work towards the Doctor of Philosophy.
- II. Due acknowledgement has been made in the text to all other material used.
- III. This dissertation is less than 100,000 words in length, exclusive of tables, figures, references appendices and front matter.

Some of the content presented under this thesis has been previously submitted as reports which are prepared under the following two R&D service contracts executed by Standards & Testing Division, Geotechnical Engineering Office, Hong Kong Special Administrative Region:

(a) Large Scale Impact Test and Computer Services for Investigation of the Structural Response of Rigid Barrier subjected to Boulder Impact.

(b) Further Large-Scale Impact Test on Structural Performance of Rigid Barriers subjected to Boulder Impact.

Disclaimer: “The Government of the Hong Kong Special Administrative Region does not accept responsibility for the accuracy, completeness or up-to-date nature of any reproduced versions of the material”

Signature: _____

Date: _____

Acknowledgements

I would like to express my deepest gratitude to my supervisors Professor Nelson Lam and Dr Mahdi Miri Disfani for their continuous guidance throughout this study. Their patience, motivation and immense knowledge have helped me to shape my current research pathway. Besides my supervisors, I would like to extend my appreciation to the support provided by Professor Emad Gad, Dr Scott Menegon and Mr Michael Calton at Swinburne University in all laboratory experiments.

My gratitude also goes to my fellow postgraduate colleague Dr Arnold Yong, Dr Shihara Perera, Dr Mahil Tharindu Pathirana and Ms Zanoofer for their constant support and help in both providing me research ideas as well as aiding my laboratory works.

I am also thankful to The University of Melbourne for providing me with a postgraduate study opportunity as well as the scholarship.

I would like to acknowledge the Head of the Geotechnical Engineering Office and the Director of the Civil Engineering and Development, the Government of the Hong Kong Special Administrative Region, for the permission to publish the material.

Last but not least, I would like to thank my parents and friends for their constant support and encouragement throughout my candidature.

Chapter 1: Introduction

This chapter outlines the background (section 1.1) and objectives (section 1.2) of the research. Finally, section 1.3 includes an outline of the remaining chapters of the thesis.

1.1 BACKGROUND

The occurrence of rockfall is related to landslides [1], earthquakes [2], jointing, chemical degradation and weathering [3], water effect, freeze-thaw [4] and tree roots [5]. Most commonly rockfall arises alongside landslides. The impact force of debris flow occurring from a landslide basically consists of two parts: the dynamic pressure of the debris flow and the impact force of a boulder. The latter typically causes severe damage to structures [6]. Figure 1.1 illustrates a rockfall scenario occurred with landslide and caused damage to a school building in Fushi town's Liuliao village in southern China. Some of the fallen rocks have been reported to be as large as 2 m in diameter. Traffic interruptions, structural damage, and sometimes fatalities are common due to rockfall in mountainous areas. For example: floods, landslides, debris flows, rockfall and rockslides caused some US\$198 million of damage in Switzerland in 2018 alone [7].



Figure 1.1 Vulnerability of a rockfall impact (Fushi town's Liuliao village)

In areas that are subject to such hazards including many parts of Switzerland, France, Northern Italy, Ohio State of Japan, South China and some overly congested metropolitan areas across Asia (e.g. Hong Kong), protective structures such as earth dams, nets, ditches, sheltering structures and reinforced concrete (RC) barriers have been erected to provide protections as passive protection measures. Thus, the total cost

invested in disaster management in these areas has increased rapidly in recent years. For example, as at 31 Mar 2019, Hong Kong city alone spent about \$23.6 billion under Landslip Prevention and Mitigation Programme (LPMitP) [8]. Safe, reliable, and robust transport corridors, especially along the coastal area, are crucial for the continued economic growth of any country. Recent investments in rockfall protection nets along Great ocean road can be taken as one such example in Australia.

Selection of a particular type of protection method typically depends on the application, hazard intensity, material availability, constructability and etc. Earth dams are massive, intrusive and require ample accessible space to build thereby posing safety issues in mountainous areas. Catchment ditches used to dissipate the block's energy before it reaches the embankment. A ditch is most often associated with the embankment at the end to collect the intercepted blocks [9]. In contrast, concrete barriers occupy much less space than earth dams but require a layer of materials to be placed on surfaces that are exposed to impact by boulders to function as “cushion”. For example, rockfall sheds (that are commonly found in Switzerland) are typically covered by a layer of sand or gravel to cushion the impact of fallen rocks. Deformable rock restraining net barriers are also quite common as the construct time of these net systems. Initial costs are comparatively low compared to many other protective structures. The deformation of the structure is very large in the case of rockfall and replacement of the net system is necessary for each event. Thus, the maintenance cost of these structures are higher [10]. In places like Hong Kong where land space availability is limited, rigid concrete barriers are commonly used as passive protective measures and cushion material (such as rockfill gabion) is used to shield the barrier from localised effects. The focus of this thesis is thereby narrowed down to RC barriers with cushion cover.

The layer of sandy or gravelly materials is normally designed to reduce the intensity of the contact pressure that is potentially generated by the impact of a boulder in view of the risks of the RC protective slab being punched through at the point of contact [11-17]. The effectiveness of the gabion cushion layer in enhancing the impact-resistant capacity of a concrete surface has been investigated [18-21]. These studies were mainly about controlling localised damage to the protective structure surrounding the point of contact. However, a rockfall barrier which is subject to horizontal impact by fallen boulders can be subjected to both an impulsive action and localised action of

the impact. Failure associated with the impulsive action of an impact can be in the form of flexural failure of the cantilevered wall or the overturning of the (free-standing) barrier as a whole. Intuitively the layer of gabion cushion placed in front of the barrier is believed to have mitigated the impulsive action of the impact, but no study has been reported in the literature to quantify the increase in stability of the barrier as a whole. In summary, current design practice does not consider the contribution of the cushion layer on the global response behaviour of the barrier.

Forced based (FB) models are conventionally used in design practices which essentially provide estimates of forces that are built up at the point of contact between the impactor and the cushion material placed in front of the barrier (or on top of the shelter). Substantial experimental investigations have also been carried out to ascertain this peak value of the highly transient contact force as well as the force transmitted to the concrete surface through the cushion layer [11, 13-17, 22-28]. Those investigations added useful intuitions into the use of different cushion materials to control the peak contact force thereby minimising the damage to the surface of the barrier. However, the concept of applying the estimated peak contact force onto the barrier in a quasi-static manner essentially disregard the transient nature of the impact action and the time-dependent inertial reactions that are generated within the barrier on impact. This leads to overly conservative predictions of the global effect of the barrier thus less economical design. Therefore, such inertial reactions must be considered in analysing the response behaviour of the barrier.

The alternative displacement-based (DB) modelling methodology has been proposed for use in estimating the deflection demand of a beam element taking into account the impulsive action (as opposed to the localised action). The principle of conservation of momentum and energy was employed in deriving closed-form expressions that can be used for estimating the peak deflection demand of the beam that has been struck by the impactor [29, 30]. When applying the DB methodology, the momentum transfer is taken to be instantaneous hence the effects of cushioning have not been factored into the calculation.

Placing a layer of gabions filled with gravels/crushed rock can potentially introduce fundamental change to the nature of the impact of a solid object that has been accelerated to strike the concrete surface. This change is to do with the duration of contact being prolonged significantly. In situations where the duration of contact is

much longer than the response time of the targeted element (which can be taken as one-quarter of the fundamental period of vibration of a linear elastic system) the principle of conservation of momentum (as described earlier) is no longer applicable.

In summary, the current design practice has been disadvantaged by these deficiencies and resulted in vast economical loss. The amount of global displacement incurred by a solid impact to a cushioned RC barrier cannot be predicted with confidence by the currently available calculation methods because of the complexity of the impact and the lack of available large-scale experimental validations.

1.2 RESEARCH OBJECTIVES

The main research objective of this thesis is to investigate the primary global response behaviour of a RC barrier which is protected by a gabion cushion layer subjected to impact action. Modelling of localised damage at the vicinity of impact is not studied as the cushion alleviate localised damage substantially. This research project also intends at developing a simple analytical solution that can be employed in a design environment to estimate these response behaviours. The main research objectives that are reported in this thesis are outlined as follows:

1. Provide a critical review of international literature available on the current design approaches and methodologies of protection barriers covered with cushion layer subjected to impulsive action.

2. Provide a review of studies carried out at the University of Melbourne in recent years towards designing of structures to resist impact actions.

3. Characterising gabion boxes available in the market in terms of mechanical properties.

3. Develop a two degree of freedom (2DOF) model for estimating the amount of contact force and bending displacement of a rigid barrier covered by a gabion cushion layer following an impact action.

4. Develop a simplified design methods that can be easily implemented in practice based on the use of a 2DOF model developed in objective 3.

5. Conduct a series of small-scale and large-scale impact experiments aimed at addressing all knowledge gaps.

6. Evaluate the validity of the model that has been found to perform best (objective 3 and objective 4) against test results recorded from physical experiments forming part of the study (objective 5).

7. Provide design examples and industry application on the use of the model developed in objective 4

All the listed objectives are addressed in the thesis chapters as introduced in the following paragraphs.

1.3 THESIS OUTLINE

To date, gabion has only been used to prevent localised damage to a RC structures. Global reduction of flexural behaviour due to the presence of a cushion layer is neglected. This can lead to the overdesign of structures. The first objective of this thesis is to carry out a systematic review of existing models and experiments that have been reported in the literature, along with guidelines and codes of practices. Chapter 2 provides a review of the existing design methodologies and calculation models (numerical and analytical), as well as major experimental and numerical investigations that have been carried out.

It was found that previous studies on barriers with a cushion layer are limited mostly to experiments where the focus was about controlling localised damage. Only a few studies made an attempt to derive an analytical model. Some of these developed models are empirical in nature, or only focused on calculating the contact force. No model nor design methodology are capable of accurately incorporating the mitigating effects of cushioning on the flexural response behaviour of the RC structure.

Chapter 3 considers the behaviour of the cushion layer when subjected to an impact. This chapter reviews results from small scale experimentations involving use of gabions. Experiments were performed to validate models that are already available in the literature. Contact force generated by the impact and the distribution of pressure through the cushion layer is of interest. Empirical equations from the literature were modified to be used with gabion cushions. The contents in Chapter 3 has been published in the proceedings of the 25th Australasian conference on mechanics of structures and materials (DOI: 10.1007/978-981-13-7603-0_53).

Chapter 4 is to design and perform a large-scale experimental program for investigating the bending response behaviour of a fixed base RC stem wall with the use of gabion cells (of different properties as cushion cover) when subjected to the horizontal impact of a solid object. Flexural response behaviour of the RC wall without the use of gabion cushion is also performed as a control test. Comparisons have been made to study the effect of the stiffness of the gabion cushion and the type of filling material on the flexural behaviour of the RC wall. Some recommendation of the thickness, filling material and the cage properties have been made based on results of this experimental study. The tests involved striking a 1.5 m tall and 3 m wide fixed base RC wall with impactors of three different sizes, simulating fixed foundation

rockfall barrier under boulder impact. Over 100 pieces of instruments were employed to monitor impact conditions and specimen's behaviour in response to impact. Details of the specimen, impactors, instrumentation, experimental setup and procedures are covered in this chapter. Experimental results from the relevant tests will also be presented.

Following the experimental program and results analysis, the next research objective was to provide a methodology for estimating the flexural response behavior of the RC stem wall with the aim of aiding design decisions, as presented in Chapter 5. Two Degree of Freedom modelling (2DOF) technique was employed in this study for facilitating the complex dynamic nature of RC wall and the gabion cushion under impact loading. The proposed model is first calibrated with experimental results to validate the methodology. In the end, a complete standalone calculation procedure by the use of the proposed 2DOF model without performing any experiment is presented based on empirical models developed in Chapter 3. The major findings from Chapter 4 and 5 have contributed to a technical note published by GEO: TN 7/2018 [44].

A simple closed-form calculation method is presented in Chapter 6 to further simplify the design method proposed under Chapter 5 to be used in the design office. The 2DOF model proposed in Chapter 5 is converted to a single design chart. A closed-form solution is proposed to use in conjunction with the design chart to estimate the deflection demand of the wall as well as the strain of reinforcement used. Large scale experimental results from Chapter 4 is used to validate the accuracy of the proposed simplified calculation method. Results from Chapter 4, 5 and 6 has been incorporated into a manuscript submission to the Journal of Impact Engineering.

The practical application of the proposed simplified design method is presented in Chapter 7 with regard to the design of a rigid rockfall barrier with a gabion cushion cover in the form of a design guideline. In this guideline, lateral load from debris flow which is common with rockfall has been incorporated to co-exist with the impact action of a fallen boulder. A complete calculation procedure for a real-life rockfall scenario and real scale protection wall is also presented in the format of a worked example.

Conclusions from this research project and recommendations for future research are summarised and presented in Chapter 8.

Chapter 2: Literature Review

This chapter begins with reviewing the literature in relation to the characterisation of gabion cells by means of experimental studies (section 2.1) followed by a classification of different types of rockfall protection systems (section 2.2). A comparison between RC barriers with and without cushioning is then presented in section 2.3. Local and global structural behaviour of an RC barrier under the act of impact loading is discussed under Section 2.4 along with a comparison between hard impact and soft impact. Some materials are sensitive to the rate of straining and hence behave differently under impact loading. Section 2.5 highlights the material behaviour under impact loading and the focus is being given to the behaviour of reinforced concrete. The use of a cushion layer and the basic functions of a cushion layer in a rockfall protection barrier is brought to light under Section 2.6.

The state of the art of design methods commonly adopted in impact-related structural design methodologies are widely discussed under this Chapter. Forced based designs are the most common type of design method to the date. Section 2.7 summarises some of these common models available including Hertz impact theory and standard codes (Japanese and Swiss). Displacement based design method (Section 2.8) is the alternative method of designing structures for impact loading compared to FB methods. A group of researchers at the University of Melbourne recently developed an energy partitioning method to be used with DB calculation to overcome the limitations of the DB method (which can result in the overdesigning of structures). A summary of this method is given under Section 2.9. Localized effects of the contact force are also equally important when it comes to the impact on a RC structure because of the brittle nature of reinforced concrete. Contact force at the vicinity of the impact can be very high if cushioning is not provided. Predicting this localised force based on simple experimental methods has been developed by the same group of researchers (as reviewed under Section 2.10).

Following this, basic design methods and experiments of RC structures with and without cushioning are categorised. The literature review is presented on the following topics: [Analytical models - single degree of freedom models with viscoelastic soil,

2DOF models, etc] (section 2.11); [Numerical models - Finite element models and Discrete element models] (section 2.12); [Experimental studies] (section 2.13);. Finally, Section 2.14 highlights the implications of the literature and develops the conceptual framework for the study.

2.1 CHARACTERISATION OF GABION

Gabions are rectangular steel cages made of hexagonal double twisted wire mesh or square welded wire mesh filled with appropriately sized rock particles. Simple wire mesh baskets filled with rock particles became popular in the late 19th Century as a more permanent solution to problems of erosion protection in river works and simple earth retaining structures. In the 20th Century, significant research was undertaken to study the performance characteristics of modern-day Gabion products (Figure 2.1). Steel wire coating and manufacturing techniques were also developed during this period. Today, wires are made of soft steel, annealed and zinc coated to international standards. The mechanical and qualitative characteristics of the wire, (i.e. breaking strength, elongation, and quality of zinc coating) would need to be maintained according to international standards. Although gabions produced using double twisted hexagonal wire mesh are commonly used in many countries, square welded wire mesh is common with gabion in Australia. The typical dimensions of standard gabions are shown in Table 2.1 for hexagonal twisted wire mesh and Table 2.2 for square welded mesh.

Table 2.1 Hexagonal mesh gabion cages

Hexagonal mesh type (mm)	Wire diameter (mm)	Thickness (mm)
100 × 120	2.4, 2.7, 3.0	
80 × 100	2.4, 2.7, 3.0	500
60 × 80	2.2, 2.7	1000
50 × 70	2.0, 2.4	
Width: 1000 mm – 2000 mm, Length: 2000 mm – 4000 mm		

Table 2.2 Square mesh gabion cages

Square mesh type (mm)	Wire diameter (mm)	Thickness (mm)
50 × 100	3, 4, 4.5, 5.2	300
75 × 75	3, 4, 4.5, 5.2	500
50 × 50	3, 4, 4.5, 5.2	1000
50 × 70	3, 4, 4.5, 5.2	
Width: 500 mm – 1000 mm, Length: 500 mm – 2000 mm		

Any stone or other material may be used to fill the gabion but to ensure the durability of the structure the infill material must be durable, sufficiently hard, weather-resistant, non-friable and insoluble. The most commonly used materials are river stones or quarried stones. The dimensions of the infill stones shall generally not be flaky (longest axis is not more than three times the shortest axis dimension). The most appropriate size for infill stone varies from 1 and 1.5 to 2 times the dimension of the opening of the mesh that is, the stone should be larger enough to prevent losses through the mesh [31].

2.1.1 Test on full-scale gabion

Steel wire mesh is produced to the international standard and infill material may be acquired from local sources. Strength of the infill particles and strength of the wire mesh are possible to be experimentally tested in the laboratory, but global behaviour of the gabion cage is mostly independent of these measurements. The most appropriate type of test suggested for categorising gabion cages are therefore unconfined compression test (Figure 2.1). However, particles use to fill the gabion cages are randomly configured and therefore discrepancy in the results could be very high.

A large number of experiments performed by Agostini [31] has contributed to the development of a design chart for obtaining stress-strain relationship of gabion cell as shown in Figure 2.2. Gabion cages were fabricated from 60 × 80 mm woven hexagonal mesh of wire diameter 2.7 mm. The level of compaction that could be achieved in the gabion could also influence this value and therefore both unconfined and confined gabions are being tested. According to these test results, The value of M_E

varies from 1000 kPa to 4000 kPa for unconfined conditions and about double the value for confined conditions [31, 32]

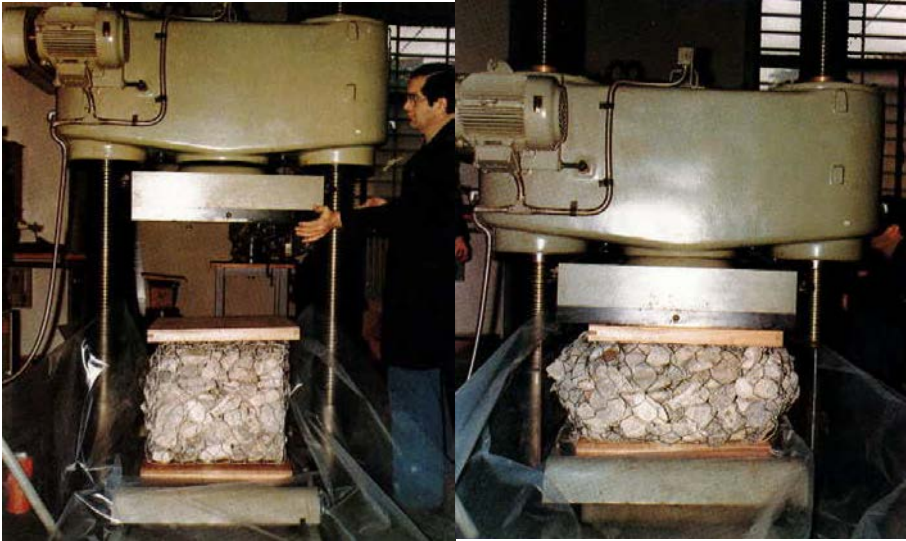


Figure 2.1 Unconfined compression test in Ref. [31]

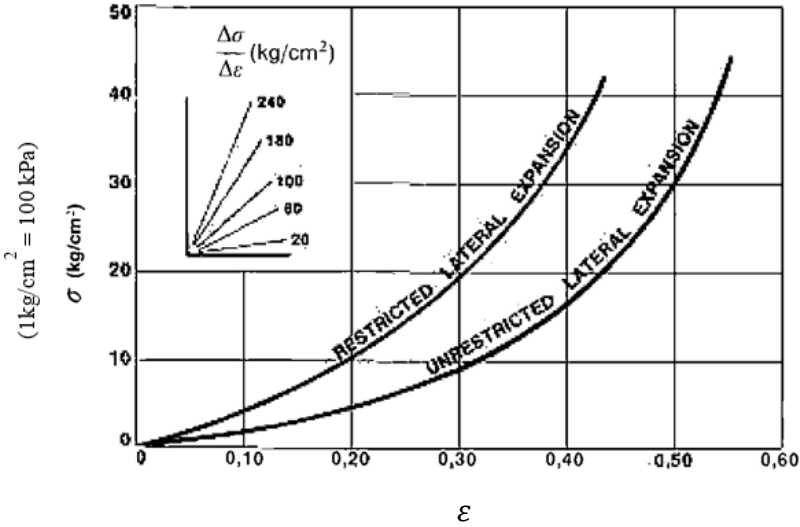


Figure 2.2 Stress-strain relationship of gabion cushion as reported in Ref. [31]

2.2 ROCKFALL PROTECTION STRUCTURES

There are lots of ambiguities involved in the prediction of rockfall hazards and there is no sufficient time to act once they occur. The level of rockfall hazard in an area is determined based on the rockfall trajectory. If there are any transport networks or infrastructure exists in these assessed areas, protection measures must be erected. Kinetic energy is usually the quantity for specifying the impact load carrying capacity (energy absorbing capability) of different protective systems. Apart from impact energy, construction cost, slope geometry, available workspace, equipment access and acceptable damage level of the structure must be considered in selecting a particular type of protective installations [33]. Comparisons of these available protection measures have been illustrated with respect to the construction cost and absorption capacity by Yoshida [33] as shown in Figure 2.3. For instance, according to this study, the construction cost of a concrete rockfall wall and mechanically stabilized earth wall are almost the same, but mechanically stabilized earth wall requires a big land area for construction and in return, it provides higher impact energy absorption capacity. The typical construction cost of a RC wall range from US\$ 2000-4000 per meter and can be constructed in an area where expected rockfall impact energy range from 100kJ to 500kJ (Figure 2.3).

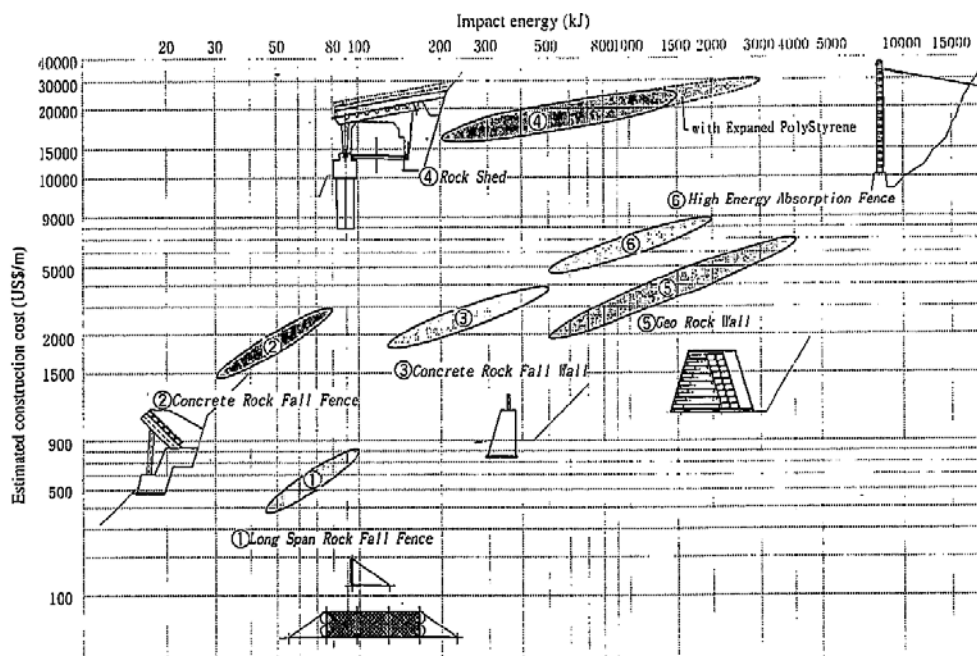


Figure 2.3 Comparison of energy absorption capacities and cost of construction per meter for different rockfall protection systems (After Yoshida [33])

Rigid concrete barriers (concrete rockfall walls) are the most common type of passive protective measure that are used in areas where space is limited (such as Hong Kong). A layer of cushion material is typically used to safeguard these RC barriers from localised damage. This thesis is only focused on the design of RC barriers with cushioning. Design of RC barriers without cushioning is also discussed for comparison purposes.

2.3 REINFORCED CONCRETE BARRIERS

Performance of RC barriers under impact loading has been first studied for projectile impacts and blast loadings [34, 35]. Later this has been extended for vehicular impact [36] and rockfall impact [14, 37-41]. Most of these studies are experimental in nature. The design methods are empirically based accordingly.

2.4 STRUCTURAL BEHAVIOUR OF AN RC BARRIER UNDER IMPACT LOADS

2.4.1 Local Structural Behavior

The impact of a boulder during a rockfall event generates strains in the impact direction at a rate higher than 0.1 s^{-1} [9]. Damage at the vicinity of impact (localised damage) is always expected at such a high strain rate. Localised damage to RC structures may include spalling of the concrete from the front face, scabbing of concrete from the rear face and partial penetration of the impactor into the structure. These failure mechanisms are further discussed in Section 2.8.3 and Figure 2.10. Until the early 1900s localised damage to structures has been evaluated mainly from military research work in the United States [35]. Until 1998, localised damage to RC structures has been only evaluated generally with empirical formulas which are based on impact experiments. As numerical analysis on fracture mechanics became more advanced, discrete element method (DEM) has been used for fracture mechanics analysis of concrete covering cracking, splitting and crushing [42]. Rockfall sheds are mainly made with slab panels placed on top of the beam layers. These slabs always fail first at the location of impact with respect to the beam elements. It was identified that concrete slabs frequently fail locally in shear with an angle of punching cone varying between about 25° and 70° during the course of the impact [43, 44]. Therefore, placing a cushion layer on top of these rockfall sheds are of immense importance in order to reduce the amount of impact energy and to minimise localised damage on the slab

panel. Apart from the rockfall galleries, cushion layers are often used for protecting rigid barriers and embankments from localised damage [9, 20, 45, 46].

2.4.2 Global Structural Behavior

The global response of a structure refers to its dynamic structural response behaviour, whereas the local response refers to indentation caused by the impact. For static loading, maximum stresses and strains occur together with maximum loading, this is no longer true for impact loading. Various analytical and numerical models have been produced for beams and slabs with respect to local and global response behaviour of the structure. In a rockfall protective barrier, global response refers to the total deflection of the barrier (which is not of interests of many because the majority of the structural damage occurs locally and more so when the gallery is not protected by cushioning).

2.4.3 Hard Impact vs Soft Impact

The impact of a flying object onto the surface of the “target” can be in either category of two conditions: (i) soft impact or (ii) hard impact. Impact action between rock and concrete can be classified as hard impact whereas impact between rock and the cushion (gabion) can be considered as a soft impact. This classification is based on the studies by Miyamoto, King [39] and is described herein.

In a soft impact, significant deformation is caused to the impactor object (or striking body), propagation of stress wave is negligible, and the mode of failure of the structure which is subject to the strike resembles failure in static conditions. In a hard impact little, or no, deformation is caused to the impactor object and the failure pattern is characterised by the effects of complex stress waves that are generated by the impact action. The duration of contact lasts much longer in a soft impact than in a hard (rigid object) impact [38]. In a soft impact, the response behavior of the structure is mainly dependent on the forcing function (time-history of contact force) delivered by the impact. The peak contact force, the duration of contact and the shape of the forcing function are all relevant to the outcome of the impact in such conditions. In a soft impact, the intensity of the peak contact force is relatively low, and the contact time is long.

2.5 MATERIAL BEHAVIOUR OF AN RC BARRIER UNDER IMPACT LOADS

It is identified from section 2.5 that the duration of contact plays a major part in the impact action. Deformation and failure of energy-absorbing structures such as the cushion layer in rockfall protection systems involve large geometry changes and interactions between inter-particles when subject to intense impact actions. The determination of dynamic strength values and stiffness for short loading periods is a viable topic of dynamic material research. Material properties like stiffness and strength increase with strain rate and sometimes reach a multiple of the static values when the loading rate is very high. With brittle materials, the ultimate strains also increase with the strain rate [47]. Different types of dynamic actions, depending on the loading rate, can result in different magnitude of strain rates as shown in Figure 2.4

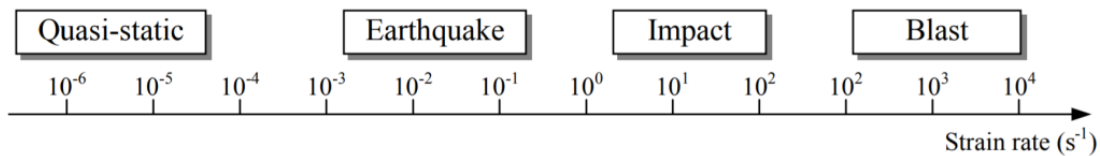


Figure 2.4 – Strain rate for different loading periods [48]

Soil behavior with high strain rates along with very high stress, applied on granular soil layer surface, could be far more complicated and different than the usual geotechnical soil modelling problems. Therefore, the identification of soil behaviour under impact condition is important in the design of cushion layers as conventional static experiments are not always useful for design purpose. Material elasticity is not likely to play an important role in the design of cushion layer which is made of highly plastic materials like foam glass [49].

On the contrary, strain hardening of concrete would need to be considered, because concrete can exhibit large ultimate strains on impact [47, 50-52]. However, the bending moment capacity of a RC section is generally insensitive to changes in the strength of concrete (unless the RC section is subjected to high axial forces or the RC section is overly reinforced which are both very unlikely). Moreover, ignoring strain rate effects in the design of the cushion and barrier both would result in conservative predictions.

2.6 FUNCTION OF THE CUSHION LAYER

The benefit of cushioning in an impact protective system is evident in view of material and structural behaviour as discussed in the previous sections. The main function of a cushion layer in a rigid barrier is to reduce localized damage to the primary structure in order that maintenance would only be required on the cushion layer. However, the absorbing cushion plays a double-fold influence on the transient forcing function. The presence of the cushion layer controls the forcing on the structure [22]. The design of the cushion layer is therefore based on two main functionalities: block deceleration and load transfer. Over the years, researchers have attempted to use various materials as cushions to fulfil these objectives. Rubber, soil, sand, expanded glass, expanded clay, recycled glass, recycled tyre and expanded clay are some examples of these materials [11, 12, 14, 16, 23-25, 27, 45, 53, 54]. Gabions are the means of using these materials in a horizontal arrangement. Sand and gravel filled gabions are tested for the performance of the RC barrier [24, 26, 45].

Designing of a RC barrier either with or without cushioning has been attempted by many researchers. Some guidelines have also been published on the design of impact-resistant structures. Following sections of the thesis are focussed on classifying those attempts into distinctive design approaches, and discuss their pros and cons.

2.7 FORCE-BASED DESIGN

Force-based (FB) design methodology can be considered as one of the oldest but simplest design method when it comes to impact engineering. The following section reviews FB design approaches developed based on experiments that are related to rockfall impact. Limitations of the FB design method are discussed at the end of the section.

2.7.1 Hertz impact equation

Simplified contact force calculation method for rockfall impact is proposed based on the use of the Hertz equation and can be found in Ng, Choi [21] and summarized herein. The elastic impact between a sphere and plane surface can be calculated based on Hertz contact theory as shown by Eq. 2.1 [55].

$$F_c = \frac{4E}{3} R^{\frac{1}{2}} (d)^{\frac{3}{2}} \quad (2.1)$$

where, F_c is the contact force (in N), E is the effective modulus of elasticity (in Pa), R is the boulder radius (in m) and d is the elastic deformation (in m). The module of elasticity (E) can be calculated using Eq 2.2.

$$\frac{1}{E} = \frac{1 - \nu_1^2}{E_1} + \frac{1 - \nu_2^2}{E_2} \quad (2.2)$$

Where ν_1 and ν_2 are the Poison's ratio of barrier and the boulder respectively, E_1 and E_2 are the elastic moduli of barrier and the boulder. Elastic deformation (d) can be represented in terms of the mass of the boulder (m in kg) and velocity of the impact (v in ms^{-1}) as shown by Eq. 2.3.

$$d = \left(\frac{15mv^2}{16ER^2} \right)^{\frac{2}{5}} \quad (2.3)$$

Substituting Eq. 2.3 into Eq. 2.1 and taking kinetic energy as $I = 0.5mv^2$ leads to Eq. 2.4.

$$F_c = 1.25E^{\frac{2}{5}}R^{\frac{1}{5}}m^{\frac{3}{5}}v^{\frac{6}{5}} \quad (2.4)$$

A load reduction factor (K_c) of 0.1 was recommended to be used by Kwan [56] to reduce the impact force calculated by use of Eq. 2.4 because Hertz equation does not consider plastic deformations. The calculations are therefore overly conservative. Eq 2.4 can be further simplified by applying typical values of Poison's ratio and elasticity modulus for a spherical boulder and concrete barrier as shown by Eq 2.5.

$$F_c = K_c 4000v^{1.2}R^2 \quad (2.5)$$

2.7.2 Modified Hertz equation

Following the same experimental study used to validate the above procedure, Geotechnical Engineering Office (GEO) of the Hong Kong government has published a geotechnical guide (GEO Report No. 270) in 2012 [56]. The modelling approach used in this report is very similar to the method used in Section 2.7.1. Eqs. 2.6 – 2.10 can be followed to determine the magnitude of the contact force between the (boulder) impactor and a concrete barrier.

$$F = K_c n \alpha^{1.5} \quad (2.6)$$

$$n = \frac{4r_b^{0.5}}{3\pi(k_b + k_B)} \quad (2.7)$$

$$\alpha = \left(\frac{5m_b v_b^2}{4n} \right)^{0.4} \quad (2.8)$$

$$k_b = \frac{1 - \mu_b^2}{\pi E_b} \quad (2.9)$$

$$k_B = \frac{1 - \mu_B^2}{\pi E_B} \quad (2.10)$$

where, K_c : Load reduction factor (which was recommended to take the value of 0.1), r_b : Radius of boulder, m_b : Mass of boulder, v_b : Velocity of boulder normal to barrier, E_b : Elastic modulus of boulder, E_B : Elastic modulus of barrier, μ_b : Poisson ratio of boulder μ_B : Poisson ratio of barrier.

GEO Report No. 270 deals with the contact force developed between a hard rock and a concrete barrier. In a large-scale experiment performed in Hong Kong University of Science and Technology used Cushioning materials (namely rock-filled gabions, cellular glass aggregates, recycled glass cullet and EVA foam) that were placed in front of a concrete barrier were struck by a hard spherical object [57]. A conservative estimate for the impact force based on the use of the Kc multiplier with a cushion protection is calibrated using the model against results from experiments. Expressions for determining the peak contact force value is specified in Lam [57].

2.7.3 Model developed by Labiouse, Descoedres [14]

Most formulas developed for determining the maximum impulsive contact force are based on the Hertz elastic contact theory. This formulation has been modified slightly by Labiouse, Descoedres [14] to take into account the non-spherical geometry of the block employed in their test as well as available modulus of subgrade reaction data for gravel cushion ($M_E = 3200 \text{ kPa}$) and shown by Eq. 2.11.

$$F_c = 1.765 M_E^{\frac{2}{5}} R^{\frac{1}{5}} W^{\frac{3}{5}} H^{\frac{3}{5}} \quad (2.11)$$

where, F_c is contact force (in kN), M_E is modulus of subgrade reaction obtained from standardised plate bearing test on the soil cushion (in kPa), R is radius of the falling block (in m), W is weight of the falling block (in kN) and H is the falling height (in m).

2.7.4 Japanese code model

A handbook including recommendations for estimate impact load with different types of protection measures has been published by The Japanese Road Association. This was first published in 1983. The new edition of the handbook was published in year 2000. The impact load (F) on galleries is given by Eq. 2.12, which is based on the Hertzian contact and this equation can be applied only for a range of application for rockfall galleries between 20 kJ and 6000 kJ.

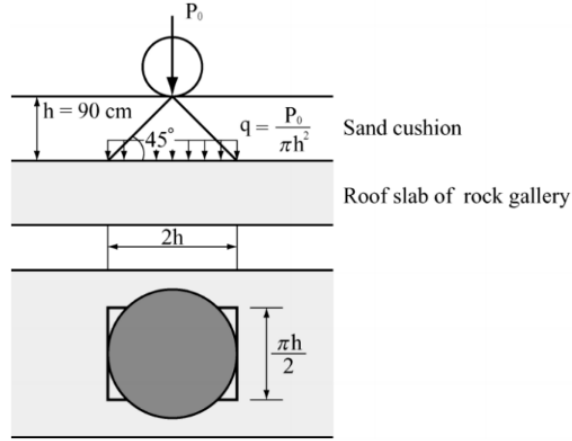
Like all the previous models, this model was also developed based on Hertz contact theory and it can be used for vertical impact on sand or soil cushion cover. Similar to Eq. 2.11 the stiffness of the impactor object is omitted because the stiffness of the cushion is relatively very small compared to the impactor object and hence dominant in the equation. Modulus of subgrade reaction in Eq. 2.11 is replaced here with *Lame's* constant (λ) which carries the same meaning and recommended to be 1000 kPa for soft soil, 3000-5000 kPa for normal soils and 10000 kPa for hard soils based on statistic data of soils and sands [58].

$$F_c = 2.108(mg)^{\frac{2}{3}}\lambda^{\frac{2}{5}}H^{\frac{3}{5}}\alpha \quad (2.12)$$

$$\alpha = \left(\frac{T}{D}\right)^{-0.5} \quad (2.13)$$

where; F_c is contact force (in kN), m is the mass of a falling rock (in ton), g gravitational acceleration (9.81 m/s²), H is the height of a rockfall (in m), α is the amplification factor for cushion thickness, D is the diameter of the impacting rock (in m)

Sand cushion layer with the conical distribution of load through the cushion layer was assumed shown in Figure 2.5. Transmitted force on roof (q) is calculated based on this assumption ($q = P_0/\pi h^2$) and applied as static load onto the roof slab.



**Figure 2.5 – Force distribution through the cushion layer
Japan Road Association [59]**

2.7.5 Swiss code model

Based on the falling-weight impact tests carried out in 1996 by Labiouse, Descoeurdes [60], the Federal Road Office of Switzerland (FEDRO) were able to derive empirical equations for an equivalent static impact force on galleries, as well as the calculation of penetration depth of the boulder into the soil. This guideline was first published in 1998 and was later released as a new code in 2008 [61] with the same technical content.

According to the ASTRA [61] code, the impact force F_c can be calculated using the Eq. 2.14 shown below which will further modify by a coefficient C , based on ductile ($C = 0.4$) or brittle ($C = 1.2$) failure of the structure to get an equivalent static force on the structure as given in Eq. 2.15. These guidelines are subjected to the limitation that the penetration depth of the cushion layer must be smaller than half of its thickness. The force distribution through the cushion layer is considered as in a 30° angle as shown by Figure 2.6.

$$F_c = 2.8 \times e^{-0.5} \times r^{0.7} \times M_E^{0.4} \times \tan \varphi_k \times \left(\frac{mv_0^2}{2} \right)^{0.6} \quad (2.14)$$

$$A_d = C \times F \quad (2.15)$$

where, e is the thickness of the cushion layer (in m), r is the radius of an equivalent sphere (in m), M_E is the soil modulus of the cover layer (in kPa), φ_k is the internal friction angle of the cover layer (in degrees), m is the characteristic block mass (in tons) and v_0 is the characteristic impact velocity (in m/s).

Surcharging the galleries with a static equivalent force is the practice used by the ASTRA [61] code, which in most cases overestimate the dynamic load. Also, the nonlinear behavior of the material in high-stress ranges was neglected in the above derivations. Therefore, the consideration of the nonlinear and dynamic response behavior of the material are important for better design practice.

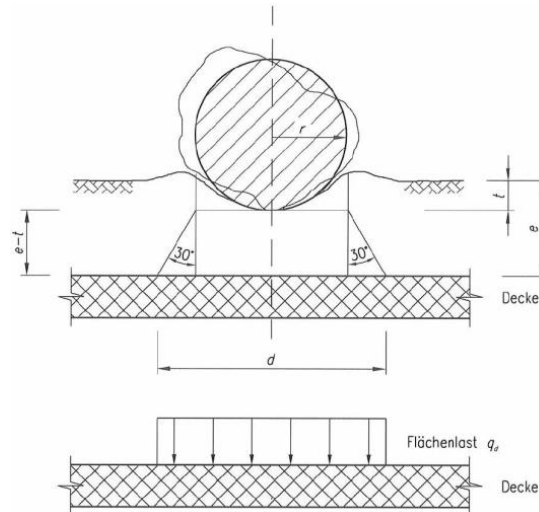


Figure 2.6 – Force distribution through cushion layer ASTRA [61]

2.7.6 Limitations of forced based design

The term “*impact force*” refers to the peak contact force which is the maximum force experienced between the target structure and the impactor at the point of contact. This contact force can be experimentally obtained by multiplying the acceleration of the impactor and its own mass. Most of the solutions for the peak contact force (as presented in the literature) gives a value of peak force which is very transient in nature and can last for only a very short duration of time to deliver an impulse to the target.

In another scenario, the term “*impact force*” can have a meaning of the “*quasi-static force*” which is the force applied to the target in order to develop the same amount of maximum deflection that can be resulted from the impact action. “*Inertia force*” is generated within the target object (or part of it) in response to the impulsive action delivered by the impact. The value of quasi-static force (F_{qs}) is equal to the difference between the contact force and the inertia force. This quasi-static force (F_{qs}) is equivalent to the product of the stiffness of the target (k) and its maximum deflection resulted from the impact action (Δ). This is illustrated in the schematic

diagram of Figure 2.7 (length of the arrow represents the amplitude of force and width of the arrow symbolizes the time it last).

In most impact scenarios the amplitude of the contact force can be an order of magnitude higher than the quasi-static force as illustrated Refs. [62] and [63]. However, when the barrier is protected by a layer of cushioning material the impact action is transformed into an impulse. The amplitude and duration of the impulse depends on the design of the cushion. The transformed impulse becomes a forcing function which is then transmitted to the barrier. This forcing function has a certain natural period which may be close to the natural period of the stem wall. If these two natural periods happen to be similar a significant dynamic amplification can occur at the target structure. This can lead to a potential scenario where the intensity of the contact force can be equal to or slightly lower than that of the quasi-static force.

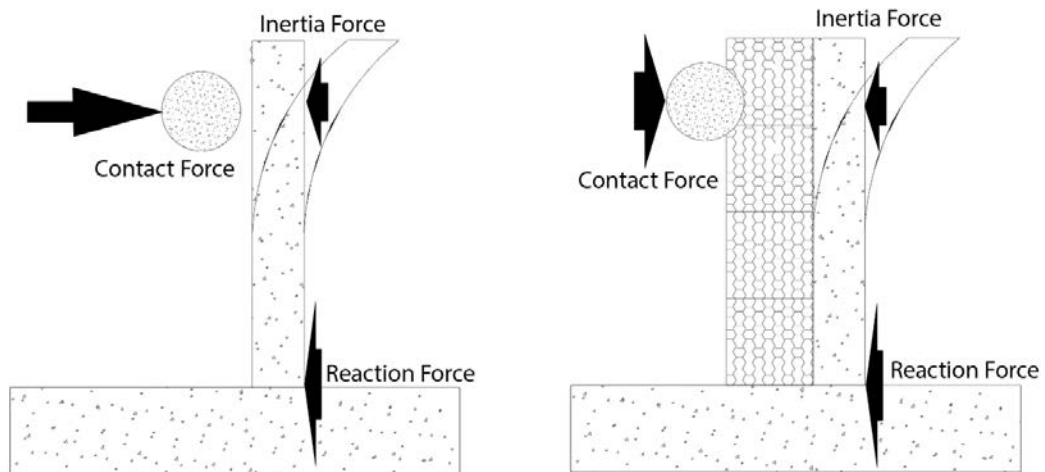


Figure 2.7 – Schematic diagram showing contact force, inertial force and reaction force

For this reason, it is erroneous to contemplate contact force as the major parameter in the design consideration of impact protective structures. Thus, force-based design methods could somewhat lead to an overestimation of the structural performance in hard impact scenarios which could lead to a not so economical design. In the case of soft impact as in gabion protected RC wall, FB designs could be unsafe. To circumvent this problem, contact force should be applied to the target in a transient manner in order to have the dynamic effects (inertia) simulated. A computer package

designed for the dynamic analysis is therefore necessary to execute the applied forcing function of this nature. This concept is demonstrated in the schematic diagram of Figure 2.8 (a) and (b) which shows the relationship between contact force and reaction force in hard and soft impact scenarios respectively.

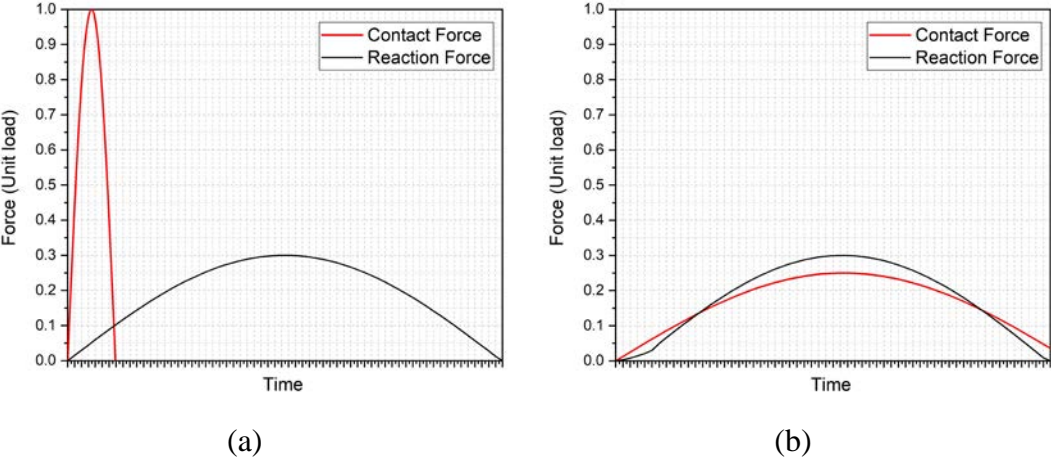


Figure 2.8 Diagrams demonstrating the difference of contact force and reaction force in (a) hard impact scenario (b) soft impact scenario

The term “*Reaction Force*” in Figure 2.8 is synonymous with the term *quasi-static force*. The *contact force* equals to the sum of the *inertia force* and *quasi-static force* and is responsible for localised damage to the surface of the target whereas *quasi-static force* is responsible for global deflection causing bending and shear of the structure. The significance of inertial resistance has been demonstrated in Refs. [29, 54, 64].

Higher rate of loading (high-velocity impact) would generate higher inertial resistance which dominates the global response behaviour. Concurrently this (*contact force = inertia force + quasi-static force*) is responsible for the higher contact force and explains the observation of damage to RC structures which are typified by punching [74] in high-velocity impact scenarios.

2.8 DISPLACEMENT BASED DESIGN

Displacement based design (DB) is an alternative way of designing structures subjected to impact hazard which is very much in alignment with performance-based design philosophy. A design methodology for countering impact action on the structure (i.e. the target) should be focused on deflection and displacement (and/or rotation).

Deflection is the most important parameter in a beam or slab element as the curvature of the deflection profile of the element is correlated with the amount of flexural stress which limits the possibilities of crushing or fracturing of the material.

2.8.1 Empirical model

The performance-based approach has been adopted in Zhan, Wang [65] to develop empirical solutions for estimating the deflection demand of a RC beam based on experiments carried out on six types of RC beam. Identical layout of reinforcement with different concrete compressive strengths and bar sizes were used in these experiments as shown by Figure 2.9 (a drop-weight of 33.6 kg was made to strike the mid-span of the RC beam). By curve-fitting the experimental results, a relationship between maximum deflection (Δ), the impacting energy (KE_0), and static flexural load-carrying capacity (F_u) has been derived as shown by Eq. 2.16. By using this equation, the displacement demand of the impact, Δ , can be calculated once the value of KE_0 , and F_u are known. This empirical formula is simple and straightforward and is also highly accurate as it is derived directly from experimental results. However, the applicability of Eq. 2.16 is limited to impact scenarios where $KE_0 < 3kJ$, $v_0 < 13m/s$ and $P_u < 30kN$ as it can only be applied with confidence for impact scenarios which the experimentations were based upon.

$$F_u = \frac{0.63KE_0}{\Delta} \quad (2.16)$$

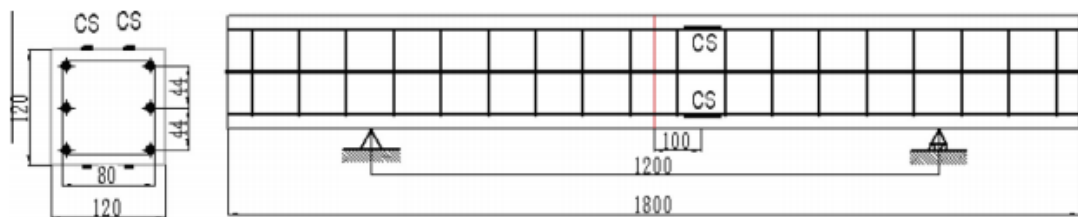


Figure 2.9 – Reinforcement layout in Zhan, Wang [65]

2.8.2 Eurocode 1 model

Equating the impacting kinetic energy to the energy absorbed by the target was adopted by Eurocode 1 as an alternative performance-based approach Ref [66]. Eq. 2.17 which is generic in nature can be used to provide estimates for the equivalent static force for hard impact (F) given that the impacting velocity (v_0), impactor's mass (m) and target's stiffness (k) can be identified easily. This calculation method essentially provides a prediction of the deflection of the barrier which is then multiplied by the lateral stiffness of the barrier to give the quasi-static impact force.

$$F = v_0 \sqrt{km} \quad (2.17)$$

2.8.3 Limitations of displacement-based design

The DB design approach is predominantly focused on demonstrating the global (overall) response behaviour of the targeted structure. Thus, the effect of failure due to the localised force has been neglected. Behaviour of a thin RC section subjected to severe impact actions can be classified into seven types of failure mechanisms [67] as depicted in Figure 2.10. The first six types, (a) to (f), can be categorized as localised damage failure modes, whereas Figure 2.10 (g) is to deal with the failure mode due to the “global” bending deformation of the target as a whole. DB design on its own would not be sufficient to design a RC protective wall from all failure mechanisms as depicted in Figure 2.10.

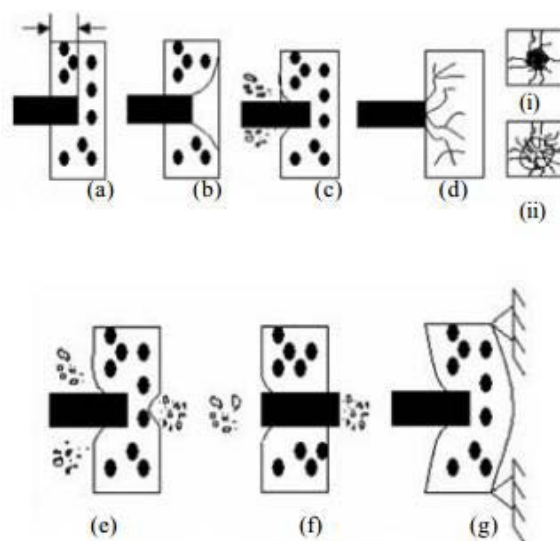


Figure 2.10 Concrete responses to impact action: (a) penetration, (b) cone cracking, (c) spalling, (d) cracks on (i) proximal face and (ii) distal face, (e) scabbing, (f) perforation, and (g) overall target structure response [67]

RC walls with thin sections are generally more vulnerable to localised damage than global deformation. However, the use of gabion cushion will eliminate most of these localised failure modes due to the much reduced velocity of impact (and hence contact force) by reducing the acceleration of impactor through interparticle interaction. Localised damage is controlled mainly by the contact force. Over the past several decades, numerous contact models have been proposed to describe the behaviour at contact between two impactor objects. The most commonly used models are introduced in Section 2.10.2.

2.9 ANALYSIS OF THE IMPACT TAKING INTO ACCOUNT ENERGY PARTITIONING

The approach of equating energy described in the previous sections does not comprise numerous energy dissipations which could occur during an impact and lead to overly conservative predictions. Energy absorbed by the target (the barrier) can be estimated with much better accuracy by considering energy partitioning. In this method, the kinetic energy delivered by the impactor object is partitioned into two parts: energy carried away by the impactor following the impact and energy absorbed by the responding target.

This DB approach with energy partitioning was initially developed by Yang, Lam [64] and further expanded for different impact scenarios by Ali, Sun [29]. It was found from early experiments that the heavier the target, the less amount of energy is absorbed by it. It was further identified that this phenomenon of energy partitioning is particularly important in situations where the barrier is much heavier than the impactor object. The parameter λ is introduced to define the ratio of the generalised mass of the target to the mass of the impactor. This has been verified by physical experimentation which involved striking the beam at mid-span by a dropped weight. The amount of energy absorbed by the target has been demonstrated to be sensitive to the value of this parameter [29, 64].

Energy is expected to be partitioned between the kinetic energy developed in the target subsequent to the impact and kinetic energy that has been carried away by the impactor object as it rebounds from the surface of the target. A reduction factor β was consequently introduced to the DB approach employing classical principles of conservation of energy and momentum to incorporate this energy partitioning into

account [64]. This has been parameterised in Eq. 2.18 for estimating the displacement demand (Δ) of the impact and in Eq. 2.19 for determining the value of the quasi-static force. Eq. 2.19 is identical to the Eq. 2.17 introduced by Eurocode 1 except for the reduction factor β as introduced herein.

$$\Delta = \beta \frac{mv_0}{\sqrt{mk}} \quad (2.18)$$

$$F = \beta v_0 \sqrt{km} \quad (2.19)$$

Separate equations have been developed to determine the value of β as shown by Eqs. 2.20 and 2.21 depending on whether the impactor is embedded (travelling together) into the surface of the target or not.

$$\beta = \sqrt{\frac{4\lambda}{(1 + \lambda)^2}} \quad (2.20)$$

$$\beta = \sqrt{\frac{1}{1 + \lambda}} \quad (2.21)$$

Eq. 2.20 assumes no energy dissipation in the course of the impact (including sound and heat) and valid for the case of an impactor experiencing “perfect re-bounce”. Eq. 2.21 was developed for impact scenario involving lightweight impactor impacting to a heavy target (higher λ) wherein impactor travels together with the target or in high-intensity impact scenarios wherein impactor gets embedded into the surface of the target instantaneously following the contact phase. Two conditions considered in Eq. 2.20 and Eq. 2.21 are two extreme ends of impact scenarios. It was identified that this model was overly conservative in the case where the impact was elastic (neither perfect rebound nor embedded).

According to Newton's law of restitution when two objects collide, their velocities following the collision depend on the material from which they are made. This measure is represented by a number called the coefficient of restitution (*COR*) which represents the 'bounciness' of the collision as a number. *COR* is simply defined as ratio of the final to initial relative velocity between two objects after they collide [68]. It normally ranges from 0 to 1 where 1 would be a perfectly elastic collision. In a more recent publication of Ref. [69], *COR* which defines the amount of energy retained in the system (which can be calculated from velocities of the two object before

and after collision) has been used to incorporate the energy lost to the surrounding (in the form of heat and sound) in calculation of β as shown by Eq. 2.22

$$\beta = \sqrt{(\alpha + \lambda) \left(\frac{1 + COR}{1 + \lambda} \right)^2} \quad (2.22)$$

where $\alpha = 1$ for an impactor becoming embedded into the target and $\alpha = 0$ for a rebounding impactor. Note, Eq. 2.20 is a special case of Eq. 2.22 when $\alpha = 0$ and $COR = 1$ representing the conditions of a perfect re-bounce whereas Eq. 2.21 deals with a special condition where $\alpha = 1$ and $COR = 0$ representing the conditions of no re-bounce.

The COR value between boulder and concrete can range from 0.18 to 0.45 based on results from drop tests that have been documented in the literature [70-72]. However, the value of COR has not been adequately studied to allow design recommendations to be given with good confidence (but $COR = 0.5$ is considered to be conservative enough).

Eqs. 2.20 and 2.21 have been validated for the case of a vertical impact in the form of drop tests, and target specimens used were made of homogeneous materials such as timber and steel [29, 73]. The effect of energy partitioning was validated further under horizontal impact scenarios by considering different target mass ratio in a pendulum impact arrangement by Yong [74]. The use of Eq. 2.22 which incorporate COR as a parameter has been also verified to reinforce concrete design which involves more complicated material mechanics [74].



Figure 2.11 – Experimental setup for cantilever lumped mass

Eq. 2.18 is only valid under the condition of elastic deformation of the target structure. Consequently, Equation 2.23 was derived for predicting the deflection of a structure assuming rigid-perfectly plastic behaviour and Eq. 2.24 for predicting deflection assuming elastoplastic behaviour [29].

$$\Delta = \frac{mv_0^2}{2F_y(1 + \lambda)} \quad (2.23)$$

$$\Delta = \frac{mv_0^2}{2F_y(1 + \lambda)} + \frac{\Delta_y}{2} \quad (2.24)$$

where, F_y is the yield strength of the structure and Δ_y is the deflection of the structure at yield as illustrated in the schematic diagram of Figure 2.12.

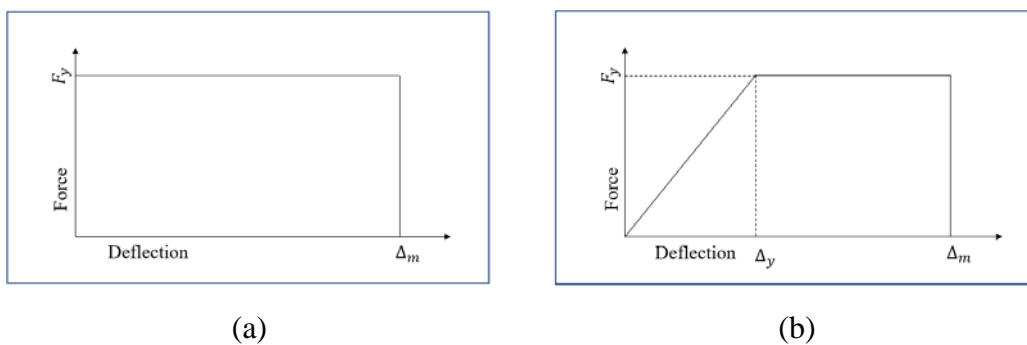


Figure 2.12 – Force displacement diagram for (a) perfectly plastic system (b) elastoplastic system

2.10 PREDICTION OF LOCALISED EFFECTS OF IMPULSE

2.10.1 Spring connected lumped mass models

Spring connected lumped mass modelling is a well-established technique in dynamic analysis that can be used for predicting the time histories of the impact force and the target deflection. In this modelling method, both the impactor and target are idealised as lumped masses and connected through springs which emulates the indentation or deflection by means of stretching/contraction of the connecting springs. Therefore, selection of an appropriate spring connected lumped mass system model based on the physical system is important. Selection of higher number of freedom system will increase the degree of accuracies of the simulated impact responses with the sacrifice of computational time. There are two common types of spring-mass model:

- (i) Single-Degree-of-Freedom (SDOF) model; and
- (ii) Two-Degree-of-Freedom (2DOF) model

A low-velocity impact of a heavy impactor to a lightweight flexible structure can be transformed into a SDOF as presented in Figure 2.13, by neglecting the contact interaction. In this model, a flexible structure is idealised as a linear spring with spring constant k_2 . Mass of the structure is assumed to be negligible compared to that of the impactors so only the mass of the impactor (m_1) is of interest. The corresponding equation of motion for the SDOF system can be written as in Eq. 2.25.

$$m_1 \ddot{x}_2 + k_2 x_2 = 0 \quad (2.25)$$

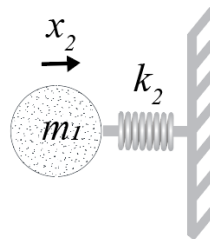


Figure 2.13 – Hard impact of a rigid body on a lightweight target

When the target is stiffer and hence the total deflection is negligible but purely elastic contact behaviour occurs between the impacting object and target, the system can be transformed to SDOF system as depicted in Figure 2.14 in which m_1 represents

the impactor mass and k_1 represents the linear contact stiffness. The corresponding equation of motion for the SDOF can be written as in Eq. 2.26.

$$m_1 \ddot{x}_1 + k_1 x_1 = 0 \tag{2.26}$$

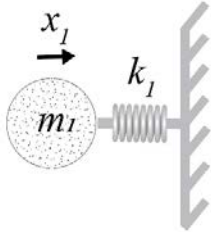


Figure 2.14 – Impact on elastic half-space

Single-degree-of-freedom (SDOF) system is the simplest form in spring-mass models. The calculation process is easier and more transparent. However, a predefined forcing function is required for input into the SDOF model. This is difficult to achieve compared to blast, wind and seismic actions.

The contact interaction between an impactor and a target structure was emulated using a 2DOF system model with linear spring by Lam, Tsang [75] and shown in Figure 2.15. Excel spreadsheet calculations with standard row and column operations are used in the calculation process which can be used conveniently by practising Engineers in the design office environment.

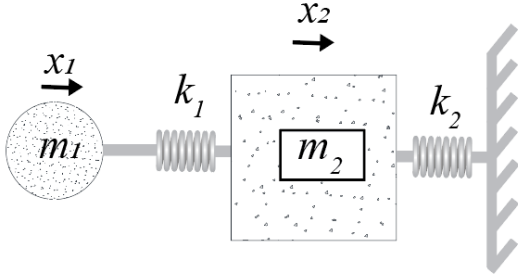


Figure 2.15 – Linear elastic 2DOF model

The Equation for the dynamic equilibrium of forces can be written as shown in Eq. 2.27:

$$\begin{bmatrix} m_1 & 0 \\ 0 & m_2 \end{bmatrix} \begin{Bmatrix} \ddot{x}_1 \\ \ddot{x}_2 \end{Bmatrix} + \begin{bmatrix} k_1 & -k_1 \\ -k_1 & k_1 + k_2 \end{bmatrix} \begin{Bmatrix} x_1 \\ x_2 \end{Bmatrix} = \begin{Bmatrix} 0 \\ 0 \end{Bmatrix} \tag{2.27}$$

Energy dissipation around the area of contact can be integrated into the above 2DOF model through a damping coefficient (D_1) as shown in Figure 2.16 [76]. This can be linear (D_l) or non-linear (D_n) depending on the simplification of original contact. The contact interaction occurred in the course of the impact is represented by a spring and a damper. The governing equations are accordingly shown as follows:

$$m_1 \ddot{x}_1 + D_l(x_1 - x_2) + k_1(x_1 - x_2) = 0 \quad (2.28)$$

$$m_2 \ddot{x}_2 + k_2 x_2 - D_n(\ddot{x}_1 - \ddot{x}_2)(\dot{x}_1 - \dot{x}_2) - k_1(x_1 - x_2) = 0$$

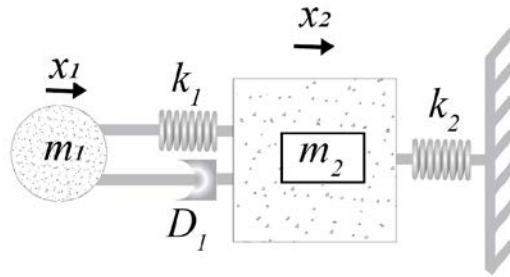


Figure 2.16 – Linear viscoelastic 2DOF model

In addition to the aforementioned models, other models have also been developed for use in impact analyses. Interested readers can find them in Refs. [57, 60, 77-83].

2.10.2 Estimating the contact force

A 2DOF system partitions the impact action into two separate parts namely the contact interaction and structural reaction. This step is important because the forcing function of an impact is not readily available unlike wind, blast, or earthquake load. Thus, the reliability of modelling of impact actions using the 2DOF system primarily relies on the accuracy of the adopted contact law and its input parameters. Theory of contact and related contact mechanisms are required to calculate the deformation and the magnitude of the contact force in the vicinity of the contact region. The first and most established theory of contact between two elastic solids was proposed by Hertz [23, 83, 84] and is based on the following assumptions:

- i. The surfaces are continuous and non-conforming
- ii. The strains are small
- iii. The target can be considered as an elastic half-space

iv. The surfaces are frictionless [83]

The relationship between the contact force and the indentation under the Hertz theory is shown by Eq. 2.29 and illustrated in Figure 2.17.

$$F_c = k_n \delta^p \quad (2.29)$$

where p is the non-linear power exponent and k_n is the Hertzian contact stiffness.

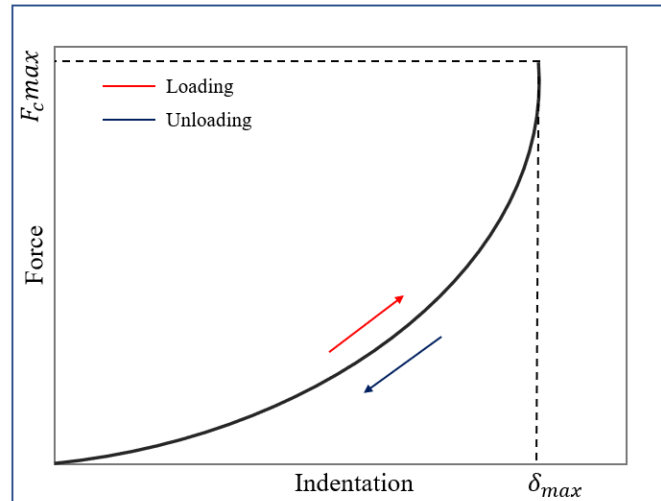


Figure 2.17 – Schematic diagram of Hertz theory

The Hertzian contact stiffness (k_n) for non-adhesive elastic contact between a sphere and a half-space is given by Eq. 2.30.

$$k_n = \frac{4}{3} ER^{\frac{1}{2}} \quad (2.30)$$

Even though Hertz Contact theory has many advantages, one major drawback of this model is that it does not account for energy dissipations. Moreover, it is noteworthy that one must satisfy all the assumptions made in theory to obtain accurate results and is limited to applications of quasi-static conditions.

Impact actions are generally associated with energy dissipation, such as wave propagation, plastic deformation, material damping, sound, and heat [85]. Plastic deformation and the material damping are identified as the main contributors to energy dissipation and hence impact process between two objects can be classified into five types: elastic, viscoelastic, elastoplastic, viscoelastic-plastic and perfectly plastic.

Energy dissipation during an impact by all different means is generally quantified by introducing a factor called the Coefficient of Restitution (COR). This is

similar to the *COR* defined in Section 2.9. The most widely used definition for *COR* is the ratio between the final relative velocities and the initial relative velocities of the two impacting objects. Practically, $COR < 1$, even though the contact is purely elastic because energy can be dissipated by other means such as sound and heat.

The type of surface deformation developed at the point of contact governs by the hardness of the impacting objects and the magnitude of the initial relative velocities. If the developed maximum contact stress from impact is less than the dynamic yield strength of the softer material of the two objects elastic indentation would occur [85]. Plastic deformation would occur at other times. This is common in high-velocity impact scenarios and impact between two materials of relatively quite different strengths.

The model introduced by Lankarani and Nikravesh [86] can be considered as a common way of modelling plastic deformation. Two different force indentation relationships are used for the loading and unloading phase of this model. During the compression phase, the contact force behaves as per the Hertz contact law. The maximum contact force is calculated at the end of the loading phase and is included in the unloading phase. Apart from the maximum contact force, maximum indentation and permanent indentation must be known to the use of this model. The Force-indentation relationship for the post-restitution phase is as given by Eq. (2.31) [87, 88]. The schematic diagram of the model is shown in Figure 2.18. Unknown parameters (F_{max} , δ_{max} and δ_p) in relation to the coefficient of restitution and initial relative velocity based on the energy and momentum considerations are also evaluated by Lankarani and Nikravesh [86].

$$F_c = F_{max} \left[\frac{\delta - \delta_p}{\delta_{max} - \delta_p} \right]^q \quad (2.31)$$

where F_{max} , δ_{max} , δ_p , and q are the maximum contact force, the maximum indentation at the end of compression phase, the permanent deformation, and the non-linear exponent for the unloading phase of the contact, respectively. The value of q is normally taken as 2.5 [89, 90].

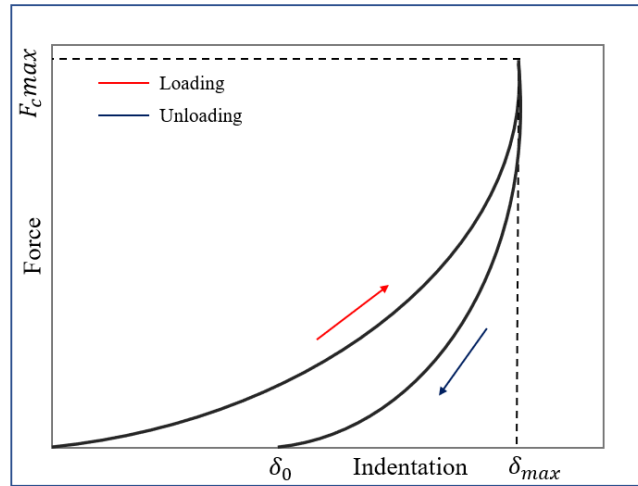


Figure 2.18 Non-linear Elastic model

Alternatively, impact action can be modelled as two components. The first component is the normal contact force based on the Hertz theory, and the second component is the damping force to account for all energy dissipation mechanisms.

In a model introduced by Kelvin-Voigt [85] (Figure 2.19), the contact force is represented by a linear spring and a linear damper for energy dissipation, as presented in Eq. (2.32):

$$F_c = k\delta + D\dot{\delta} \quad (2.32)$$

where the damping coefficient D is given by Eq. (2.33):

$$D = 2\sqrt{mk}\sqrt{(lne)^2/[(lne)^2 + \pi^2]} \quad (2.33)$$

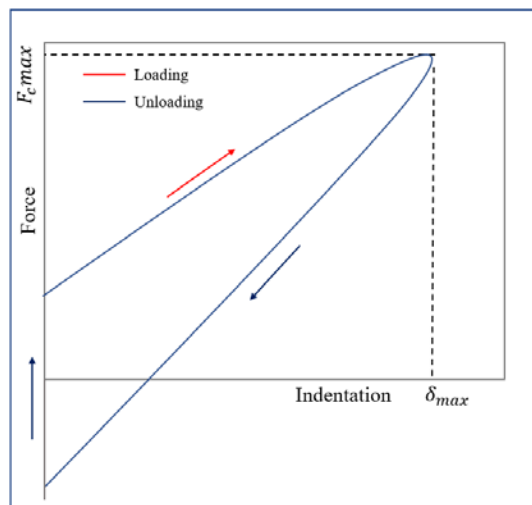


Figure 2.19 Kelvin-Voigt model

Many researchers have used the Kelvin-Voigt model because of its uncomplicatedness however simplification of the nonlinearity of real contact-impact process is the main drawback of this model. Also, the contact force given by the Kelvin-Voigt model at the beginning of impact ($\delta = 0$) violates the initial condition in an impact event ($F > 0$).

As a result, the non-linear visco-elastic contact force model developed by Hunt and Crossley [83] has become more popular among researchers. In this model, a non-linear damping term (D_n) is introduced in terms of the coefficient of restitution (COR) to accurately represents energy dissipation in the course of the contact. The relationship between COR and D_n was derived using energy balance principles.

The Hunt & Crossley non-linear visco-elastic model is presented in Eq. (2.34):

$$F_c = k_n \delta + D_n \delta^p \dot{\delta} \quad (2.34)$$

Where p , is the shape factor (for spherical objects 1.5, as suggested by Hertz), k_n is the non-linear contact stiffness, and D_n is the damping coefficient.

Note that in Eq. 2.34, contact force is a function of indentation and the amount of force attributed to viscous damping increases with increasing indentation. This simplification is logical because increasing deformation increases the contact area as well.

Much research has been conducted to determine the value of the damping coefficient (D_n). The methods that have been developed to evaluate the value of D_n can be categorized into two parts which involve:

- (i) Energy balance principles. Ex: Hunt and Crossley [83], Lankarani and Nikravesh [86]
- (ii) Equations of motion. Ex: Herbert and McWhannell [91] and Lee and Wang [92]

Hunt and Crossley [83] used energy balance principles to develop the damping factor given by Eq 2.35.

$$D_n = \frac{3\alpha k_n}{2} \quad (2.35)$$

Alternatively, more complicated damping factor, as shown in Eq. (2.36) was obtained by Lankarani and Nikravesh [86].

$$D_n = \frac{3k(1 - COR^2)}{4(\text{initial relative velocities})} \quad (2.36)$$

Although many expressions have been suggested for the damping coefficient in the literature, most are limited to use for only small deformation contact or impact, which involves little energy loss. The expression of Eq. (2.37) is more suitable for use when there are large deformation and large energy losses [93]. However, it is only valid when $p = 1.5$, as per the Hertz law.

$$D_n = \frac{8}{5} \left(\frac{1 - COR}{COR} \right) \left(\frac{k_n}{\dot{\delta}_0} \right) \quad (2.37)$$

where $\dot{\delta}_0$ is the initial indentation velocity.

A general expression for D_n for values of p other than 1.5 was derived by Sun, Lam [94] and shown by Eq. 2.38.

$$D_n = (0.2p + 1.3) \left(\frac{1 - COR}{COR} \right) \left(\frac{k_n}{\dot{\delta}_0} \right) \quad (2.38)$$

Taking into account the surface geometry through the shape factor p is the main advantages of nonlinear contact models. However, the accuracy of the contact model depends on both the contact stiffness (which controls the amount of force generated) and the damping factor or COR (which characterizes the amount of energy dissipated). Therefore, accurately calibrating these parameters are important when using these models. Small integration time step size during the simulation and the requirement of a very precise contact detection algorithm are weaknesses of these models [95].

The main advantage of 2DOF model is that it can develop results time history, but calculation process required a computer tool like Excel or MATLAB. Alternatively, closed-form expressions can be used to calculate the maximum results which are of interests to engineers on many occasions. The simplest form of closed-form solution for calculating the maximum contact force has been studied by Hertz as shown in Eq. 2.1 and Eq. 2.2. Energy dissipation occurring on contact has not been considered in the model and hence a closed-form expression was derived by Sun, Lam [96] using the aforementioned non-linear-visco-elastic model and energy balance principle. One main drawback of this closed-form solution is the assumption of a very

stiff target (i.e. k_2 close to infinity) with an infinite mass (i.e. m_2 close to infinity). This generic closed-form solution which can be used to calculate the magnitude of the contact force is shown by Eq 2.39. Selection of appropriate parameters to this equation is really important. The range of values for hailstone and for other impactor objects are illustrated in Perera [97]. Details of the derivation can be found in Sun, Lam [96]

$$F_c = k_n \left[1 + (0.2p + 1.3) \left(\frac{1 - \text{COR}}{\text{COR}} \right) \left(\frac{-b + \sqrt{b^2 + 4c}}{2} \right) \right] \quad (2.39)$$

$$\times \left(\frac{p + 1}{2k_n} m v_0^2 \text{COR} \right)^{\frac{p}{p+1}} \times \left[1 - \left(\frac{-b + \sqrt{b^2 + 4c}}{2} \right)^2 \right]^{\frac{p}{2}}$$

Where,

$$b = \frac{p \times \text{COR}}{(p + 2)(0.2p + 1.3)(1 - \text{COR})^2} \quad \text{and} \quad c = \frac{2}{p + 2} \quad (2.40)$$

Eq. 2.39, however, which was derived in Sun, Lam [96], is essentially based on the extreme value of the target mass (e.g. m_2 close to infinity), whereas the generalized mass of the target may not be much higher than the impactor mass in real situations. In view of that, Eq. 2.39 was modified by Perera [97] as shown by Eq 2.41. Note that Eq. 2.41 makes use of mass factor λ to combine both m_1 and m_2 as a combined mass.

$$F_c = k_n \left[1 + (0.2p + 1.3) \left(\frac{1 - \text{COR}}{\text{COR}} \right) \left(\frac{-b + \sqrt{b^2 + 4c}}{2} \right) \right] \quad (2.41)$$

$$\times \left(\frac{p + 1}{2k_n} \left(\frac{\lambda}{1 + \lambda} \right) m v_0^2 \text{COR} \right)^{\frac{p}{p+1}}$$

$$\times \left[1 - \left(\frac{-b + \sqrt{b^2 + 4c}}{2} \right)^2 \right]^{\frac{p}{2}}$$

2.11 ANALYTICAL MODELS

The dynamic process of rockfall impact into a cushion layer includes soil-structure interactions, soil-geosynthetic interactions, geotechnical dynamic aspects and structural dynamic aspects. Force-based (Section 2.7) and displacement-based (Section 2.8) models have been developed for analysing these behaviours in a simplified way by resolving them into local and global behaviour. In contrast, numerical modelling has an advantage of implementing complex nonlinear properties of material over-analytical models (Schellenberg [47]) but it is still a very time-consuming method for engineers to use in design practice. Before numerical simulation techniques became a common tool, most researchers used spring connected lumped mass systems for analysing complicated multi-degree of freedom dynamic systems. Simple laboratory experiments can be used to identify properties of these spring connected lumped mass models for input into software like MATHLAB or EXCEL. This section discusses some of those common analytical methodologies.

Idealising a layer of soil as spring and a dashpot is quite common in geotechnical engineering and more so in piled foundation. A similar concept is used when a solid object impact into a layer of soil cushion [47, 98-100]. Gabion cells are only idealised as spring and mass system [24, 26, 101] whereas damping is considered in models involving a layer of soil as cushion [47, 98, 102]. When the cushion layer is made of gabion cells, the compressive behaviour of the cushion can be represents by a spring the properties of which can be obtained experimentally by calibration [24, 26, 101].

These models have presumed a simplified linear material behaviour of the cushion layer and omitted the hysteric behavior of stress development under high strain rates [24, 26, 98, 101, 102] or allowed a power function [47]. Limited penetration value (μ_{lim}) value has introduced in Ref. [26] to the proposed analytical model to incorporate different possible confinement conditions that are possible with gabion cushion. For penetrations larger than (μ_{lim}), the same linear relationship can be used under rigid confinement conditions (very tightly packed gabion cushion layer with rigid boundaries) whereas the intensity of the impact force remains constant. This is the case for both free to deform (no lateral restriction) and confined (lateral restraint provided by adjacent gabion cells) conditions. Finally, for any confinement condition, the unloading phase is characterized by a strong linear decrease of the force for

decreasing penetrations as shown by Figure 2.20 (a). The behaviour of the gabion cushion layer in this model can be considered as a linear elastic-plastic model. In contrast, hardening soil behavior of the cushion layer is approximated by a hyperbola in Ref. [47], and the model is similar to a non-linear elastic model (Figure 2.20 (b)).

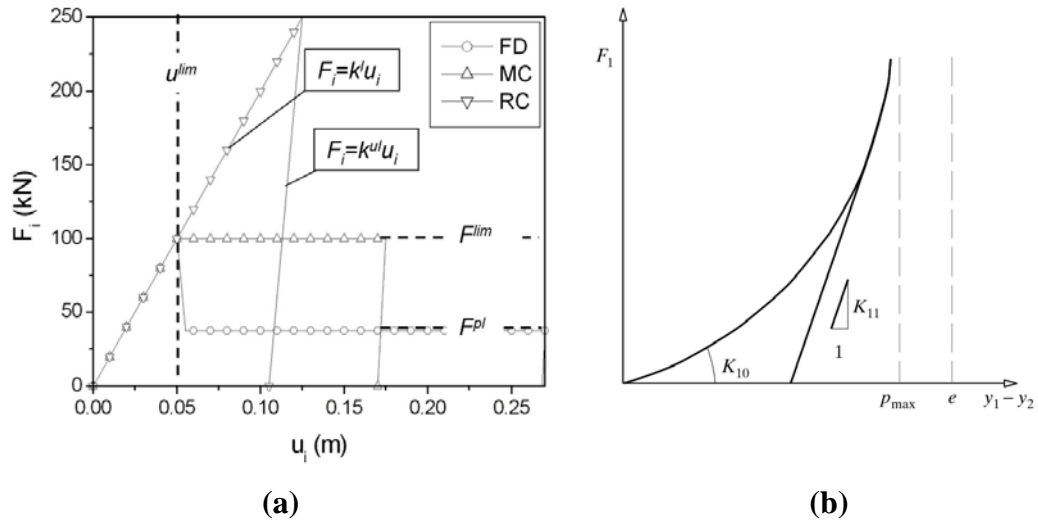


Figure 2.20 (a) Bourrier, Gotteland [26] model and b. Schellenberg [47] model

The idealisation of real impact scenario into spring lumped mass system with multiple degrees of freedom depends on the requirements of design. The higher the number of degrees of freedom systems, the more complex the analysis can become. For example, di Prisco and Vecchiotti [98] used single degree of freedom system to analyse impact force transmitted to the structure through the cushion layer (Figure 2.21). The main focus of the study was to analyse the transmitted force, and rest of the design was based around that model. Apart from the elastic spring, viscous damper, viscoelastic slider and plastic slider have also been used to idealise the interaction of the impactor and the surrounding soil as a single degree of freedom system.

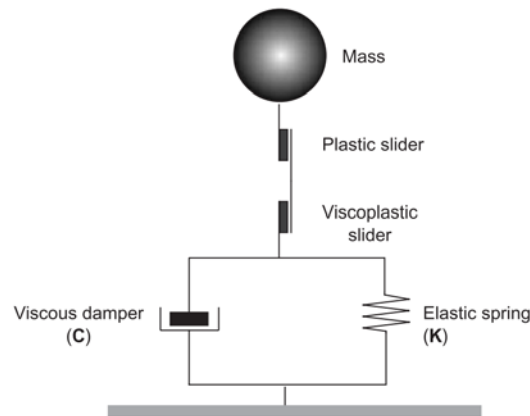


Figure 2.21 – Single degree of freedom system used by Schellenberg and Vogel [77]

Layered geo-cell system was used as cushion layer for a soil embankment by Nicot, Gotteland [24] and again the focus was only on the force transmitted to the main structure. However, the number of degrees of freedom used in this analysis was based on the number of gabion layers in actual design (instead of one spring representing the entire thickness of the cushion layer as shown by Figure 2.22). However, its worthy of note that the two springs were used to represent a single gabion cell with the mass of the gabion cell idealised at the middle of the two springs.

Design of complete rockfall protection shed using three degrees of freedom system was of interest to the study by the Schellenberg [47]. The stiffness of the structural elements (slab and column) was included in the analytical model as shown by Figure 2.23.

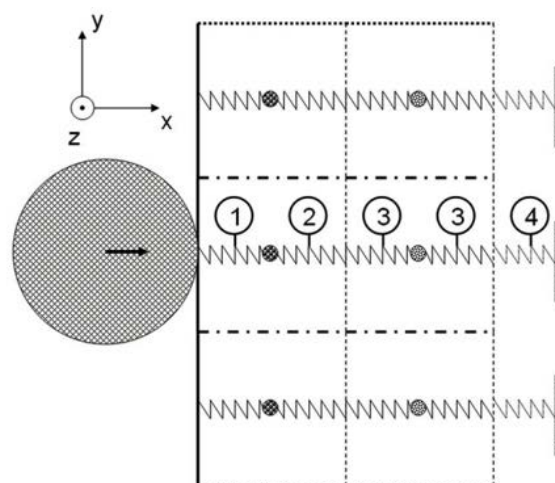


Figure 2.22 – Multi degree of freedom system used by Bourrier, Gotteland [26]

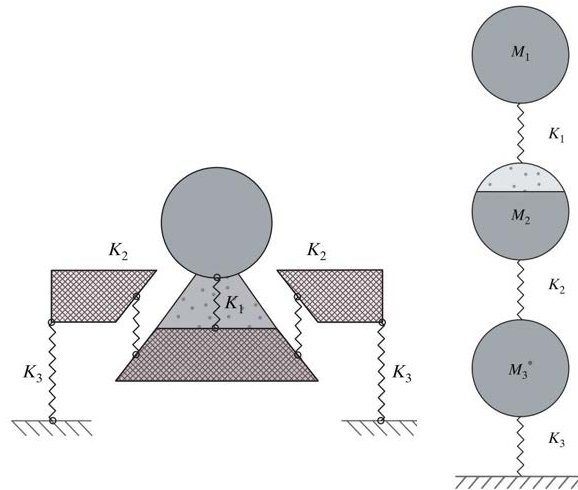


Figure 2.23 –Three degree of freedom model used by di Prisco and Vecchiotti [98]

In some of these analytical models the mass of the cushion layer was neglected in the calculation [98, 100] whereas in other models the mass of the cushion was taken as a concentrated as lumped mass at the centre of the two springs [24, 26, 101] or the end of one spring [77]. In the analytical model introduced by Schellenberg and Vogel [77] the mass M_1 represent the mass of the impactor. M_2 corresponds to the mass of the assumed punching cone in the cushion layer at the point of impact and M_3 is the mass of the surrounding structure as shown in Figure 2.23. Similarly, the stiffness matrix for the gallery was represented by three nonlinear springs: K_1 (properties of the cushion layer), K_2 (shear behavior of an assumed critical section), and K_3 (bending stiffness of the global system). In all other models, there is one spring stiffness representing the stiffness of the soil cushion.

The distribution of contact force is also of interest to models described in Refs. [24, 26, 101]. The force transmitted to the adjacent cell was defined from the standard Coulomb law with friction between adjacent cell units for the given confinement when individual cell units were considered as a group forming a cushion. In contrast, when a layer of granular material was modelled as a cushion, the punching cone at the point of impact was considered for the calculation of the model proposed by Schellenberg [47].

Once the design impact scenario has idealised into spring lumped mass model these selected parameters (i.e. mass and the stiffness) must be calibrated against

experimental results. Stiffness parameters were experimentally calibrated using real scale static tests and validated through impact tests [24, 101, 103]. In a simplified one-dimensional version of the constitutive model used by Refs. [98, 100]. Hertz theory was used for defining the non-linear elastic relationship for the spring. In addition, the values for the spring stiffness of the cushion layer at any time, when soil is used as a layer of cushion undergoing impact action as expressed by Schellenberg [47] according to an extension of Terzaghi's formulation considering the limited soil depth. More details of this calculation are expressed in Chikatamarla [99].

For practical applications, the damping properties of the structure are of minor importance because of the first or at most, the first two load peaks are important for the design load [47]. Nevertheless, the damping within the cushion layer plays a decisive character, since it cuts down the quantity of energy that is transferred to the structure. A viscous damper introduced in a rheological model by di Prisco and Vecchiotti [98] was used to take into account the damping effects due to the diffusion of the elastic waves in an infinite elastic stratum. In another study, Schellenberg [47] assumed a damping coefficient of the layer is a function of compression wave propagation velocity, density and loading area of the cushion layer. A study by Chikatamarla [99] has presented a list of damping properties of cushion layers with different materials.

In the end, all these analytical models need to be calculated using a computational tool in order to simplify the rigours recurring calculation. Even though PFC3D is a software capable of doing very complex full-scale numerical analysis it was used in Refs. [24, 101, 103] for macro-scale analysis by assuming one cell as one particle for calculating the global response behaviour of the geo-cell system. Hence computational time for the large-scale numerical model was reduced. This model was later calibrated with large-scale field experiments by the same group of researchers. The model described by Schellenberg [47] was evaluated using Excel spreadsheet. A study by di Prisco and Vecchiotti [98] used explicit finite difference numerical discretization with time to solve their differential equations. Despite the type of software used in comparison to the more sophisticated finite element models, computation time is nothing, and calculations are straightforward when computations are based on these simple analytical models.

2.12 NUMERICAL MODELS

Repeating the number of impact experiments that have been carried out is not always realistic despite physical experimentation delivers the most accurate and realistic response behavior. Therefore, software has been developed to simulate experiments on the computer so that the results of physical tests can be repeated under numerical simulations or expand the study into physically unrealistic scales. Numerical models can be used in analysing and visualizing both the effects of static and dynamic loads. Finite element modelling (FEM) and Discrete element modelling (DEM) are two different approaches to numerical simulation methods frequently used by researchers. Even though this thesis is not involved in any FEM or DEM modelling, a simple discussion of these two common modelling methods are described in the following subsections for the completeness of this review.

2.12.1 Finite element modelling (FEM)

The FEM method approximates the unknown function over the domain by subdividing a large system into smaller, simpler parts that are called finite elements. These finite elements constitute a system of algebraic equations which can be analysed to solve for a large system. Finite element modelling (FEM) software packages such as ANSYS, LS-DYNA and ABAQUS are frequently used to simulate the effects of an impact action on structures including granular cushions. A layer of granular material approximates as a continuum system with inherent properties of granular material which can ultimately simulate the behaviour of a large system as a whole (but not the behaviour of particles individually).

Selection of appropriate material models to represent the granular cushion along with parameter calibration are essential in FEM modelling. Two main software used for FEM modelling of a granular cushion layer are LS-DYNA [28, 104, 105] and ABAQUS [25]. While some FEM models are designed specifically for a certain real-life rockfall protection structures [28], many are focused on developing FEM models of standalone granular cushion layer for analysing cushioning behaviour [104, 105].

LS-DYNA alone provides more than 250 material models to be chosen by the user [106]. Selection of proper element type, material model and calibrate parameters through laboratory experiments are important to develop an accurate FEM model. Many authors used eight-node or four-node solid elements to discretise the impactor,

sand or soil layer and other structural elements [25, 28, 105] whereas reinforcement bars can be modelled using two-node beam elements [107]. Linear-elastic perfectly-plastic soil behaviour was considered to be appropriate to model cushion by Degago, Ebeltoft [25]. “Soil and crushable foam with failure” material model available in LS-DYNA was used by Sy HO and Masuya [105] for model the sand layer. The fabric material model, which is a variation of layered orthotropic composite materials, was employed to describe the mechanical properties of the textile bag [105]. Most of the material parameter calibrations are achieved through laboratory triaxial experiments of a sample which gives the stress-strain relationship of sand cushions [25, 28, 104]. Some researchers have used impact test on a sand tank to calibrate material parameters which can be very expensive [105].

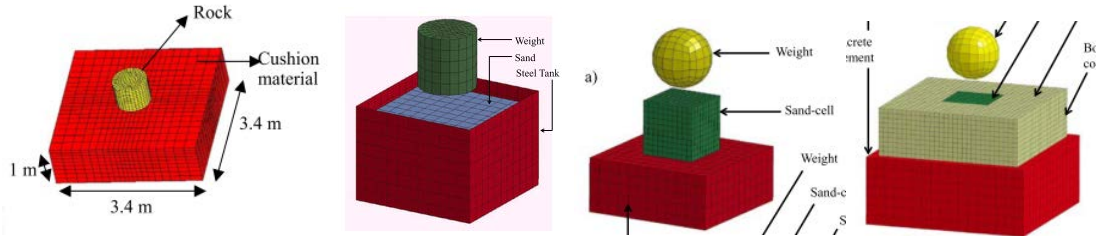


Figure 2.24 – Different FEM model used by researchers [104, 105]

2.12.2 Discrete element modelling (DEM)

It is not realistic to model discrete particles as an equivalent continuum with similar global properties because it does not thoroughly represent the discrete nature of the particle and energy dissipation through interaction (friction) between particles. As an alternative modelling methodology, discrete element modelling techniques were introduced by Cundall and Strack [108] for considering the discrete nature of the particle which is mostly found in geological materials.

In the DEM approximation, distinct particles assumed to be displaced independently from one another and interact with each other only at the contact point. The equilibrium contact forces and shifts of a stressed assembly of particles are found through a series of calculations tracing the individual particle motion. These movements of particles are the result of disturbances originating at the boundaries. The speed of propagation is a subprogram of physical attributes of the discrete medium. An initial study of this concept was modelled in a software code called BELL [108]. At the early development stage of DEM, each particle was assumed to be rigid (Distinct Element Model), but

later included the local deformation and permitted a more rigorous treatment of both the contact conditions and energy preservation requirements (Discrete Element Model) [109]. the interaction between each particle was governed by its normal and shear (tangential) stiffness (K_n and K_s), normal and shear damping (D_n and D_s) and viscosity (when particles are wet) as represented by Figure 2.25.

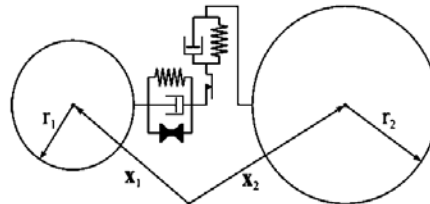


Figure 2.25 – Schematic representation of sphere-sphere interaction in LS-DYNA

DEM modelling can only be used with granular particles and all other elements (solid elements, beam elements and plate elements) have to be idealised as DEM in order to be used in the same environment. Most common commercially available software for DEM is PFC2D and PFC3D developed by Itasca consulting group which was originally founded by faculty members of the Department of Civil and Mineral Engineering at the University of Minnesota with the help of Cundal and Strack who is the very first developers of DEM. Many researchers in the rockfall impact have used PFC as a software tool to apply discrete element modelling method in solving impact problems [11, 22, 110, 111].

PFC has an advantage over other software as new constitutive relationships can be easily introduced by the user based on their requirements and is highly versatile. Generic contact constitute model which includes a numerical formula for kinetic energy on impact rebound was introduced and simulated in the dynamic process involving rock impact by An and Tannant [112]. Moreover, in Ref. [113] PFC2D was used for modelling debris-avalanche impact on earth fill barriers. Impact of rock on a layer of granular cushion was simulated using PFC2D and PFC3D [11, 22]. Furthermore, PFC 3D has been used to model the impact response behaviour of geocells [24].

The global behaviour of the DEM model predominantly depends on the mechanical properties assigned to contact between particles. Identifying these parameters and

validation of the model is important before using the model for advanced analysis. An experimental arrangement similar to the sand tank was used to calibrate the DEM model by Calvetti [22]. In a subsequent study, confined compression test of real size gabion cell (500 mm × 500 mm × 500 mm) was used to calibrate the normal and tangential stiffness of the contact model [110]. Once the contact stiffness magnitude has been assessed using a confined compression test, unconfined compression tests can be performed on the same cell to calibrate the friction angle and corresponding friction coefficients. This model has been verified for impact actions using real scale impact experimental studies [24]. Quasi-static loading was first considered on a DEM model to reproduce the mechanical characteristics of soil as filling material, and calibrated against results from laboratory tri-axial tests in Refs. [46, 114]. Since DEM particles cannot be modelled in actual scale in many cases due to high computation costs, local parameters must be chosen (through calibration) to model the mechanical behavior of a granular material at a chosen macro scale [114].

One drawback of DEM modelling is that it does not make allowance for possible element failure when modelling one element as a single particle [24]. It is important to model a single particle by the use of a cluster of small particles with breakage probability calibrated through experiments when modelling large particles of size: 80 – 120 mm. This method might help to overcome degradation process in particles under impact actions [110]. Cluster model has been used to model a gabion cell in the DEM environment as illustrated in Figure 2.26.

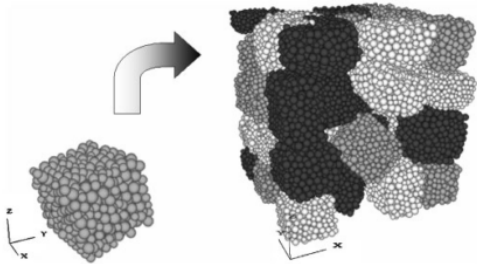


Figure 2.26 – DEM Geo-cell model by [110]

2.13 EXPERIMENTAL STUDIES

The performance behaviour of the target (barrier) is best obtained by physical experimentations. However, observations from experiments are specific to conditions of the applied actions and behaviour of the specimens that have been tested. The impact energy, type and shape of the impactor, cushion material and structural element are different in each physical experiment. Therefore, it is important to have an analytical or numerical model along with experimental data for extrapolating results for a range of conditions. This section outlines various impact tests that have been conducted on slabs, rockfall sheds, beams, walls and embankments. In addition, impact experiments on RC slabs and galleries that are covered by soil and concrete, and by a layer of gabion cell are also described. Experimental studies available in the literature are first divided into two main categories as vertical and horizontal impact tests. The methods and instruments used in the two categories of tests are significantly different. Experimental setup, method, instruments, structural elements and impactor are the main considerations of this section as that would lay the background for designing a proper physical experimental setup which is one of the main objectives of the study described in this thesis.

2.13.1 Vertical Impact experiments

Rockfall sheds are the most common type of impact protection structure encountering a vertical impact. Main structural elements in a rockfall shed are RC slab supported by a series of beams. Therefore, most of the vertical impact tests are performed based on structural elements related to the rockfall shed. Vertical impact tests are frequently reported in the literature as it is easy to perform in the field.

Real scale experimental study on rockfall sheds made of two different precast structures with a cushion layer was examined by Kishi, Konno [13]. Instead of doing an actual experiment, a prototype RC girder was used in the experimental study by Bhatti and Kishi [28] in order to validate a FEM model. The FEM model was then scaled up numerically in order to model a real rock-shed and to analyse the impact action. In another study, a small-scale steel H-beam was used with a sand tank to study the performance behaviour of different cushion materials. The effect of beam response for impact action with different span lengths of the beams from 1.3 m, 1.8 m, 2.8 m and 3.8 m have also been studied [53]. Pre-constructed structure built up of four pillars,

four foundation beams, 4 upper beams, and a roof slab of $2\text{m} \times 2\text{m} \times 100\text{ mm}$ was used in a scaled-down experiment to study the load path of the impact with a cushion [54]. The effect of cushioning in vertical impact was tested by many researchers using slab panels covered with different types of cushion materials [11, 12, 16, 22, 25]. Slab panels having different thickness with and without shear arrangements were also studied [17]. A special experimental arrangement was used to determine the radial stress and force distribution through the cushion layer and later extended that into the cracking of the slab panel. The impact force generated by a rock vertically impacting on the ground was also studied experimentally [27]

When it comes to cushioning a rockfall shed or similar impact resting structure laying a granular material on top of the structure is common. Soil has been used as the most common cushioning material in rockfall shed structures because of higher availability and lower cost [22, 23, 27]. Coarse granular sand [11, 16, 25, 53, 54] expanded clay aggregate [11], Sand [28], Cellular glass (Misapor) [12, 16, 17], Gravel [16, 53] are some of other cushion materials that are experimentally studied. As a hybrid system, Field test on impact absorbing capacity of three-layered absorbing system was studied by Kishi, Nakano [115]. This system composed of 200 - 300 mm thick RC core slab, 500 - 1000 mm thick Expanded Poly-Styrol (EPS) block as the bottom layer and 500 mm thick sand cushion as the top layer. The design procedure has also been established by the same researcher in a later publication [116]. Effect of dry density and thickness of sandy soil on impact was tested by Kawahara and Muro [23].

Most of the researchers adopted the sand tank methodology to place a layer of granular material on top of the structure. Layer thickness used in large scale experiments was varied from 500 mm [53] to 900 mm [28] whereas 100 mm to 300 mm cushion layer thickness was used in small scale experiment [23]. Steel wire net of the high tensile strength (1770 kN/m^2) and 3 mm in diameter and a layer of geotextile were used by another group of researchers to contain granular material on top of the slab [12, 16, 17]. A gabion cell made out of 2.7 mm diameter steel wire mesh with $80 \times 120\text{ mm}$ opening were used to confine gravel (size ranging from 80 mm to 120 mm) and tested for the cushioning effect under vertical impact [24]. Four lateral sides of the gabion cell were free to move (unconfined conditions) or were blocked using steel/wooden frame during the impact to compare the cushioning effect with different confinement levels.

The irregularity of the impacting rock can lead to different impact forces. Performing experiments with different shapes of impacting rocks are practically impossible. Hence different shapes of the impactor were used to overcome this issue of uncertainty. Using impact energy which is similar to the actual rockfall scenario is important in successfully demonstrating the actual rockfall impact scenario in the experiment. Real rocks and concrete have lower density and therefore the size of the rock (or similar concrete object) limits the ability to perform higher impact energy experiments, and steel was used as an alternative solution. These different types of impactors used in vertical impact experiments and recorded in literature are listed under Table 2.3. Using following impactors researchers have achieved to simulate impact energies ranging from 245.25 J to 588.6 kJ.

Table 2.3 Shapes of impactors

	[22], [13], [28], [53]
Steel shell and concrete fill	
	[11, 16]
Concrete	
	[17], [12], [27], [54]
Steel	
	[23]
Steel	
	[25]
Concrete	

Experimental layout and arrangement of relevant instruments to capture vital data is the most challenging aspects of an experiment. Accelerometer is used to record the deceleration of impacting object and hence calculate the impact force [11, 12, 16, 22,

23, 28, 53]. Accelerometer was attached on top (vertical impact) of the impacting block in the study by Gerber and Volkwein [27] whereas it was cast to the block in the centre of the block in the study by Ho, Masuya [53]. The capacity of accelerometers used ranged from $\pm 500g$ [27] to $\pm 1000g$ [28]. More than one accelerometer (4 [27], 6 [12] and 8 [16]) was also used in some studies to record deceleration in all degrees of freedoms.

Load cells were used to measure the fraction of load transmitted through the cushion layer and the slab panel [16, 22, 28, 53]. In addition to the transmitted load, the reaction force wave (dynamic wave analysis) were also of interests [28]. Four, 1000 kN load cells placed with two steel beams, concrete slab and a layer of cushion is shown in Figure 2.27.



Figure 2.27 - Load-cell arrangement in Schellenberg, Volkwein [16]

In addition to load cells, pressiometers (Figure 2.28, P1-P5) which were laid at the cushion slab interface were used for measuring of pressure acting on the slab panel [22]. Earth pressure cell is another instrument that can achieve the same objective [23]. Strain gauges were used to measure the strain in the axial direction [22, 53] and laser displacement meters were used to measure displacement waves [28, 53].

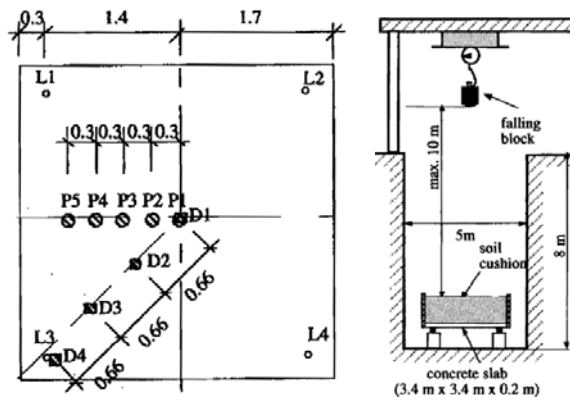


Figure 2.28 – Experimental arrangement used by Calvetti [22]

2.13.2 Horizontal Impact tests

Horizontal impact tests are less commonly found in the literature than vertical tests, due to the difficulty in nature to conduct. First multi-scale horizontal test on a cushion layer was carried out by Heymann, Lambert [19]. A pendulum setup is mainly used in horizontal impact tests [19, 21, 117]. Rolling down a boulder tough a slope [117] or long slide cable setup [18, 20] is also another possibility as shown in Figure 2.29.



Figure 2.29 – Horizontal impact experimental arrangements

Some of these experimental arrangements used soil embankment as a structural component [18, 20] and some used concrete wall as a structural element [19, 21]. A spherical impactor is used by almost all researchers.

260 kg spherical boulder was raised by a height of 4 m using a cable winch in a pendulum setup and was released to achieve 10kJ impact energy by Heymann, Lambert [19]. In a later study spherical boulder of 1.6 m diameter and 6500 kg weight was used to get more realistic impact energy to mimic real conditions. Boulder was released from different heights to produce 200 kJ to 2000 kJ impact energy [18, 20]. A boulder with similar dimensions and properties was used by another researcher with RC wall structure as a retaining structure in contrast to the earth dam used by previous researchers [21].

Gabion (geocell) is the most common type of cushion layer used on many occasions because of the confinement requirement when vertically stacked. Apart from the conventional gravel fill, feasibility of rubber and recycle glass retained inside the steel cage and used as a cushion was also tested [18, 21]. Few layers of gabion boxes with different materials (sandwich structures) was identified as a promising technical solution for rockfall impact [33]. A mixture of sand and rubber were also tested as a cushion layer [19, 20].

The steel net used for the geo-cell in these studies mainly consisted of a hexagonal wire mesh made of 2.7 mm diameter wire with 80×120 mm opening. Crushed quarry limestone, 80 -120 mm in grain size were used by [18-20] and 160 – 300 mm were used by [21]. Nine gabion cells of size $500 \times 500 \times 500$ mm were arranged in a 3×3 matrix as the cushion layer setup and confinement from other adjacent layers were achieved through a steel frame [19, 21]. In a different study, a real scale gabion cushion walls with 4×8 gabion cells arrangement was tested for real-world confinement conditions [18, 20].

Impactor was equipped with accelerometers in order to measure impact force [18-21]. Similar to the vertical impact experiments, an accelerometer was attached at the opposite side of the impacting plane [18, 19, 21] or at the centre [20].

Apart from accelerometers attached to the impactor, some accelerometers can be placed inside the cushion layer on PVC supports and protected from impact by a cap to monitor the compression wave propagation and soil particle displacement during impact [20]. Load sensors were used at the wall and cushion layer face to measure the transmitted impact force through the cushion. Noises due to high-frequency phenomena can be reduced by submitting the signals to a low-pass Butterworth filter with a cut off frequency of 1 kHz [19]. Topographical survey and seismic testing were used in subsequent experiments by the same author to measure the external deformation and damage to the protecting soil embankment at the back. Shifts within the embankment were measured using rod displacement sensors connected to six different points in the impact plane. Laser sensors with 1.5 mm accuracy were used in an experiment performed in Hong Kong in a similar experimental arrangement to measure the deformation of the cushion layer at the horizontal centreline at 100 mm

intervals. In this study, 200 frames per second high-speed camera were also used to measure the impact velocity and penetration depth [21].

Some rockfall produces energy more than 6000 kJ and that level of impact energy are difficult to achieve on the laboratory scale. As explained in the above experimental studies, researchers were able to produce impact energy up to 600 kJ in vertical tests and up to 2000 kJ in horizontal tests. Higher energies are very hard to achieve in 1g small-scale tests in lab, and full-scale field trials are mostly expensive. An alternative method was proposed by Chikatamarla, Laue [104] using geotechnical drum centrifuge to keep the stress levels in the prototype and the model equal by reducing the model size by “ n ” and increasing the gravity value by “ n ” times. Accelerometers, strain gauges, force transducers and Tekscan pressure plate were used to measure the response of the scaled-down model.

2.14 SUMMARY, RESEARCH GAP AND PROPOSED STUDY

Few experimental investigations involving impact testings of a rigid RC barrier which was fitted with a gabion cushion cover have been reported in the literature, but these investigations were limited to studying the localised actions of impact. The change of structural response behaviour of the barrier as a whole by the presence of a cushion layer is typically not within the scope of the reported investigations. All these experimental studies reviewed under this subsection are considered in the planning stage of the small-scale and large-scale laboratory experiments. Small-scale drop test (vertical impact test), small-scale pendulum test (horizontal impact test) and large-scale pendulum test were the three types of tests performed in this study.

Design methodologies that have been developed are typically limited to overly simplified calculations based on applying an equivalent static force to the barrier. To fill this knowledge gap an analytical procedure employing the Hunt and Crossley contact model, Swiss code model and two-degrees-of-freedom (2DOF) system modelling technique is presented in this thesis for calculating the flexural response demand of the cushioned barrier.

Chapter 3: Behaviour of the Gabion Cushion Layer under Impact Load

The majority of investigation reported in the literature is focused on the localised effect of the impact of the cushion layer including contact force and pressure distribution. Cushion layers that have undergone these studies comprise a layer of gravel particles without any supporting structure. Experiments over the use of gabion cushion do reported in the literature have already been discussed in Section 2.13. However, there is no report of any rigorous study on the distribution of contact force through the cushion layers. Force distribution models for a layer of granular material is presented in Section 3.1.

In view of the lack of understanding of the behaviour of gabion cushion under impact action, a series of small-scale drop tests was performed by the author to study the distribution of force through the cushion layers (Section 3.2.1). The same set of experiments were then used to validate an equation to be used with a gabion cushion which was originally developed for calculating the contact force experienced by the layer of gravels (Section 3.2.2). This model is further improved in Section 3.2.3 by incorporating the multiple impact on the same layer of gabion cushion. Finally, in Section 3.3, another set of small-scale horizontal pendulum tests were performed to modify the validated model for horizontal impact in contrast to the way the model was originally developed (vertical impact).

3.1 FORCE DISTRIBUTION THROUGH GRANULAR CUSHION LAYER

It has been proposed that the portion of the cushion material that is activated by the impact in the immediate surroundings of the contact point is funnel in shape [22, 59, 61]. For gabions that are filled with particles of crushed rocks, the angle of the funnel may be taken as 30° as per recommendations by Refs. [22, 61]. According to Stoffel [80] this value can vary from 33° to 47° . The main drawback of these studies is the assumption of forces that are distributed uniformly to the transmitted surface. In

a real impact scenario, the impact generated pressure decreases gradually from the point of impact.

According to Zhang, Lambert [118], force acting on the top of a granular layer are distributed to the bottom of the layer through force chains. These force chains were to transfer the contact force from one side of the gabion layer to the other side in a radially distributed manner. The number of force chains and the stability of those chains were higher when closer to the point of impact. This force distribution has been identified and used in their modelling approaches [81, 98].

3.2 SMALL SCALE DROP TEST

A small-scale drop test was performed by the author in order to study the force distribution in a layer of gabion cells. In addition, the same experiment was extended to identify an appropriate contact force model for gabion cells. Two different gabion fill materials were used in order to evaluate the effect of particle properties on the force distribution behaviour. The shape and roughness of the fill particles were of interests.

Pebbles and gravels were selected as fill materials for the experimental investigations encompassing extreme differences in shape and roughness properties of particles which can be used in a gabion box. Pebbles are round smooth particles whereas crushed gravels are rough angular particles. Selected pebbles for this experiment were of size 15-20 mm in diameter with an average area of 305 mm², specific gravity of 2.83, average particle crushing strength of 1890 N, repose angle of 21.9 ° and circularity value of 0.81. Gravel particles also had the same range of particle size with an average area of 389.15 mm², specific gravity of 2.68, average particle crushing strength of 2635N, repose angle of 26.4 ° and circularity value of 0.69. Circularity (C_i) value was calculated by the use of the Eq. 3.1 and a value of 1 stands for a perfectly spherical shaped particle.

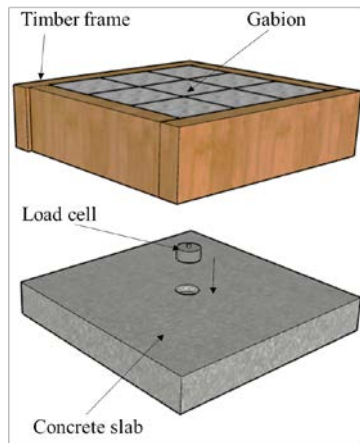
$$C_i = \frac{4\pi A_p}{P^2} \quad (3.1)$$

where, P is the perimeter length of the particle and A_p is the area of the particle when rested on a flat surface. Sieve analysis was performed for both particle types. It was found that the particle size distribution was identical and hence only the roughness and shape was dissimilar in the two selected types of filling materials.

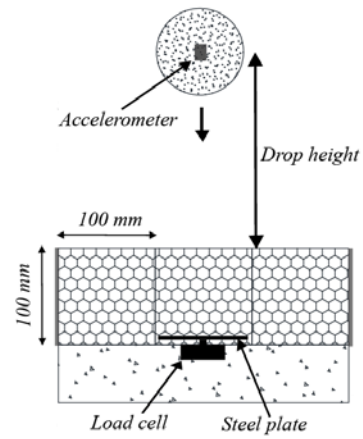
Real life gabions are rectangular cages made of hexagonal double twisted wire filled with quarry stones. Commonly available bird netting meshes are ideal for making gabion boxes in a small scale because they are made of hexagonal double twisted 0.56 mm diameter steel wires. This mesh had openings of size 13 mm from one double twist end to the other. A cubical shape gabion box with a side length of 100 mm was also made using 0.7 mm diameter lacing wires. This scaled-down gabion box represents 1:5 small scale model of 500 mm cubical shape hexogen wire mesh gabion box (details of standard gabion boxes are discussed in Section 2.1). Nine of these gabion cages were arranged in a 3 by 3 matrix, and surrounded by a wooden frame made of 90×35 mm timber planks as shown by Figure 3.1(a). Boundary conditions were fixed for gabions placed closer to the timber plank whereas the gabion in the middle was surrounded by the other eight gabions. Only the gabion in the middle was struck by the impactor object in material confined conditions.

A 5 kg weight and 50 mm radius cast iron ball which was fitted with a 2500g accelerometer (DJB A/123 Ts) for measuring the level of shock (de-acceleration) as contact was made with the gabions. The magnitude of contact force generated by the impact could simply be obtained as product of the de-acceleration and mass of the impactor. A release shackle as shown in Figure 3.3 was used to release the “ball” at the required height. The release shackle was attached to a timber beam fitted with a steel frame in a height-adjustable manner. Three different drop heights 0.5 m, 1 m and 2 m were used for comparing the change in stress distribution and energy dissipation under different impact energy levels.

A 30 kN button load cell (KELBA KPAMNC) which were embedded into small concrete slab as shown in Figure 3.1 was used to capture the transmitted force to the concrete panel. Plates varying in size (20 mm to 300 mm) as shown by Figure 3.2 were then placed on top of the load cell to study the distribution of pressure extending from the point of impact (at the centre). The timber frame with nine gabion cells was carefully placed on top of the steel plate.



(a) 3D view



(b) 2D view

Figure 3.1 Experimental arrangement

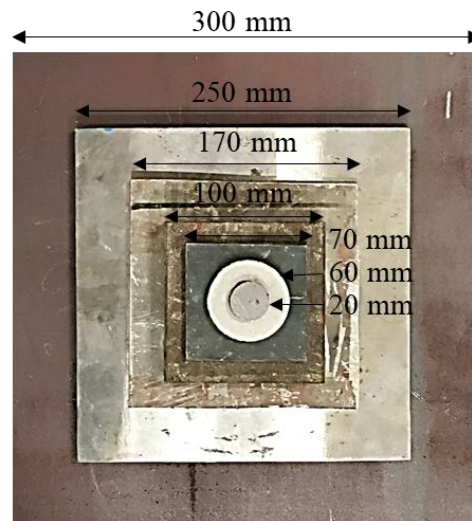


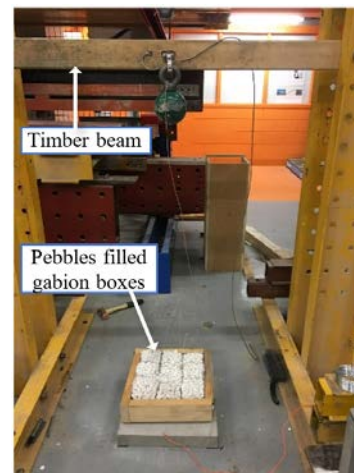
Figure 3.2 Steel plates



(a) Impactor



(b) Gravel



(c) Pebbles

Figure 3.3 Experimental setup

3.2.1 Stress distribution in cushion layer

The transmitted force recorded by the load cell with different plate sizes have been converted to stress (by dividing the transmitted force by the area of the plate). The stress distribution on the plate is shown in Figure 3.4. It was assumed that particles of up to the 95% of the stress region are within the active zone and hence contributed to the force transfer. This is presented by a horizontal line in each graph. It was found that the higher the impact energy the higher the penetration depth of the steel ball and the area of contact. Consequently the 95% stress limit moves further away from the centre with a higher impact energy.

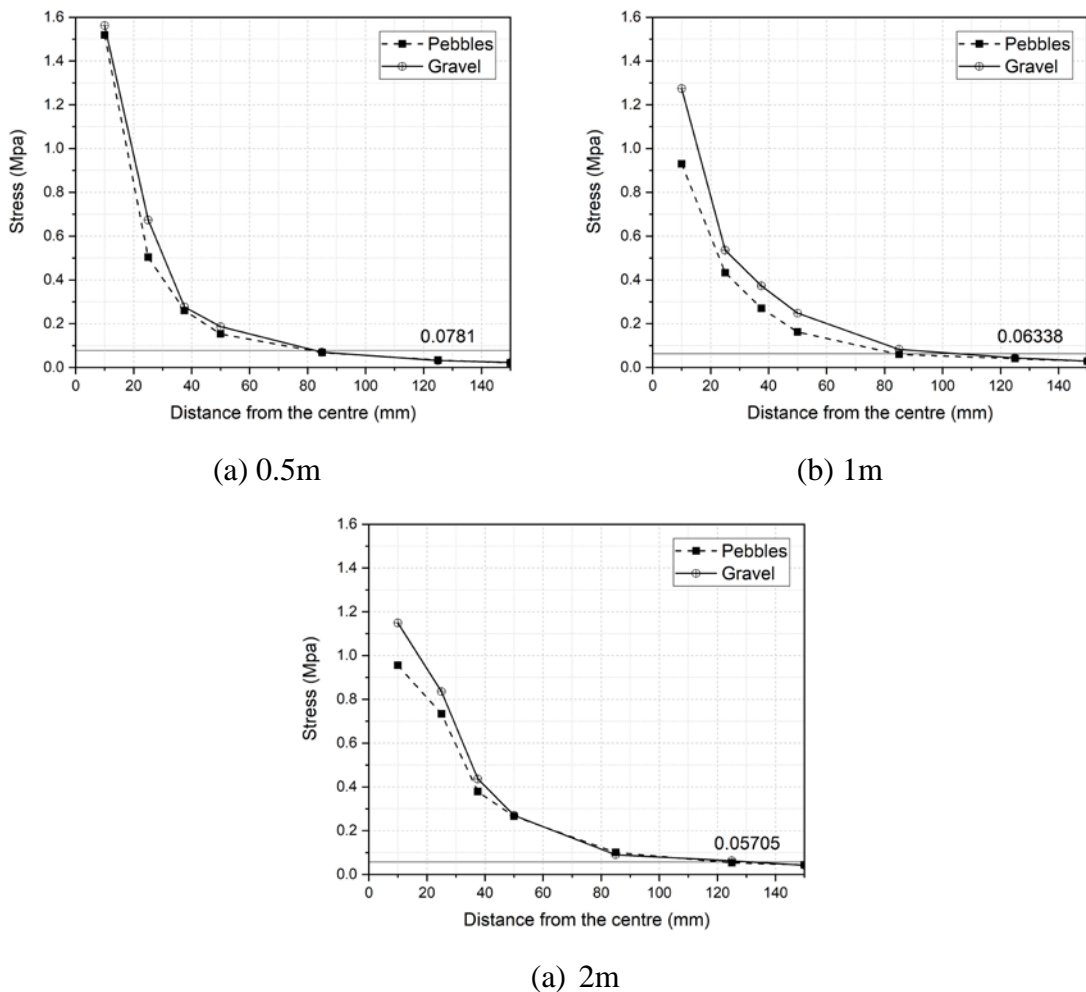


Figure 3.4 Stress distribution

The stress intensity is shown to reduce gradually from the point of impact. The intensity becomes less than 5% beyond 85 mm from the point of impact. The amount of stress transmitted to the concrete surface was slightly higher when gravel was used as filling materials as opposed to pebbles. However, this difference is negligible. It can

be inferred from the stress distribution profile that the volume of particles engaged in resisting the impact was funnel in shape as shown by Figure 3.5 (for both gravel and pebbles) showing funnel angles of 20°, 27°, 37° for 0.5 m, 1 m and 2 m drop heights respectively. This narrower angle value observed for lower drop heights could be caused by (i) gabions used in this test had not been compacted to the specified level (ii) the invalid assumption of the impactor penetrating halfway (i.e. contact surface diameter equals to impactor diameter). The angle can be wider for higher impact energy as the distribution of force changes with increased impact penetration depths. Higher stress distribution from the centre and lower peak stress at the centre was also observed for higher impact energy.

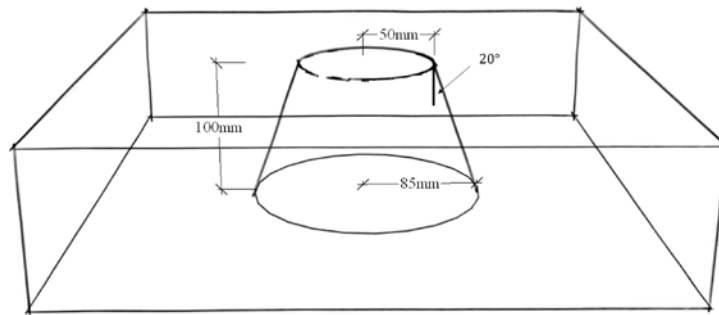


Figure 3.5 Volume of the particles under impact loading (0.5m)

The stress distribution at the concrete surface level can be presented graphically in a colour-coded profile as shown in Figure 3.6. This stress distribution can be compared with that without the cushion. Highly established Hertz method was also used to calculate the contact force distribution on the increased surface area when without cushioning for comparison purposes.

Steel impactor - $R = 50mm$, $mass (m) = 5kg$, $v_o = 4.3ms^{-1}$, $\nu = 0.3$, $E_s = 110GPa$

Concrete surface - $E_c = 30GPa$, $\nu = 0.2$

$$\frac{1}{E} = \frac{1 - \nu_1^2}{E_1} + \frac{1 - \nu_2^2}{E_2}$$

$$E = 24.7 \times 10^6 \text{ kN/m}^2$$

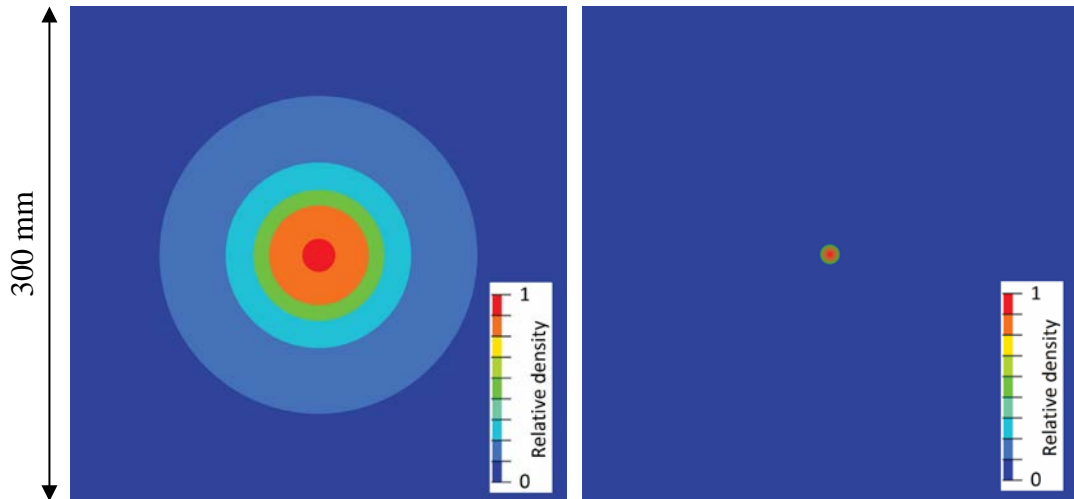
$$F_c = \frac{4}{3} E \sqrt{R} \left[\frac{mv_0^2}{E \sqrt{R}} \right]^{\frac{3}{5}} = 159 \text{ kN}$$

$$159 = \frac{\pi^3}{6} \times \frac{P_0^3 \times R^2}{E^2}$$

$$P_0 = 1958.1 \text{ Mpa}$$

$$a = \frac{\pi p_0 R}{2 E} = 12.4 \text{ mm}$$

where, a is the radius of the contact surface, R is the radius of the impactor and P_0 is the maximum pressure.



(a) With cushion ($a = 170\text{mm}$) (b) Without cushion ($a = 12.4\text{mm}$)

Figure 3.6 Stress distribution at concrete surface

3.2.2 Contact force models for gabion cushion

Numerous contact force models that have been used to guide the design of soil cushion for rockfall protection have been reported in the literature, discussed in the previous chapter, and summarised here.

The empirical formula of Eq. 3.2 for estimating contact force (F_c) is stipulated for use by the Swiss code [61].

$$F_c = 2.8 \times e^{-0.5} \times r^{0.7} \times M_E^{0.4} \times \tan\phi_k \times \left(\frac{mv_0^2}{2}\right)^{0.6} \quad (3.2)$$

Japan Road Association [59] and an article presented by Labiouse, Descoedres [60] both provided empirical formulae for estimating contact forces which are similar in form to the Hertz equation as shown by Eq. 3.3, Eq. 3.4 and Eq. 3.5 (more details are presented in Section 2.7).

$$F_c = 2.108(mg)^{\frac{2}{3}}\lambda_c^{\frac{2}{5}}H^{\frac{3}{5}}\left(\frac{e}{2r}\right)^{-0.5} \quad (3.3)$$

$$F_c = 1.765M_E^{\frac{2}{5}}r^{\frac{1}{5}}W^{\frac{3}{5}}H^{\frac{3}{5}} \quad (3.4)$$

$$F_c = 1.94 M_E^{\frac{2}{5}}r^{\frac{1}{5}}W^{\frac{3}{5}}H^{\frac{3}{5}} \quad (3.5)$$

The modulus of subgrade reaction (M_E) in Eq. 3.2, Eq. 3.4 and Eq. 3.5 or the Lamé constant (λ_c) in Eq. 3.3 is the key parameter for input into the formulae. In the Swiss code both M_E and the internal friction angle $\tan\phi_k$ are used jointly as input parameters to characterise the mechanical properties of the cushion material filling the gabions. Plate bearing test has been recommended by ASTRA [61] and Stoffel [80] for obtaining the value of M_E experimentally. The friction angle between particles (ϕ_k) as defined in Eq. 3.2 is commonly taken as 35° for normal soil and $40^\circ - 45^\circ$ for crushed rocks or pebbles [119]. M_E value of 3200 kPa is recommend for a gravel cushion layer by Labiouse, Descoedres [60] which was essentially the same experiment used for developing the Swiss code guidelines. According to statistic data collected by Masuya [58] on different soils types, $\lambda = 1000$ kPa for soft soil, $\lambda = 3000 - 5000$ kPa for normal soil and $\lambda = 10000$ kPa for hard soil is recommended. There is no recommendation for value of M_E in the literature for gravels restrained inside a

gabion box. Alternatively, static test performed on gabion boxes in laboratory environment can be used to obtain the value of M_E .

Large number of experiments performed by Agostini [31] on gabion boxes has contributed to the development of a design chart for obtaining M_E values as shown in Figure 2.2 in chapter 2. The value of M_E varies from 1000 kPa to 4000 kPa for unconfined conditions and double the value for confined conditions [31, 32]. The level of compaction that could be achieved in the gabion could also influence the value of M_E . This could depend on the infill particle properties, steel wire mesh properties and filling methods. To obtain a more reliable estimate for the value of M_E it is recommended to conduct static test on a single cell of gabion in order that specific properties of the gabion can be taken into account. The higher the assumed value of M_E the higher the predicted contact force value.

Unconfined compression test was performed on single gabion boxes using an 11kN ‘GEOCOMP’ compression testing machine to further validate the effect of particle properties on global properties of the gabion box. In addition, modulus of elasticity (M_E) of the gabion cells used in the drop test was calculated using the same unconfined compression test for higher accuracy instead of using values from the literature. Unconfined compression tests conducted by the author of the thesis recorded on average a M_E value of 2066 kPa (based on results obtained from the testing of 3 samples: 2348 kPa, 2390 kPa and 1460 kPa). A conservative value of $M_E = 3000$ kPa is recommended for material confined conditions used in the experiment. It was identified that the particle shape and the roughness have a negligible effect on the modulus of elasticity of the gabion boxes used in this test. One sample results of the stress-strain diagram of gravel filled gabion box is presented in Figure 3.7 showing results of a test conducted by the author of the thesis.

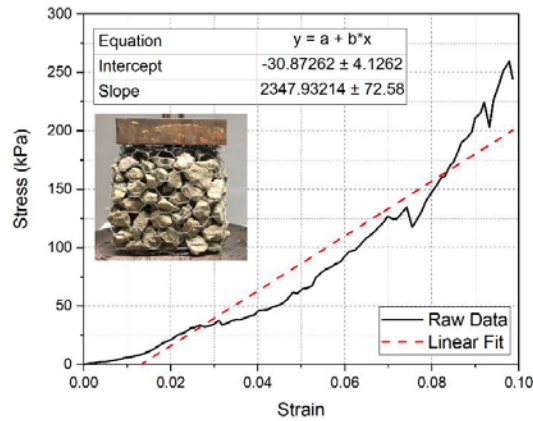


Figure 3.7 Stress-strain diagram of 100mm cubical gabion box

The accelerometer attached to the impactor in drop tests (Section 3.2) is used for measuring the level of shock (de-acceleration) as contact was made with the gabions. The magnitude of contact force generated by the impact was obtained as a product of the de-acceleration and mass of the impactor. Results from these tests are presented in Figure 3.8 as contact force time history for gravel and pebbles separately. It can be seen from results that the peak contact force is very similar for all three test heights despite the fill material. After each drop test, the middle gabion cell was replaced with a new sample.

Intermodel comparison of Eq. 3.2 to Eq 3.5 with the peak contact force recorded from small-scale drop tests are presented in the form of a bar chart in Figure 3.9. The Swiss code equation (Eq. 3.2) is shown to perform best in terms of achieving an agreement with experimental measurements. Calculations of values used for developing Figure 3.8 and Figure 3.9 (a) are presented in Appendix [A] and [B].

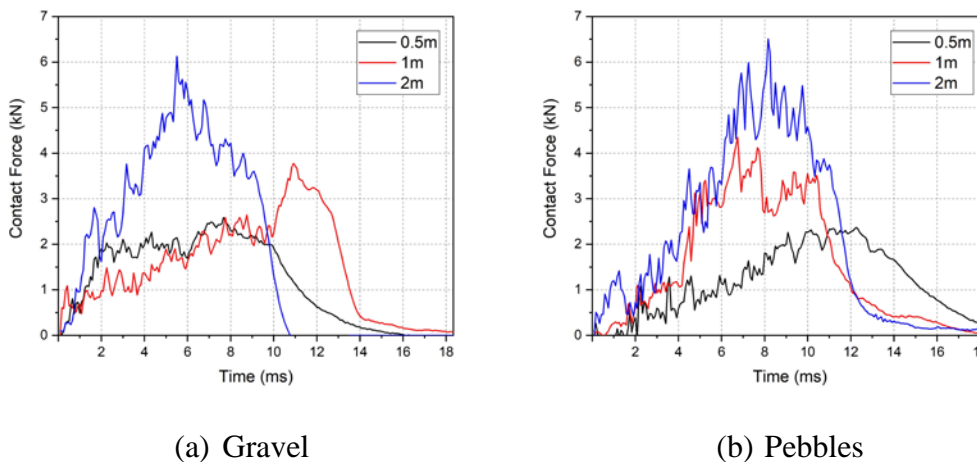


Figure 3.8 Contact force time history for small scale drop test

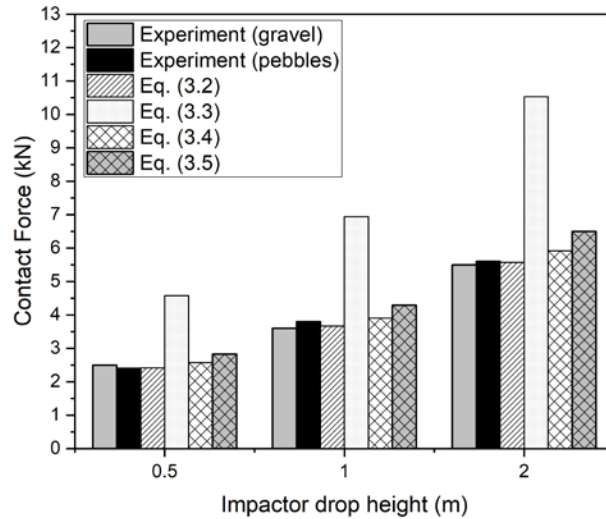


Figure 3.9 Comparison of Eq. 3.2 to Eq 3.5 with peak contact force of small-scale drop test

Although experimental results show promising agreement with calculations based on swiss code equation it's important to study the limitations of the swiss code. The Swiss guideline on the design of passive structures to resist impact was first published in 1998 and was later adapted to a new generation of SIA codes (Swiss structural codes) in 2008 [120]. There was no significant change to the technical content in the two documents. Two main points are outlined in ASTRA [61]: (a) the code is applicable for all rockfall conditions including falling, jumping and rolling of individual stones (of diameter < 50 cm) and blocks (of diameter > 50 cm) and (b) the required minimum thickness of the cushion layer to apply this code is determined as follows: Thickness of the cushion must equal to or exceed the larger of (i) 0.5 m (ii) $\delta_p + 3\phi_{max}$ and (iii) $2 \cdot \delta_p$ where both δ_p and ϕ_{max} are expressed in meters.

Guidelines stipulated in ASTRA [61] were derived from experimental studies performed by Stoffel [80] and numerical analyses undertaken by Bucher [81]. A square-shaped slab of dimensions: 3.4 m × 3.4 m × 0.2 m was subject to the impact of a dropped hemispherical shaped steel shell filled with concrete. It was revealed from experimental and numerical investigations performed on hemispherical and pyramidal shaped impactor objects that a hemispherical impactor induced higher impact force and less penetration into the surface of the target [25]. Thus, the impact of a piece of rock (with sharp corners) is expected to have lower deflection demand on the wall than what was recorded from tests when other parameters are kept unchanged. Design methods developed using a hemispherical shaped impactor object for cushioned impact is therefore conservative.

Three different types of cushion materials comprising crushed gravels, alluvial cones and scrap rocks were used in the experimental study. The geotechnical properties and particle size distribution of each material are shown in Table 3.1 and Figure 3.10 respectively. The key objective of the experimental work was in studying the impact resisting performance of the concrete slab. Numerical analyses undertaken by Bucher [81] to study contact force behavior, involved much larger impactor objects and delivered much higher amount of impact energy than experiments undertaken by Stoffel [80]. Values of parameters characterising both experimental and numerical studies are shown for comparison in Table 3.2.

Table 3.1 Geotechnical properties of cushion materials reported in Ref. [33]

Soil type	Density (kg/m^3)	Angle of friction
Gravel	1650	41
Alluvial cone	1890	45
Scrap rocks	1790	47

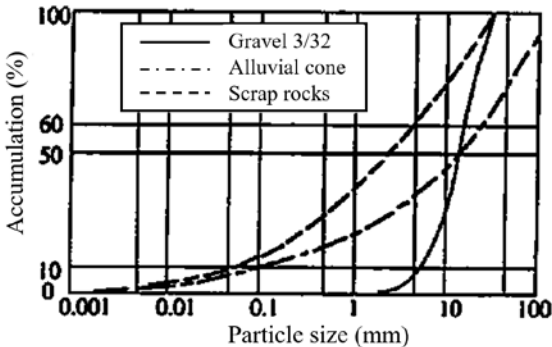


Figure 3.10 Particle size distribution curves for soil cushions reported in Ref. [33]

Table 3.2 Range of parameters used to develop Swiss code

Parameter	Experiment [80]	Numerical Analysis [81]
Impact or mass (ton)	0.1, 0.5, 1	1, 5, 10, 20
Radius of the block (m)	0.21, 0.36, 0.45	0.45, 0.77, 0.97, 1.22
Velocity of the impact (m/s)	4.4 - 14	10, 20, 30, 50
Thickness of the cushion (m)	0.35, 0.5, 1	0.5, 1, 2, 3, 4
Friction angle	42°, 45°	35°, 38°, 42°
Soil modulus M_E (Mpa)	2 - 20	15, 34, 55

3.2.3 Multiple strikes on the same cushion

When experiencing multiple successive strikes by fallen boulders, a cushion layer is expected to have been consolidated (thereby resulting in a progressive increase in the value of M_E) following multiple striking. The initial value of M_E prior to the delivery of the first strike can be obtained experimentally by conducting unconfined quasi-static compression testing of a representative sample of a gabion cell. However, determining the value of M_E which takes into account the consolidating actions of multiple striking has to be based upon results from dynamic testings (as opposed to quasi-static testings). In view of this requirement, a series of small-scale drop tests (with the same setup as Section 3.2) was carried out to model the progressive compaction of gabion materials in a multiple-strike impact scenario and the resulting effects on the contact force behaviour of a cushioned impact. Impact testings involving up to four strikes have been undertaken. The recorded contact force time-histories for a 1 m drop-test involving four multiple strikes on gravel filled cushion are presented in Figure 3.11. Empirical data of the observed peak values of the contact force were then analysed. It was identified from the experiment that the strength of the gabion cage is lesser than that of filler particles and hence the cage breaks prior to the particle breakage. Therefore, the effect of compaction is only due to the relocation of particles and not because of particle breakage. Indentation after each test was not part of this study.

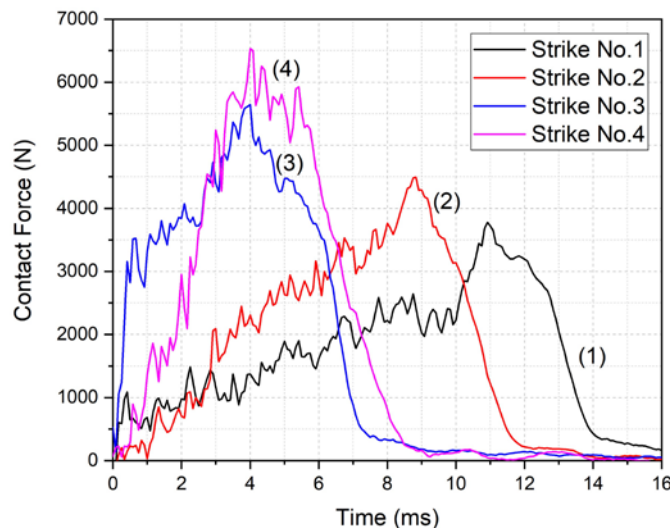


Figure 3.11 Multiple impact 1 m drop height on gravel filled cushion

The increase in value of the contact force (with respect to measurements taken from the first strike) was the focus of interest. Results obtained from tests associated with a

range of drop-heights and use gravel, or pebble, as filler materials were analysed. For example, contact force delivered by the 2nd strike was observed to be 1.19 times that from the 1st strike (4494 N/3776 N) as shown in Figure 3.11. These factors have been obtained for all other drop tests as presented in Figure 3.12. Results from the 1 m drop tests on the (pebbles-filled) cushion were found to be corrupted and hence not presented herein. These results were then subject to statistical analyses the results of which are presented in Figure 3.13.

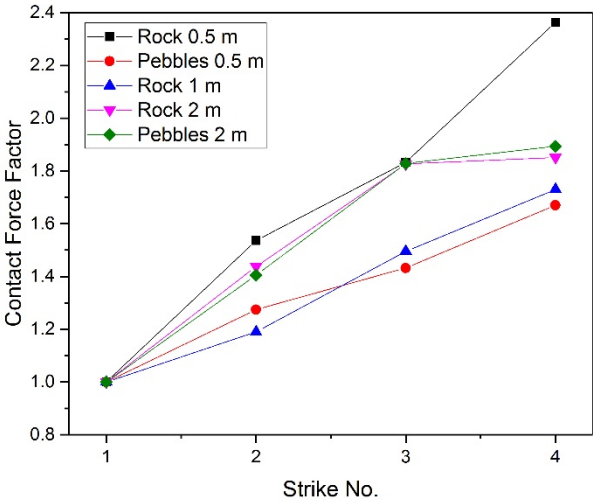


Figure 3.12 Multiple impact contact force factor for different impact conditions

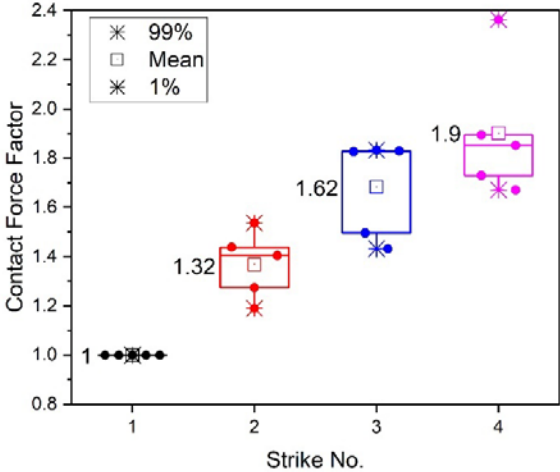


Figure 3.13 Statistical analysis of contact force factor

Given that M_E is the only parameter in Eq. 3.2 that can change in values following each strike for a given test setup, all other parameters in the predictive expression can be consolidated into a constant (C_{ME}) for the calculation of the contact force. Thus, Eq. 3.2 can be re-written as Eq. 3.6 in which C_{ME} is a constant for the given impact scenario

characterised by the velocity of impact, impactor mass, cushion thickness and the diameter of the impactor.

$$F_c = C_{ME} \times M_E^{0.4} \quad (3.6)$$

Following each strike, the cushion layer can become compacted and thus resulted in an increase in the M_E value. The integer in the subscript (denoted herein as ‘ n ’) is used to represent the “strike number”. For example $M_{E,1}$ ($n = 1$) represents the compression modulus of the cushion layer prior to the delivery of the first strike (the modulus value can be obtained from quasi-static compression testing of a gabion sample); $M_{E,2}$ ($n = 2$) refers to the value associated with the condition of the gabion prior to the delivery of the second strike, and so on. As the value of M_E increases progressively, the value of F_c would increase accordingly. The contact force factor ($C_{F,n}$) as shown in Eq. 3.7 is introduced as a multiplier to take into account the effects of the resulting increase in the contact force.

$$C_{F,n} \times F_c = C_{ME} \times M_{E,n}^{0.4} \quad (3.7)$$

Eq. 3.7 can be re-written as Eq. 3.8 for estimating the value of $M_{E,n}$ (modulus of elasticity of compacted gabion cushion) for any strike as a factor of M_E .

$$M_{E,n} = \sqrt[0.4]{\frac{C_{F,n} \times F_c}{C_{ME}}} = \sqrt[0.4]{C_{F,n}} \times \sqrt[0.4]{M_E^{0.4}} = \sqrt[0.4]{C_{F,n}} \times M_E \quad (3.8)$$

Results from the statistical analysis of small-scale tests (Figure 3.13) were then used to calculate the $M_{E,n}$ of each impact as shown below.

$$1^{\text{st}} \text{ impact, } M_{E,1} = 1 \times M_E$$

$$2^{\text{nd}} \text{ impact, } M_{E,2} = \sqrt[0.4]{C_{F,2}} \times M_E = \sqrt[0.4]{1.32} \times M_E = 2 \times M_E$$

$$3^{\text{rd}} \text{ impact, } M_{E,3} = \sqrt[0.4]{C_{F,3}} \times M_E = \sqrt[0.4]{1.62} \times M_E = 3.34 \times M_E$$

$$4^{\text{th}} \text{ impact, } M_{E,4} = \sqrt[0.4]{C_{F,4}} \times M_E = \sqrt[0.4]{1.9} \times M_E = 5 \times M_E$$

The value of M_E (or $M_{E,1}$) of the cushion layer was measured from (small-scale) unconfined compression tests to be 3000 kPa. The values of $M_{E,2}$, $M_{E,3}$ and $M_{E,4}$ are accordingly calculated as 6000 kPa, 10000 kPa and 15000 kPa respectively based on the expressions presented in the above. The amount of contact force delivered by the impactor was then estimated by substituting these $M_{E,n}$ values into the Swiss code

model of Eq. 3.2. The estimated contact force values are compared with results from the multiple impact drop tests in Figure 3.14. It can be seen from the comparison that the predicted contact force values employing the proposed methodology are generally consistent with results from the drop tests. There are a few instances where the predictions are exceeded slightly, and this is much to do with variability in the degree of compactness of the hand filled gabion specimens used in the miniature drop tests (whereas the value of the coefficients employed in the predictions is based on the mean values shown in Figure 3.14).

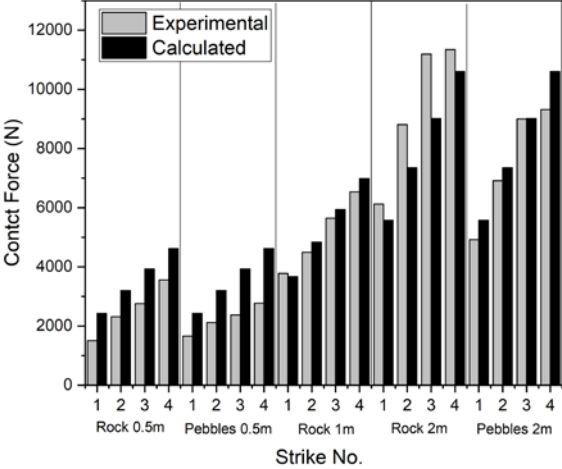


Figure 3.14 Comparison of contact force results with calculated values

3.3 APPLYING THE SWISS CODE MODEL FOR HORIZONTAL IMPACT BY A BOULDER

The validity of Swiss code equations (Eq. 3.2) in dealing with horizontal impact (as delivered by the pendulum) has yet to be established given the very different conditions that are associated with a vertical and a horizontal impact. Horizontal impact tests have been carried out subsequently using the same array of gabion cells as used in the drop tests (refer Figure 3.15 in comparison with Figure 3.3). It is shown from results obtained from the (reduced scale) impact experiments that a reduction factor need be introduced to factor down the magnitude of the contact force that was derived from drop tests if the projected impact scenario is instead a horizontal strike. Applying a reduction factor of 0.65 results in the modification of Eq. 3.2 into Eq. 3.6.

$$F_c = 1.82 \times e^{-0.5} \times r^{0.7} \times M_E^{0.4} \times \tan\phi_k \times \left(\frac{mv_0^2}{2}\right)^{0.6} \quad (3.6)$$

The modified Swiss equation of Eq. 3.6 has been verified by comparison with results recorded from a series of impact test results which featured the use of the pendulum to deliver the strike as opposed to dropping the impactor object onto the cushion; refer Figure 3.13 for the bar chart showing the comparison.

Estimates derived from the original Swiss code equation of Eq. 3.2 is also shown on the same bar chart. The need for applying a reduction factor of 0.65 is evident. A detailed illustration of the calculations for the magnitudes of the contact force that are plotted in Figure 3.16 (a) is shown in Appendix [C]. Values of input parameters used in this calculation are as follows: $e = 0.1$ m, $r = 0.05$ m, $M_E = 2066$ kN/m² (unconfined conditions), $\phi_k = 40^\circ$, $m = 5$ kg, $v_0 = 1$ m/s to 3.13 m/s.

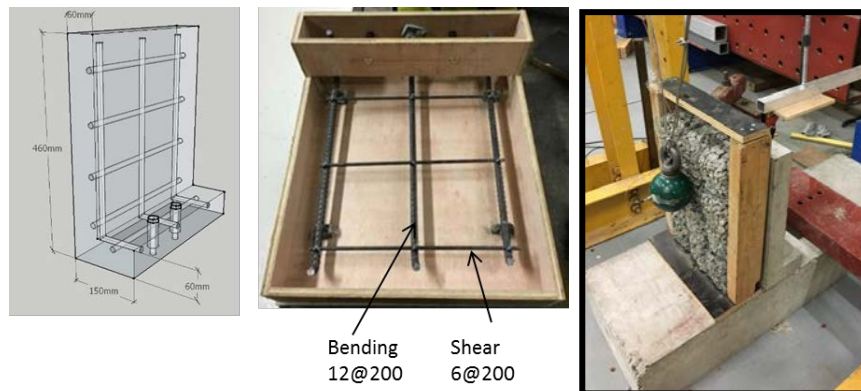
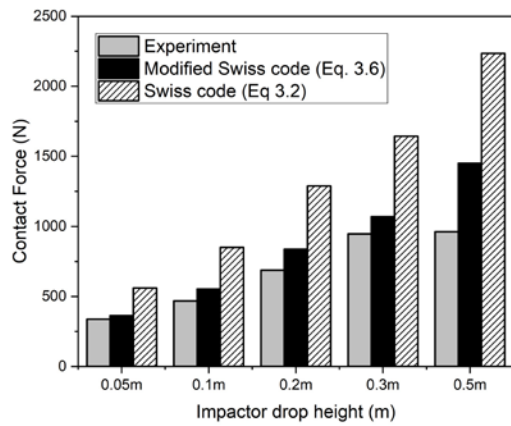
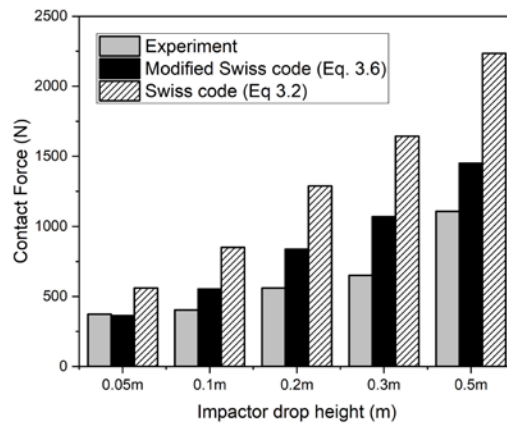


Figure 3.15 Horizontal impact test setup



(a) Gravel



(b) Pebbles

Figure 3.16 Comparison of experimental results with Swiss code equation (Eq. (3.2)) and modified Swiss code equation (Eq. (3.6))

This chapter reviewed results from small scale experimentations involving the use of gabions. Experiments were performed to validate models that are already available in the literature. Contact force generated by the impact and the distribution of pressure through the cushion layer is of interest. Empirical equations from the literature were modified to be used with gabion cushions in a horizontal arrangement. Effect of multiple strikes was also the interest of these studies. In order to establish a robust design methodology, concepts developed using these small-scale experiments must be validated in a large-scale experimental study. This is discussed in the next chapter.

Chapter 4: Large Scale Experimental Studies

Large-scale tests were performed by the author of this thesis in order to establish a robust design methodology and validate concepts developed using small scale experiments in previous chapter. All content in this chapter are the original work of the author of the thesis. Experimental setup, results and results comparison are presented. Chapter 4 starts with description of the specimens (Section 4.1) followed by that of the impactors (Section 4.2) and details of the cushion layer (Section 4.3). Description of the instrumentations used in the tests is then presented in Section 4.4. This is followed by the explanation of experimental setup and procedure of the test performed (Section 4.5) which is used to categorise the entire sequence of tests in a more systematic manner (Section 4.6). Finally, Section 4.7 is used to present results from the tests and analysis of the test results.

The RC barrier specimen used for large scale test had a stem wall of 1.5 m high and 0.23 m thick. Three “torpedo” shaped solid steel impactors with mass of 280 kg, 435 kg and 1020 kg have been used to deliver impact carrying different amount of energy. A layer of gabion cushions with thicknesses: 0.3 m, 0.5 m and 1.0 m was placed in front of the wall in separate tests as a protective layer. Over 100 pieces of instruments across two different wall specimens were employed to record the velocity and acceleration of the impactor, displacement of the barrier, and strains in both the reinforcement and the concrete. The conditions of the impact actions and the structural response behaviour of the impacted stem wall specimen were both monitored. The experimental program comprised a total of 51 impact tests which were conducted in three test series each having its own feature as indicated in the following list:

- Test Series A: Wall specimen 1 without gabion cushion
- Test Series B: Wall specimen 1 with different gabion fill materials
- Test Series C: Wall specimen 2 with different gabion cushion thicknesses

4.1 SPECIMEN

Two RC barrier specimens were cast with similar technical details as discussed in below but occupied with different instruments. The RC barrier specimens had a stem wall with dimensions of 1.5 m tall, 3 m wide and 0.23 m thick, and were found on a base slab of 0.5 m thick and 1.23 m long, as shown in Figure 4.1(a). Standard strength grade N40 concrete to AS 1379 [121], which has a minimum characteristic compressive strength of 40 MPa (based on 28 days of standard curing), was used to construct the specimen. The concrete mix had a standard density of 2400 kg/m³ and maximum aggregate size of 20 mm. Compression tests were carried out on six concrete cylinders per wall specimen during the time the impact tests were carried out. Cylinders were tested in different time intervals (after 28 days, 2 days before the beginning of the test and two weeks after the test). The concrete strength was found to not vary significantly across the six tests, and the test results averaged at 47 MPa for specimen 1 and 50.7 MPa for specimen 2 as listed in Table 4.1. Note that the wall casting was done in two stages.

Grade D500N reinforcing steel bars to AS/NZS 4671 [122] were used as vertical and horizontal reinforcement in the stem wall, and reinforcement in the base slab, as shown in Figure 4.1 (b). The minimum characteristic yield strength and the strain hardening ratio of these reinforcing bars were 500 MPa and 1.08, respectively. N20 (i.e. grade D500N with nominal diameter of 20 mm) bars at 200 mm spacing were used for both the vertical and horizontal reinforcement of the stem wall. There were 15 tensile bars and 15 compressive bars in total. Similar reinforcement arrangement was used for the base slab to ensure that the stem wall was fixed rigidly to the foundation which was in turn held down onto the strong floor of the laboratory. Tensile tests were carried out on six bar samples per wall to obtain the in-situ material properties which are summarised in Table 4.1. Concrete cover of 30 mm was specified. The wall was designed to have reinforcement ratio of more than 0.8% for grade N40 concrete to ensure that the stem wall would experience a well distributed crack pattern when subject to bending [123].

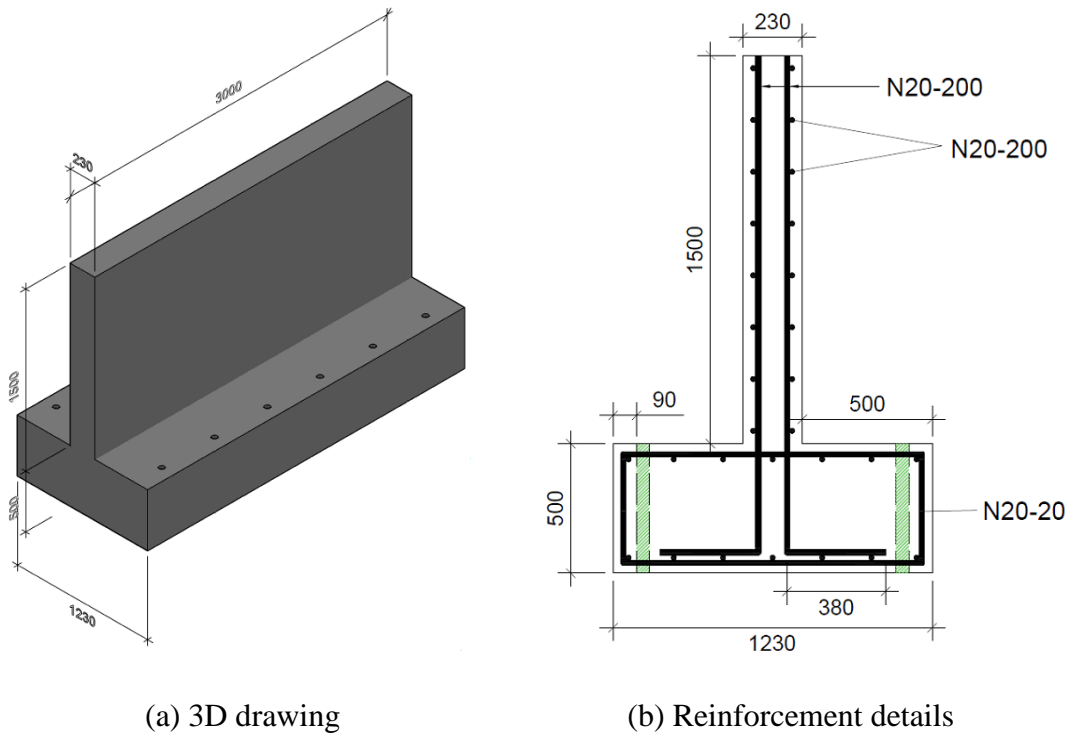


Figure 4.1 Reinforced concrete specimen

Table 4.1 In-situ material properties of reinforcing bars and concrete

Material Properties	Values – specimen 1	Values – specimen 2
E	194 GPa	194 GPa
f_y	543 MPa	526 MPa
f_u	636 MPa	629 MPa
f_y/f_u	1.17	1.2
ε_{sy}	0.0028	0.0027
f'_c	47 MPa	50.7 MPa

There were six openings (with diameter of 50 mm and spacings of 500 mm) through the base slab and on each side of the wall for accommodating the holding down bolts for securing the barrier rigidly onto the strong floor of the laboratory. The specimen was painted in white with a 150 mm x 150 mm grid drawn on the surface for the purpose of tracking concrete crack profiles following each test. Photographs of the two specimens are shown in Figure 4.2.



(a) Specimen 1

(b) Specimen 2

Figure 4.2 Photograph of reinforced concrete specimens

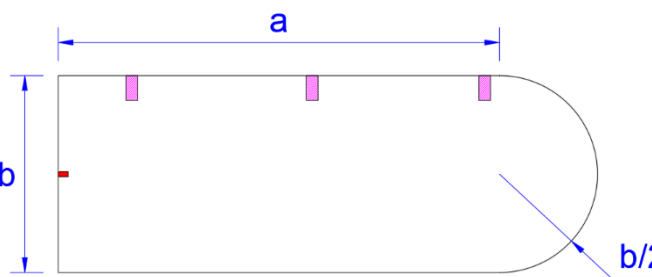
4.2 IMPACTOR OBJECTS

Three impactors made of solid steel with density of 7850 kg/m^3 were used to strike the specimen. Steel was chosen to be the impactor material to ensure repeatability of the tests. Note that the contact force developed with the presence of a cushion layer is insensitive to the choice of the impactor material as the cushion is very soft compared to the hardness of steel (or rock). Moreover, the contact force model introduced in Chapter 3 (Eq. 3.6) transform the shape of the impactor into two parameters namely mass and the radius. Therefore, as long as the contact surface of the impactor is spherical, Eq.3.6 is applicable. The shape of the impactor used in this large scale experiment was selected based on practical reasons as explaining bellow.

The following descriptions hold true for all three impactors. The “torpedo” shaped impactor object had one end (that was intended to be in contact with the barrier specimen) machined into a hemispherical surface. The hemispherical fitting had the same diameter as the cylindrical body. At the other end (flat end), a 1/4-28 UNF-2B hole was tapped for securing an accelerometer to the impactor object. On the curved cylindrical surface, three holes were tapped for the purpose of lifting, with the middle hole tapped at the centre of mass of the impactor. Eye nuts were secured onto the holes. The impactors were numbered as shown in Table 4.2 alongside Figure 4.3(a) which shows the dimensions of the impactors and disposition of the tapped holes. A photograph of the impactors is shown in Figure 4.3(b).

Table 4.2 Impactor object dimensions

Impactor	Mass (kg)	a (mm)	b (mm)
Impactor 1 (S-1)	280	400	300
Impactor 2 (S-2)	435	700	300
Impactor 3 (S-3)	1020	900	400



(a) Drawing

(b) Photograph

Figure 4.3 Torpedo shaped impactor objects

4.3 CUSHIONING MATERIALS

The experiment was carried out in multiple test series. Two of the test series (Test series B and Test series C) involved the use of gabions forming a cushioning protective layer which was placed in front of the stem wall. Details of the cushion materials are described in this section.

Two fill materials were used for making the gabion boxes: crushed gravel (70 - 100 mm) and river pebbles (50 - 200 mm). The shape and roughness profiles of fill particles were used for characterising gabion fill materials for functioning as cushion. Specific gravity, shape, gradation and crushing strength of particles were parameters for identifying the fill materials whereas Young's modulus and bulk density were used for characterising the gabion cell as a whole.

4.3.1 Particle properties

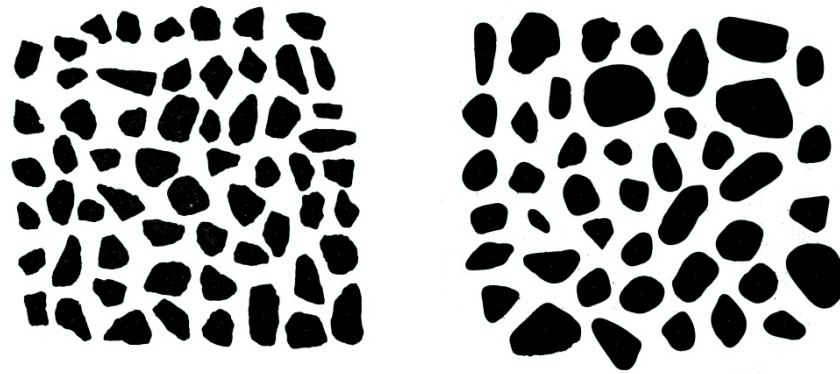
Particle shape properties can be defined with three different scales: global shape, scale of major surface features and roughness of the surface [124]. Readings from these scales are indicative of particle packing and hence the potential mechanical response behaviour of the gabion to a projected impact action. To identify the fill materials in the current study, parameters such as aspect ratio (AR) and circularity of the fill particle (C_i) as defined by Eqs. 4.1 and 4.2 respectively are used. Note that determining the value of AR requires (i) fitting an ellipse onto the gabion fill particle being examined, (ii) measuring the length of the major and minor axes of the ellipse, and (iii) applying Eq. 4.1.

$$AR = \frac{\text{Major Axis Length}}{\text{Minor Axis Length}} \quad (4.1)$$

$$C_i = \frac{4\pi A_p}{P^2} \quad (4.2)$$

where P is the perimeter length of the particle and A_p is the largest area of the particle that can be captured when rested under gravity on a flat surface, as illustrated in Figure 4.4. It can be shown that $C_i = 1$ for a circle, $C_i < 1$ for a square and $C_i \ll 1$ for a rectangle with a high aspect ratio.

Image analysis was carried out in order that value of the factors as defined by Eqs. 4.1 and 4.2 can be calculated readily. Sample particles (which were taken randomly from the same batch of materials used to fill the gabion boxes) were placed and held down by gravity on a flat surface. The array of particles was captured using a digital camera (Canon D760) from plan view. The captured images were then analysed with the software package *ImageJ*. Sixty crushed gravel particles and forty-three river pebble particles have been analysed. Results of the analyses are listed in Table 4.3.



(a) Crushed Gravel particles (b) River pebble particles

Figure 4.4 Image analyses

Table 4.3 Results from image analyses of gabion materials

Gabion Materials	Circularity	Aspect Ratio
Crushed Gravel	0.715 ± 0.06	1.56 ± 0.37
River Pebbles	0.779 ± 0.05	1.48 ± 0.37

Particle packing under natural condition is highly affected by the gradation of the aggregates. Sieve analysis test cannot be performed due to the scale of the particles and hence the size properties captured from image analysis were used to produce a sieve analysis curve as shown in Figure 4.5.

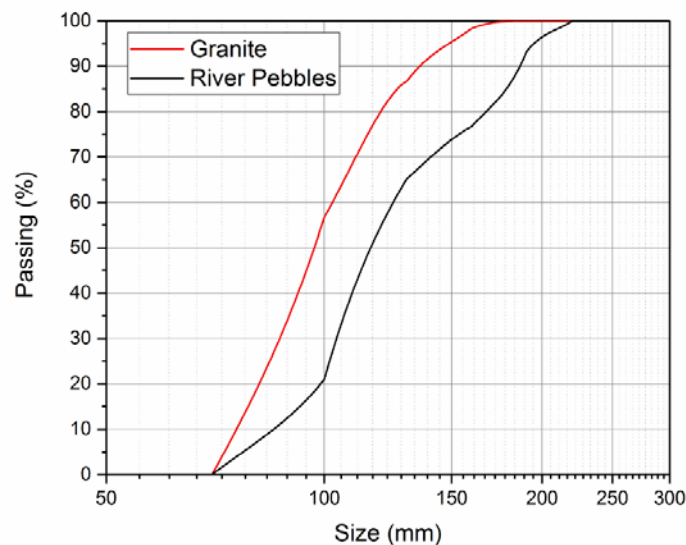


Figure 4.5 Particle size distribution curves

4.3.2 Gabion properties

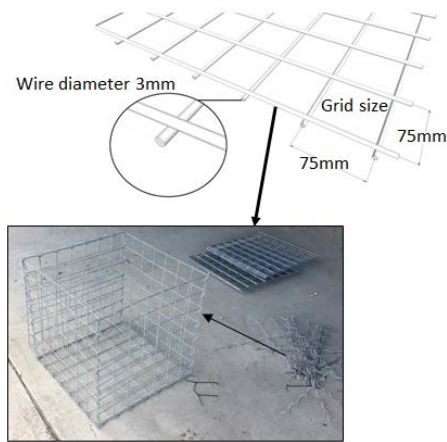
Two different types of gabion cells were used in the large-scale test. Test series B was focused on the particle infill properties and thus fairly flexible cages were used for both particle fill types. In Test series C, same crushed gravel infill used in Test series B was used but with stronger gabion cages. Details of these gabion properties are discussed in detail in the following sections.

The envelope of the gabion cell used in Test series B was made up of squared wire meshes (which were inter-connected by helices) forming a box. All square openings of the wire mesh were of size 75 mm, and the wires were 3 mm in diameter as shown in Figure 4.6(a). The gabions boxes were cubical in shape with side lengths of 525 mm. Prior to filling the gabion boxes, internal connecting wires in two directions were placed across the cell in order to prevent any lateral deformation while filling.

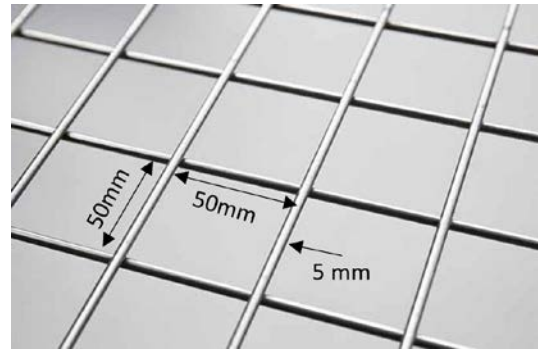
The envelope of the gabion cell in Test series C was made up of squared wire meshes similar to Test series B but all square openings of the wire mesh were of size 50 mm, and the wires were 5 mm in diameter as shown in Figure 4.6 (b). The gabion boxes which were cubical in shape had two different dimensions: 500 mm × 500 × 500 mm and 500 mm × 500 mm × 300 mm. For both types of gabion boxes, the largest surface area of 500 × 500 mm was taken as the loading (frontal) surface in the impact and static experiments whereas the remaining dimension (i.e. 500 mm and 300 mm respectively) were the “thickness”. Gravel particles were placed inside the gabion boxes which were stacked vertically. Gabion boxes were pre-filled prior to their delivery to the laboratory (where tests were conducted). In test series B, a sling was trapped inside each gabion box while the material was filled to provide a hook-up point when placing gabions in the laboratory. Gabion boxes used in Test series C were much stronger and hence this was not necessary. Photographs of filled gabions are shown in Figure 4.7 (a) & (b) for Test series B and (c) & (d) for Test series C.

In Test series B, the average cell weight was measured at 210 kg and 215 kg for gravel and river pebbles cells respectively. The bulk density of a gabion box was accordingly 1451 kg/m³ for a gravel filled gabion and 1486 kg/m³ for river pebbles filled gabion based on dividing the gross weight by the volume. It is shown that neither the shape nor the specific density of the fill particles had much influence on the bulk density of the gabion boxes used in this study. In Test series C, the average gabion box of thickness 300 mm and 500 mm weighed 115 kg and 190 kg respectively. Their bulk

density (based on dividing the gross weight of the gabion box by its volume) was accordingly 1533 kg/m^3 and 1520 kg/m^3 .



(a) Flexible gabion mesh



(b) Stronger gabion mesh

Figure 4.6 Dimensions of wire net and production of gabion box



(a) Crushed gravel



(b) River pebbles



(c) 500 mm thick



(d) 300 mm thick

Figure 4.7 Photographs showing samples of gabions

Static tests in unconfined conditions were carried out on gabion cells to obtain their stiffness properties and have the results expressed in terms of the modulus of elasticity. Two static tests were carried out for each gabion fill material in Test series B, and the average results were taken. Each gabion cell box was loaded by an actuator which was rated to 5 MN (Model No. DYNS produced by Instron) as shown in Figure 4.8 (a) & (b). In Test series C, four tests were carried out on the 500 mm thick gabion boxes and three tests on the 300 mm thick gabion boxes. Each gabion box was loaded by an actuator which was rated to 1 MN (MTS 311.31) at a rate of 1 mm/s as shown in Figure 4.8 (c) & (d). A 32 mm thick steel plate was placed on top of the gabion box to distribute the compressive force evenly on its upper surface. Compression strains of up to 0.2 were applied at a rate of 1 mm/s. The test results are shown in Figure 4.9 (a) & (b) for Test series B and (c) & (d) for Test series C.



(a) Crushed Gravel



(b) River Pebbles



(c) 500 mm thick



(d) 300mm thick

Figure 4.8 Static test setup

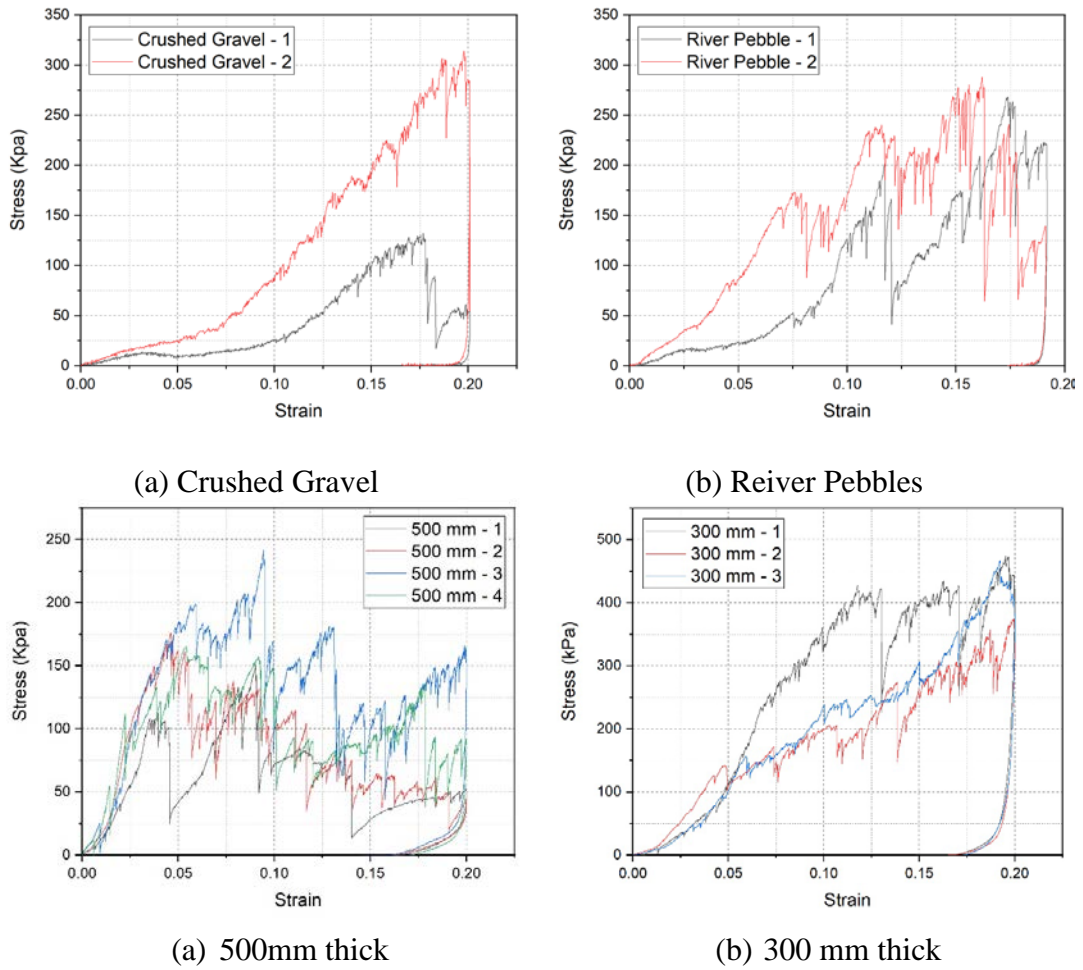


Figure 4.9 Stress-strain diagram

Modulus of elasticity (M_E) of the gabions was inferred from test results based on the average slope of the stress-strain diagram as illustrated in Figure 4.9. Note that only the elastic region of the graph (up to 0.05 strain) was considered. The value of M_E from each test using 500 mm or 525 mm cubical gabion boxes is shown in Table 4.4, and the average value was found to be 1172 kPa for flexible cage used in Test series B and 2985.3 kPa for stronger cage used in Test series C. The compressive stiffness of the gabion box was mainly dependant on the strength of the box. This is because its stiffness can vary significantly depending on whether the gabion box is broken during the compression test.

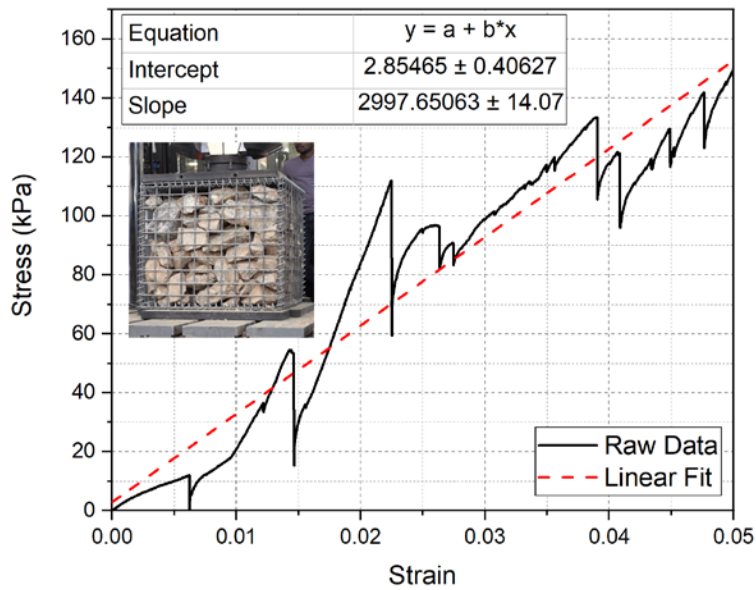


Figure 4.10 Sample calculation of modulus of elasticity (500 mm – 4)


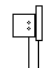

Table 4.4 Modulus of elasticity values

Sample	M_E (kPa)	Average M_E (kPa)
Flexible cage – crushed gravel -1	1282	1172
Flexible cage – crushed gravel -2	750	
Flexible cage – river pebble -1	744	
Flexible cage – river pebble -2	1911	2985
Strong cage – crushed gravel -1	2815	
Strong cage – crushed gravel -2	4233	
Strong cage – crushed gravel -3	4140	
Strong cage – crushed gravel -4	2998	

4.4 INSTRUMENTATION

Various instruments and equipment were employed in the experiment, including strain gauges, linear variable differential transformers (LVDTs), laser sensors, accelerometer and high-speed camera (HSC). The disposition of the instrumentation is shown in Figure 4.11 through 4.13 for specimen 1 and Figure 4.14 through Figure 4.16 for specimen 2. This amount of instrumentation served the following purposes:

- a) Capturing the behaviour of the specimen during the course of the impact,
- b) Exercising control of the tests, and
- c) Recording displacement and motion behaviour with redundancies.

-  : Laser sensor attached to specimen
-  : LVDT attached to specimen
-  : Laser sensor at a distance away from the specimen

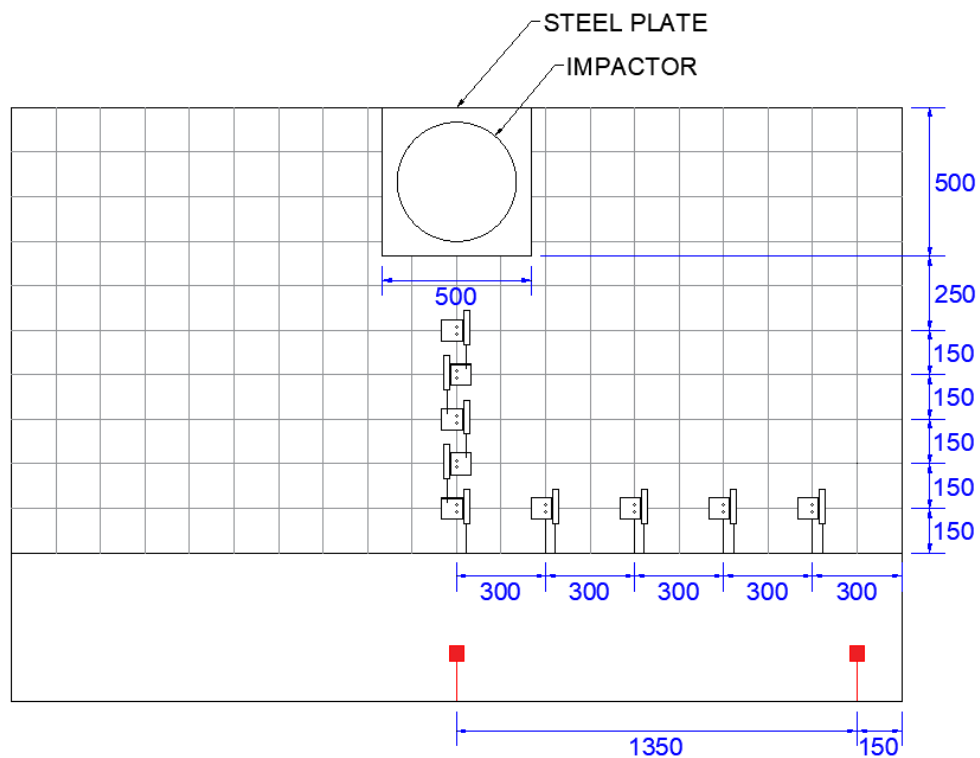


Figure 4.11 Front view (tensile side) of specimen showing instrumentations

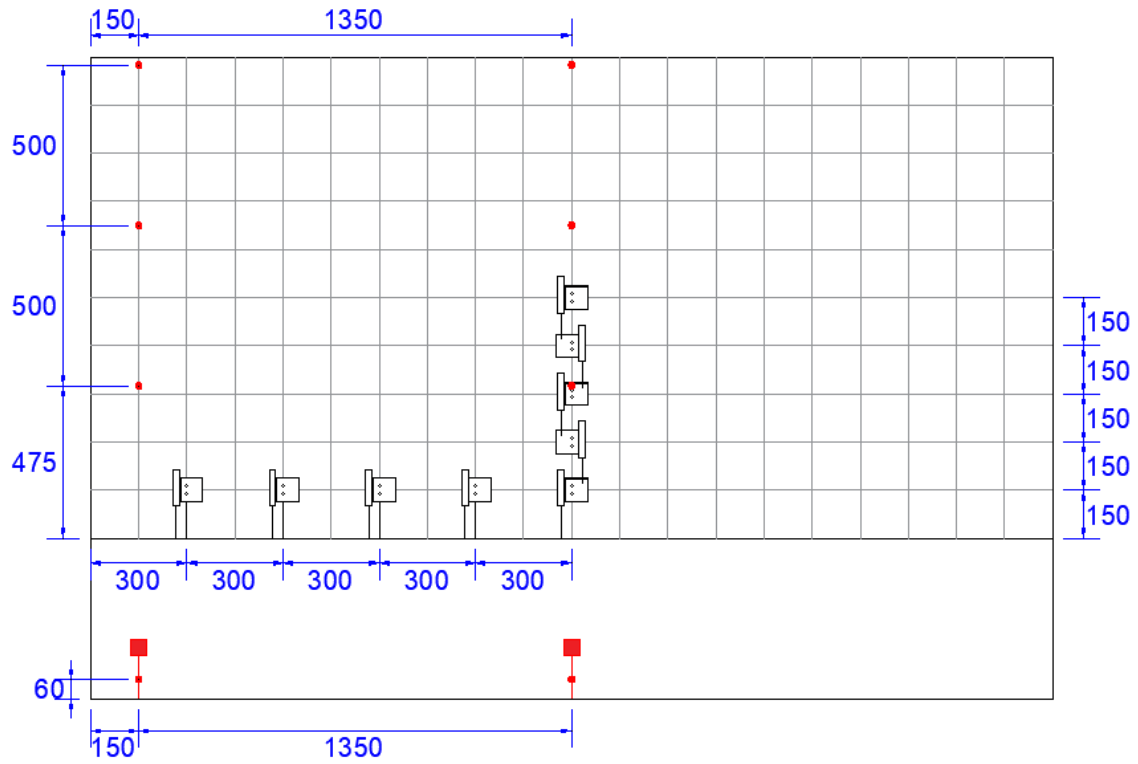


Figure 4.12 Rear view (compressive side) of the specimen showing instrumentations

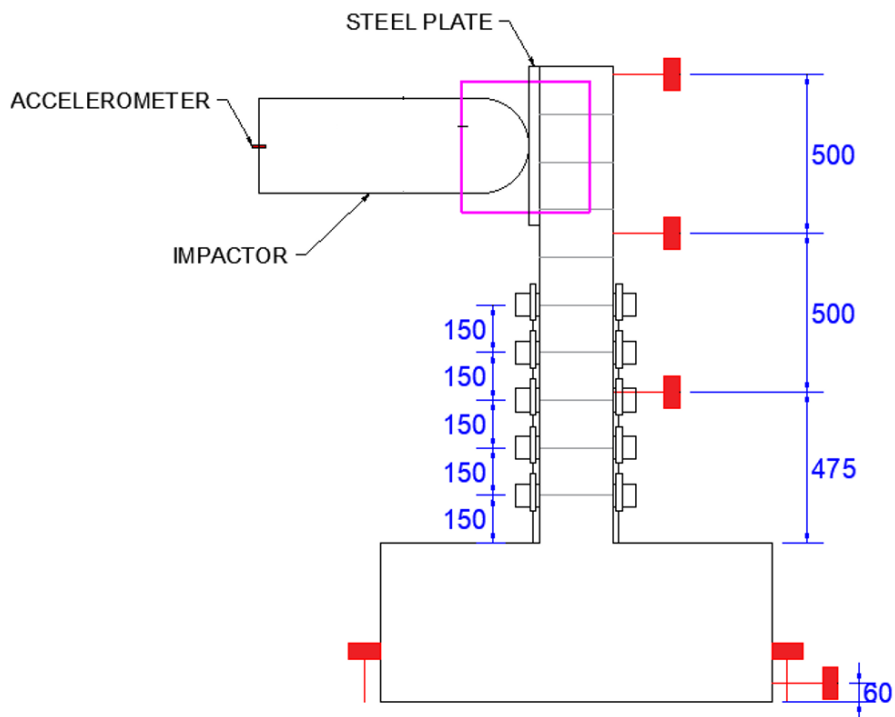





Figure 4.13 Side view of specimen showing instrumentations

-  : Laser sensor attached to specimen
-  : Strain gauge attached on concrete surface
-  : Laser sensor at a distance away from the specimen

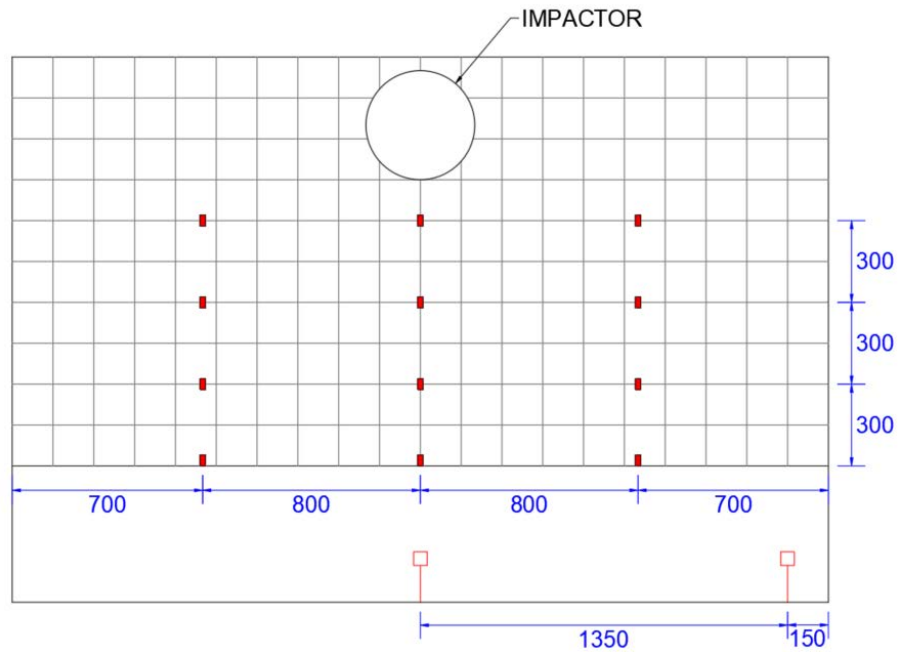


Figure 4.14 Front view (tensile side) of specimen showing instrumentations

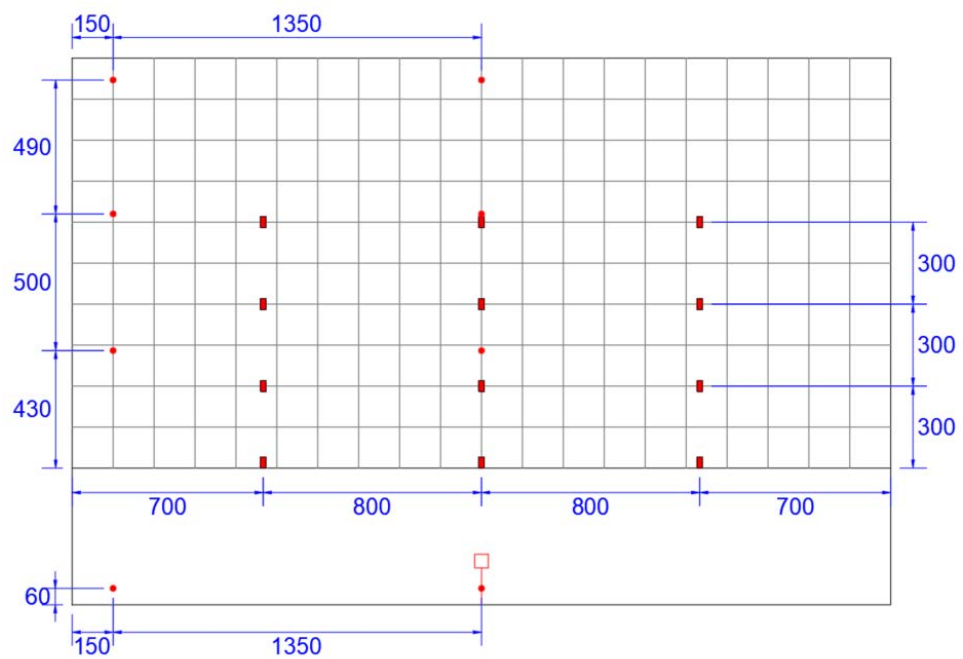


Figure 4.15 Rear view (compressive side) of the specimen showing instrumentations

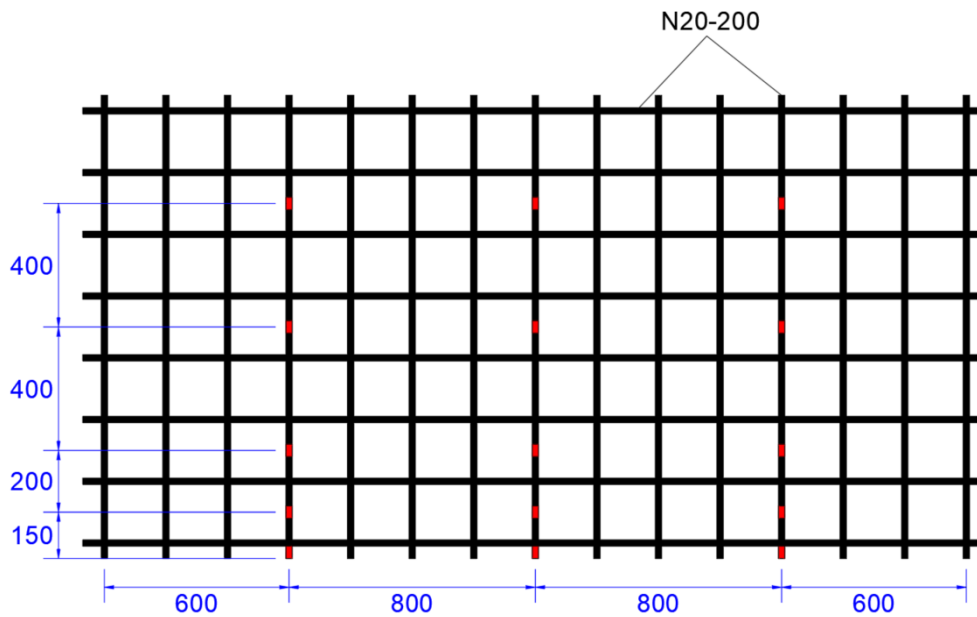


Figure 4.16 Front and rear view of reinforcement showing instrumentations

4.4.1 Strain gauges

In the specimen 1, post-yield strain gauges (series YEFLA-5 by Tokyo Sokki Kenkyujo Co. Ltd.) were attached to the base of the stem wall on each reinforcement bar prior to the casting of the concrete, resulting in the deployment of 30 strain gauges in total (15 on the tensile side and 15 on the compressive side), as shown in Figure 4.17. These strain gauges were designed to measure repeated strain in the elastic range as well as (large) post-yield strain of up to 15 %.

In specimen 2, same post-yield strain gauges were attached up the height of three of the vertical reinforcement bars of on each side of the wall prior to pouring concrete into the mould. A total of 30 strain gauges were deployed (with 15 on each side of the wall) as shown in Figure 4.18. Their locations are shown in Figure 4.16 (as indicated by the red squares). These strain gauges were to measure strains in the elastic range as well as (large) post-yield strain of up to 15 % as the wall was impacted repeatedly.



Figure 4.17 Photographs of strain gauges on reinforcement bar -specimen 1

Apart from the strain gauges used in reinforcement bars, polyester wire strain gauges (series PL-60-11 by Tokyo Sokki Kenkyujo Co. Ltd.) as shown in Figure 4.19 were also attached on the concrete surface on both sides of the wall up its height. A total of 24 strain gauges were deployed, with 12 on each side of the wall. Their locations are shown in Figure 4.14 and 4.15 (as indicated by the red squares). During the test series C, strain gauges connected to the tension side of the stem wall was covered with a 17 mm timber plywood plate prior to placing the gabion cushion layer.

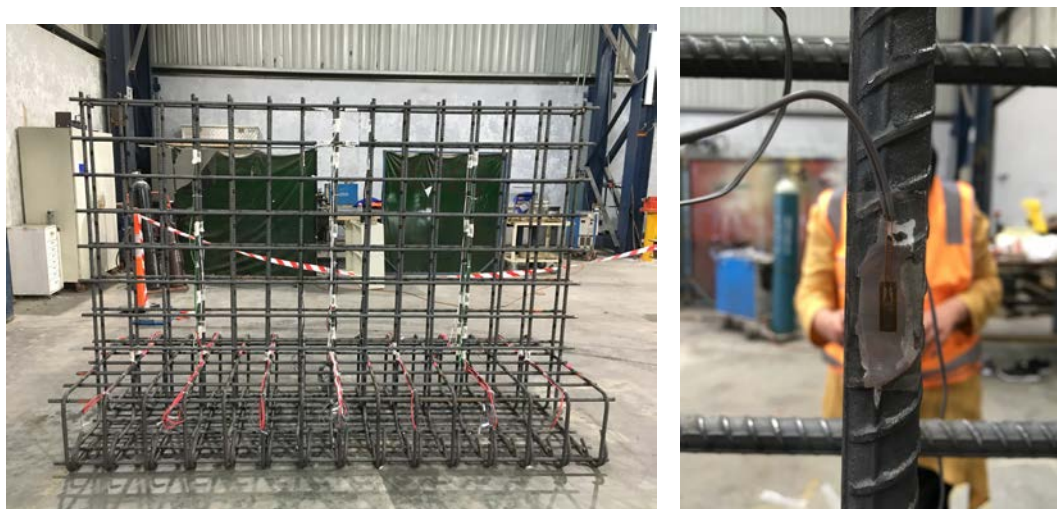


Figure 4.18 Photographs of strain gauges on reinforcement bar - specimen 2



Figure 4.19 Photograph of a strain gauge on concrete surface – specimen 2

All the strain gauges were installed with the appropriate type of adhesives. Those strain gauges that were attached to the reinforcement were coated with waterproof and mechanical protection as recommended by the manufacturer. Data recorded from the strain gauges were acquired by National Instruments (NI) PXI strain/bridge input module (PXIe-4330) at an acquisition rate of 2 kHz. Resolution of the measurements was dependant on both the mechanical limit of the strain gauges as well as the electronic resolution of the data acquisition module. It was found by a trial run of the test that the resolution of the strain gauges was ± 1 micro-strain. All strain gauges were pre-calibrated with gauge factors as specified by the manufacturer for converting the recorded electrical resistance to actual strain values.

4.4.2 Linear variable differential transformers (LVDTs)

Only in specimen “1”, LVDTs (S series) produced by Solartron Metrology with measurement frequency of up to 500 Hz were used to measure strains within the concrete. A series of LVDTs were attached to the tension and compression side of the stem wall by aluminium brackets. Five LVDTs were distributed evenly across the base from one end of the wall to the centre line where four additional LVDTs were stacked vertically, as shown in Figure 4.20. Their locations are shown in Figure 4.1 and 4.13. The measurement range of the LVDTs varied from 5 mm to 50 mm (which corresponds to resolution ranging from 0.0001 mm to 0.0003 mm) depending on the

location. As the LVDTs were positioned at 150 mm vertical spacing (starting from the base), the maximum strain that can be measured by the shortest LVDT (5 mm) was 3.3 % which was well beyond the ultimate strain limit of concrete. The use of such technique for measuring concrete strain is common with post-yield testing employed in structural engineering investigations of seismically damaged RC specimens [125-127]. However, the use of this style of instrumentation on impact experiments has not been reported in the literature. Note that only half of the wall was instrumented with LVDTs because of considerations of symmetry. Calibration procedures of the LVDTs were similar to that of the laser sensors. More details are given in Section 4.4.3 alongside descriptions of the laser sensors. During the test series B, LVDTs connected to the tension side of the stem wall was removed and concrete strain was not measured as LVDT cannot be used in conjunction with a gabion cushion layer.



Figure 4.20 Photograph of LVDTs at the front of the wall

4.4.3 Laser sensors

Laser sensors arrangement was similar in both specimens. Model ILD 1302 laser sensors (Micro-Epsilon) with measurement frequency of up to 750 Hz were used in the experiment, as depicted by the red boxes as shown in Figure 4.11 to Figure 4.15. As shown in Figure 4.21, some of the laser sensors were not fixed directly to the specimen but were attached to a separate timber frame that was erected behind the stem wall to record displacement from the rear (compressive side) of the wall specimen. The points of interest, as represented by the red dots shown in Figure 4.12 and Figure 4.15, were located at (i) close to the top edge of the wall, (ii) two-third

height, (iii) one-third height and (iv) close to the ground surface. Measurements were taken at both the centre line and near the edge of the wall. The two sensors close to the ground surface were used to detect possible sliding action of the base slab. Those laser sensors for measuring deflection at the top of the stem wall and at two-third height had measurement range of 200 mm (ILD 1302-200, with resolution of 0.1 mm). Other sensors had measurement range of 100 mm (ILD 1302-100, with resolution of 0.05 mm). On each side of the specimen, two laser sensors (ILD 1302-100, with resolution of 0.05 mm) were secured to the base slab by aluminium brackets for measuring any possible uplift movement.



Figure 4.21 Photographs showing laser sensors attached to the timber frame

Readings from the LVDTs and laser sensors were in voltages. Thus, calibrations were carried out with the use of a digital height calliper to convert the recorded voltage readings to displacement values (Figure 4.22). Note that the recorded results were acquired using NI PXI multifunction I/O module (PXI-6255) at a sampling rate of 750 Hz.



(a) LVDT (b) Laser sensor

Figure 4.22 Photographs showing calibration

4.4.4 Accelerometers

An accelerometer (Model: 3200B6M by Dytran, electrical noise: 0.035 g) with measurement range of up to 2500 g was screwed onto the flat end of the impactor objects (Figure 4.23) to record the acceleration time-history which can be used for calculating the amount of contact force that was delivered at the point of contact in an impact. The accelerometer had a frequency response of up to 10 kHz. Data recorded from all three accelerometers were acquired using NI PXI sound and vibration module (PXIe-4496) at an acquisition rate of 100 kHz. When sampling accelerometer data using a data acquisition device, the rate of sampling had to be at least twice the highest frequency of interest. The acquired data was then filtered to eliminate high frequency noise. Thus, a sampling rate of 100 kHz was used although the frequency of accelerometers was only 10 kHz. Butterworth filter of 1000 Hz to 2000 Hz was used for low-pass filtering. The accelerometers had been pre-calibrated with sensitivity factors as specified by the manufacturers.



Figure 4.23 Photographs showing the accelerometer sensor attached to 280 kg impactor

Note that all the NI modules (for all instrumentation described in Section 4.4) were slot into an NI PXI chassis (PXIe-1078) which had an embedded PXI controller (PXIe-8135) with Windows operating system installed for acquiring data with the aid of software package LabView which was developed by National Instruments. A sub program was written using LabView virtual programming language to acquire impact data from different instruments at different frequencies.

4.4.5 High-speed camera (HSC)

Another piece of physical equipment which had no direct contact with the specimen was the HSC (model Phantom v2512 produced by Vision Research). This piece of equipment was capable of recording video images at a rate of up to 25,000 frames-per-second at full resolution of 1280 x 800, and was used to capture images taken at the location of contact in order to (i) determine the velocity of the impactor object prior to and following the impact, and (ii) visualise actual conditions (at the point of contact) during the course of the impact. The frame that was recorded by the HSC is shown in Figure 4.13 (look for the magenta box).

4.5 EXPERIMENTAL SET-UP AND PROCEDURES

4.5.1 General Set-up

A 3D drawing displaying an overview of the planned test set-up including the specimen, the impactor objects and details of the instrumentation is shown in Figure 4.24, alongside a photograph showing the actual test set-up used in Test series A (Figure 4.25). As shown in Figure 4.24, there were two steel frames fixed to the ground. The first steel frame that was positioned close to the specimen was used to secure the impactor object in place. Each impactor object was initially positioned at the centre line of the specimen and at 250 mm measured from the upper edge of the stem wall. The first and third hole on the impactor object (Figure 4.3(a)) was connected to the steel frame using chains to ensure that the impactor would fall towards the barrier specimen following the pendulum trajectory and then strike the specimen at the intended location. A quick release hook was attached to its centre of mass (i.e. the second hole). The hook was in turn secured to a cable extending from a hand winch via a pulley which was attached to the second steel frame. During the course of lifting, a laser level was used to ensure that the impactor had been raised to the desired height with good accuracies. The impactor was then released using the quick release hook.

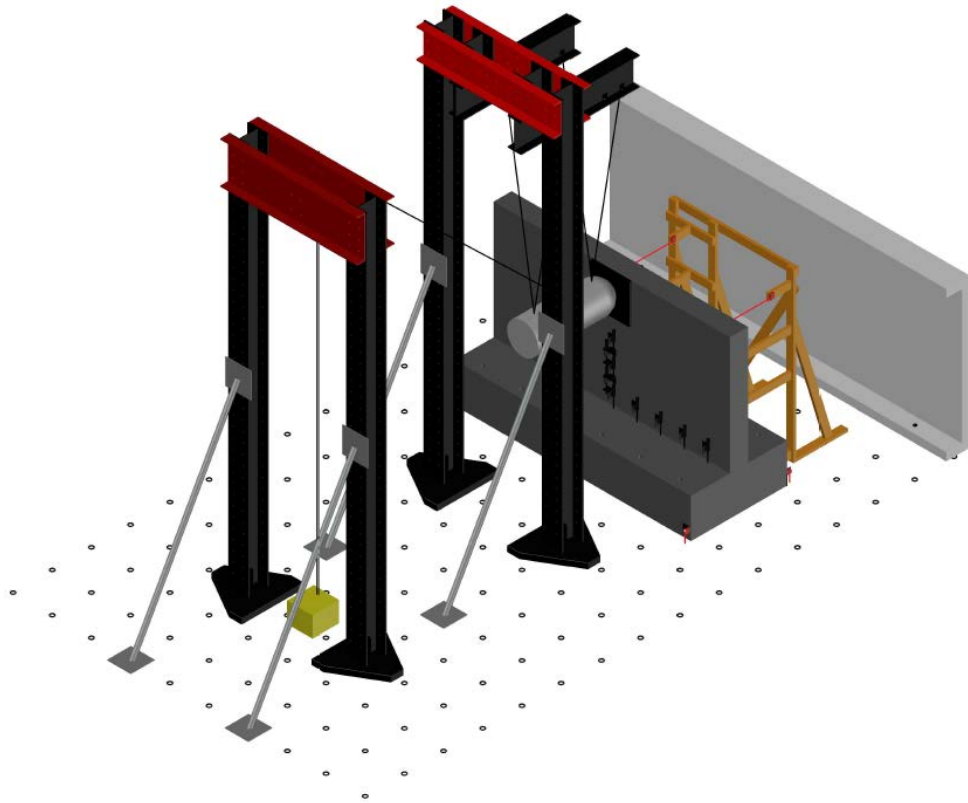


Figure 4.24 Drawing showing overview of test set up

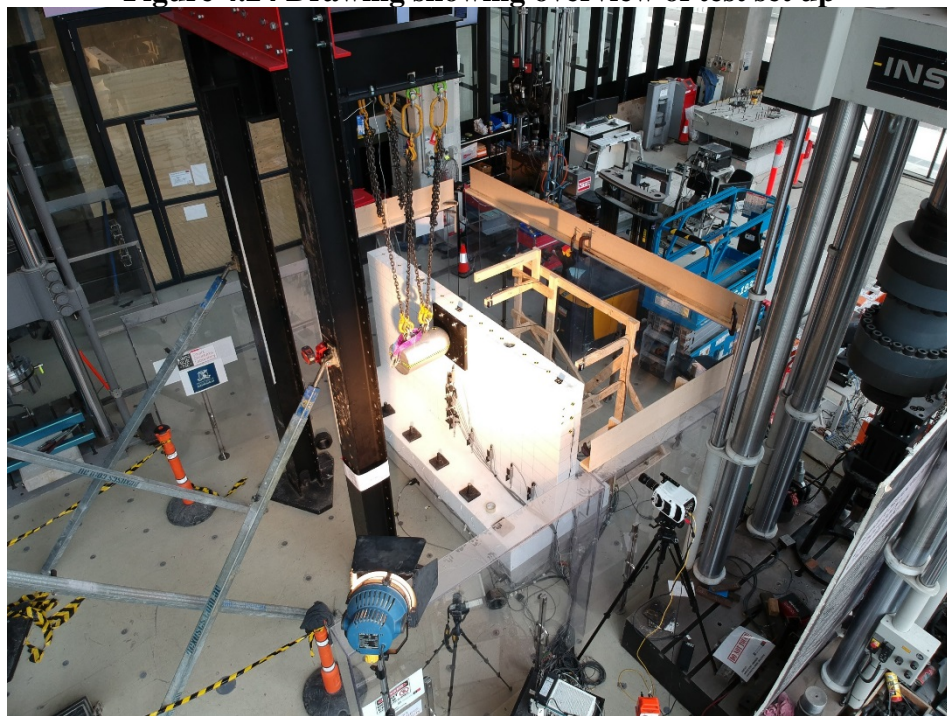


Figure 4.25 Photograph showing overview of test set up

In order to ensure a fully fixed foundation, the base slab of the barrier specimen was bolted to the strong floor of the laboratory (which is approximately 1 m thick) using six threaded rods on both sides of the wall, as illustrated in Figure 4.26. Each of these threaded rods was post-tensioned to 200 kN to prevent any uplift or sliding, movement of the barrier to take place.

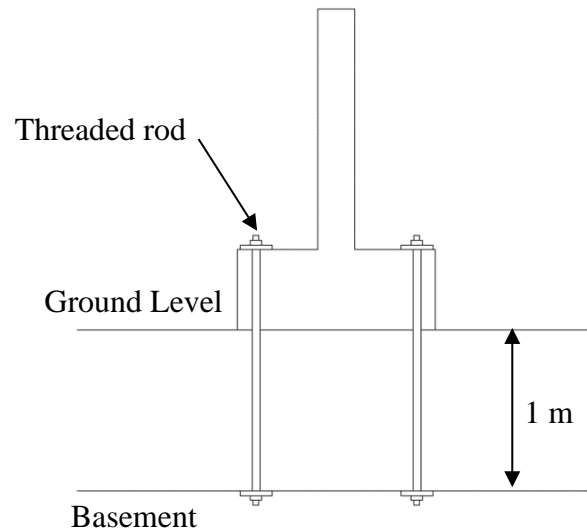


Figure 4.26 Sketch illustrating fixed base wall

4.6 TEST SERIES

In the experimental program, 51 tests were carried out in three stages: Test Series A to C. Details in each test series are described in the following sub-sections.

4.6.1 Test Series A: Pre-yield bending tests (without cushion)

The first phase of the experiment was carried out with a protective steel plate with dimensions: 500 mm x 500 mm x 32 mm which was attached to the stem wall at the location where the impactor was to strike (i.e. the top centre of the wall) as shown in Figure 4.27(a) and (b). This measure was put in place to ensure that the bending behaviour of the wall was comparable across multiple tests without being distorted by cumulative localised damage surrounding the point of contact. Test series A has provided well distributed cracks to the wall so that the wall behaves similarly across all tests in the Test series B. A similar method was used in Specimen 2 to develop well distributed cracks prior to the Test series C as well. Strain and deflection profiles of the wall were constantly monitored to confirm that the wall had not yielded. Impactor S-1 and S-2 were used to strike the steel plate. The release heights were selected so

that both impactors could deliver the same level of impact energy. Four tests were carried out in total and these tests were numbered as A1 to A4.

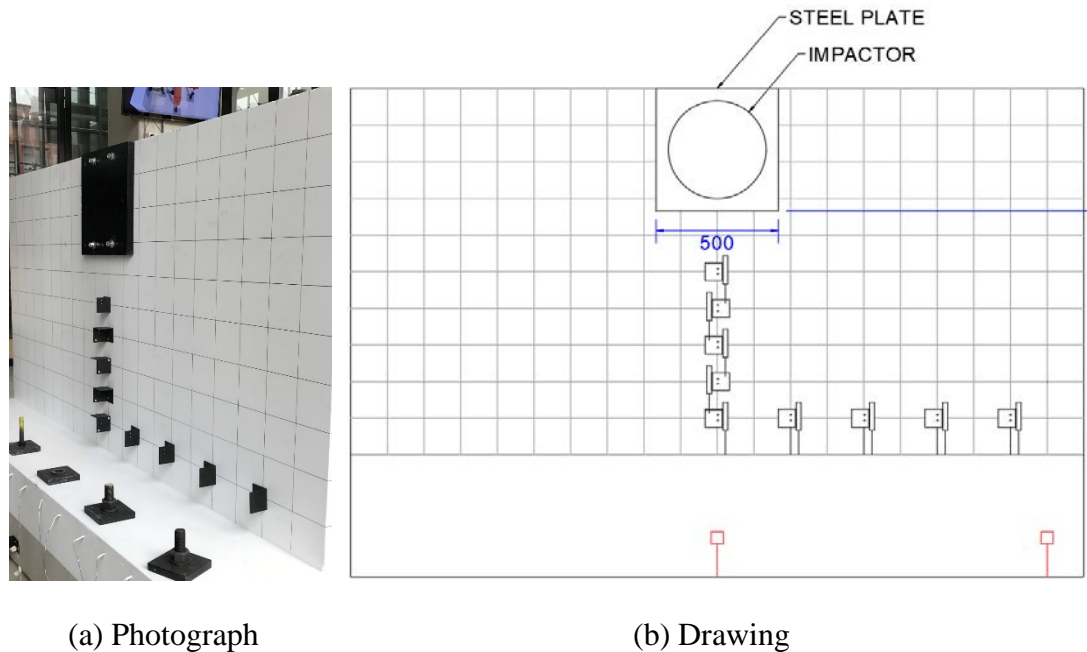


Figure 4.27 Position of protective steel plate

4.6.2 Test Series B: Gabion cushion with different fill materials

Gabion cushion cells filled with crushed gravel and river pebbles were placed in front of the stem wall for Test Series B (refer Section 4.3 for detailed descriptions of the cushion materials). Nine gabion boxes were placed in a 3 by 3 matrix. A frame made of 17 mm thick plywood was used to hold the gabion boxes in position and providing confinement from both sides. A plywood stage was used at the base to prevent any contact of the gabion boxes with the threaded rods that were used to hold the base slab down onto the strong floor of the laboratory. The frame and gabion boxes were then secured to the stem wall using truck lashing belts. A typical set-up of the gabion boxes and timber frame used in Test series B is shown in Figure 4.28. The use of two different cushions materials is illustrated in Figure 4.29.

Impactor objects S-1 and S-2 were used to strike the cushion layer multiple times (up to four times) before the gabions were replaced. The highest release height from Test Series A was used to strike the cushion layer three times consecutively, following by the fourth impact which was released from a lower height. Fifteen tests were carried out in total. Individual tests were identified by the serial number: $Xn - i$ which refers to the n^{th} test in Test Series X and the i^{th} strike repeated at the same location. Accordingly, these tests were numbered as B1-1 to B2-4 and B3-1 to B4-3 for gabions

filled with crushed gravel and river pebbles respectively. Test B4-4 involving the use of Impactor S-2 released from a lower height was not carried out because the gabion cage was destroyed entirely in Test B4-3. Note that the gabions were replaced following the completion of Test B1-4, B2-4 and B3-4. A total of 15 tests were carried out in this test series.



Figure 4.28 Typical set-up of cushion protective layer



(a) Test B1-1 (crushed gravel)



(b) Test B3-1 (river pebbles)

Figure 4.29 Front view of specimen with cushion layer prior to Test B1-1 and Test B3-1

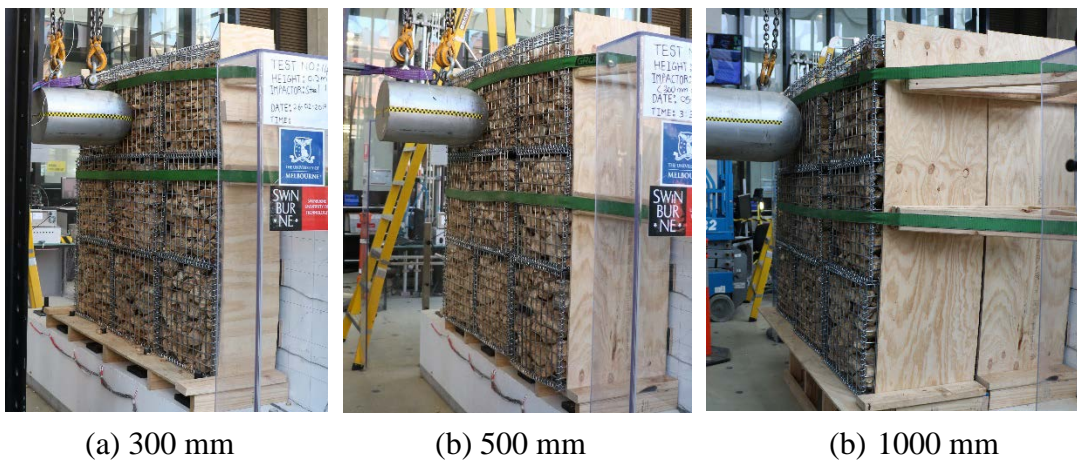
4.6.3 Test Series C: Gabion cushion with different thicknesses

In Test Series C, a layer of gabion boxes that were filled with crushed gravel were placed in front of the stem wall to function as cushion (refer Section 4.3 for detailed descriptions of the cushion materials). Similar to Test series B nine gabion boxes were placed in a 3 by 3 matrix. Cushion layers of three different thicknesses were employed in the tests: 300 mm, 500 mm, and 1000 mm. The 1000 mm thick cushion layers were provided by placing two layers of 500 mm thick gabion cages side-by-side in the direction of impact. A frame made of 17 mm thick plywood was used to hold the gabion boxes in position and providing confinement from both sides. Different design compared to Test series B was used as the frame need to be changed for three different thicknesses of the cushion layer. A plywood stage has also been erected (at the base) to prevent any contact of the gabion boxes with the threaded rods that were used to hold the base slab down onto the strong floor of the laboratory. An additional plywood stage has been used in 1000 mm thick gabion cushion (Figure 4.31(c)) setup to hold gabion boxes extend beyond the base of the slab. The frame and gabion boxes were secured to the stem wall using truck lashing belts as similar to Tests Series B. A typical set-up of the gabion boxes (500mm thick) and timber frame is shown in Figure 4.30. The scope of this test series which involved the use of cushion layers with three different thickness is illustrated by the photos of Figure 4.31.

All three torpedo shaped objects made of solid steel (Impactor S-1, S-2 and S-3) were employed as impactors in this test series (refer section 4.2 for more details). Each gabion layer was struck four times at the same location before being replaced. The exception to this was tested involving the use of Impactor S-3 (of mass 1020 kg) in which case the gabion cages were destroyed entirely after the second strike. Note that the tests employing Impactor S-3 were only carried out on cushion layers with a thickness of 500 mm and 1000 mm. The gabion boxes were replaced following the completion of Test C1-4, C2-4, C3-4, C4-4, C5-4, C6-2, C7-4 and C8-4. A total of 32 tests were carried out in this test series.



Figure 4.30 Typical set-up of cushion protective layer



(a) 300 mm

(b) 500 mm

(b) 1000 mm

Figure 4.31 Test setup for gabion cages with different thicknesses

A listing of the relevant parameters includes the impactor mass (m), release height (H) and cushion thickness (t) for the individual tests across all the test series are provided in Table 4.5. and illustrated in Figure 4.32.

Table 4.5 Impact conditions for all test series

Test No.	Impactor Mass (kg)	Release Height (m)	Impact Energy (kJ)	Protective Layer	Thickness	Fill material
A1	280	0.5	1.37	SP	32 mm	N/A
A2	280	1.4	3.85	SP	32 mm	N/A
A3	435	0.322	1.37	SP	32 mm	N/A
A4	435	0.579	2.47	SP	32 mm	N/A
B1-1 to B1-3	280	1.4	3.85	FG	500 mm	CG
B1-4	280	0.5	1.37	FG	500 mm	CG
B2-1 to B2-3	435	0.579	2.47	FG	500 mm	CG
B2-4	435	0.322	1.37	FG	500 mm	CG
B3-1 to B3-3	280	1.4	3.85	FG	500 mm	RP
B3-4	280	0.5	1.37	FG	500 mm	RP
B4-1 to B4-3	435	0.579	2.47	FG	500 mm	RP
C1-1 to C1-4	280	0.5	1.37	SG	300 mm	CG
C2-1 to C2-4	280	1.4	3.85	SG	300 mm	CG
C3-1 to C3-4	280	0.5	1.37	SG	500 mm	CG
C4-1 to C4-4	280	1.4	3.85	SG	500 mm	CG
C5-1 to C5-4	435	0.579	2.47	SG	500 mm	CG
C6-1 to C6-2	1020	1.0	10	SG	500 mm	CG
C7-1 to C7-4	280	0.5	1.37	SG	1000 mm	CG
C8-1 to C8-4	280	1.4	3.85	SG	1000 mm	CG
C9-1 to C9-2	1020	1.0	10	SG	1000 mm	CG

*SP – Steel Plate, FG – Flexible Gabion, SG – Stronger Gabion, CG – Crushed Gravel, RP – River Pebbles, N/A – Not Available

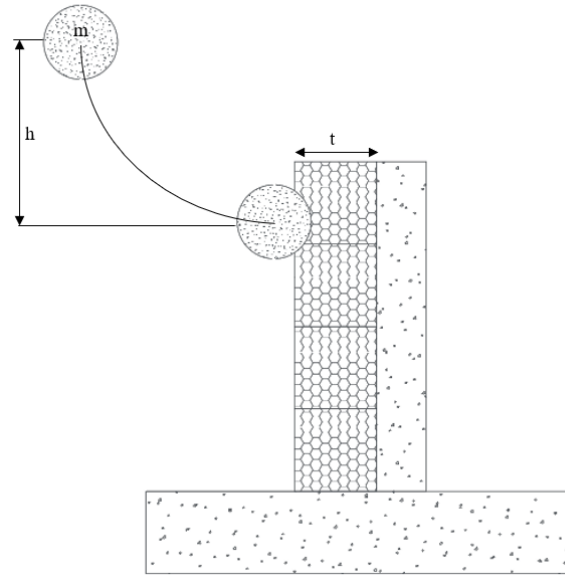


Figure 4.32 Schematic diagram

4.7 TEST RESULTS AND ANALYSIS

4.7.1 Cushioning effect of the gabion layer

Highspeed camera was used to record images of the impact between the steel impactor and the surface of the target (steel plate/gabion cushion). Impact between the steel impactor and the steel plate is shown in Figure 4.33 which was extracted from HSC video of Test A1. Each screen capture is taken in 2.3 ms intervals. Figure 4.34 shows the impact between the steel impactor and the gabion cushion layer of Test B1-1. It is evident from these captured images that impact between steel-steel occurs over a very short period of time. The introduction of the cushion layer prolonged this duration by more than 20 times.

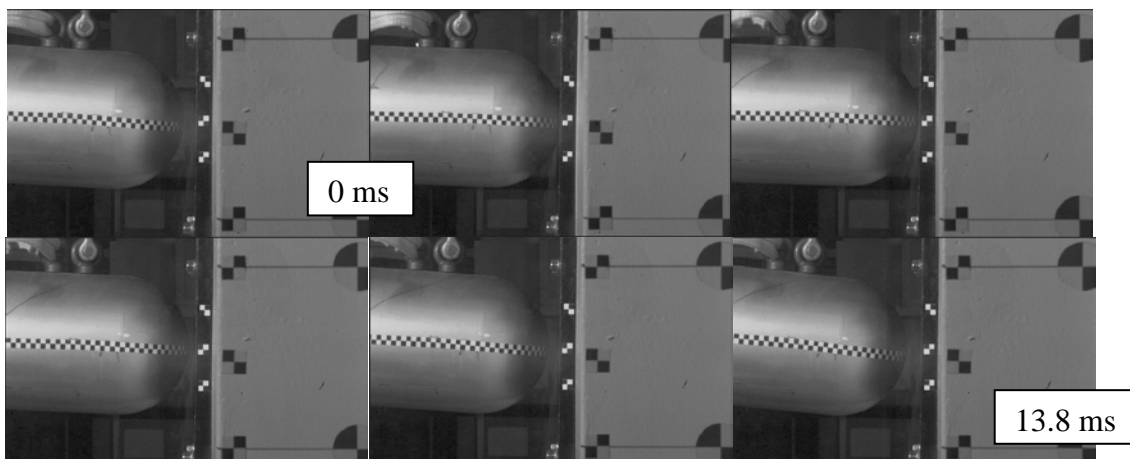


Figure 4.33 Sample screen captures of HSC for Test A1

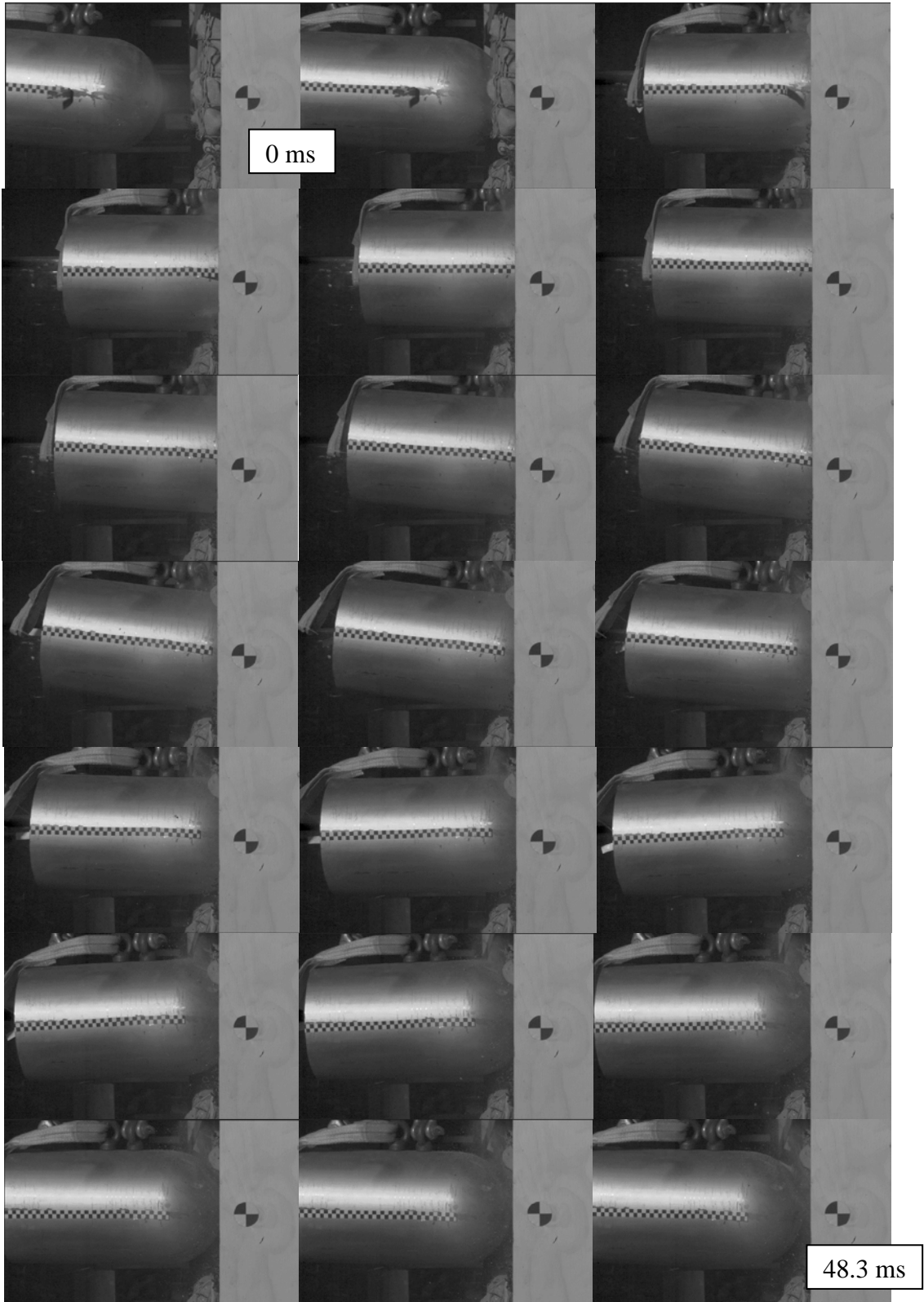


Figure 4.34 Sample screen captures of HSC for Test B1-1

4.7.2 Contact force

The amount of contact force delivered in an impact test can be taken as the product of the mass of the impactor object and the highest level of de-acceleration experienced by it (as recorded by an accelerometer attached to the rear of the object). Declaration results acquired from the accelerometer were filtered to eliminate high frequency noises as explained in Section 4.4.4. Results from Test Series A are shown in Figure 4.35.

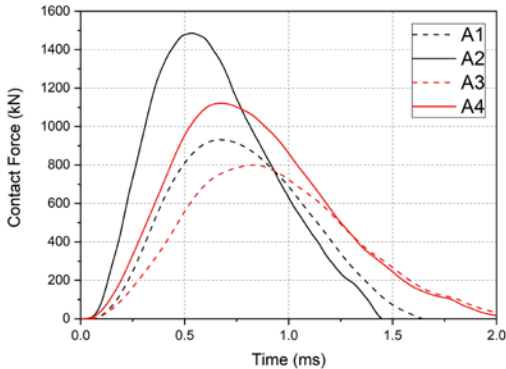
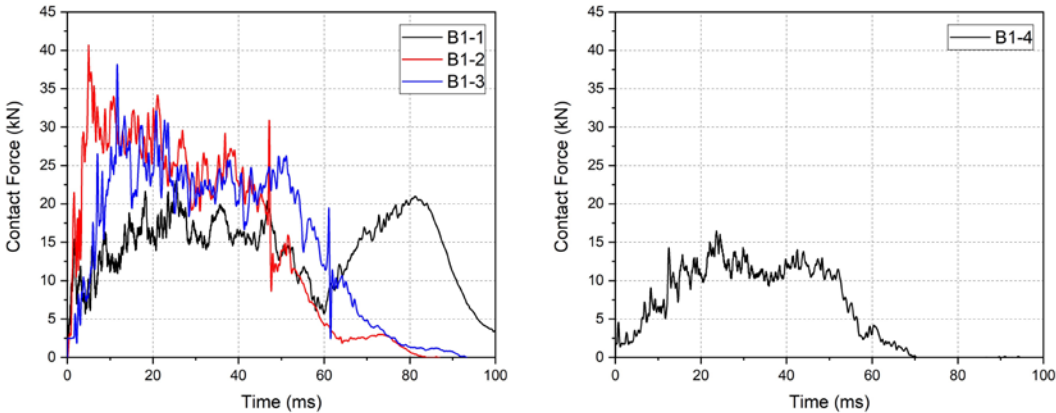
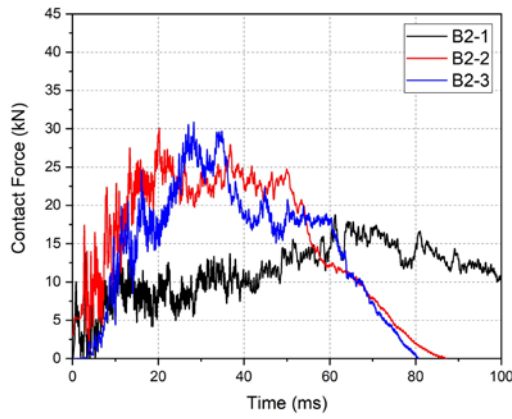


Figure 4.35 Contact force time-history from Test Series A

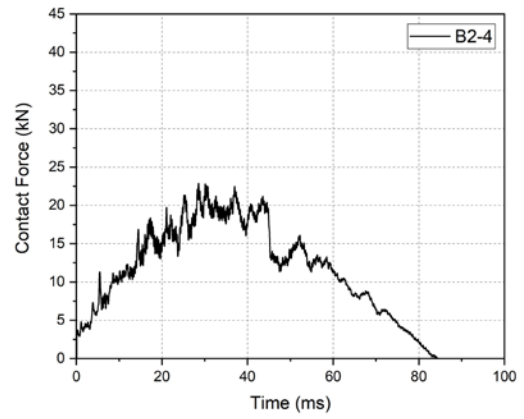
Similarly, contact force time history from the Test series B (cushioned wall with different fill materials and flexible gabion cage) was calculated from the accelerometer results and presented in Figure 4.36. The impactor was released at the same height for first three strikes and contact force results from all three strikes are shown in one figure while the lower height impact is shown in a separate figure. Accelerometer results from the Test B3-1 were not recorded correctly and hence not shown herein.



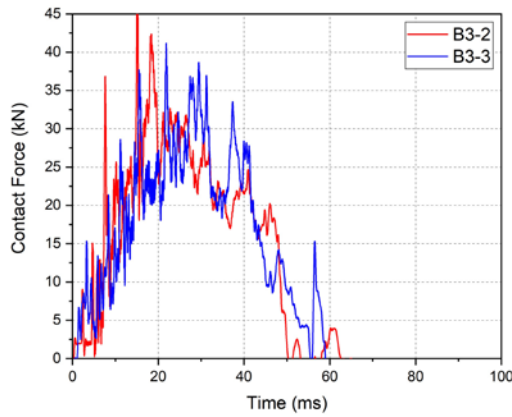
m – 280 kg; h – 1.4 m; t – 500 mm; (FG/CG) m – 280 kg; h – 0.5 m; t – 500 mm; (FG/CG)



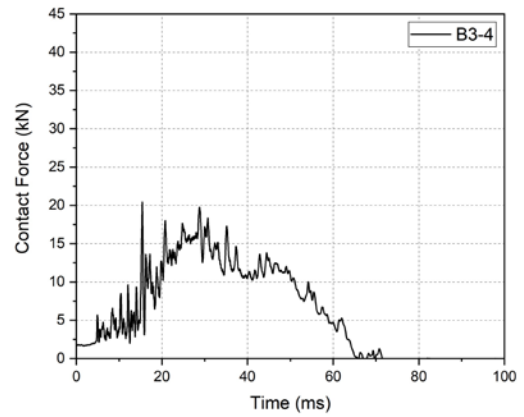
m – 435 kg; h – 0.58 m; t – 500 mm;
(FG/CG)



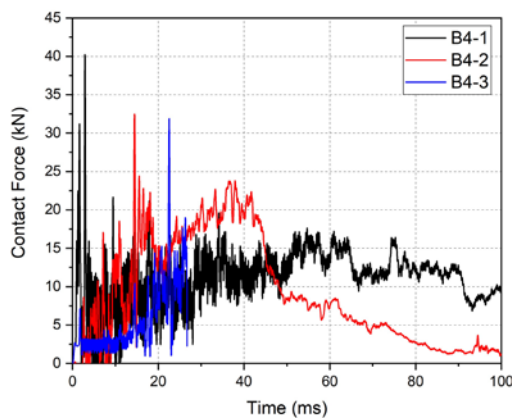
m – 435 kg; h – 0.32 m; t – 500 mm;
(FG/CG)



m – 280 kg; h – 1.4 m; t – 500 mm;
(FG/RP)



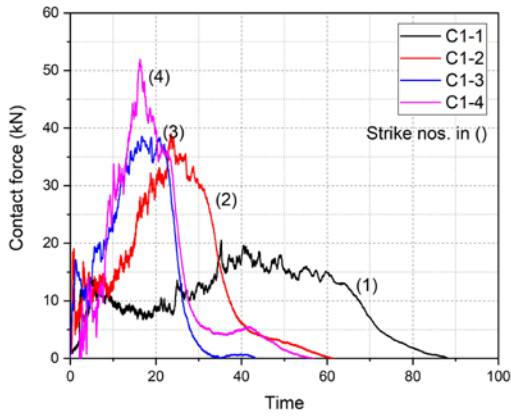
m – 280 kg; h – 0.5 m; t – 500 mm;
(FG/RP)



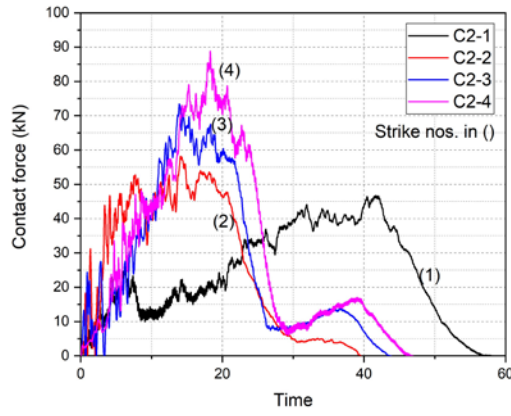
m – 435 kg; h – 0.58 m; t – 500 mm;
(FG/RP)

Figure 4.36 Contact force time-history from Test Series B

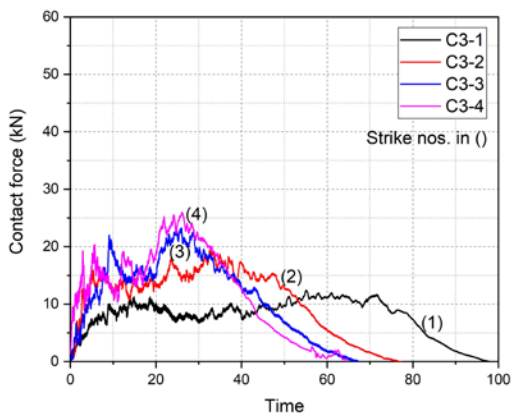
The time-histories of the contact force delivered by the impact are shown in Figure 4.37 for Test series C. Each of these figures contains four continuous strikes to the same point of the cushion. Note that test results from Test C7-1 were not available as the accelerometer was faulty.



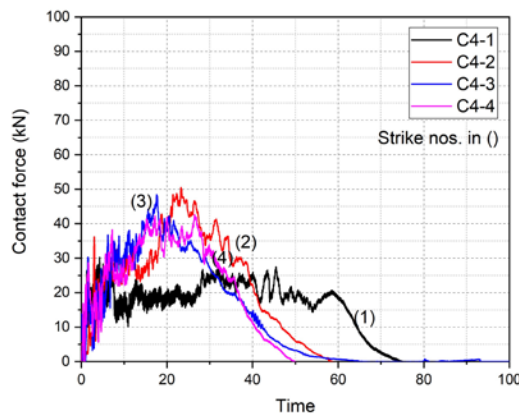
(a) $m = 280 \text{ kg}$ $H = 0.5 \text{ m}$ & $t = 300\text{mm}$



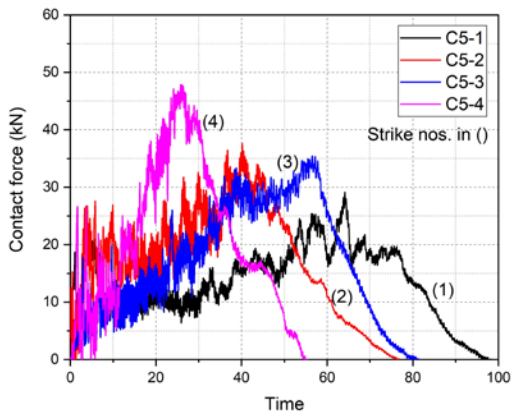
(b) $m = 280 \text{ kg}$ $H = 1.4 \text{ m}$ & $t = 300\text{mm}$



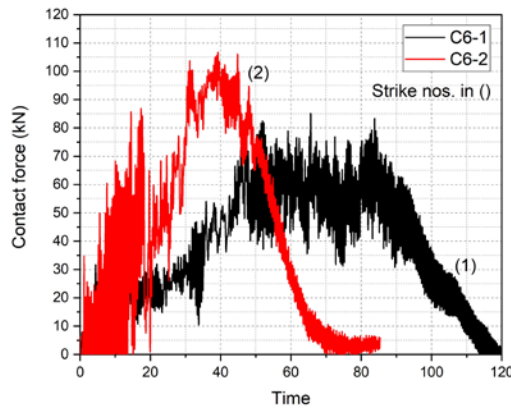
(c) $m = 280 \text{ kg}$ $H = 0.5 \text{ m}$ & $t = 500\text{mm}$



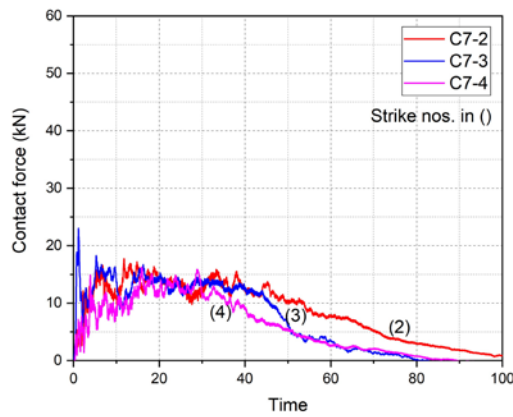
(d) $m = 280 \text{ kg}$ $H = 1.4 \text{ m}$ & $t = 500\text{mm}$



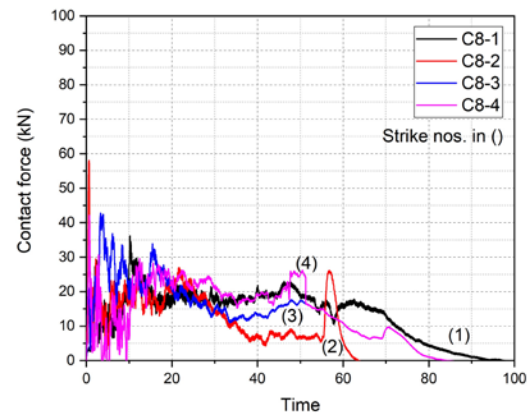
(e) $m = 435 \text{ kg}$ $H = 0.579 \text{ m}$ & $t = 500\text{mm}$



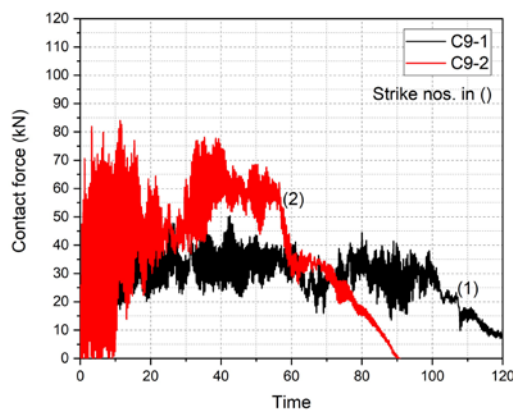
(f) $m = 1020 \text{ kg}$ $H = 1 \text{ m}$ & $t = 500\text{mm}$



(g) $m = 280 \text{ kg}$ $H = 0.5 \text{ m}$ & $t = 1000\text{mm}$



(h) $m = 280 \text{ kg}$ $H = 1.4 \text{ m}$ & $t = 1000\text{mm}$

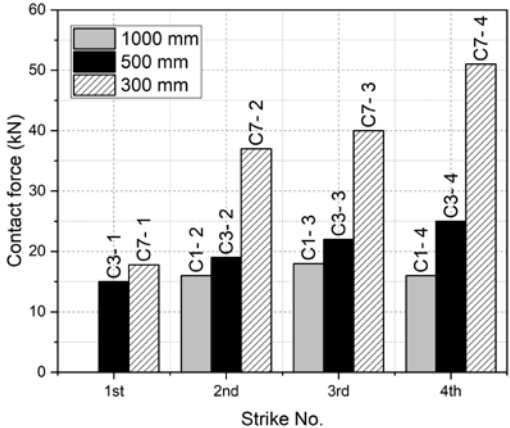


(i) $m = 1020 \text{ kg}$ $H = 1 \text{ m}$ & $t = 1000\text{mm}$

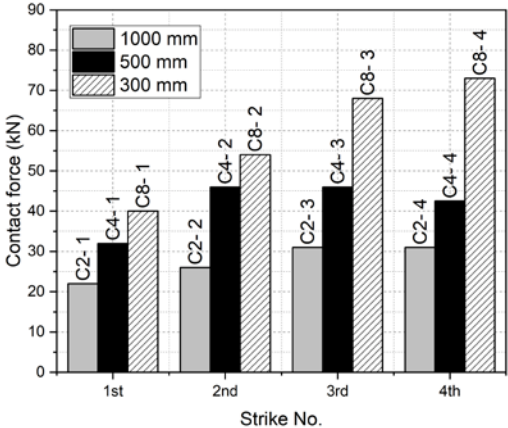
Figure 4.37 Contact force time-history from Test Series C

As compared to time-histories of contact force presented for Test Series A (where no cushion was used), test results on a cushioned wall (Test Series B and Test Series C) feature a significant reduction in the peak contact force along with an increase in the duration of contact. Contact force delivered to the cushion layer mainly depends on the confinement of the gabion cushion. Confinement of gabion cushion is governed by the geometrical arrangement of clumps inside the cell and the condition of the cage prior to the impact. The amount of contact force delivered by the first strike depends on the initial particle arrangement. After the first strike, particles inside the cell became compressed. Consequently, the level of intensity of the contact force delivered by the second strike was always higher than that by the first strike. However, in some cases, the strike led to breakage of the gabion cage thereby reducing the level of confinement. This behaviour was clearly illustrated in some experimental results.

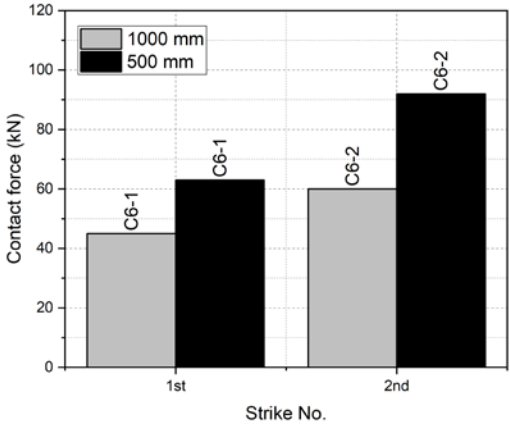
Contact force time history results were used to determine the peak contact force experienced by the cushion layer in each impact. Average value of peak points was selected because results contained some occasional peaks generated by mechanical noise of the accelerometer. Test results feature an increment in the peak contact force with reducing cushion thickness as shown in Figure 4.38. Peak contact force results from Test C4 and Test C5 are compared with results from Test Series B which comprised flexible gabion boxes as shown in Figure 4.39. Results demonstrated that the value of the contact force increases with the M_E value of the gabion box and decreases with increasing thickness of the cushion layer



(a) $m = 280 \text{ kg} \ \& \ H = 0.5 \text{ m}$

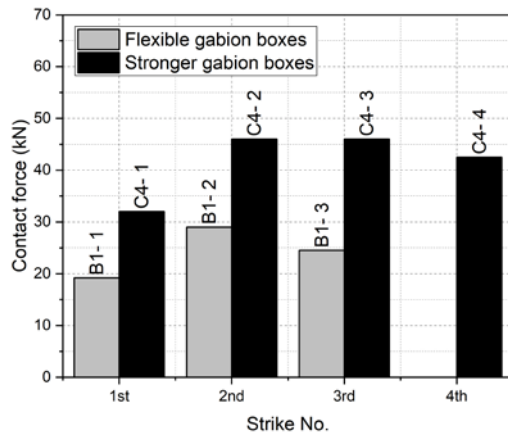


(b) $m = 280 \text{ kg} \ \& \ H = 1.4 \text{ m}$

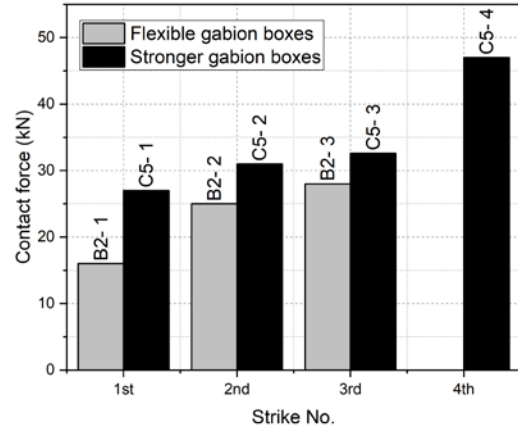


(c) $m = 1020 \text{ kg} \ \& \ H = 1 \text{ m}$

Figure 4.38 Variation of peak contact force with cushion thickness



(a) Test C4 vs Test B1 – $m = 280 \text{ kg}$ & $H = 1.4 \text{ m}$

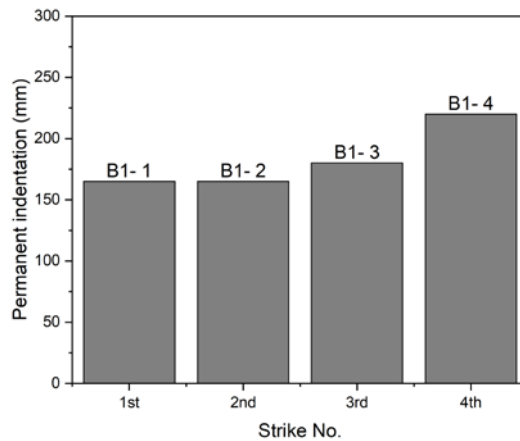


(b) Test C5 vs Test B2 – $m = 435 \text{ kg}$ & $H = 0.579 \text{ m}$

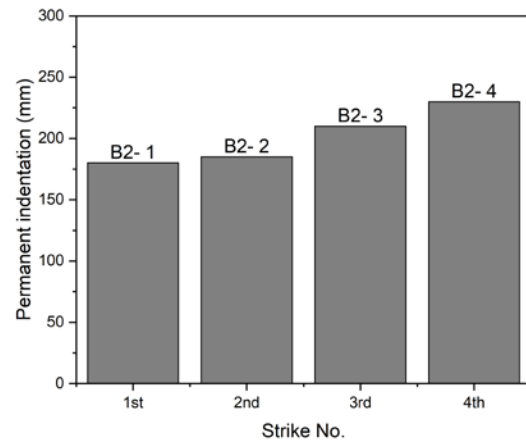
Figure 4.39 Variation of peak contact force with cushion M_E

4.7.3 Permanent indentations of the cushion layer

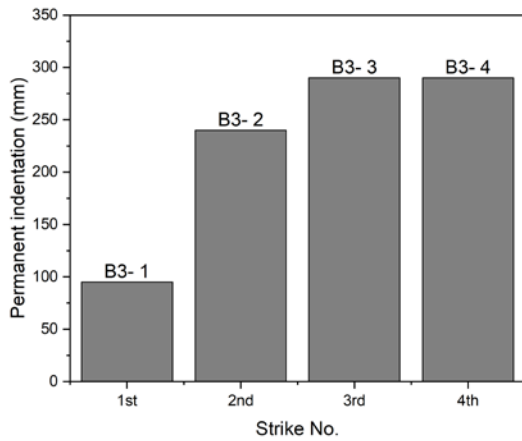
Permanent indentations of cushion layer measured after each test using a ruler and illustrated in Figure 4.40 for Test series B and in Figure 4.41 for Test series C. Each figure represents a one gabion cell which was struck multiple times (up to 4) before being replaced.



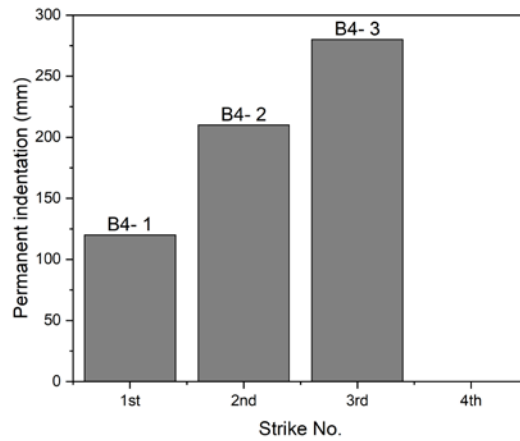
$m = 280 \text{ kg}$; $t = 500 \text{ mm}$; (FG/CG)



$m = 435 \text{ kg}$; $t = 500 \text{ mm}$; (FG/CG)

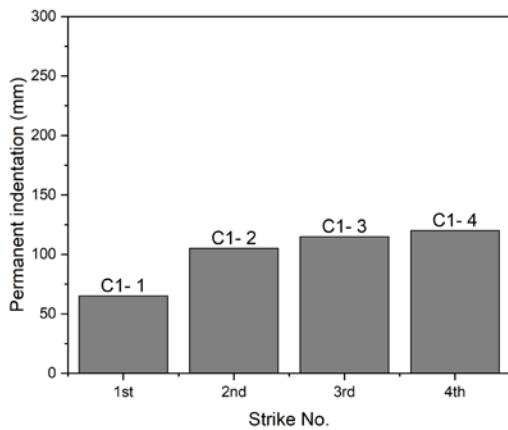


$m = 280 \text{ kg}; t = 500 \text{ mm}; (\text{FG}/\text{RP})$

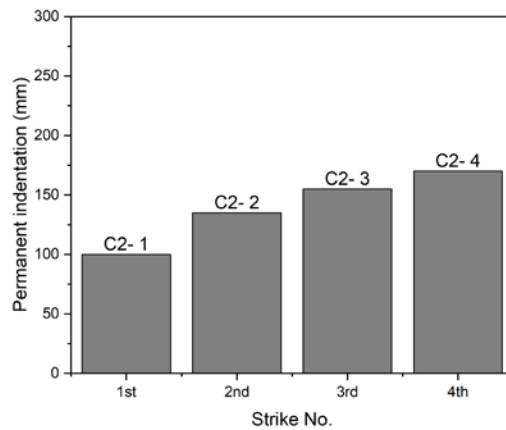


$m = 435 \text{ kg}; t = 500 \text{ mm}; (\text{FG}/\text{RP})$

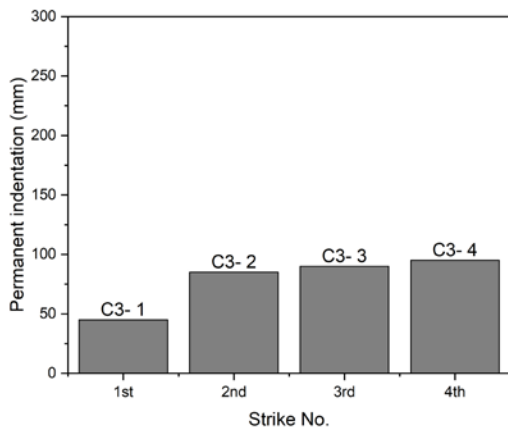
Figure 4.40 Permanent indentation after each strike on same cushion layer-Test Series B



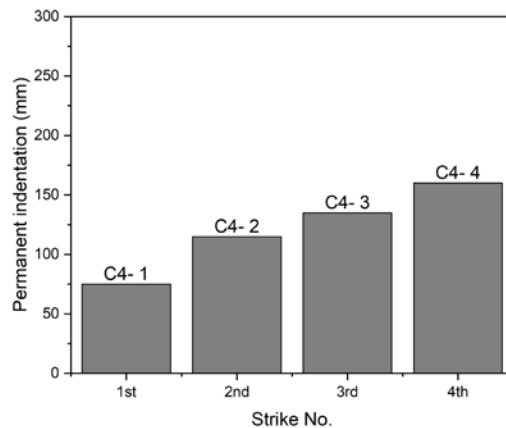
$m = 280 \text{ kg } H = 0.5 \text{ m} \ \& \ t = 300 \text{ mm}$
(SG/CG)



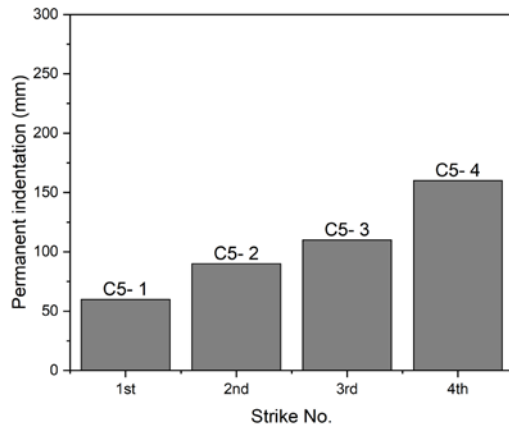
$m = 280 \text{ kg } H = 1.4 \text{ m} \ \& \ t = 300 \text{ mm}$
(SG/CG)



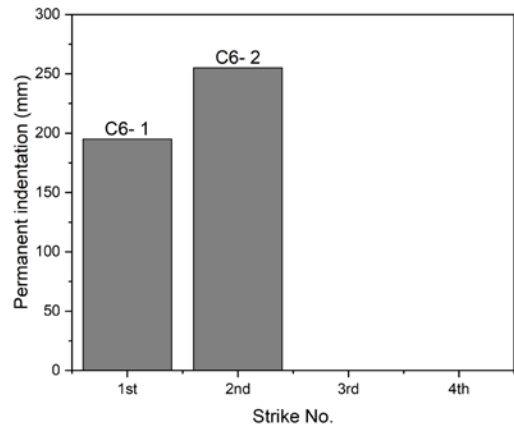
$m = 280 \text{ kg } H = 0.5 \text{ m} \ \& \ t = 500 \text{ mm}$
(SG/CG)



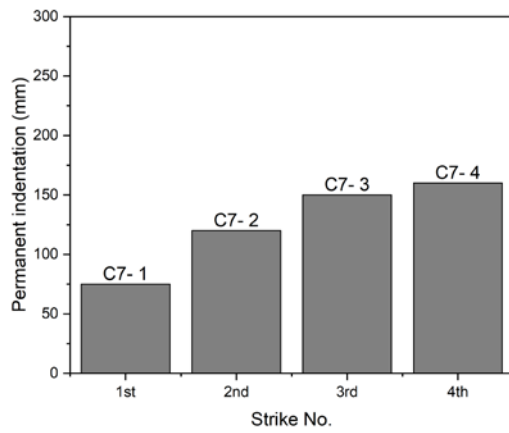
$m = 280 \text{ kg } H = 1.4 \text{ m} \ \& \ t = 500 \text{ mm}$
(SG/CG)



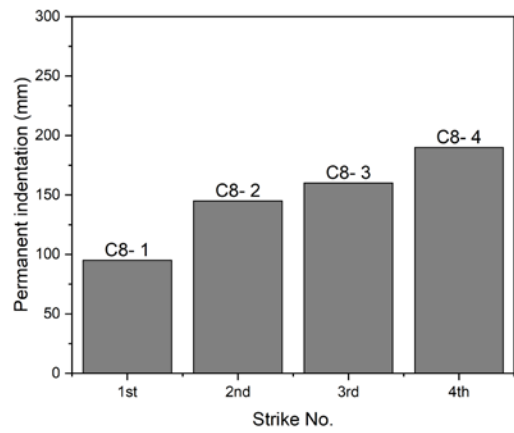
$m = 435 \text{ kg}$ $H = 0.579 \text{ m}$ & $t = 500\text{mm}$
(SG/CG)



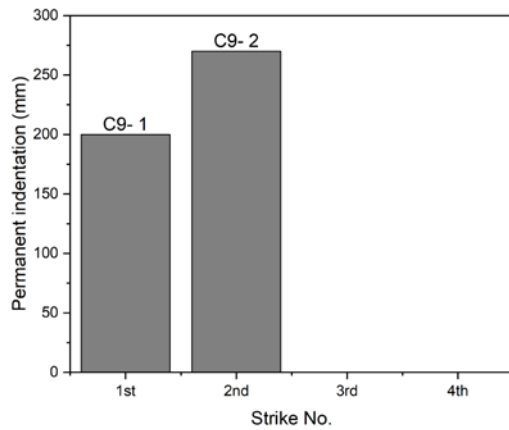
$m = 1020 \text{ kg}$ $H = 1 \text{ m}$ & $t = 500\text{mm}$
(SG/CG)



$m = 280 \text{ kg}$ $H = 0.5 \text{ m}$ & $t = 1000\text{mm}$
(SG/CG)



$m = 280 \text{ kg}$ $H = 1.4 \text{ m}$ & $t = 1000\text{mm}$
(SG/CG)



$m = 1020 \text{ kg}$ $H = 1 \text{ m}$ & $t = 1000\text{mm}$
(SG/CG)

Figure 4.41 Permanent indentation after each strike on same cushion layer-Test Series C

Photographs were taken from the (damaged) gabion following each test (refer Figure 4.42). The correlation between the extent of damage and the recorded peak contact force is evident from the presented photographs.



Figure 4.42 Damage to the gabion cushion following the impact – Test Series B

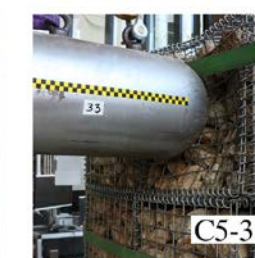
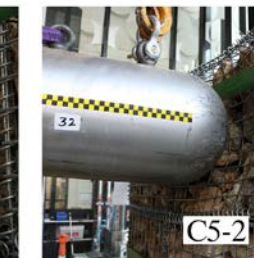
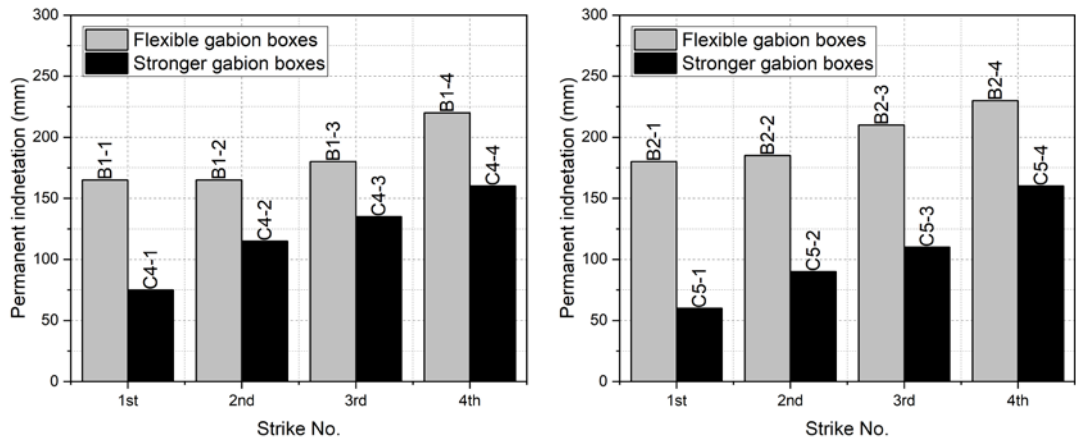




Figure 4.43 Damage to the gabion cushion following the impact – Test Series C

It was evident from permanent indentation results and photographs that there is no significant trend between the indentation and thickness of the cushion layer and hence not compared further. However, the different strength of gabion boxes (flexible gabion and stronger gabion) used in Test series B and Test series C have shown a substantial difference in both indentation and damage to the cushion in multiple strikes. Test B1 was compared with Test C4 and Test B2 was compared with Test C5 to illustrate this variation graphically and shown in Figure 4.44. The permanent indentation to the cushion layer is smaller when the stronger gabion boxes are used (Test series C) compared to flexible gabion boxes (Test series B).



(a) Test C4 vs Test B1 – $m = 280 \text{ kg}$ & $H = 1.4 \text{ m}$ (b) Test C5 vs Test B2 – $m = 435 \text{ kg}$ & $H = 0.579 \text{ m}$

Figure 4.44 Effect of the permanent indentation with the gabion cage strength

4.7.4 Deflection of the wall

The maximum deflection of the wall was obtained based on reading from laser sensors mounted at multiple locations, with those recorded at the top centreline of wall presented in Figure 4.45, Figure 4.46, Figure 4.47 for Test Series A, B and C respectively.

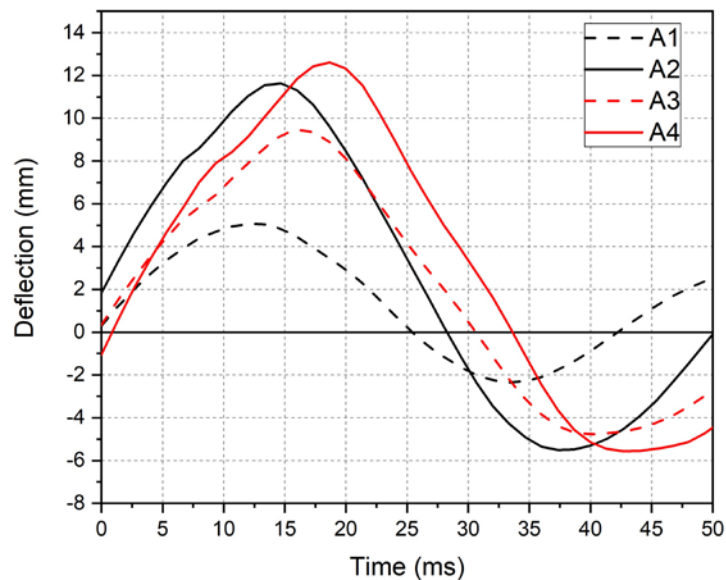
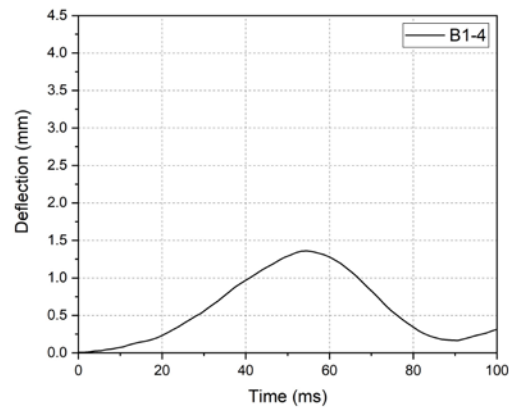
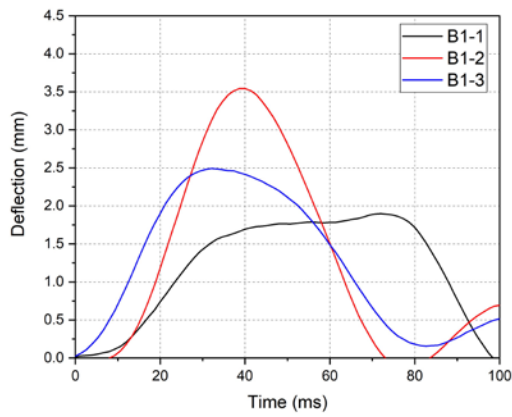
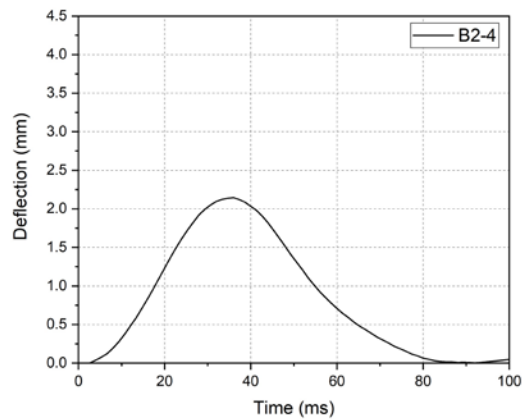
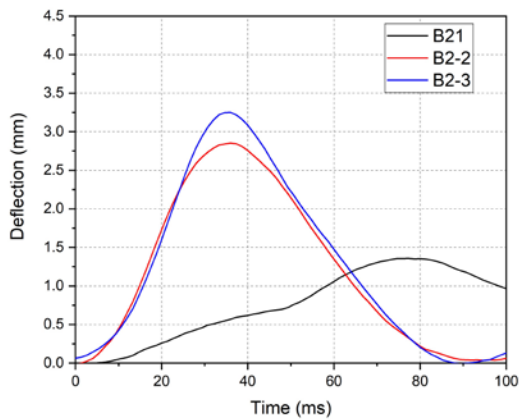


Figure 4.45 Deflection time-histories recorded at top centreline of wall from Test Series A



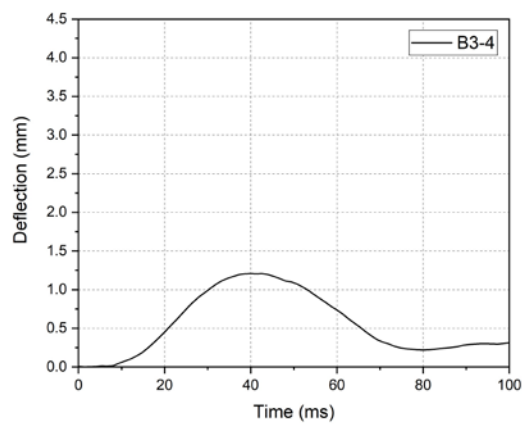
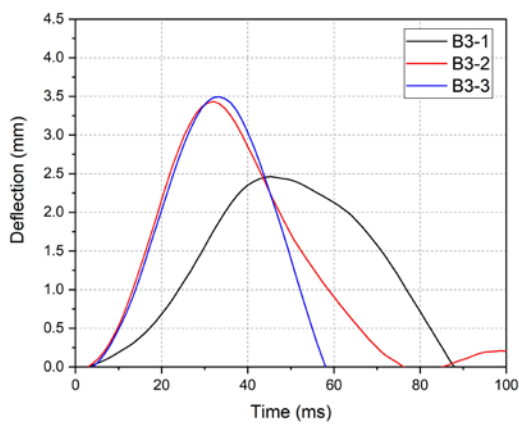
$m = 280 \text{ kg}$; $h = 1.4 \text{ m}$; $t = 500 \text{ mm}$;
(FG/CG)

$m = 280 \text{ kg}$; $h = 0.5 \text{ m}$; $t = 500 \text{ mm}$;
(FG/CG)



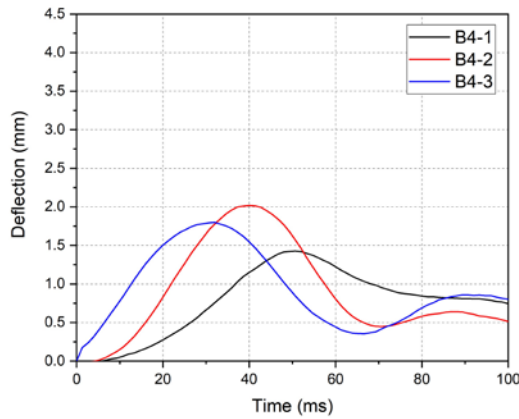
$m = 435 \text{ kg}$; $h = 0.58 \text{ m}$; $t = 500 \text{ mm}$;
(FG/CG)

$m = 435 \text{ kg}$; $h = 0.32 \text{ m}$; $t = 500 \text{ mm}$;
(FG/CG)



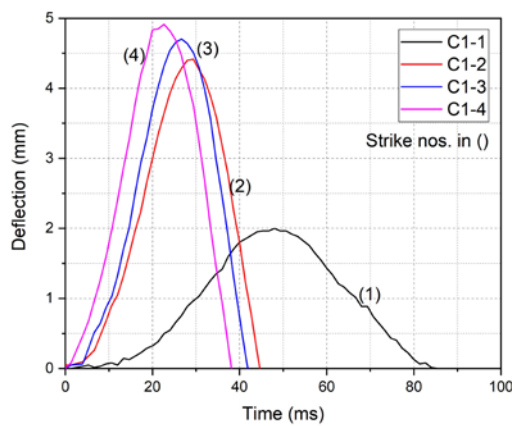
$m = 280 \text{ kg}$; $h = 1.4 \text{ m}$; $t = 500 \text{ mm}$;
(FG/FP)

$m = 280 \text{ kg}$; $h = 0.5 \text{ m}$; $t = 500 \text{ mm}$;
(FG/FP)

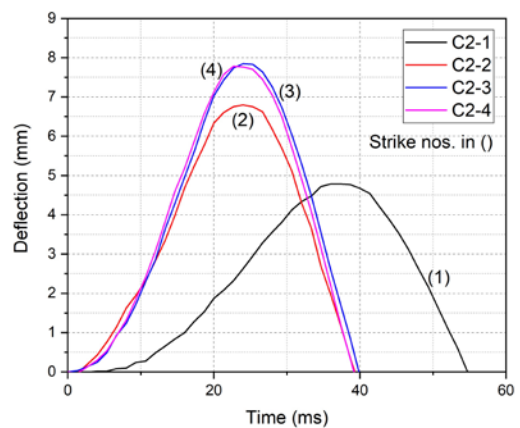


m – 435 kg; h – 0.58 m; t – 500 mm;
(FG/RP)

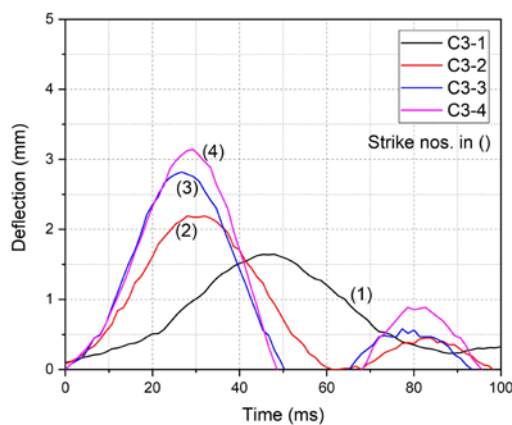
Figure 4.46 Deflection time-histories recorded at top centreline of wall from Test Series B



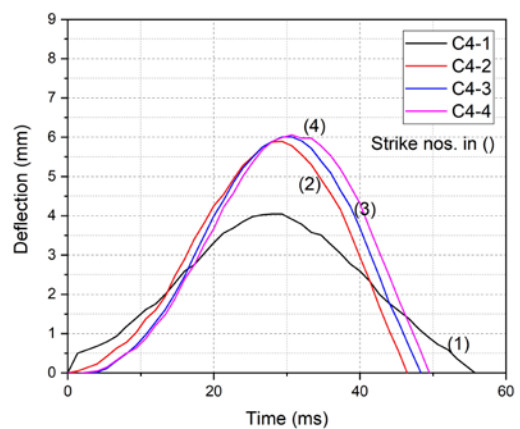
(a) m = 280 kg H = 0.5 m & t = 300mm



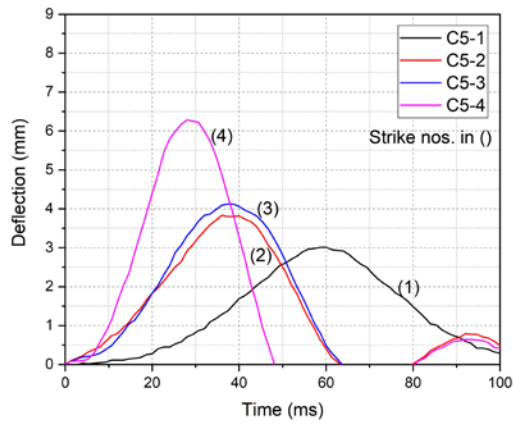
(b) m = 280 kg H = 1.4 m & t = 300mm



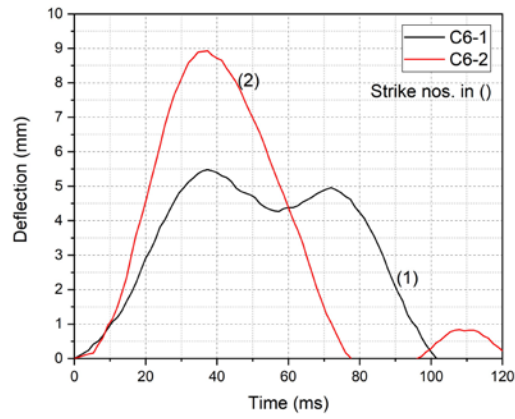
(c) m = 280 kg H = 0.5 m & t = 500mm



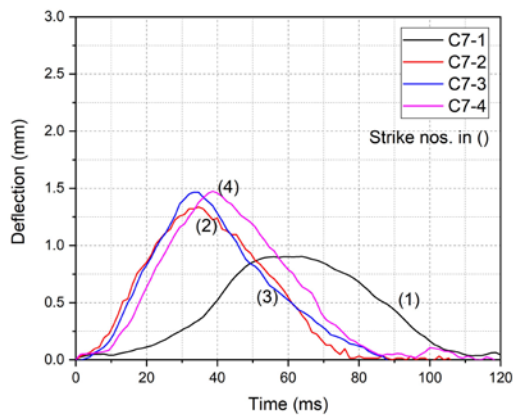
(d) m = 280 kg H = 1.4 m & t = 500mm



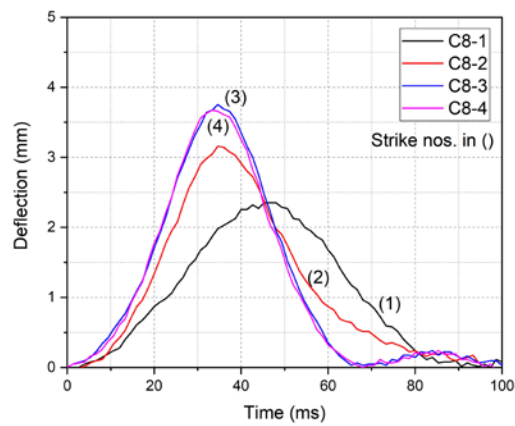
(e) $m = 435 \text{ kg}$ $H = 0.579 \text{ m}$ & $t = 500\text{mm}$



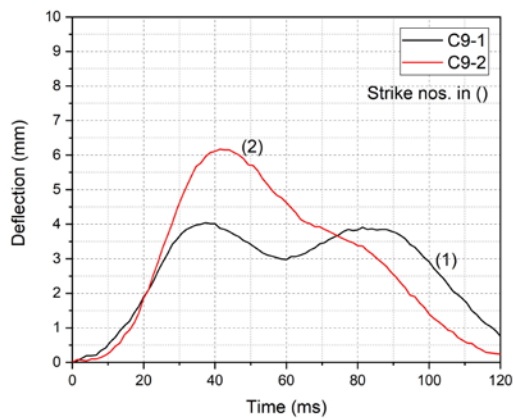
(f) $m = 1020 \text{ kg}$ $H = 1 \text{ m}$ & $t = 500\text{mm}$



(g) $m = 280 \text{ kg}$ $H = 0.5 \text{ m}$ & $t = 1000\text{mm}$



(h) $m = 280 \text{ kg}$ $H = 1.4 \text{ m}$ & $t = 1000\text{mm}$



(i) $m = 1020 \text{ kg}$ $H = 1 \text{ m}$ & $t = 1000\text{mm}$

Figure 4.47 Deflection time-histories recorded at top centreline of wall from Test Series C

The maximum deflection of the wall, which is of engineering interests, was found by reading off from the recorded time-history data and then correlated with its level up the height of the wall as shown in Figure 4.48, Figure 4.49 and Figure 4.50 for Test Series A, B and C. Variation of contact force for continuous impact identified in Figure 4.36 and Figure 4.37 has shown to be repeated in a similar way with the deflection time history results as well.

Values of maximum deflection of the wall at the top are compared across different tests (Test Series A and B) in Figure 4.51. Results recorded from Test Series A (without use of cushion) have also been included in the comparison. The use of cushion has resulted in some 70% to 90% reduction in the deflection of the wall. Another important observation is that the amount of reduction of the wall deflection (because of the introduction of the cushion) is always the highest in the first strike than the second and third strike. Note that dubious results were recorded from the laser sensor located at 1475 mm from the base in Test B1-2 due to interferences from truck lash belt; those data have been discarded.

As shown from the test results, contact force and wall deflection values resulted from the second strike were always higher than that from the first strike on the same cushion layer, but this is not necessarily the case with the third and second strike. Contact force delivered to the cushion layer mainly depends on the confinement of the gabion cushion. Confinement of gabion cushion is governed by the geometrical arrangement of clumps inside the cell and the condition of the cage prior to each impact. The contact force delivered by the first strike depended on the initial particle arrangement. The geometrical arrangement of the clumps inside each cell can be different even if the porosity was kept the same. This is a classical trend that has been reported for discrete materials [128-130]. After the first strike, particles inside the cell become compressed. Consequently, the contact force delivered by the second strike was always larger than that by the first strike. However, in some cases, the second strike led to breakage of the gabion cage thereby reducing the level of confinement. As a result, contact force delivered by the third strike could be lower than that by the second strike in some cases. Similar observations can be drawn from the deflection of the wall. It is worthy to note that these variations due to the breakage of the cage were not observed in the small-scale pendulum experiments presented in Chapter 3.

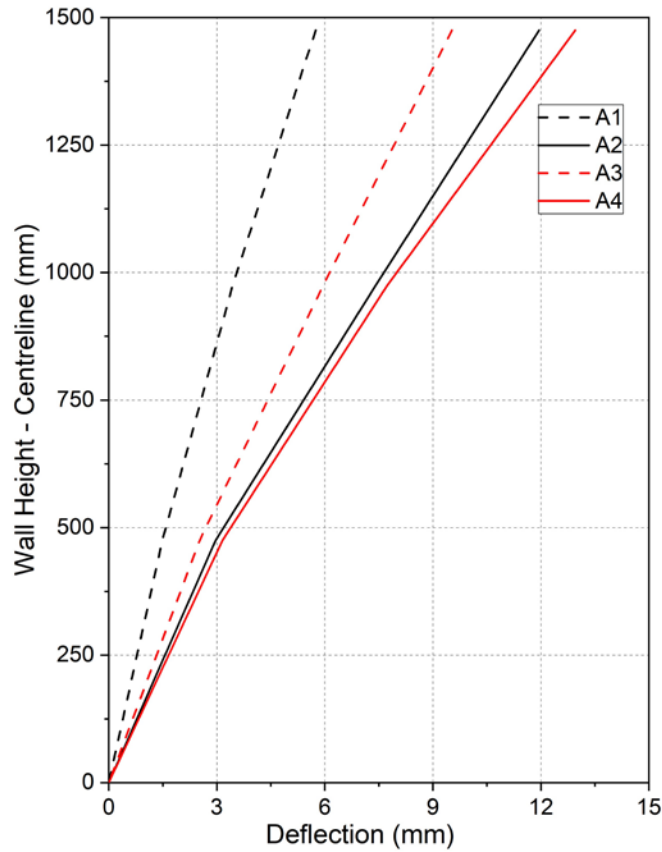
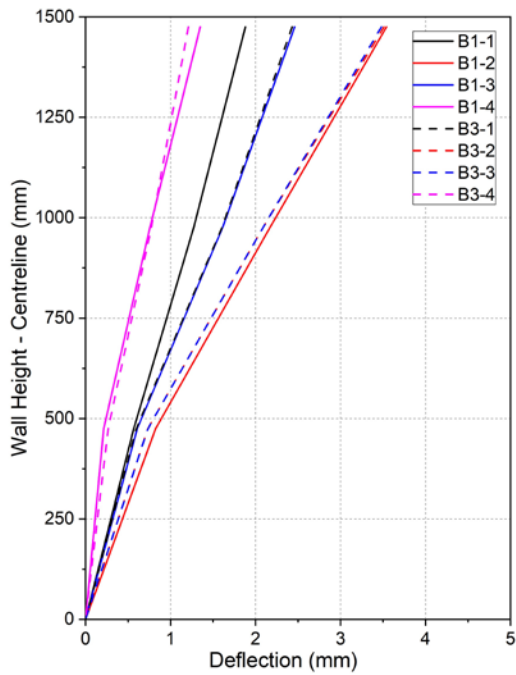
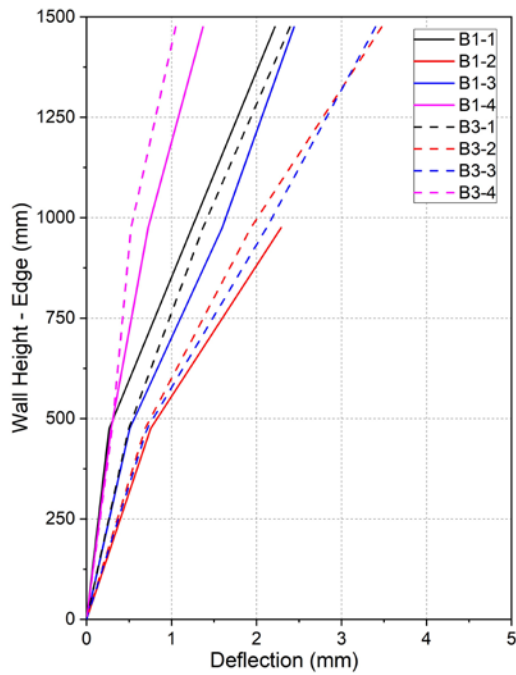


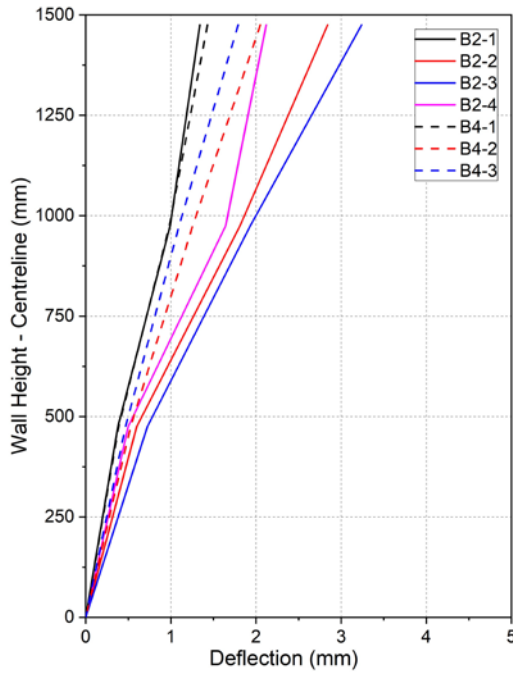
Figure 4.48 Maximum deflection values recorded from Test Series A



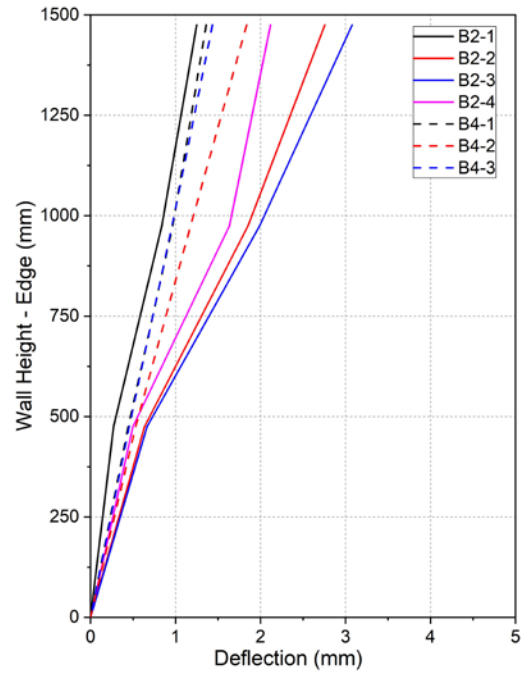
(m – 280 kg; wall centreline)



(m – 280 kg; wall edge)

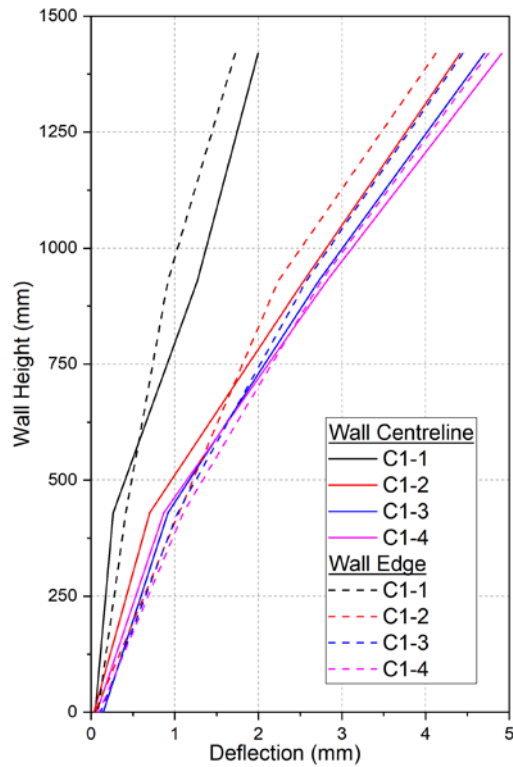


(m – 435 kg; wall centreline)

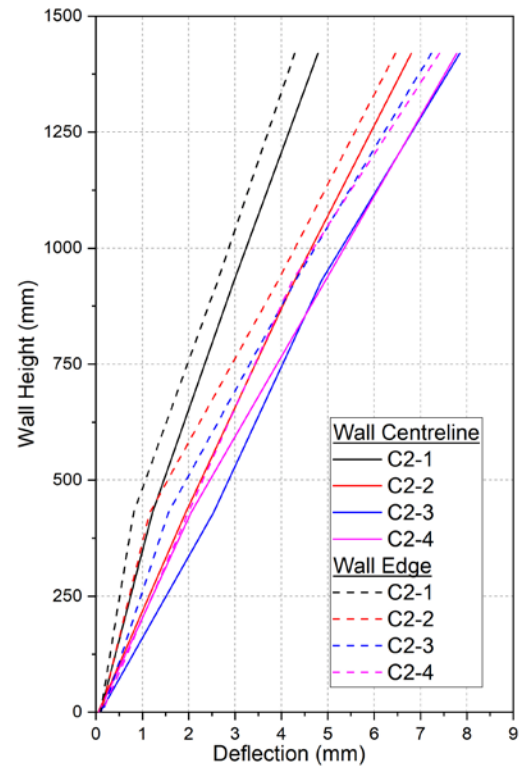


(m – 435 kg; wall edge)

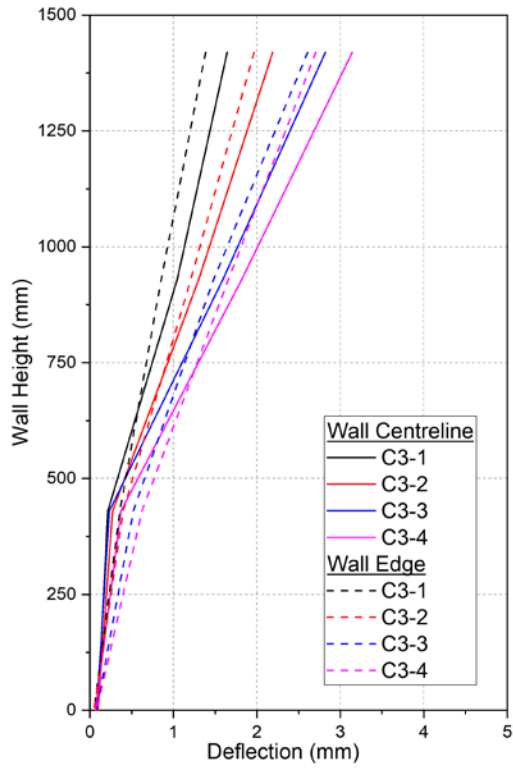
Figure 4.49 Maximum deflection values recorded from Test Series B



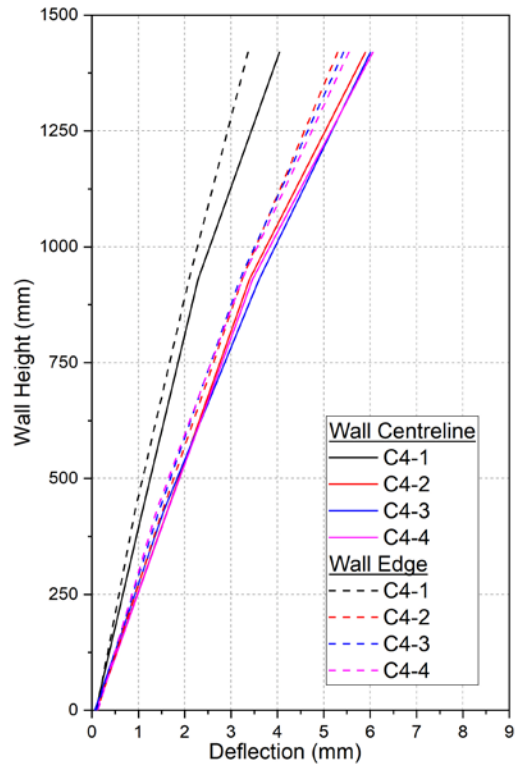
(a) Test C1-1 to C1-4



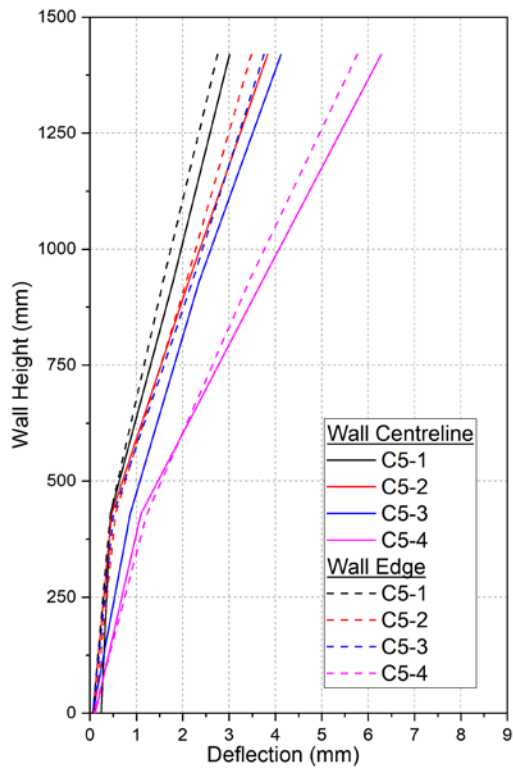
(b) Test C2-1 to C2-4



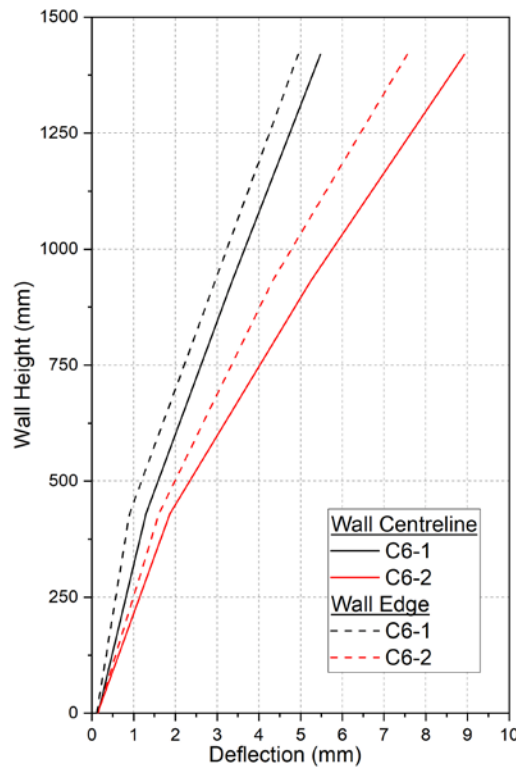
(c) Test C3-1 to C3-4



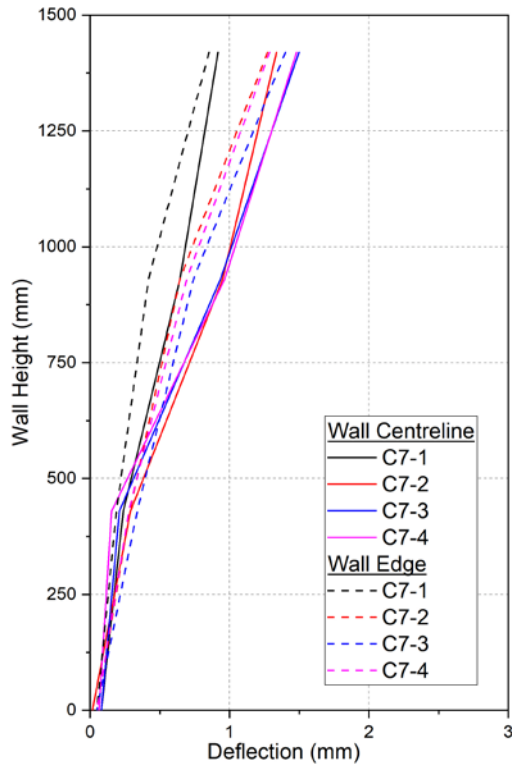
(d) Test C4-1 to C4-4



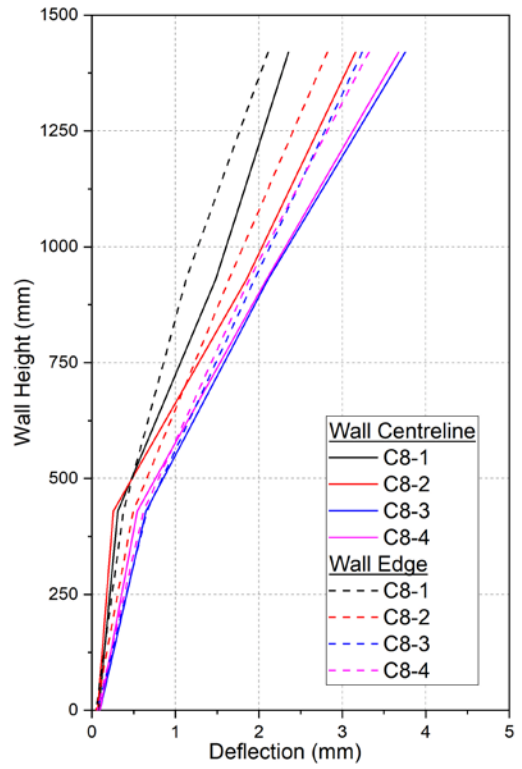
(e) Test C5-1 to C5-4



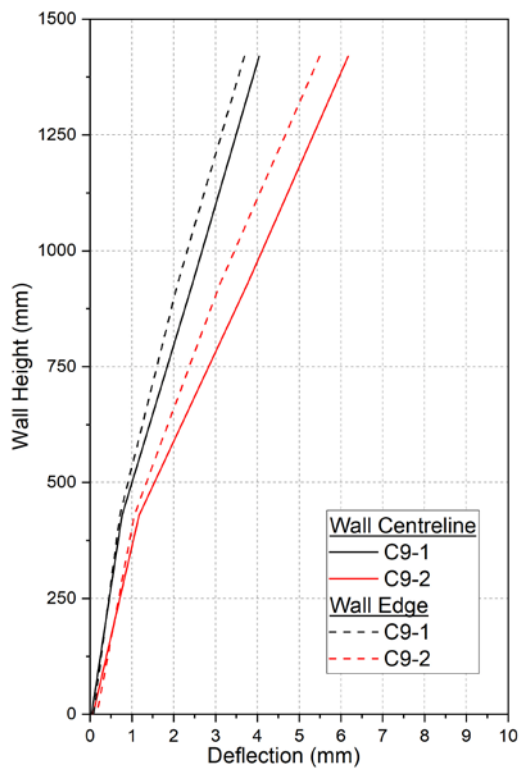
(f) Test C6-1 to C6-2



(g) Test C7-1 to C7-4



(h) Test C8-1 to C8-4



(i) Test C9-1 to C9-2

Figure 4.50 Maximum deflection values recorded from Test Series C

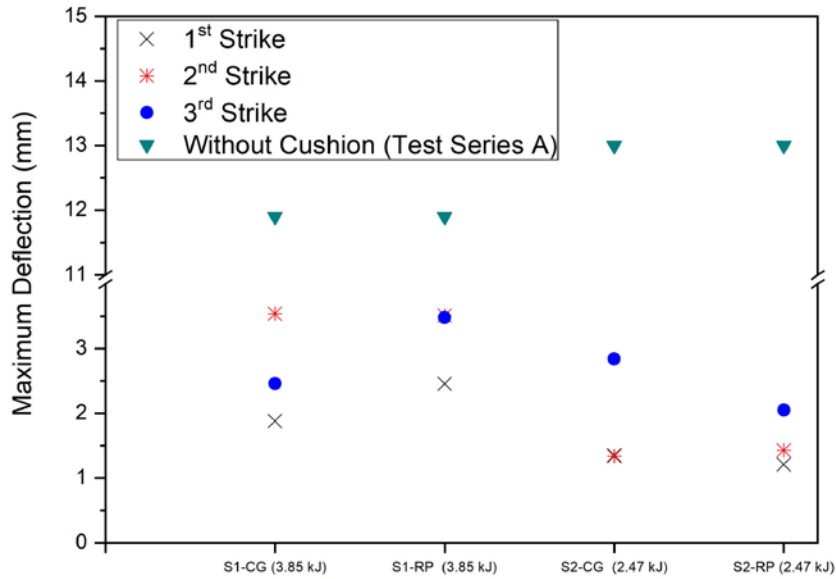
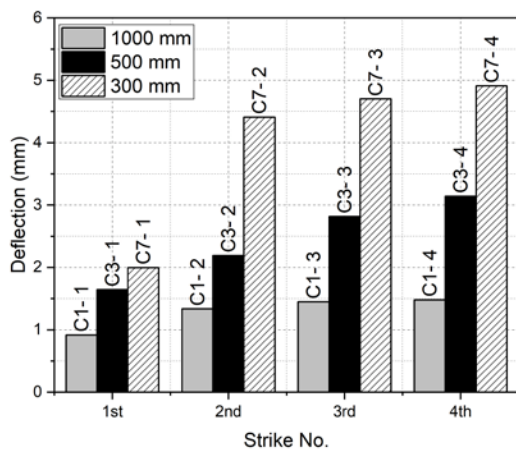
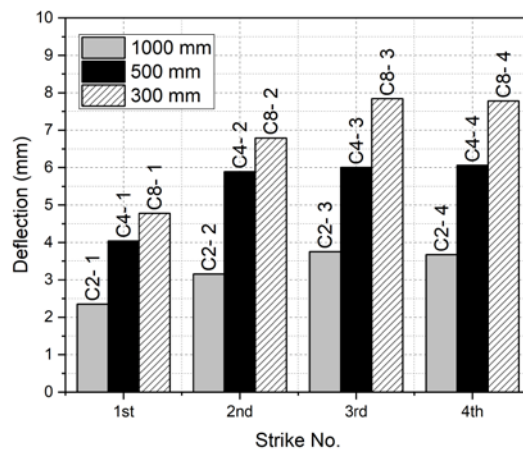


Figure 4.51 Maximum wall deflection for comparison between Test Series A and B (with cushion and without cushion)

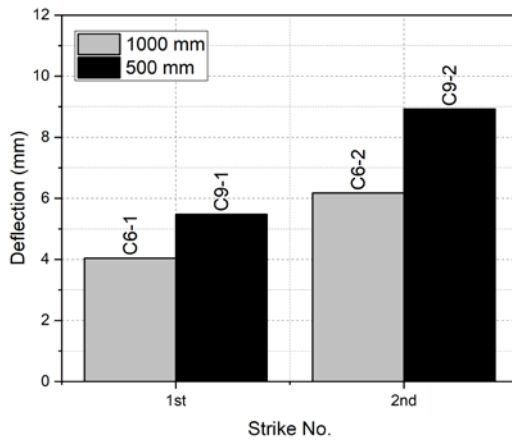
The maximum deflection of the wall for different cushion thicknesses was compared. Test results feature an increment in the deflection with the reducing cushion thickness as shown in Figure 4.52. The maximum deflection of the wall from Test C4 and Test C5 were compared with Test Series B which comprised flexible gabion boxes and shown in Figure 4.53. Results demonstrated that the maximum deflection of the wall increase with the M_E value of the gabion box.



(a) $m = 280 \text{ kg}$ & $h = 0.5 \text{ m}$

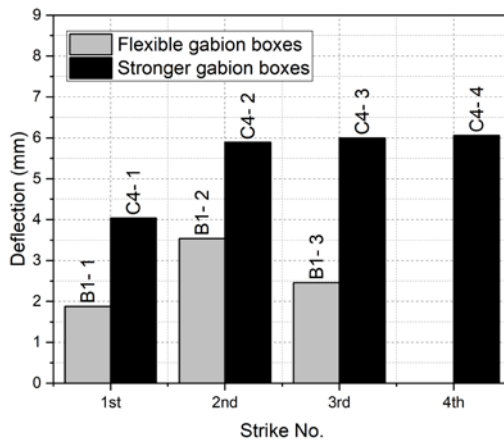


(b) $m = 280 \text{ kg}$ & $h = 1.4 \text{ m}$

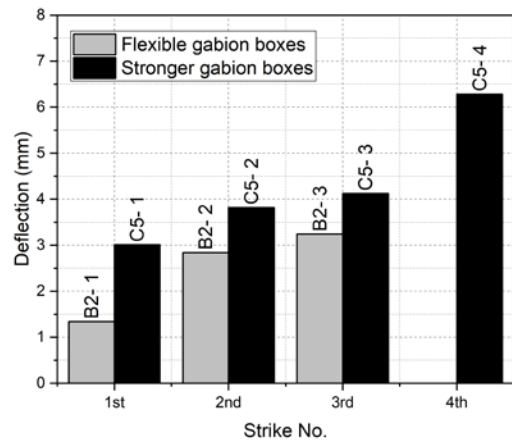


(c) $m = 1020 \text{ kg}$ & $h = 1 \text{ m}$

Figure 4.52 Variation of peak deflection with cushion thickness



(a) Test C4 vs Test B1 - $m = 280 \text{ kg}$ & $h = 1.4 \text{ m}$



(b) Test C5 vs Test B2 - $m = 435 \text{ kg}$ & $h = 0.579 \text{ m}$

Figure 4.53 Variation of peak deflection with cushion M_E

4.7.5 Strain

The amount of tensile strain experienced by reinforcing bars close to the base of the wall has also been recorded by strain gauges. Maximum strain values that were read off from strain gauges positioned along the length of the wall are presented in Figure 4.54 for Test Series A, Figure 4.55 for Test series B and Figure 4.56 for Test series C. It is shown that the reinforcing bars responded well within the yield limit of 0.0028 for Test series A & B and 0.00271 for Test series C.

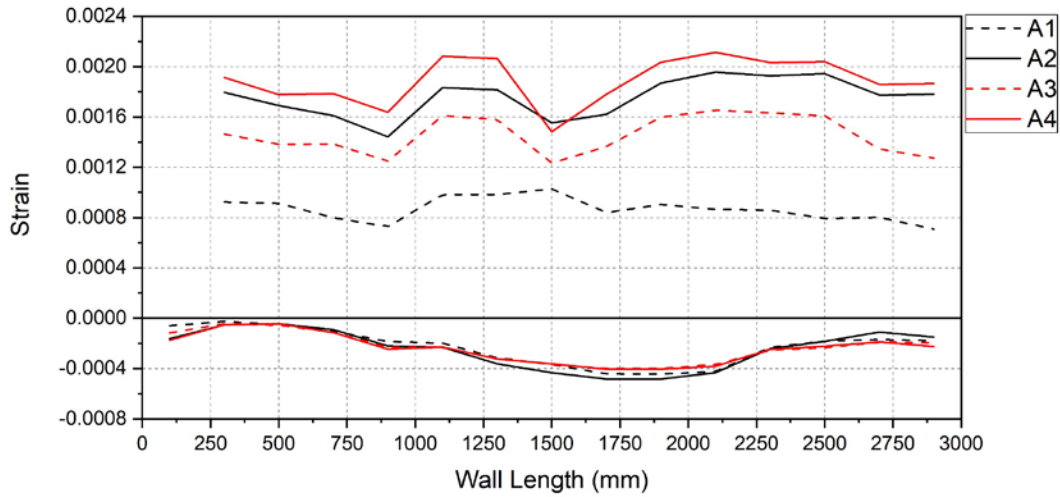
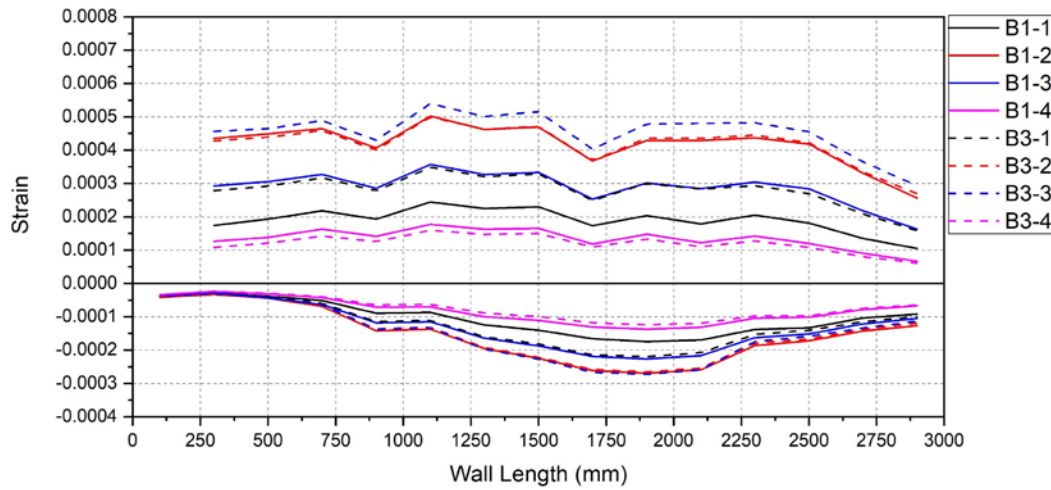
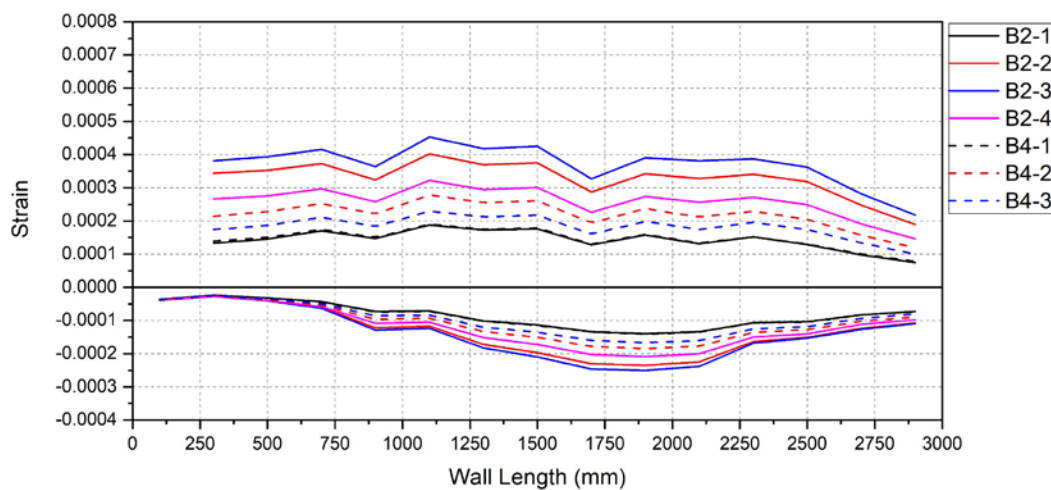


Figure 4.54 Reinforcement strain over the length of the wall



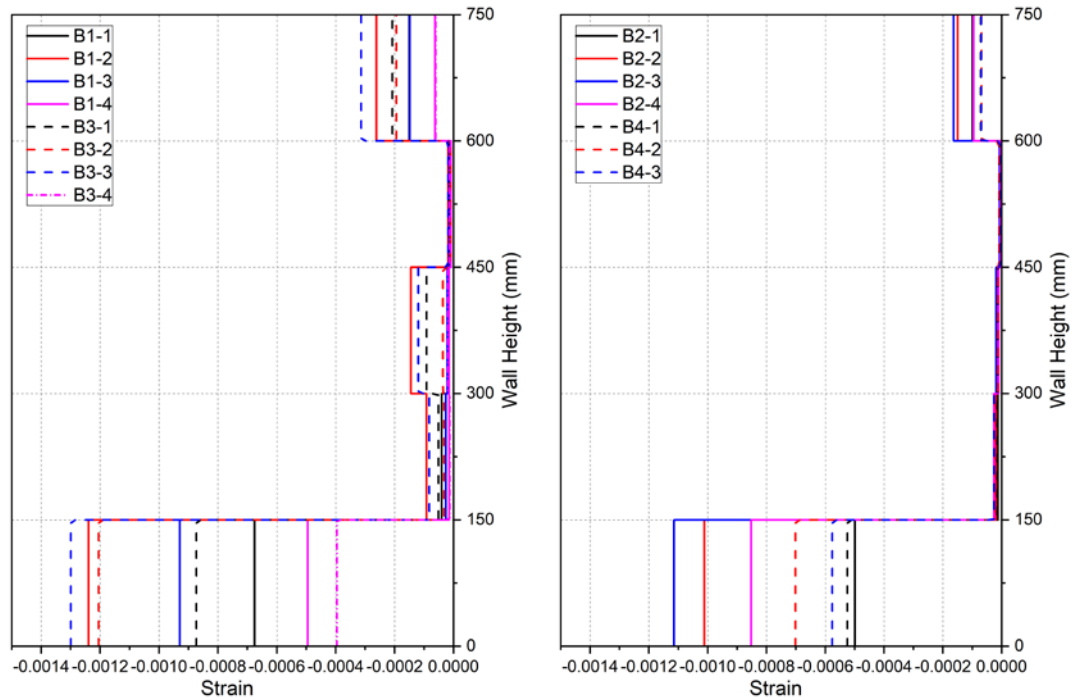
(a) Tests employing 280 kg impactor



(b) Tests employing 435 kg impactor

Figure 4.55 Maximum reinforcement strain recorded along wall length

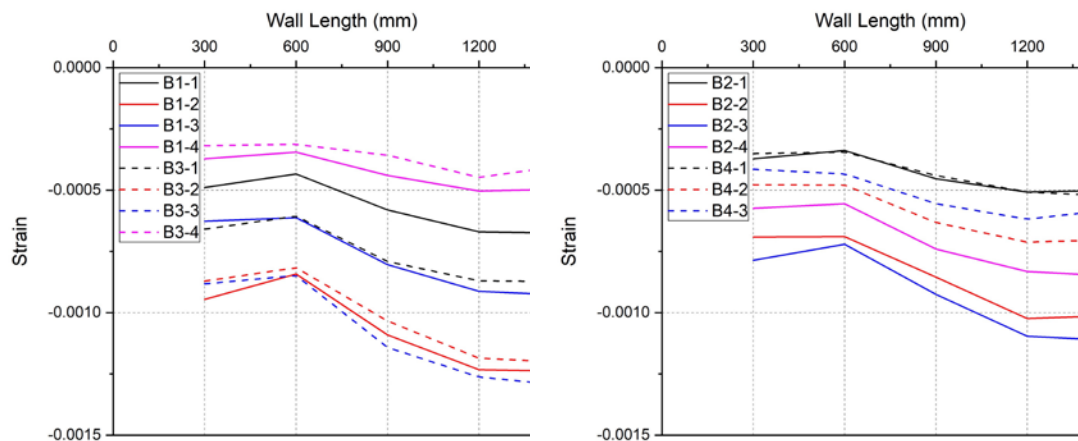
Average concrete strain values have also been measured using LVDTs. Strain values presented in Figure 4.56 were measured from the vertically stacked LVDTs at the centreline of the wall, whereas results presented in Figure 4.57 were derived from strain gauge readings taken at the base of the wall across its length.



(a) Tests employing 280 kg impactor

(b) Tests employing 435 kg impactor

Figure 4.56 Concrete strain profiles on the compressive side of the wall (on concrete surface) at the wall centreline

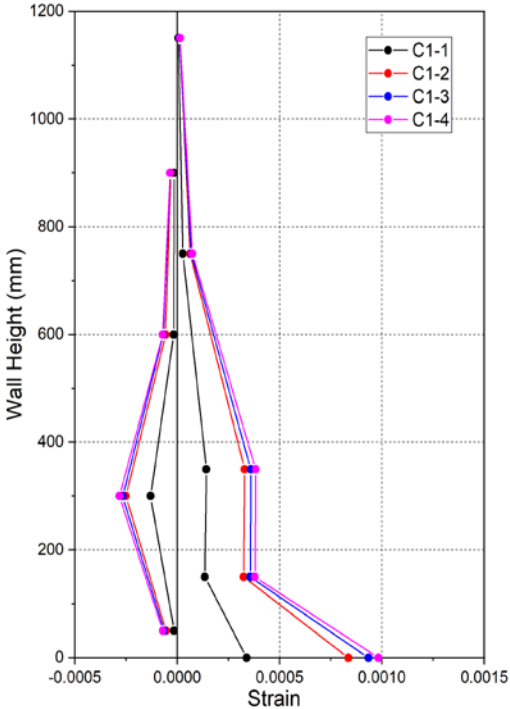


(a) Tests employing 280 kg impactor

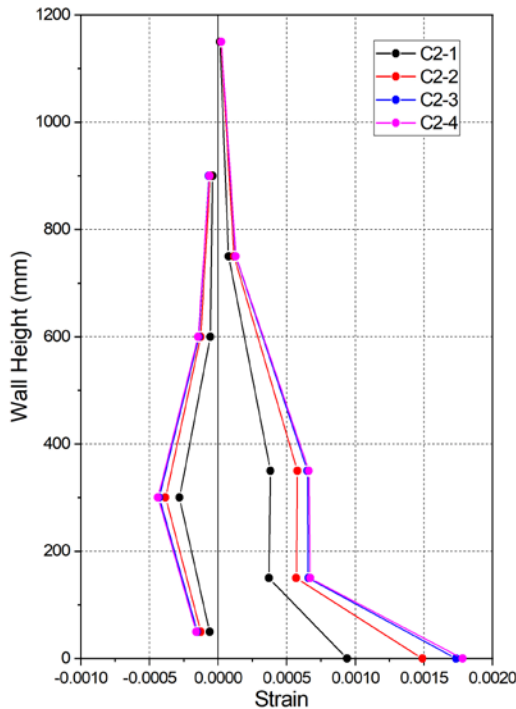
(b) Tests employing 435 kg impactor

Figure 4.57 Concrete strain at base of wall taken across its length

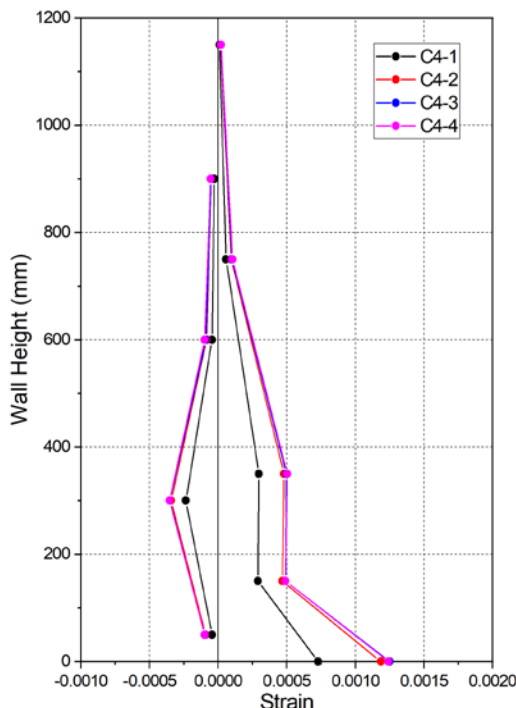
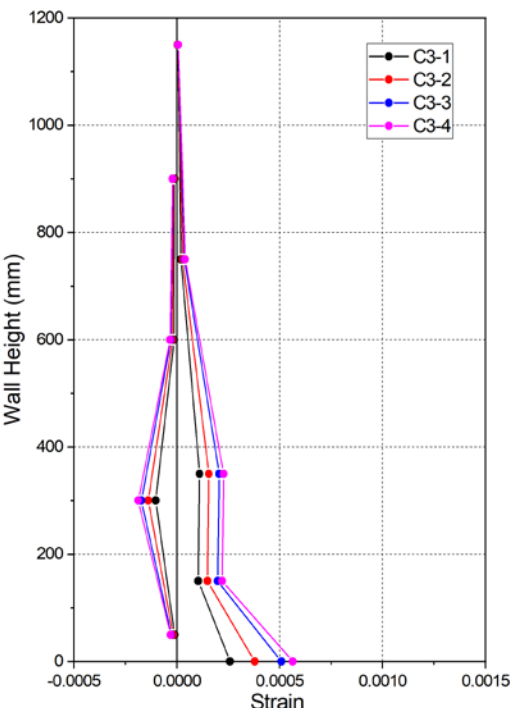
Strain gauges fixed to the reinforcement at the tension side and strain gauges fixed to the concrete surface on the compression side of the Test Series C was used to develop Figure 4.58 which illustrates the stress distribution over the height of the wall in centreline.



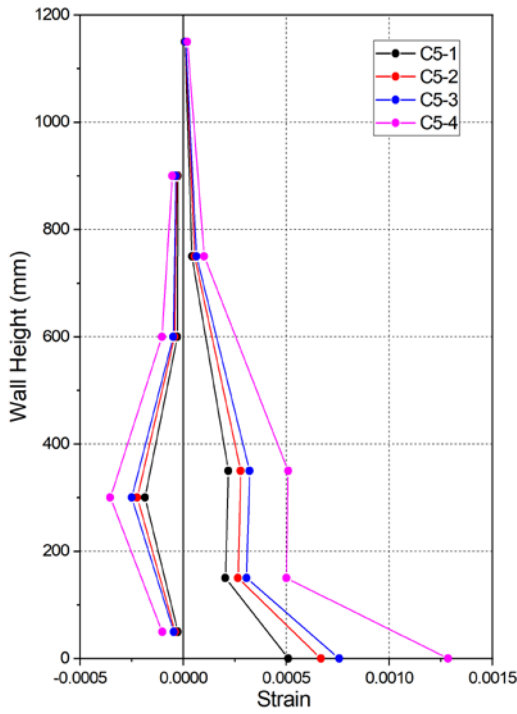
$m = 280 \text{ kg}$ $H = 0.5 \text{ m}$ & $t = 300\text{mm}$
(SG/CG)



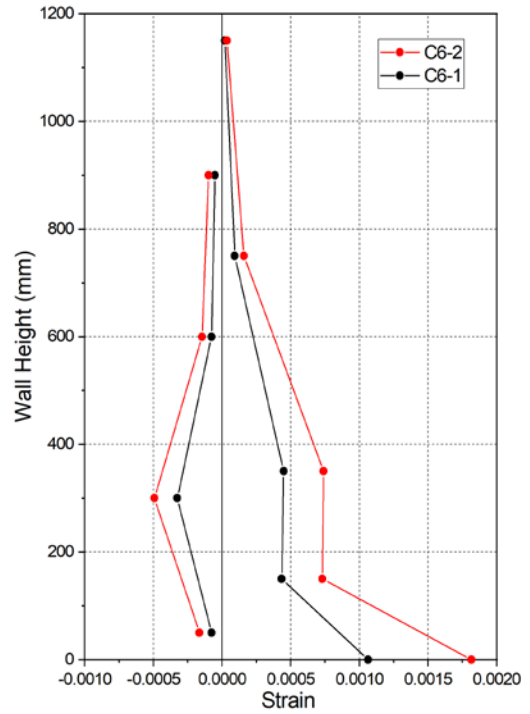
$m = 280 \text{ kg}$ $H = 1.4 \text{ m}$ & $t = 300\text{mm}$
(SG/CG)



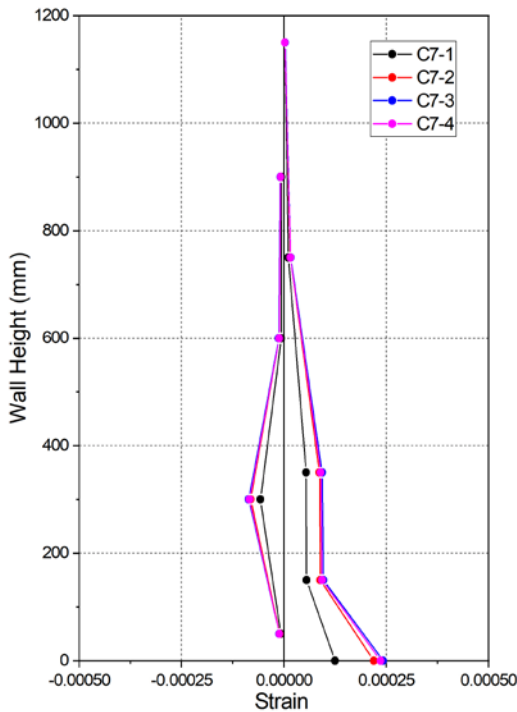
m = 280 kg H = 0.5 m & t = 500mm
(SG/CG)



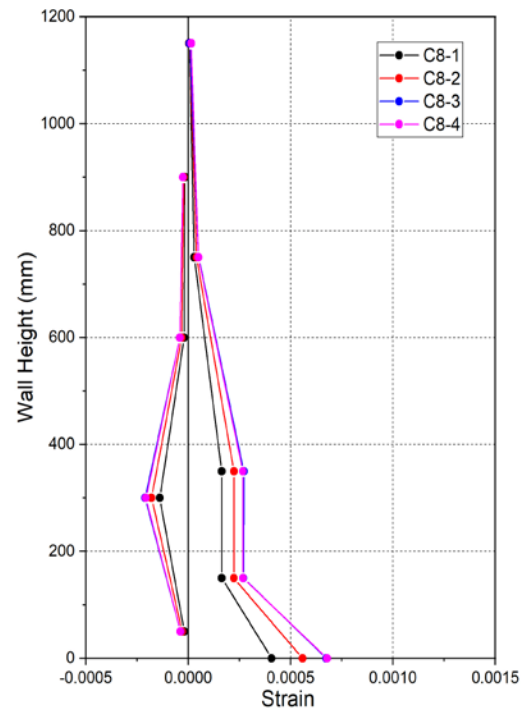
m = 280 kg H = 1.4 m & t = 500mm
(SG/CG)



m = 435 kg H = 0.579 m & t = 300mm
(SG/CG)

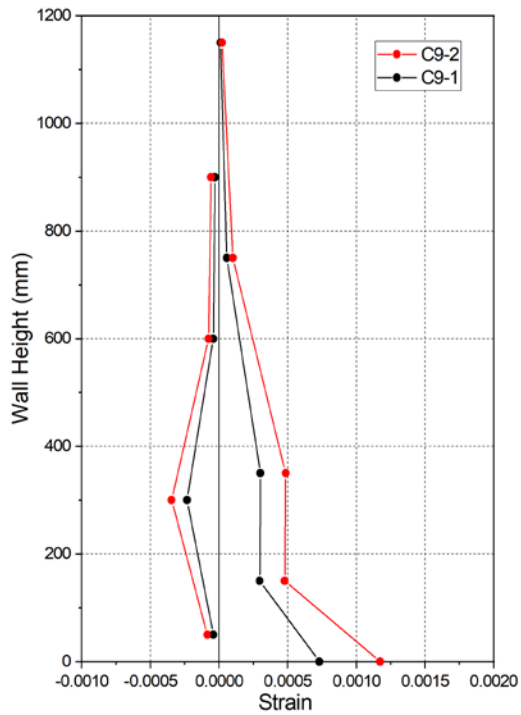


m = 1020 kg H = 1 m & t = 300mm
(SG/CG)



m = 280 kg H = 0.5 m & t = 1000mm
(SG/CG)

m = 280 kg H = 1.4 m & t = 1000mm
(SG/CG)



$m = 1020 \text{ kg}$ $H = 1 \text{ m}$ & $t = 1000\text{mm}$
(SG/CG)

Figure 4.58 – Strain diagram

No visible cracks were observed on the concrete surface at the conclusion of Test Series B, except for one small crack developed close to the top of the wall on the compressive side of the wall (as shown by the blue line in Figure 4.59).

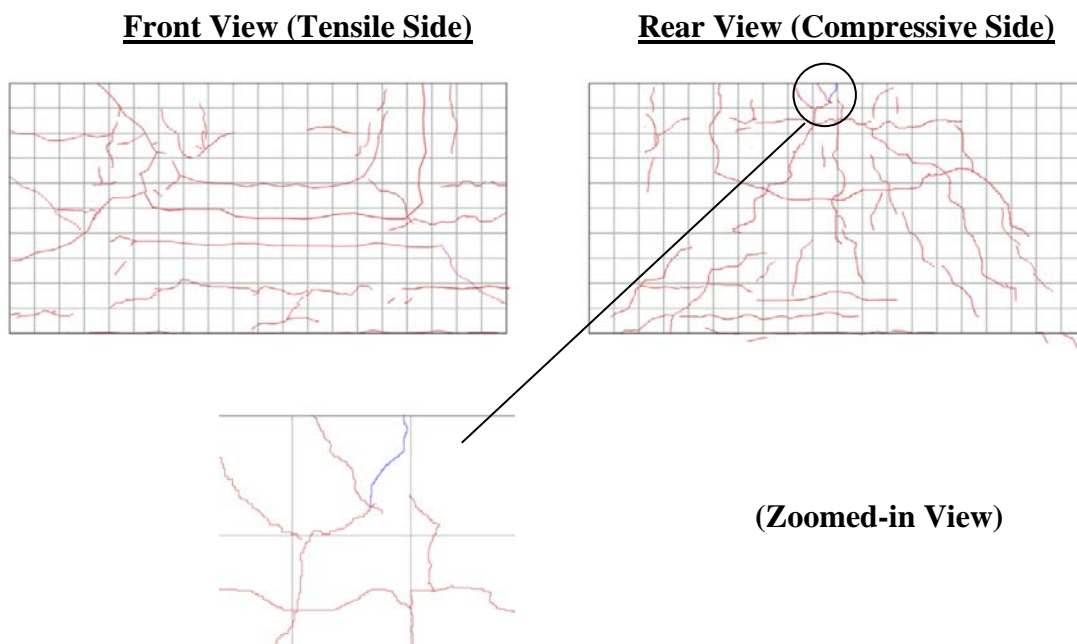


Figure 4.59 Crack profile observed following Test Series B

In this chapter, pendulum style impact tests have been performed on a full-scale RC barrier specimen which had the protection of a layer of gabion cushion cover of two different filling materials, two different cushion strengths and three different thicknesses. Over 100 pieces of instruments were employed in order to identify and record all characteristics of gabion cushioned RC barrier wall impacted by a solid impact object. One important finding is that the peak contact force has been reduced significantly by the extra gabion cushion protection whilst the duration of contact is prolonged. It was found from deflection measurements of the wall that use of gabion cushion has achieved some 50% to 90% reduction of the deflection of the wall. Same observations were reflected in the strain measurements as well which is of interest to the design engineer. Even though this large-scale experiment results give a clear picture of the flexural behaviour of cushioned RC wall, repeatability of this finding in the real-life design problem is not so apparent. This was established through an analytical model in the next chapter and validated from results presented in this chapter.

Chapter 5: Analytical Modelling of Cushioned Impact

Followed by the large-scale tests in Chapter 4, this chapter is focused on the development of an analytical model to calculate the flexural demand of the wall. Nonlinear viscoelastic model (Section 5.1) is used in conjunction with the 2DOF model (Section 5.2) to develop a complete analytical model which can be used to calculate the flexural demand of an RC wall with gabion cushion. In Section 5.3, some parameters of the proposed model are calibrated against experimental results from Chapter 4. Calculation of the stiffness of the gabion cushion by simplifying it to spring is explained under Section 2.4. Finally, the deflection results simulated by the proposed model is compared with experimental results in Section 5.5. Tensile reinforcement strain results are compared in Section 5.6 in the same manner.

5.1 NON-LINEAR VISCOELASTIC MODEL

The non-linear viscoelastic model originally proposed by Hunt and Crossley [131] has been proposed for calibrating the simulated forcing function (i.e. contact force time-histories) against experimentally recorded results. The hysteric model of Hunt and Crossley is defined by Eq. 5.1 which is an additive expression comprising a term which resembles Hertzian contact law and a second (velocity dependent) term representing the effects of damping. The frontal spring possessing hysteretic properties forming part of the 2DOF lumped mass system (Figure 5.1) is to simulate the condition of impact at the point of contact between the impactor object and the surface of the target. Parameters characterising the frontal spring are namely the spring stiffness k_n , exponent p and damping coefficient D_n . Different expressions for determining the value of D_n can be found in the literature [132-136], whereas the value of factor p is commonly taken to be equal to 1.5 as per Hertz law [137]. The recently derived expression of Eq. 5.2 which presents D_n as function of k_n and p has been demonstrated to provide accurate estimates of the contact force generated by an impact [96, 138, 139]. When operating on Eq. (5.1), $\dot{\delta}_0 = v_0$ may be assumed given that the target (the barrier) is initially at rest.

$$F_c = k_n \delta^p + D_n \delta^p \dot{\delta} \quad (5.1)$$

$$D_n = (0.2p + 1.3) \left(\frac{1 - \text{COR}}{\text{COR}} \right) \frac{k_n}{\dot{\delta}_0} \quad (5.2)$$

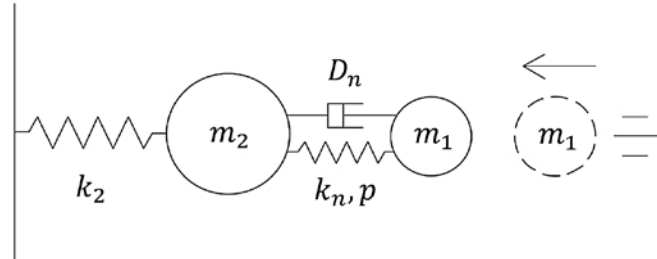


Figure 5.1 2DOF spring mass system utilising Hunt and Crossley Model

5.2 2DOF MODEL FOR CUSHIONED IMPACT

A rockfall barrier which is fitted with a layer of cushion material to resist the impact of a boulder can be idealised into a 2DOF lumped mass system as shown in Figure 5.2. The frontal spring can be assumed to possess the hysteretic properties as per the Hunt and Crossley model (as introduced above) whereas the second lumped mass (m_2) which is supported by the rear spring represents a portion of cushioning material in the vicinity of the point of contact in combination with the participating mass of the stem wall.

5.3 CALIBRATION OF PARAMETERS

A layer of granular material has been found to possess viscoelastic plastic indentation behaviour as reported in Refs. [99, 100]. The force-displacement behaviour of a gabion filled with the material is accordingly characterised by parameters D_n , k_n and p which are parameters in the governing expression of Eq. 5.1. The other parameters of the model are the targeted lumped mass (m_2) and stiffness (k_2) of the supporting spring which may be assumed to possess linear elastic properties. The calculation of these parameters and the method of calibration will be presented in the rest of this chapter under separate sub-headings.

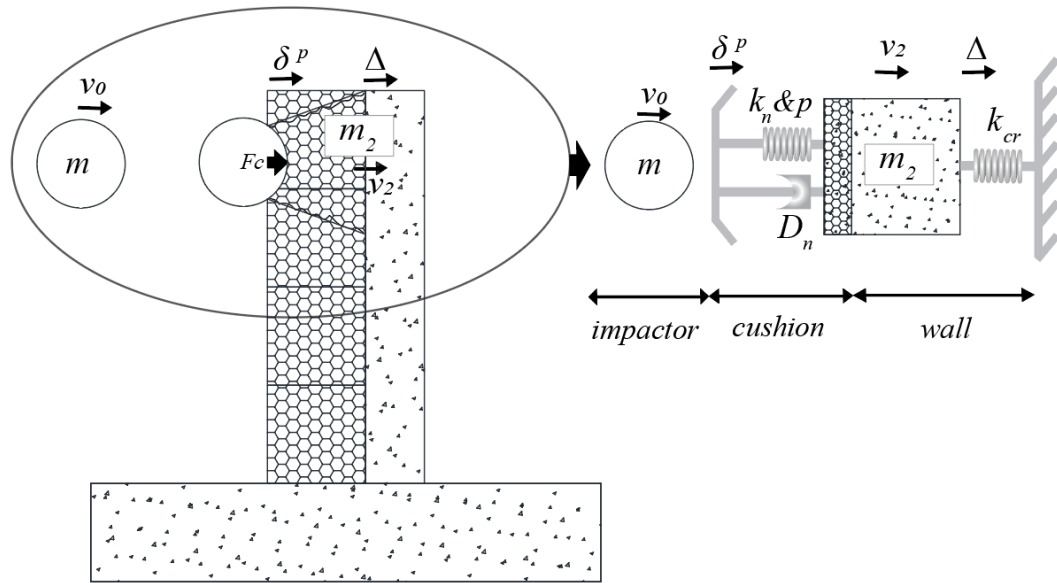


Figure 5.2 Force distribution in structure and 2DOF simplification

5.3.1 Calibration of COR

The value of COR would need to be determined from experimental measurements of the motion of the impactors. Alternatively, a method for finding the value of COR in an elastoplastic contact has been proposed by Thornton [140]. However, the proposed methods would only be applicable in situations where the response time of the stem wall of the barrier (wall placed behind the cushion) is considerably longer than the duration of contact. This condition is normally not satisfied in a cushioned impact because of the prolonged nature of the impact generated compression of the cushion material. It was observed from video capture of the cushioned impact that the impactor became attached to, or embedded into, the gabion cushion. Thus, in theory, $COR = 0$ may be assumed. However, the value of D_n as defined by Eq. 5.2 would be mathematically undefinable if $COR = 0$. To circumvent around this issue a very small value of COR ($= 0.01$ say) may be assumed. It was found from a sensitivity analysis (Figure 5.3) that varying the value of COR within the range of 0.01 to 0.2 would result in insignificant changes to the simulated response behaviour of the target.

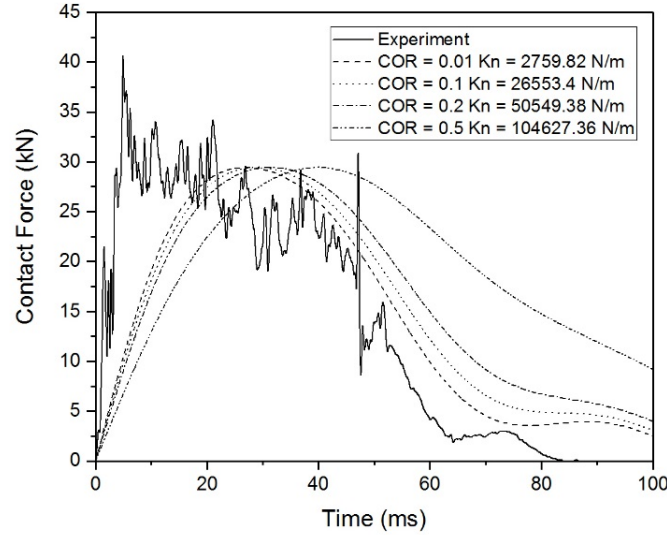


Figure 5.3 Sensitivity analysis of COR : Test B1-2 (m = 280 kg H = 1.4 m & t = 500mm (FG/CG))

5.3.2 Calibration of p

The deformation behaviour of the cushion layer can be modelled assuming viscoelastic plastic behaviour when subject to an impact [98-100]. To simplify computations linear viscoelastic behaviour (i.e. $p = 1$) may be assumed whereas the assumption of non-linearity on contact (i.e. $p > 1$) would delay the occurrence of the rise of the contact force. Such a delay phenomenon was not observed in the impact tests. It has also been observed in the loading phase of the gabion cell that the force-indentation behaviour is approximately linear [24, 101]. Three types of forcing functions are shown for comparison in Figure 3.4 based on taking $COR = 0.01$. It was found from sensitivity analyses (Figure 3.5) in which the value of p was varied within the range: $1 < p < 2$ that the simulated response behaviour matched best with experimental recorded behaviour when $p = 1$ was assumed. The contact force model of Eq. 5.1 is accordingly simplified into Eq. 5.3.

$$F_c = D_l \delta \dot{\delta} + k_l \delta \quad (5.3)$$

where k_l is the linear spring stiffness and D_l is the damping coefficient ($k_n = k_l$ and $D_n = D_l$ when $p = 1$). The value of parameter D_l may be found using Eq. 5.4.

$$D_l = 1.5 \left(\frac{1 - COR}{COR} \right) \frac{k_l}{\dot{\delta}_0} \quad (5.4)$$

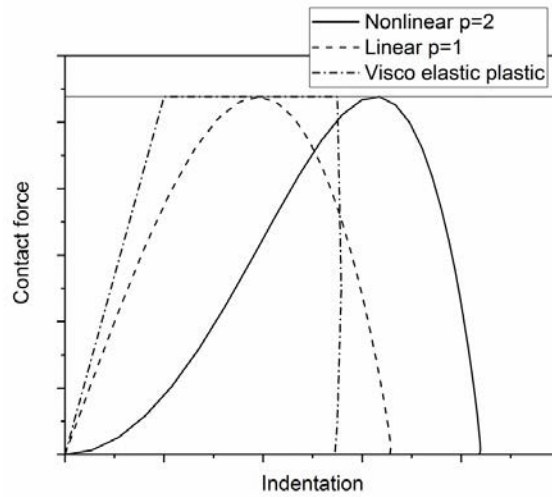


Figure 5.4 Force displacement diagram for different analytical models

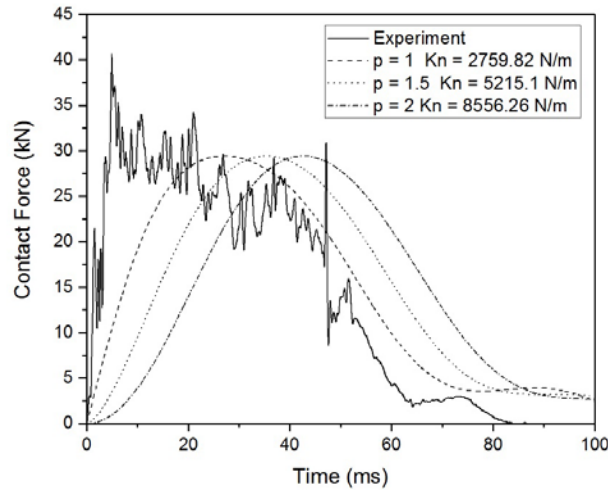


Figure 5.5 Sensitivity to change in the value of p : Test B1-2 ($m = 280$ kg $H = 1.4$ m & $t = 500$ mm (FG/CG))

5.3.3 Calculation of the mass of structure (m_2)

Both the gabion cushion and the stem wall may be considered to be part of the “target”. Thus, the combined mass participating in the response to the impact can be represented by Eq. 5.5. As explained in Section 3.2.1 for gabions that are filled with particles of crushed rock, the angle of the funnel may be taken as 20° as shown in Figure 5.6. Eq. 5.6 can be used to calculate the mass of the gabion cushion.

$$m_2 = m_{wall} + m_{gabion} \quad (5.5)$$

$$m_{gabion} = \frac{1}{3}\pi(r_1^2 + r_1r + r^2)ep \quad (5.6)$$

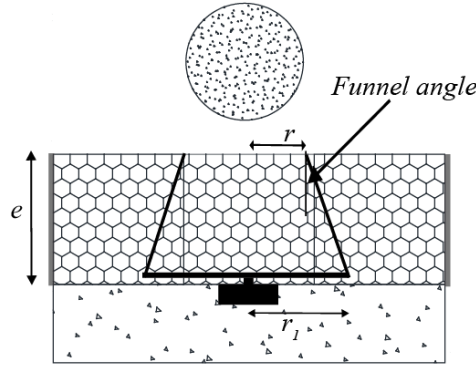


Figure 5.6 Calculation of cushion volume under load

5.3.4 Calculation of the stiffness of structure (k_2)

Eq. 5.7 for calculating the bending stiffness of a cracked RC stem wall based on structural dynamics principles can be identical to the expression for calculating the static stiffness.

$$k_{cr} = \frac{3EI_{cr}}{h^3} \quad (5.7)$$

Given that the height of the stem wall (h) is readily known, the only remaining input parameter to Eq. 5.7 is the wall flexural rigidity (EI_{cr}). Note that subscript cr denotes cracked concrete. Three methods may be used for calculating the value of EI_{cr} :

Method 1 - by moment-curvature analysis which is executable using program *Response 2000* [141].

Method 2 - moment-curvature analysis by fibre-element analysis which can be implemented on an Excel spreadsheet as proposed by Lam, Wilson [142].

Method 3 - Simplified method of calculation employing Eqs. 5.8 to 5.10. Eq. 5.8 is based on the well-established Whitney stress block model (as introduced in Ref. [143]). Eq. 5.9 was derived by Priestley, Calvi [144] based on extensive moment-curvature analyses carried out on lightly (axially) loaded structural element which is consistent to the conditions of the stem wall of a rockfall barrier.

$$M_y = \phi M_u = 0.8A_{st}f_y d \left(1 - 0.6 \frac{A_{st}f_y}{Bdf'_c} \right) \quad (5.8)$$

$$\phi_y = \frac{1.7 \varepsilon_{sy}}{D} \quad (5.9)$$

$$EI_{cr} = \frac{M_y}{\phi_y} \quad (5.10)$$

Calculation of EI_{cr} by following method 1 is extensively studied in Ref. [74]. A complete calculation of the wall specimen 1 is also given in the same reference. The value of the k_{cr} parameter used in this thesis was calculated using method 1 which may be taken as constant: $k_{cr} = 14379 \text{ kN/m}$ across all scenarios for specimen 1 and $k_{cr} = 14020 \text{ kN/m}$ for specimen 2. Calculation of these values using Method 1,2 and 3 are further shown in Appendix [D]

5.3.5 Calibration of the stiffness of cushion (k_n)

It was identified from impact experiments performed under Test Series B that the forcing function generated by the impact could vary considerably when subjected to repeated impact actions on the same position multiple times because of change in the degree of confinement of the particles filling the gabion. The stiffness of the frontal spring (k_n) would accordingly vary significantly because of its sensitivity to changes in the degree of confinement. Thus, the best way of obtaining the value of k_n would be through calibration following every strike by the impactor.

When calibrating the value of k_n based on matching the simulated forcing function with the experimentally recorded function the value of the other parameters: COR, p , m_2 , k_2 were kept constant. One of such forcing function calibration is illustrated in Figure 5.7 (a) for Test series B and Figure 5.7 (b) for Test series C (the rest of the results could be found in Appendix [E]). The calibrated values of k_n across all the tests that have been conducted is shown in Figure 5.8 and Figure 5.9 for Test Series B and C respectively. Calculation of values employing Excel spreadsheet for developing Figure 5.8 and Figure 5.9 is presented in Appendix [F]. A consistent trend of significant increase in the stiffness of the gabion from the first to the second strike (for an equal amount of delivered energy) is shown. There is almost a factor of 2 difference in most cases and this validates the model presented in Section 3.4. The value of k_n may, or may not, decrease to a lower value from the third to fourth strike. The cause of the decrease is believed to be resulted from the sudden loss of

confinement because of damage to the cage which provides the confinement as illustrated in Figure 4.42. Hence adopting appropriate multiplication factor for third and fourth strike needs to be decided based on the performance of the cage after subsequent strikes.

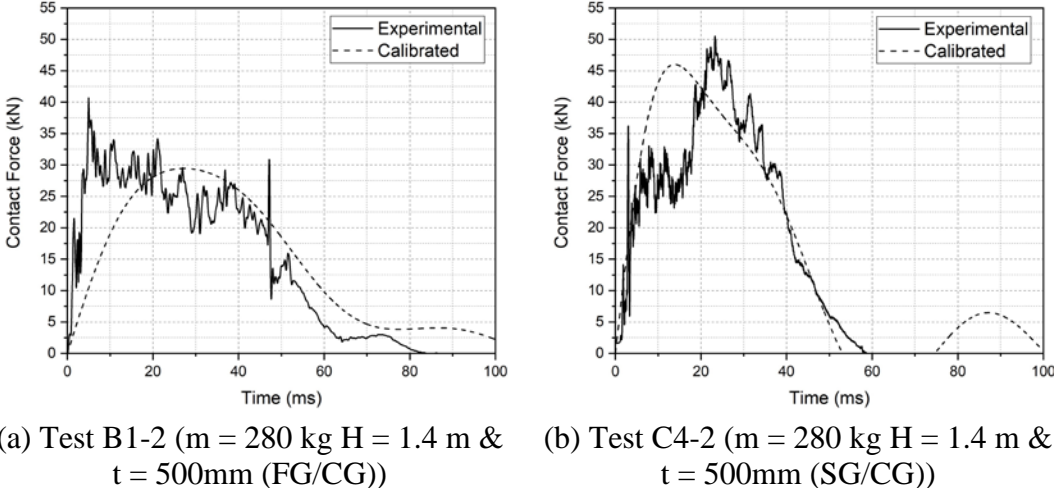


Figure 5.7 2DOF model calibration

The calibrated k_n values that are presented herein are specific to the impact scenarios, types of materials used for filling the gabions, and the design of the gabion that were tested (including its dimensions). The stiffness difference between flexible and stronger gabion is evident in Figure 5.8 and Figure 5.9. The damage to the gabion box in 3rd and 4th strike of Test series B is also evident.

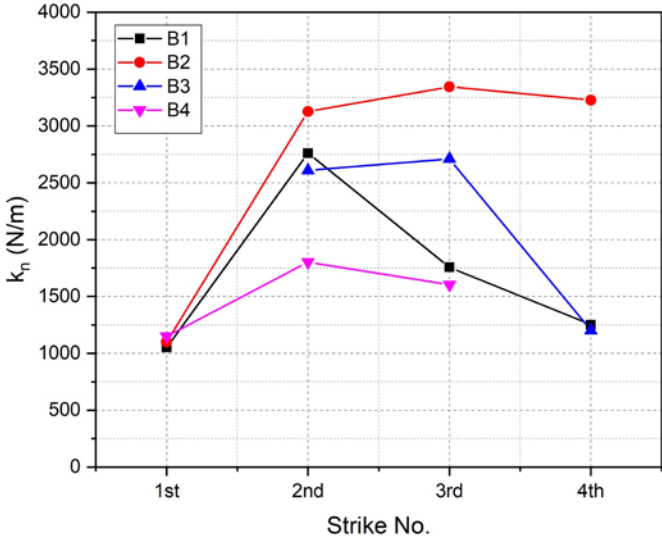


Figure 5.8 Calibrated k_n values for Test Series B

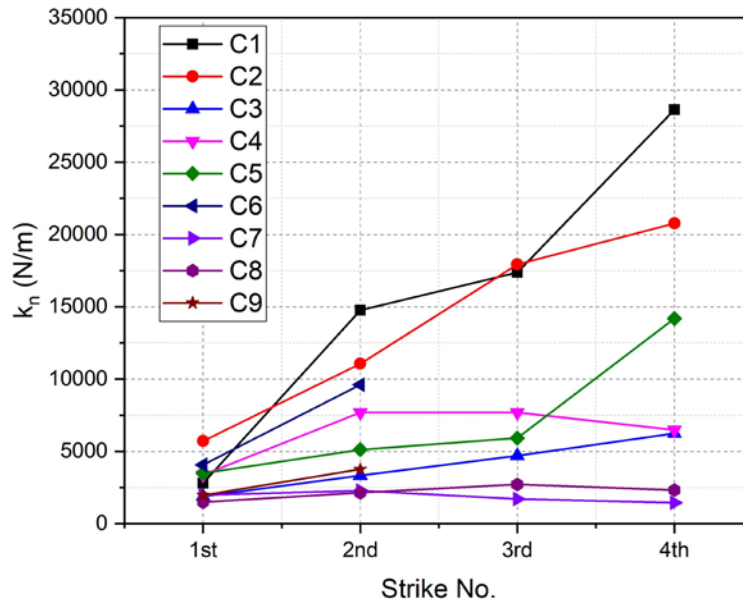


Figure 5.9 Calibrated k_n values for Test Series C

This is further illustrated in Figure 5.10 where statistical analysis was performed with all flexible and strong gabion boxes. Results show that the flexible gabion box tends to break after the 2nd impact and hence k_n is lower in 3rd and 4th impact than the 2nd impact. The mean value of k_n for stronger gabion boxes increases with multiple impacts. Higher standard deviation of k_n values indicates that it can be very stiff or completely broken at the subsequent strikes after the 2nd strike.

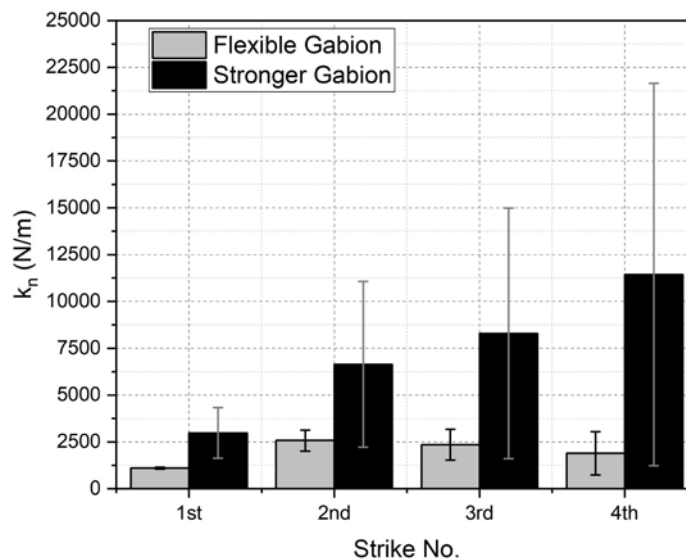


Figure 5.10 Comparison of stiffness of the frontal spring (k_n) under different cushion strengths

The effect of the thickness of the cushion is also compared with the calibrated values of k_n as illustrated in Figure 5.11. Results demonstrate that the thickness of the gabion boxes has an influence on the k_n following multiple strikes. Gabion boxes with lower thickness (300 mm) tend to become more compact following multiple strikes due to less space availability for compaction compared to thicker gabion boxes.

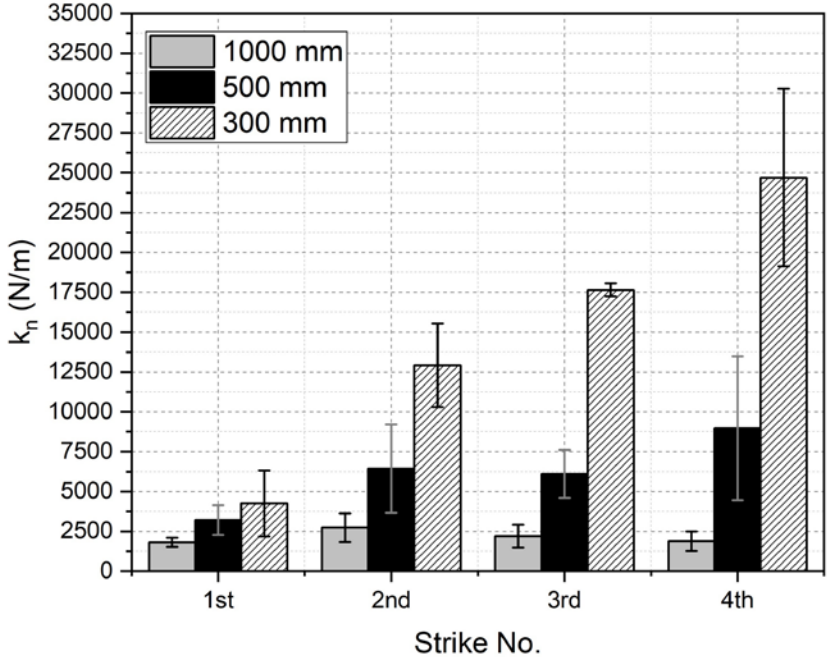


Figure 5.11 Comparison of stiffness of the frontal spring (k_n) with different cushion thicknesses

An analytical contact force model is therefore required for predicting the value of k_n forming part of the proposed calculation procedure details of which are presented in the next sub-section. Experimental results that have been recorded will be used to validate the proposed calculation methodology.

5.4 CALCULATION OF THE STIFFNESS OF CUSHION (k_n) BASED ON CONTACT FORCE MODEL

The forcing function of the impact is controlled by the following parameters of the Hunt and Crossley model: k_n , p and COR which characterise the properties of the frontal spring forming part of the 2DOF system. The latter two parameters take on the constant value of 1 and 0.01 respectively. Thus, the value of the remaining parameter k_n can be calibrated against the simulated forcing function in order that the maximum contact force of the simulated pulse is in agreement with the value predicted by the empirical expression of Eq. 3.6 which was introduced in Section 3.5. The calibration

can be operated on an Excel spreadsheet which has the built-in facility to iterate (using the GOAL SEEK function – Appendix [G]).

When applying Eq. 3.6 for calculating the maximum contact force, M_E value should be calculated based on unconfined compression test and multiplication factors introduced in Section 3.4. It is worthy to note that only the top middle gabion was impacted during the experiment, and it was not fully confined from surrounding cells. It was observed from unconfined compression test results presented under Section 4.3 that flexible gabion had a M_E value of 1250 kPa and stronger gabion had a M_E value of 3000 kPa.

As discussed earlier, it was observed from the cushioned impact experiments that the gabion material was much more compact in second impact than the first impact. Further increase in the compactness of the gabion on the third, or fourth, impact can be minor if the gabion is not strong. To err on the safe side, recommended values of k_n for input into Eq. 3.6 is given in Table 5.1. The calculated values of the maximum contact force across the series of cushioned impact experiments (of Test Series B and Test Series C) using Eq. 3.6 are shown in Figure 5.12 along with the experimentally measured values (as recorded from the pendulum testing of the full-scale stem wall).

Table 5.1 Modulus of elasticity values for multiple impact

	Factor	(M_E) Flexible Gabion*	(M_E) Stronger Gabion*
1 st Strike	1	1250 kPa	3000 kPa
2 nd Strike	2	2500 kPa	6000 kPa
3 rd Strike	3.54	4425 kPa (2500 kPa if cage is broken)	10000 kPa
4 th Strike	5	6250 kPa (2500 kPa if cage is broken)	15000 kPa

* Flexible gabions - gabions made of 75 mm openings and 3 mm diameter wire mesh

* Stronger gabions - gabions made of 50 mm openings and 5 mm diameter wire mesh

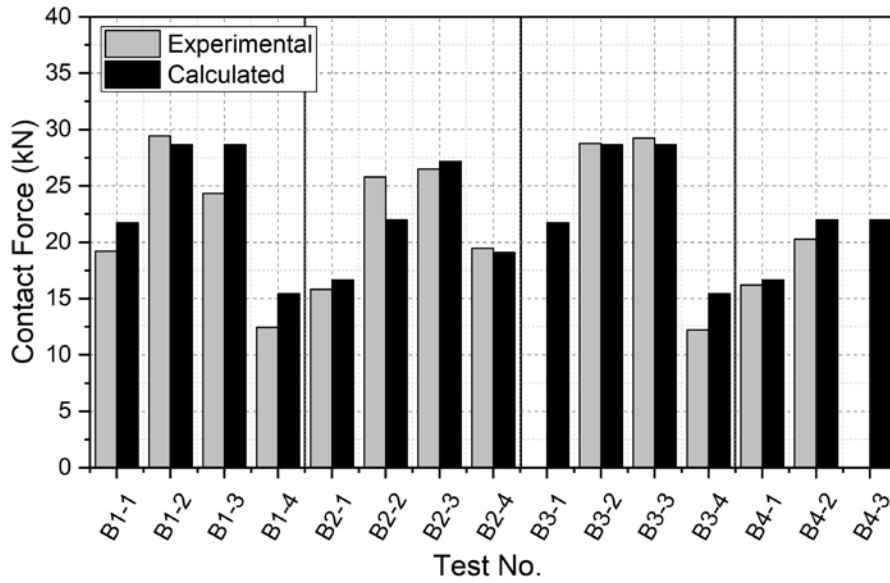


Figure 5.12 Comparison of peak contact forces – Test Series B

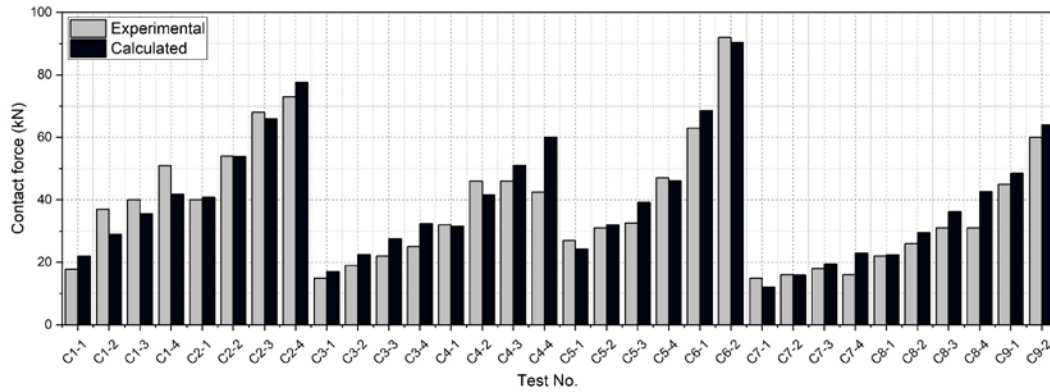


Figure 5.13 Comparison of peak contact forces – Test Series C

Finally, in Figure 5.14, forcing functions that are simulated as per the Hunt & Crossley model based on taking the (modelled/calculated) value of k_n , $p = 1$ and $COR = 0.01$ are compared with the respective experimentally measured forcing functions for the same examples presented in Figure 5.7. The rest of the comparisons can be found in Appendix [H].

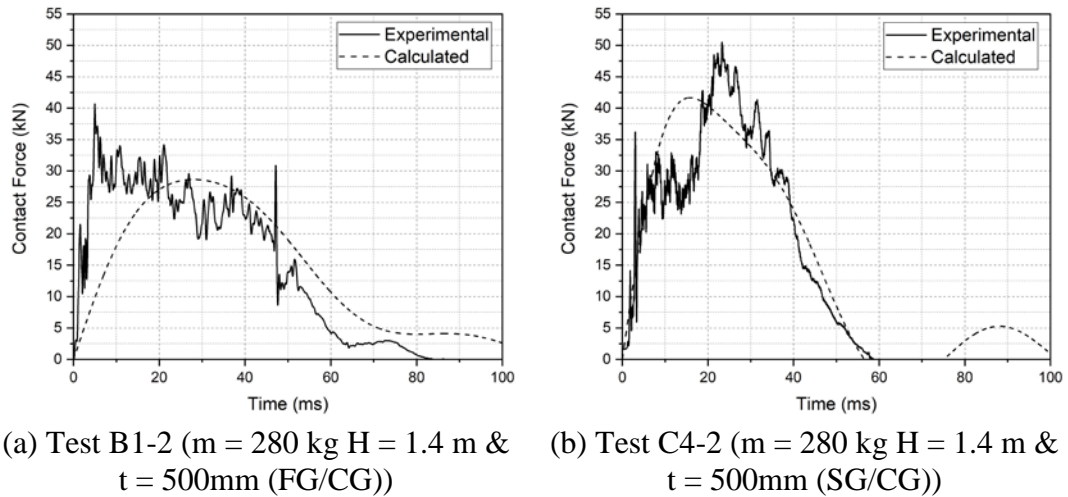


Figure 5.14 2DOF model – contact force diagram

5.5 WALL DEFLECTION SIMULATED BY 2DOF MODEL COMPARISONS

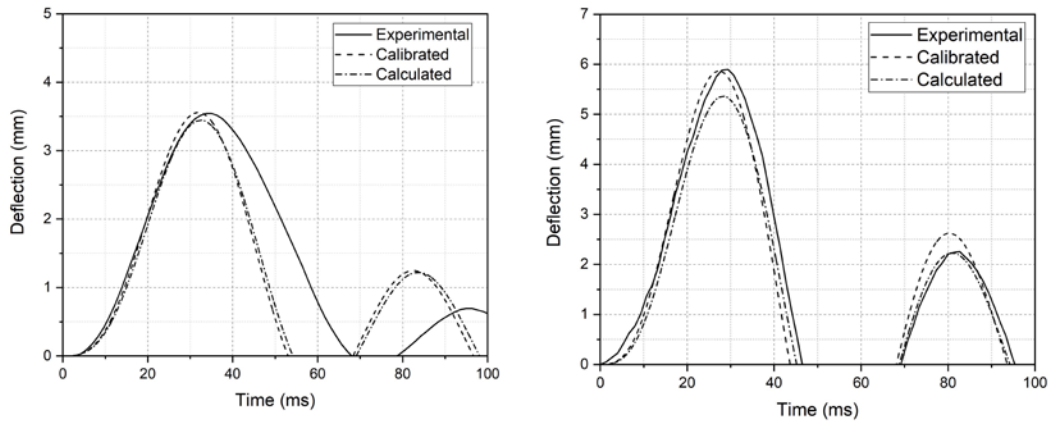
The simulated forcing functions as presented in the previous section was based on the modelled behaviour of the frontal spring (what is assumed to possess non-linear visco-elastic properties as per the Hunt and Crossley model). The frontal spring forms part of the 2DOF system for modelling conditions of the gabion cushion surrounding the point of contact whereas the rear spring is for modelling the deflection behaviour of the stem wall of the barrier which is placed behind the gabions. Thus, once the forcing function has been simulated the deflection time-histories of the stem wall is automatically known.

In Figure 5.15 two graphs are presented from each test series (B&C) on the full-scale barrier wall showing deflection time-histories that have been obtained in three different ways: (See Appendix[I] for rest of the calculated results)

Option (i) - By measurement using the laser device placed behind the stem wall

Option (ii) - By simulation using the Hunt and Crossley model based on calibrating the value of k_n to match with the experimentally measured maximum value of the contact force (referred in the figure legend as: “Calibrated”).

Option (iii) - By simulation using the Hunt & Crossley model based on calibrating the value of k_n to match with the maximum value of the contact force calculated from Eq. 3.6 (referred in the figure legend as: “Calculated”).



(a) Test B1-2 (m = 280 kg H = 1.4 m & t = 500mm (FG/CG)) (b) Test C4-2 (m = 280 kg H = 1.4 m & t = 500mm (SG/CG))

Figure 5.15 Deflection time histories of the wall

In the absence of results from representative impact experiments, Option (iii) is the only option to adopt for predicting the deflection demand behaviour of the stem wall. Hence further comparisons are only performed between experimental and calculated values. In Figure 5.16 and Figure 5.17, the measured and simulated maximum deflection values of the wall (as per options (i) and (iii) as described) are presented for comparison in the form of a bar chart for each Test Series B and Test Series C. A reasonable degree of conservatism is well demonstrated across all the tests.

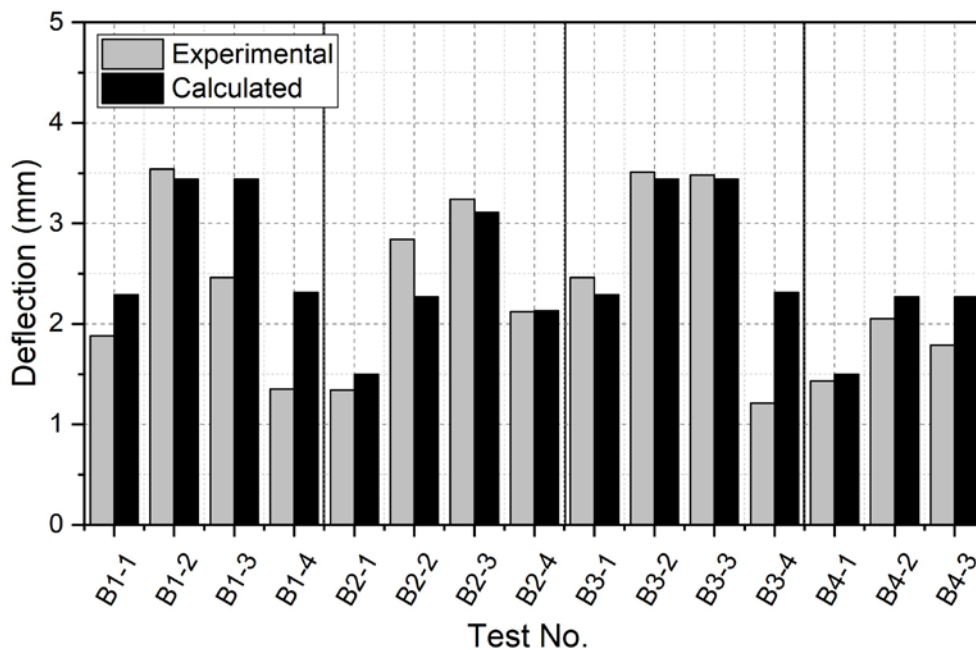


Figure 5.16 Maximum deflection of the wall – Test Series B

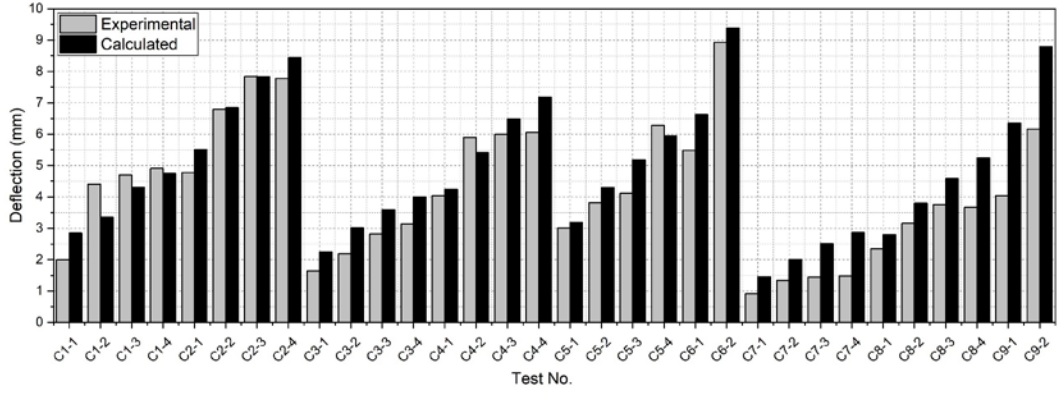


Figure 5.17 Maximum deflection of the wall – Test Series C

5.6 ESTIMATION OF TENSILE REINFORCEMENT STRAIN

Given that the value of the yield curvature (ϕ_y) of the cantilevered walls (see Section 4.1 for details) has been calculated using Eq. 5.9, being 0.021 rad/m for Test Series B and 0.023 rad/m for Test Series C, the value of the yield deflection (Δ_{yi}) can be estimated using Eq. 5.11. The amount of yield deflection at the top of the wall (Δ_y) can be then calculated by use of Eq. 5.12 based on employing fundamental principles of structural mechanics (being 15.5 mm for Test Series B and 15.6 mm for Test Series C). Note that the height of the wall is h and not to be confused with h_i .

$$\Delta_{yi} = \frac{\phi_y h_i^2}{3} \quad (5.11)$$

$$\Delta_y = \Delta_{yi} \left(\frac{3h - h_i}{2h_i} \right) \quad (5.12)$$

The maximum strain ε_s of the tensile reinforcement may be linearly correlated with the maximum deflection of the wall as shown by Eqs. 5.13 and 5.14 in which the limit of yield (ε_{sy}) can be taken as 0.0028 mm for Test Series B and 0.00272 mm for Test Series C.

$$\frac{\varepsilon_s}{\varepsilon_{sy}} = \frac{\Delta}{\Delta_y} \quad (5.13)$$

$$\varepsilon_s = \varepsilon_{sy} \times \frac{\Delta}{\Delta_y} \quad (5.14)$$

In Figure 5.18 and 5.19, the peak recorded strain value for each test is compared with the respective calculated value in the form of a bar chart for Test Series B and C. Both figures demonstrate a good degree of conservatism with the proposed modelling methodology.

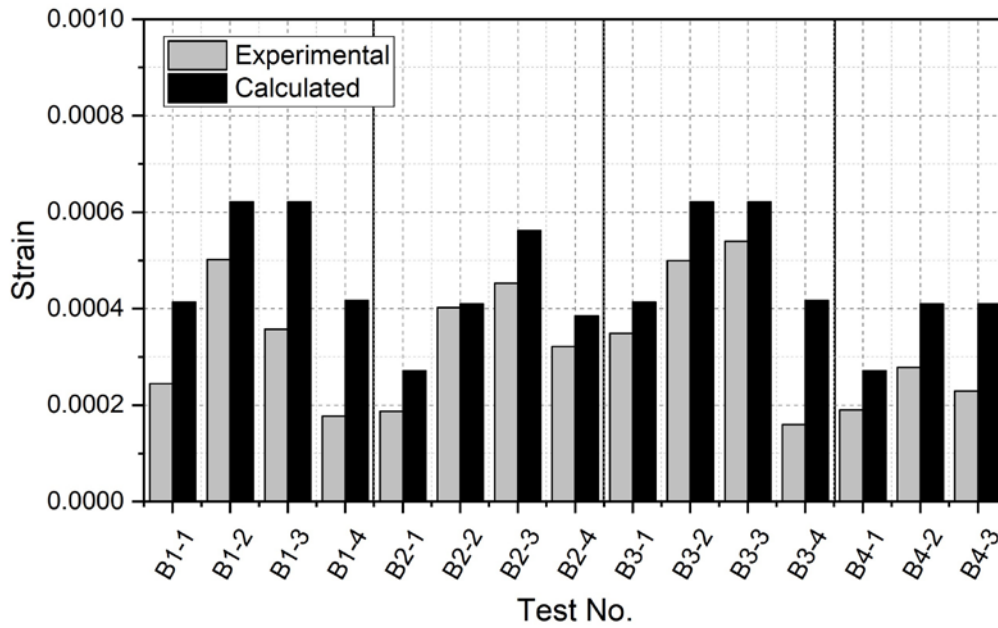


Figure 5.18 Comparison of peak tensile reinforcement strain

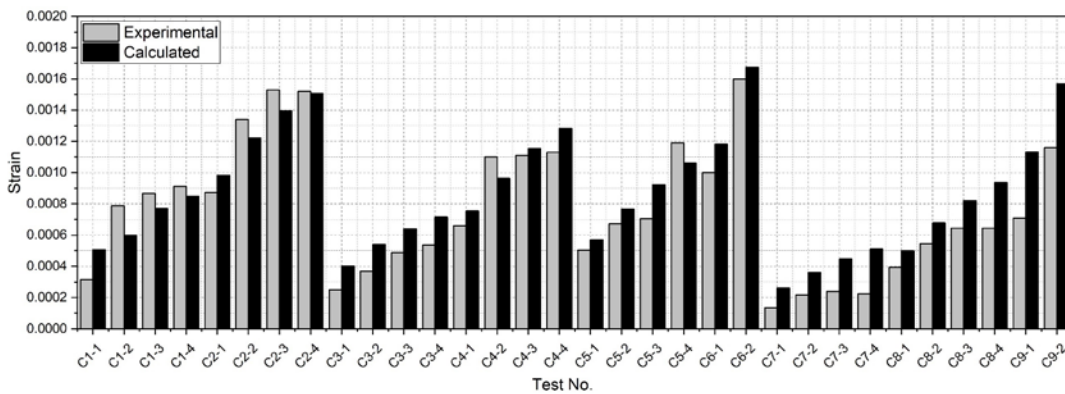


Figure 5.19 Comparison of peak tensile reinforcement strain

2DOF technique was employed in this study for facilitating the complex dynamic nature of RC wall and the gabion cushion under impact loading. The proposed model is first calibrated with experimental results to validate the methodology. In the end, a complete standalone calculation procedure by the use of the proposed 2DOF model without performing any experiment is presented. The ability of the proposed model for guiding the structural design of a RC rockfall protection barrier which has incorporated a layer of gabion cushion for additional protection is well demonstrated. The proposed method in this chapter can be implemented in a simple MATLAB code or Excel spreadsheet which is less computer intensive. Although this calculation method can develop a complete time history of the contact phase as well as the reaction phase, engineers are more interest in the peak values for their designs. Therefore, it is more beneficial if the procedure is simplified to a closed-form solution as discussed in the next chapter.

Chapter 6: Simplified Design Approach

Chapter 6 contains a simplified design method which can be used by practising engineers in a design office environment. This chapter contains basically three sections. The first section (Section 6.1) is focussed on the development of a closed-form solution compared to the complex calculation method discussed in the previous chapter. This is developed as an extension to the energy partitioning method discussed in Section 2.9, literature review. Section 6.2 illustrates the conversion of 2DOF model which can be calculated by only using computer software such as Excel or MATLAB to a graphical design chart by performing numerous combinations of design scenarios. Finally, in Section 6.3, the deflection demand of the wall and tensile reinforcement strain obtained from the proposed simplified method is compared with large scale experimental results. It is shown from the comparisons that the simplified approach gives reasonable estimates and is more user-friendly.

6.1 DEVELOPMENT OF A CLOSED FORM SOLUTION

A displacement-based model using energy partitioning was developed by Lam, Yong [30] to predict the performance behaviour of RC barrier when subjected to the impact of a boulder on the cantilevered wall causing it to deflect and bend. Detailed descriptions and derivations of the model by the authors and co-workers have been reported in the literature [29, 69, 145, 146] and summarised in Section 2.9.

The analytical model of Eq. 6.1 for estimating the displacement demand of an impact has been derived and experimentally validated, for conditions where the target is responding within the elastic limit [30]. Eq. 6.1 is a combination of Eqs. 2.18 & 2.22 presented in Section 2.9. Input to the equation is the impactor mass (m), stiffness of the target responding within the elastic limit (k), generalised mass of the target (λm), and coefficient of restitution (COR).

$$\Delta = \frac{mv_0}{\sqrt{mk}} \sqrt{(\alpha + \lambda) \left(\frac{1 + COR}{1 + \lambda} \right)^2} \quad (6.1)$$

For specific conditions where the impactor does not rebound (i.e. $COR = 0$) but is instead attached to (or embedded into) the surface of the target ($\alpha = 1$) Eq. 6.1 is reduced to Eq. 6.2 which was first presented in Ref. [29]. This is consistent with what has been observed from all the tests conducted by the investigators when cushioning was put in place.

$$\Delta = \frac{mv_0}{\sqrt{mk(1 + \lambda)}} \quad (6.2)$$

If the target is a lightly loaded RC element such as a RC stem wall which is susceptible to cracking on impact “ k ” is replaced by “ k_{cr} ” where subscript “cr” denotes cracked concrete. To facilitate modelling the effects of cushioning a new notation: λ_2 is introduced herein to denote the ratio of the combined target mass (i.e. the effective mass of the stem wall plus the mass of a portion of the gabion materials disturbed by the impact) to the mass of the impactor object (i.e. m_2/m). In the case of an impact that is cushioned by a layer of gabion cushion Eq. 6.2 is modified further into Eq. 6.3.

$$\Delta = \gamma \times \frac{mv_0}{\sqrt{mk_{cr}(1 + \lambda_2)}} \quad (6.3)$$

This second term has incorporated a reduction factor which is based on the assumption of no re-bounce ($COR = 0$) and an instantaneous transfer of momentum from the impactor object to the target. One of the main functionalities of the cushion is to delay this momentum transfer thereby resulting in a further reduction in the deflection demand of the impact. The γ factor (the first term in Eq. 6.3) is to represent this further reduction that is resulted from the delay which is shown to be correlated with the time taken for the contact force to rise to the peak (i.e. “*rise time*”) relative to the time taken by the target to deflect to the full extent in response to the impact. (i.e. “*response time*”). The *rise time: response time* ratio can be represented by the natural period ratios (T_m/T_{m_2}) of the two lumped masses in the two-degree-of-freedom (2DOF) system representation.

The value of the γ factor can be found by applying the following calculation:

1. Calculation for determining the value of T_m/T_{m_2} using Eqs. 6.4 and

2. Calculation for determining the value of γ as function of T_m/T_{m_2} and λ_2 using the chart in Figure 6.1. The chart was developed from a parametric study which involved analyses making use of the 2DOF system as introduced in Chapter 5 and depicted in Figure 5.2. The development of this chart is further explained in Section 6.2

$$\frac{T_m}{T_{m_2}} = 2\pi \sqrt{\frac{mk_{cr}}{m_2k_n}} \quad (6.4)$$

where m , m_2 , k_{cr} and k_n are as defined in Figure 5.2.

The value of k_n which characterises the cushion stiffness must be known before in determining the value of $\frac{T_m}{T_{m_2}}$ (based on use of Eq. 6.4) can be found by calibration against experimentally recorded results. From the practical perspectives (in situations where experimental results are not readily available) a more expedient way of determining the value of k_n is by use of a closed form expression (Eq. 6.5). The derivation of Eq. 6.5 based on the Hunt and Crossley model can be found in Perera [97] which is an earlier publication by the authors and co-worker on storm debris and summarised in Section 2.10.2.

$$F_c = k_n \left[1 + (0.2p + 1.3) \left(\frac{1 - \text{COR}}{\text{COR}} \right) \left(\frac{-b + \sqrt{b^2 + 4c}}{2} \right) \right] \times \left(\frac{p + 1}{2k_n} \left(\frac{\lambda_2}{1 + \lambda_2} \right) mv_0^2 \text{COR} \right)^{\frac{p}{p+1}} \times \left[1 - \left(\frac{-b + \sqrt{b^2 + 4c}}{2} \right)^2 \right]^{\frac{p}{2}} \quad (6.5)$$

where

$$b = \frac{p \times \text{COR}}{(p + 2)(0.2p + 1.3)(1 - \text{COR})^2} \quad \text{and} \quad c = \frac{2}{p + 2}$$

Take $p = 1$ and $\text{COR} = 0.01$ as justified earlier in Chapter 5, Eq. 6.5 can be simplified into Eq. 6.6.

$$F_c = k_n \times \left(\frac{1}{k_n} \left(\frac{\lambda_2}{1 + \lambda_2} \right) mv_0^2 \right)^{\frac{1}{2}} \times 7.07 \quad (6.6)$$

Eq. 6.6 can be then rearranged into Eq. 6.7 in which k_n is expressed as a function of the peak contact force F_c along with impact parameters: m , v_o and λ_2 .

$$k_n = \frac{F_c^2}{50mv_o^2} \times \left(\frac{1 + \lambda_2}{\lambda_2} \right) \quad (6.7)$$

The value of F_c required for substitution into the Eq. 6.7 can be found using the Modified Swiss Code Equation (Eq. 3.6). The factor $\left(\frac{1+\lambda_2}{\lambda_2} \right)$ in Eq. 6.7 represent the contribution of mass ratio into the calculation of k_n and only valid when the $\left(\frac{1+\lambda_2}{\lambda_2} \right) \geq 1$.

6.2 DEVELOPMENT OF THE DESIGN CHART

A design chart has been developed by comparing estimates of the deflection demand of the impact based on the use of Eq. 6.3 with that calculated by the 2DOF lumped mass model.

Details of the calculations along with the predicted values are presented in Table 6.1 in below. Results are grouped in the form of sub-tables (each of which represents scenarios that are identified with the same value of λ_2). The underlying rationale of the development of the design chart is presented below:

- Values of m and m_2 were first selected to give different values of λ_2 which control the outcome of the cushioned impact. Thus, varying the values of m and m_2 by the same amount without changing the value of λ_2 would not affect predictions as reflected in the design chart.
- Parameter v_o representing the velocity of impact has been eliminated from the design chart because of the negligible influence of this parameter on the γ factor (as demonstrated in Table 6.2). Each sub-table (in Table 6.2) is associated with a different value of v_o . The resulting values of T_m/T_{m_2} and γ are shown to be mostly unchanged across all the sub-tables.
- Values of k_n were selected to give a range of values of T_m (and hence T_m/T_{m_2} which is represented by the x-axis of the design chart).
- Values of k_2 were chosen to give a reasonable set of values of T_{m_2} (and hence values of T_m/T_{m_2} ranging from 1 to 100) with the aim of covering different

values of the relative stiffness (of the frontal spring and rear spring) in the 2DOF model.

- Values of T_m/T_{m_2} were then calculated using Eq. 6.4.
- Values of Δ were then obtained from numerical simulations of the 2DOF model which can be implemented on Excel spreadsheet (as presented in Chapter 5).
- Predictions for the values of Δ based on the condition of a “Bare Wall” were then obtained by the use of the second term (only) on the right-hand side of Eq. 6.3.
- The values of the γ factor were taken as the ratio of the deflection estimates obtained from the previous two steps; i.e. Δ (2DOF)/ Δ (Bare Wall).

Note that in Table 6.1 only those columns that have been highlighted were used for developing the design chart (whereas the other columns are presented to show details of the calculations). The first row of each table (as highlighted in green) corresponds to the “bare wall” scenarios that were without any protection by gabions ($\gamma = 1$). Note that the design chart has omitted cases in which $\gamma > 1$ as is unrealistic.

Table 6.1 Calculations for development of the design chart

$\lambda_2=0.1$										
m (kg)	v_0 (m/s)	k_n (N/m)	T_m (s)	m_2 (kg)	c_r (N/m)	T_{m_2} (s)	T_m/T_{m_2}	Δ (2DOF) (mm)	Δ (Bare Wall) (mm)	γ
115	0.511	N/A	N/A	11.5	569772	0.028227878	N/A	N/A	6.92	1
115	0.511	600000	0.086986762	11.5	569772	0.028227878	3.08159	6.59	6.92	0.952312139
115	0.511	100000	0.21307318	11.5	569772	0.028227878	7.548324	6.1	6.92	0.88150289
115	0.511	50000	0.301330982	11.5	569772	0.028227878	10.67494	5.77	6.92	0.833815029
115	0.511	30000	0.389016625	11.5	569772	0.028227878	13.78129	5.47	6.92	0.790462428
115	0.511	10000	0.673796559	11.5	569772	0.028227878	23.8699	4.59	6.92	0.663294798
115	0.511	5000	0.952892232	11.5	569772	0.028227878	33.75713	3.87	6.92	0.559248555
115	0.511	3000	1.230178581	11.5	569772	0.028227878	43.58027	3.28	6.92	0.473988439
115	0.511	2000	1.506654908	11.5	569772	0.028227878	53.37471	2.8	6.92	0.404624277
115	0.511	1500	1.739735234	11.5	569772	0.028227878	61.63181	2.47	6.92	0.356936416
115	0.511	1000	2.130731805	11.5	569772	0.028227878	75.48324	2.02	6.92	0.291907514
115	0.511	800	2.382230579	11.5	569772	0.028227878	84.39283	1.81	6.92	0.261560694
115	0.511	500	3.013309816	11.5	569772	0.028227878	106.7494	1.46	6.92	0.210982659
$\lambda_2=0.2$										
m (kg)	v_0 (m/s)	k_n (N/m)	T_m (s)	m_2 (kg)	k_{cr} (N/m)	T_{m_2} (s)	T_m/T_{m_2}	Δ (2DOF) (mm)	Δ (Bare Wall) (mm)	γ
N/A	0.722	N/A	N/A	11.5	569772	0.028227878	N/A	N/A	6.62	1
57.5	0.722	600000	0.061508929	11.5	569772	0.028227878	2.179014	6.36	6.62	0.960725076
57.5	0.722	100000	0.150665491	11.5	569772	0.028227878	5.337471	5.96	6.62	0.900302115
57.5	0.722	30000	0.275076293	11.5	569772	0.028227878	9.744845	5.43	6.62	0.820241692
57.5	0.722	10000	0.476446116	11.5	569772	0.028227878	16.87857	4.68	6.62	0.70694864
57.5	0.722	5000	0.673796559	11.5	569772	0.028227878	23.8699	4.04	6.62	0.610271903
57.5	0.722	2000	1.065365902	11.5	569772	0.028227878	37.74162	3.05	6.62	0.460725076
57.5	0.722	1200	1.375381466	11.5	569772	0.028227878	48.72422	2.47	6.62	0.373111782
57.5	0.722	800	1.684491397	11.5	569772	0.028227878	59.67474	2.03	6.62	0.306646526
57.5	0.722	600	1.945083123	11.5	569772	0.028227878	68.90646	1.73	6.62	0.261329305
57.5	0.722	450	2.245988529	11.5	569772	0.028227878	79.56632	1.45	6.62	0.219033233
57.5	0.722	300	2.750762932	11.5	569772	0.028227878	97.44845	1.11	6.62	0.167673716
57.5	0.722	250	3.013309816	11.5	569772	0.028227878	106.7494	1.04	6.62	0.157099698

$\lambda_2=0.5$										
m (kg)	v_0 (m/s)	k_n (N/m)	T_m (s)	m_2 (kg)	k_{cr} (N/m)	T_{m_2} (s)	T_m/T_{m_2}	Δ (2DOF) (mm)	Δ (Bare Wall) (mm)	γ
23	1.14	N/A	N/A	11.5	569772	0.028227878	N/A	N/A	5.914	1
23	1.14	600000	0.038901662	11.5	569772	0.028227878	1.378129	5.77	5.914	0.975650998
23	1.14	100000	0.095289223	11.5	569772	0.028227878	3.375713	5.53	5.914	0.935069327
23	1.14	10000	0.301330982	11.5	569772	0.028227878	10.67494	4.67	5.914	0.789651674
23	1.14	3000	0.550152586	11.5	569772	0.028227878	19.48969	3.79	5.914	0.640852215
23	1.14	1200	0.869867617	11.5	569772	0.028227878	30.8159	2.89	5.914	0.48867095
23	1.14	800	1.065365902	11.5	569772	0.028227878	37.74162	2.46	5.914	0.415962124
23	1.14	600	1.230178581	11.5	569772	0.028227878	43.58027	2.15	5.914	0.363544133
23	1.14	450	1.42048787	11.5	569772	0.028227878	50.32216	1.85	5.914	0.312817044
23	1.14	300	1.739735234	11.5	569772	0.028227878	61.63181	1.46	5.914	0.24687183
23	1.14	200	2.130731805	11.5	569772	0.028227878	75.48324	1.12	5.914	0.18938113
23	1.14	150	2.460357162	11.5	569772	0.028227878	87.16054	0.907	5.914	0.153364897
23	1.14	100	3.013309816	11.5	569772	0.028227878	106.7494	0.685	5.914	0.115826852
$\lambda_2=1$										
m (kg)	v_0 (m/s)	k_n (N/m)	T_m (s)	m_2 (kg)	k_{cr} (N/m)	T_{m_2} (s)	T_m/T_{m_2}	Δ (2DOF) (mm)	Δ (Bare Wall) (mm)	γ
11.5	1.615	N/A	N/A	11.5	569772	0.028227878	N/A	N/A	5.13	1
11.5	1.615	600000	0.027507629	11.5	569772	0.028227878	0.974484	5.07	5.13	0.988304094
11.5	1.615	100000	0.067379656	11.5	569772	0.028227878	2.38699	4.93	5.13	0.961013645
11.5	1.615	10000	0.21307318	11.5	569772	0.028227878	7.548324	4.4	5.13	0.857699805
11.5	1.615	3000	0.389016625	11.5	569772	0.028227878	13.78129	3.77	5.13	0.734892788
11.5	1.615	1200	0.615089291	11.5	569772	0.028227878	21.79014	3.03	5.13	0.590643275
11.5	1.615	500	0.952892232	11.5	569772	0.028227878	33.75713	2.18	5.13	0.424951267
11.5	1.615	300	1.230178581	11.5	569772	0.028227878	43.58027	1.69	5.13	0.329434698
11.5	1.615	200	1.506654908	11.5	569772	0.028227878	53.37471	1.34	5.13	0.261208577
11.5	1.615	150	1.739735234	11.5	569772	0.028227878	61.63181	1.11	5.13	0.216374269
11.5	1.615	100	2.130731805	11.5	569772	0.028227878	75.48324	0.835	5.13	0.162768031
11.5	1.615	80	2.382230579	11.5	569772	0.028227878	84.39283	0.706	5.13	0.137621832
11.5	1.615	50	3.013309816	11.5	569772	0.028227878	106.7494	0.5	5.13	0.097465887
$\lambda_2=2$										
m (kg)	v_0 (m/s)	k_n (N/m)	T_m (s)	m_2 (kg)	k_{cr} (N/m)	T_{m_2} (s)	T_m/T_{m_2}	Δ (2DOF) (mm)	Δ (Bare Wall) (mm)	γ
5.75	2.28	N/A	N/A	11.5	569772	0.028227878	N/A	N/A	4.18	1
5.75	2.28	600000	0.019450831	11.5	569772	0.028227878	0.689065	4.17	4.18	0.997607656
5.75	2.28	60000	0.061508929	11.5	569772	0.028227878	2.179014	4.07	4.18	0.973684211
5.75	2.28	5000	0.21307318	11.5	569772	0.028227878	7.548324	3.64	4.18	0.870813397
5.75	2.28	1500	0.389016625	11.5	569772	0.028227878	13.78129	3.06	4.18	0.732057416
5.75	2.28	700	0.569462028	11.5	569772	0.028227878	20.17375	2.51	4.18	0.600478469
5.75	2.28	400	0.753327454	11.5	569772	0.028227878	26.68736	2.06	4.18	0.492822967
5.75	2.28	250	0.952892232	11.5	569772	0.028227878	33.75713	1.67	4.18	0.399521531
5.75	2.28	150	1.230178581	11.5	569772	0.028227878	43.58027	1.27	4.18	0.303827751
5.75	2.28	100	1.506654908	11.5	569772	0.028227878	53.37471	0.99	4.18	0.236842105
5.75	2.28	75	1.739735234	11.5	569772	0.028227878	61.63181	0.816	4.18	0.195215311
5.75	2.28	55	2.031573064	11.5	569772	0.028227878	71.97045	0.652	4.18	0.155980861
5.75	2.28	40	2.382230579	11.5	569772	0.028227878	84.39283	0.511	4.18	0.122248804
5.75	2.28	25	3.013309816	11.5	569772	0.028227878	106.7494	0.361	4.18	0.086363636
$\lambda_2=3$										
m (kg)	v_0 (m/s)	k_n (N/m)	T_m (s)	m_2 (kg)	k_{cr} (N/m)	T_{m_2} (s)	T_m/T_{m_2}	Δ (2DOF) (mm)	Δ (Bare Wall) (mm)	γ
3.83	2.8	N/A	N/A	11.5	569772	0.028227878	N/A	N/A	3.63	1
3.83	2.8	600000	0.015874631	11.5	569772	0.028227878	0.562374	3.63	3.63	1
3.83	2.8	30000	0.070993507	11.5	569772	0.028227878	2.515014	3.54	3.63	0.975206612
3.83	2.8	3000	0.22450118	11.5	569772	0.028227878	7.953172	3.14	3.63	0.865013774
3.83	2.8	900	0.409881202	11.5	569772	0.028227878	14.52044	2.58	3.63	0.710743802
3.83	2.8	500	0.549913338	11.5	569772	0.028227878	19.48121	2.2	3.63	0.606060606
3.83	2.8	250	0.7776949	11.5	569772	0.028227878	27.5506	1.7	3.63	0.468319559
3.83	2.8	150	1.003999799	11.5	569772	0.028227878	35.56767	1.33	3.63	0.366391185
3.83	2.8	100	1.229643605	11.5	569772	0.028227878	43.56132	1.06	3.63	0.292011019
3.83	2.8	75	1.419870132	11.5	569772	0.028227878	50.30028	0.89	3.63	0.245179063
3.83	2.8	55	1.658051098	11.5	569772	0.028227878	58.73807	0.724	3.63	0.199449036
3.83	2.8	40	1.94423725	11.5	569772	0.028227878	68.87649	0.576	3.63	0.158677686
3.83	2.8	35	2.078477048	11.5	569772	0.028227878	73.63207	0.521	3.63	0.143526171
3.83	2.8	25	2.459287209	11.5	569772	0.028227878	87.12264	0.4	3.63	0.110192837
3.83	2.8	18	2.898297771	11.5	569772	0.028227878	102.675	0.305	3.63	0.084022039
$\lambda_2=5$										
m (kg)	v_0 (m/s)	k_n (N/m)	T_m (s)	m_2 (kg)	k_{cr} (N/m)	T_{m_2} (s)	T_m/T_{m_2}	Δ (2DOF) (mm)	Δ (Bare Wall) (mm)	γ
2.3	3.611	N/A	N/A	11.5	569772	0.028227878	N/A	N/A	2.96	1
2.3	3.611	600000	0.012301786	11.5	569772	0.028227878	0.435803	2.98	2.96	1.006756757
2.3	3.611	30000	0.055015259	11.5	569772	0.028227878	1.948969	2.93	2.96	0.989864865
2.3	3.611	3000	0.173973523	11.5	569772	0.028227878	6.163181	2.7	2.96	0.912162162
2.3	3.611	900	0.317630744	11.5	569772	0.028227878	11.25238	2.33	2.96	0.787162162
2.3	3.611	500	0.426146361	11.5	569772	0.028227878	15.09665	2.05	2.96	0.692567568
2.3	3.611	250	0.602661963	11.5	569772	0.028227878	21.34989	1.66	2.96	0.560810811
2.3	3.611	150	0.778033249	11.5	569772	0.028227878	27.56258	1.35	2.96	0.456081081
2.3	3.611	90	1.004436605	11.5	569772	0.028227878	35.58314	1.06	2.96	0.358108108
2.3	3.611	65	1.18191735	11.5	569772	0.028227878	41.87057	0.879	2.96	0.296959459
2.3	3.611	50	1.347593117	11.5	569772	0.028227878	47.73979	0.749	2.96	0.253040541
2.3	3.611	40	1.506654908	11.5	569772	0.028227878	53.37471	0.647	2.96	0.218581081
2.3	3.611	30	1.739735234	11.5	569772	0.028227878	61.63181	0.53	2.96	0.179054054
2.3	3.611	20	2.130731805	11.5	569772	0.028227878	75.48324	0.392	2.96	0.132432432
2.3	3.611	15	2.460357162	11.5	569772	0.028227878	87.16054	0.312	2.96	0.105405405
2.3	3.611	10	3.013309816	11.5	569772	0.028227878	106.7494	0.232	2.96	0.078378378

$\lambda_2=10$										
m (kg)	v_0 (m/s)	k_n (N/m)	T_m (s)	m_2 (kg)	k_{cr} (N/m)	T_{m_2} (s)	T_m/T_{m_2}	Δ (2DOF) (mm)	Δ (Bare Wall) (mm)	γ
N/A	5.11	N/A	N/A	11.5	569772	0.028227878	N/A	N/A	2.19	1
1.15	5.11	600000	0.008698676	11.5	569772	0.028227878	0.308159	2.2	2.19	1.00456621
1.15	5.11	30000	0.038901662	11.5	569772	0.028227878	1.378129	2.19	2.19	1
1.15	5.11	3000	0.123017858	11.5	569772	0.028227878	4.358027	2.09	2.19	0.9543379
1.15	5.11	900	0.224598853	11.5	569772	0.028227878	7.956632	1.91	2.19	0.872146119
1.15	5.11	500	0.301330982	11.5	569772	0.028227878	10.67494	1.75	2.19	0.799086758
1.15	5.11	250	0.426146361	11.5	569772	0.028227878	15.09665	1.5	2.19	0.684931507
1.15	5.11	150	0.550152586	11.5	569772	0.028227878	19.48969	1.29	2.19	0.589041096
1.15	5.11	90	0.710243935	11.5	569772	0.028227878	25.16108	1.06	2.19	0.484018265
1.15	5.11	65	0.835741773	11.5	569772	0.028227878	29.60696	0.918	2.19	0.419178082
1.15	5.11	50	0.952892232	11.5	569772	0.028227878	33.75713	0.804	2.19	0.367123288
1.15	5.11	40	1.065365902	11.5	569772	0.028227878	37.74162	0.712	2.19	0.325114155
1.15	5.11	30	1.230178581	11.5	569772	0.028227878	43.58027	0.601	2.19	0.274429224
1.15	5.11	20	1.506654908	11.5	569772	0.028227878	53.37471	0.463	2.19	0.211415525
1.15	5.11	15	1.739735234	11.5	569772	0.028227878	61.63181	0.378	2.19	0.17260274
1.15	5.11	10	2.130731805	11.5	569772	0.028227878	75.48324	0.279	2.19	0.12739726
1.15	5.11	7.5	2.460357162	11.5	569772	0.028227878	87.16054	0.222	2.19	0.101369863
1.15	5.11	5	3.013309816	11.5	569772	0.028227878	106.7494	0.165	2.19	0.075342466

$\lambda_2=50$										
m (kg)	v_0 (m/s)	k_n (N/m)	T_m (s)	m_2 (kg)	k_{cr} (N/m)	T_{m_2} (s)	T_m/T_{m_2}	Δ (2DOF) (mm)	Δ (Bare Wall) (mm)	γ
0.23	11.42	N/A	N/A	11.5	569772	0.028227878	N/A	N/A	1.02	1
0.23	11.42	30000	0.017397352	11.5	569772	0.028227878	0.616318	1.03	1.02	1.009803922
0.23	11.42	3000	0.055015259	11.5	569772	0.028227878	1.948969	1.01	1.02	0.990196078
0.23	11.42	900	0.100443661	11.5	569772	0.028227878	3.558314	0.991	1.02	0.971568627
0.23	11.42	250	0.190578446	11.5	569772	0.028227878	6.751427	0.918	1.02	0.9
0.23	11.42	90	0.317630744	11.5	569772	0.028227878	11.25238	0.795	1.02	0.779411765
0.23	11.42	50	0.426146361	11.5	569772	0.028227878	15.09665	0.693	1.02	0.679411765
0.23	11.42	30	0.550152586	11.5	569772	0.028227878	19.48969	0.592	1.02	0.580392157
0.23	11.42	20	0.673796559	11.5	569772	0.028227878	23.8699	0.507	1.02	0.497058824
0.23	11.42	15	0.778033249	11.5	569772	0.028227878	27.56258	0.447	1.02	0.438235294
0.23	11.42	10	0.952892232	11.5	569772	0.028227878	33.75713	0.365	1.02	0.357843137
0.23	11.42	8	1.065365902	11.5	569772	0.028227878	37.74162	0.323	1.02	0.316666667
0.23	11.42	6	1.230178581	11.5	569772	0.028227878	43.58027	0.272	1.02	0.266666667
0.23	11.42	5	1.347593117	11.5	569772	0.028227878	47.73979	0.242	1.02	0.237254902
0.23	11.42	4	1.506654908	11.5	569772	0.028227878	53.37471	0.209	1.02	0.204901961
0.23	11.42	3	1.739735234	11.5	569772	0.028227878	61.63181	0.17	1.02	0.166666667
0.23	11.42	2	2.130731805	11.5	569772	0.028227878	75.48324	0.125	1.02	0.12254902
0.23	11.42	1.5	2.460357162	11.5	569772	0.028227878	87.16054	0.0995	1.02	0.09754902
0.23	11.42	1.3	2.642847539	11.5	569772	0.028227878	93.62544	0.0884	1.02	0.086666667
0.23	11.42	1	3.013309816	11.5	569772	0.028227878	106.7494	0.0742	1.02	0.072745098

Table 6.2 Calculations showing effects of varying v_0

$\lambda_2=1$										
m (kg)	v_0 (m/s)	k_n (N/m)	T_m (s)	m_2 (kg)	k_{cr} (N/m)	T_{m_2} (s)	T_m/T_{m_2}	Δ (2DOF) (mm)	Δ (Bare Wall) (mm)	γ
11.5	1.615	600000	0.027507629	11.5	569772	0.028227878	0.974484	5.07	5.13	0.99
11.5	1.615	10000	0.21307318	11.5	569772	0.028227878	7.548324	4.4	5.13	0.86
11.5	1.615	1200	0.615089291	11.5	569772	0.028227878	21.79014	3.03	5.13	0.59
11.5	1.615	300	1.230178581	11.5	569772	0.028227878	43.58027	1.69	5.13	0.33
11.5	1.615	150	1.739735234	11.5	569772	0.028227878	61.63181	1.11	5.13	0.22
11.5	1.615	80	2.382230579	11.5	569772	0.028227878	84.39283	0.706	5.13	0.14
11.5	1.615	50	3.013309816	11.5	569772	0.028227878	106.7494	0.5	5.13	0.10

$\lambda_2=1$										
m (kg)	v_0 (m/s)	k_n (N/m)	T_m (s)	m_2 (kg)	k_{cr} (N/m)	T_{m_2} (s)	T_m/T_{m_2}	Δ (2DOF) (mm)	Δ (Bare Wall) (mm)	γ
11.5	3	600000	0.027507629	11.5	569772	0.028227878	0.974484	9.42	9.53	0.99
11.5	3	10000	0.21307318	11.5	569772	0.028227878	7.548324	8.18	9.53	0.86
11.5	3	1200	0.615089291	11.5	569772	0.028227878	21.79014	5.62	9.53	0.59
11.5	3	300	1.230178581	11.5	569772	0.028227878	43.58027	3.15	9.53	0.33
11.5	3	150	1.739735234	11.5	569772	0.028227878	61.63181	2.03	9.53	0.21
11.5	3	80	2.382230579	11.5	569772	0.028227878	84.39283	1.31	9.53	0.14
11.5	3	50	3.013309816	11.5	569772	0.028227878	106.7494	0.929	9.53	0.10

$\lambda_2=1$										
m (kg)	v_0 (m/s)	k_n (N/m)	T_m (s)	m_2 (kg)	k_{cr} (N/m)	T_{m_2} (s)	T_m/T_{m_2}	Δ (2DOF) (mm)	Δ (Bare Wall) (mm)	γ
11.5	10	600000	0.027507629	11.5	569772	0.028227878	0.974484	31.4	31.76	0.99
11.5	10	10000	0.21307318	11.5	569772	0.028227878	7.548324	27.3	31.76	0.86
11.5	10	1200	0.615089291	11.5	569772	0.028227878	21.79014	18.7	31.76	0.59
11.5	10	300	1.230178581	11.5	569772	0.028227878	43.58027	10.5	31.76	0.33
11.5	10	150	1.739735234	11.5	569772	0.028227878	61.63181	6.88	31.76	0.22
11.5	10	80	2.382230579	11.5	569772	0.028227878	84.39283	4.37	31.76	0.14
11.5	10	50	3.013309816	11.5	569772	0.028227878	106.7494	3.1	31.76	0.10

Values in the T_m/T_{m2} and γ columns in Table 6.1 (which are highlighted in orange colour) were used for developing the design chart shown in Figure 6.1. This is a graphical translation of the difference between closed form calculation without considering the delay of moment transfer (Δ Bare wall) with 2DOF model estimation (Δ 2DOF) into a reduction factor (γ). This chart can be used as a standalone chart for any other combination of m, m_2, v_0, k_n and k_{cr} .

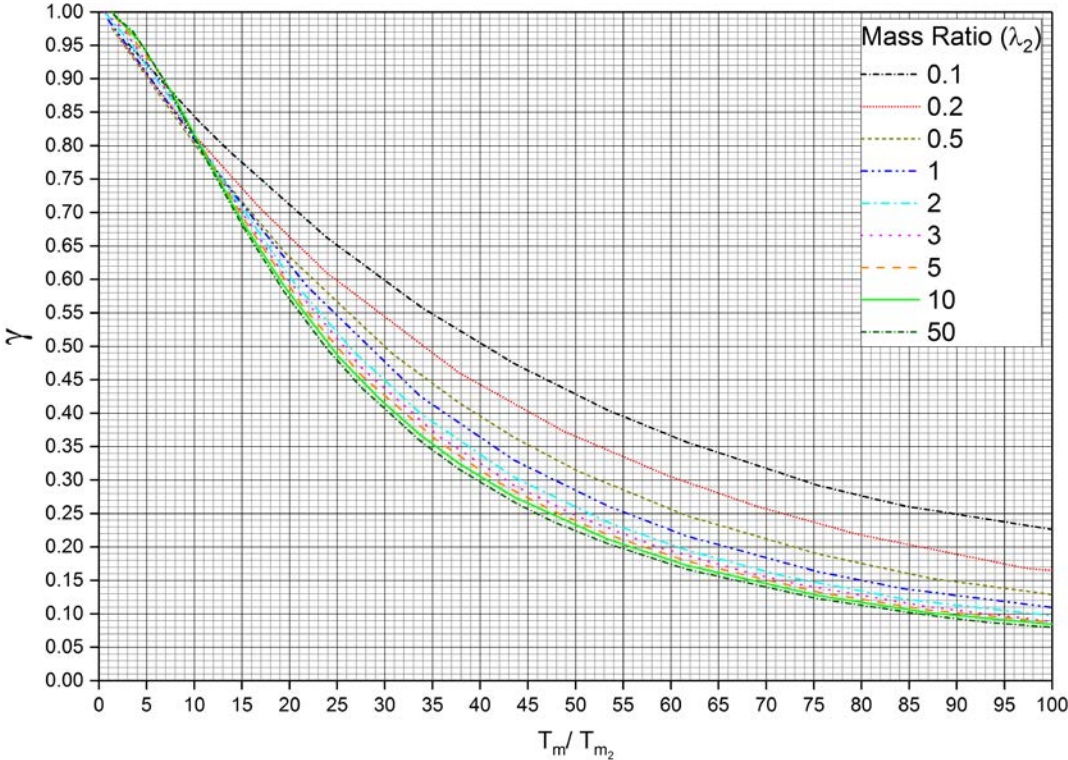


Figure 6.1 Design chart for determine the γ factor

In summary, the deflection demand of the impact can be calculated using the closed-form expression of Eq. 6.3 along with the design chart of Figure 6.1. The trends of γ varying with changes in the natural period ratio (T_m/T_{m2}) and mass ratio (λ_2) as obtained from parametric studies (based on numerical simulations of the 2DOF model) are well displayed on this chart.

6.3 RESULTS COMPARISON USING SIMPLIFIED MODEL

The comparison between the numerically simulated and calculated values of k_n is presented in the form of a bar chart as shown in Figure 6.2 and Figure 6.3 for Test Series B and C respectively. It is shown that predictions for the value of k_n as obtained from the use of Eq. 6.7 are slightly higher (mostly) and hence more

conservative than results inferred from numerical simulations of the 2DOF system model. Details of the construction of Figure 6.2 and Figure 6.3 can be found in Appendix [J].

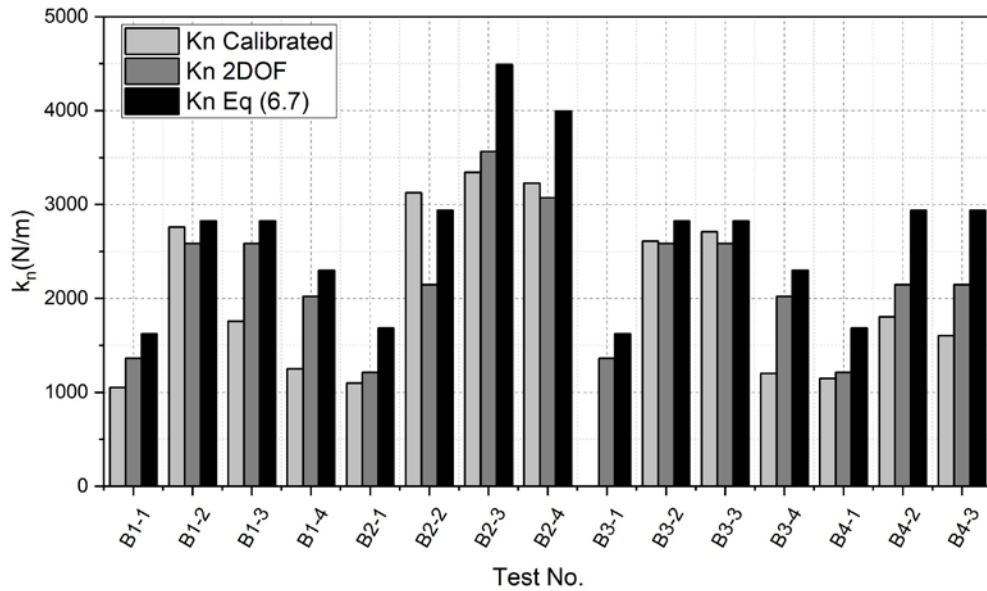


Figure 6.2 Comparison of k_n calibrated, calculated using 2DOF model and calculated using Eq. (6.7) for Test Series B

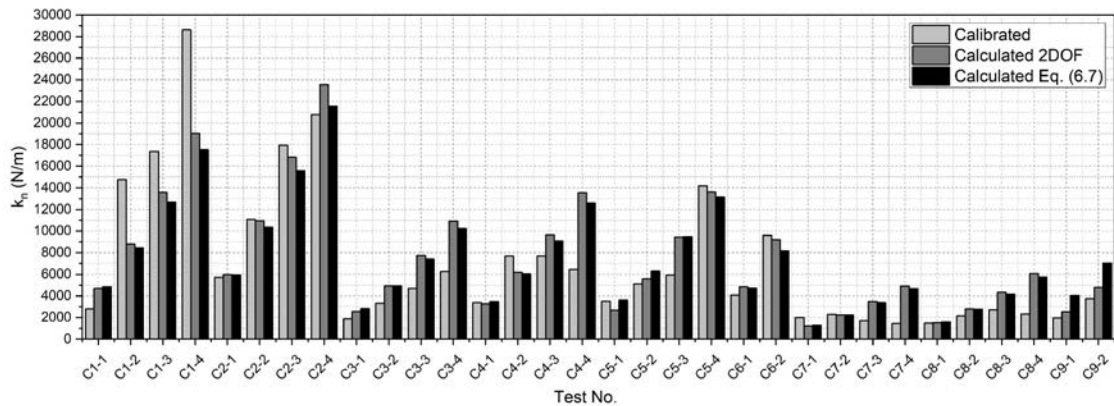


Figure 6.3 Comparison of k_n calibrated, calculated using 2DOF model and calculated using Eq. (6.7) for Test Series C

The deflection demand of the cushioned impact as obtained from the calculation procedure as described have been compared with experimentally recorded results in Figure 6.4 and Figure 6.5 for Test Series B and C respectively. The deflection demand recorded from tests of the first strike is shown to be in good agreement with analytical predictions. Numerical details of the calculations for all the considered impact scenarios covered by the experimental program are also presented in Appendix [J].

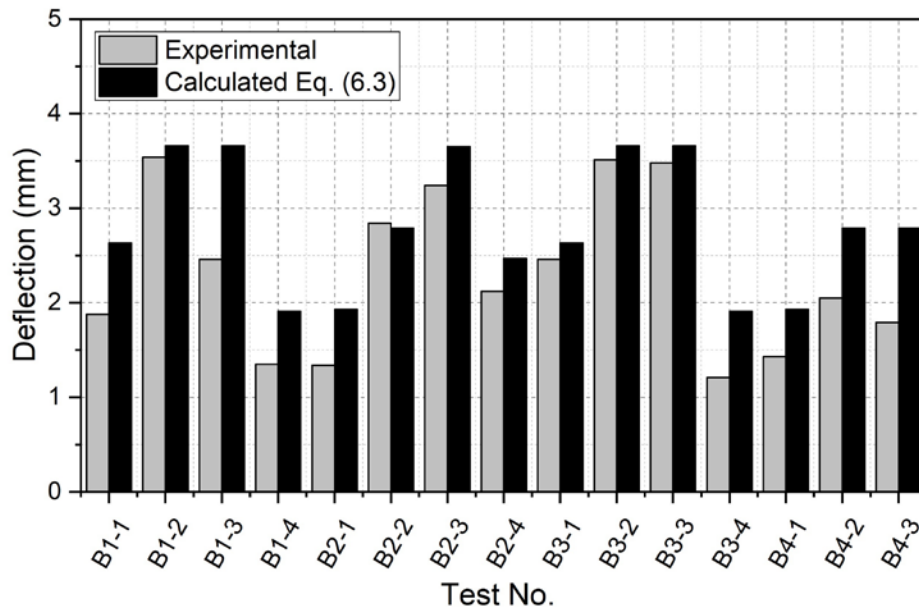


Figure 6.4 Deflection of the wall comparison

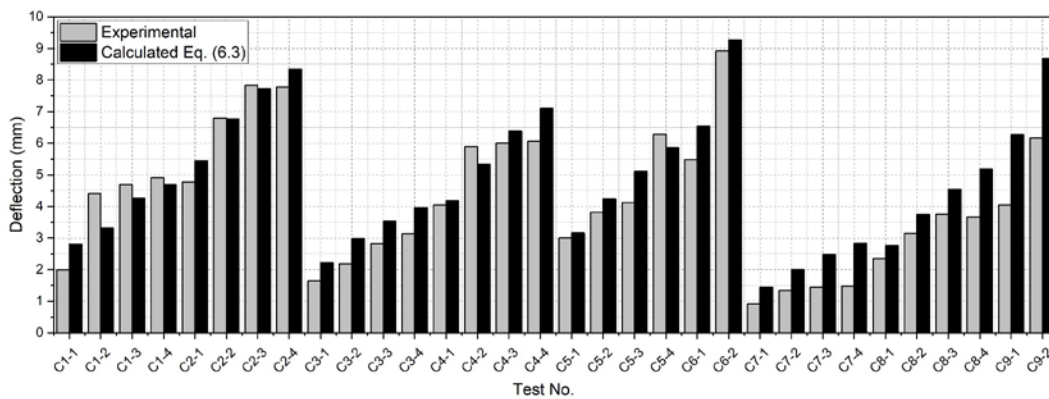


Figure 6.5 Deflection of the wall comparison

Once the deflection demand of the cushioned impact is obtained from the calculation procedure as described, the maximum strain ϵ_s of the tensile reinforcement can be calculated using Eq. 5.14 as described in Section 5.5. The maximum reinforcement strain calculated using this method have been compared with experimentally recorded results as shown in Figure 6.6 and Figure 6.7 for Test Series B and C respectively. Results show that the presented analytical model is robust and valid for all the conditions of cushioning, and conditions of impact following multiple strikes.

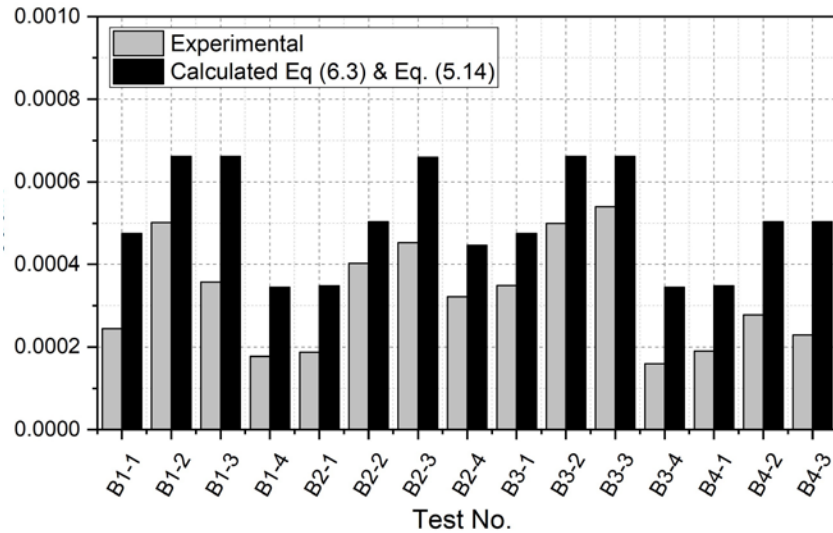


Figure 6.6 Strain comparison for Test Series B

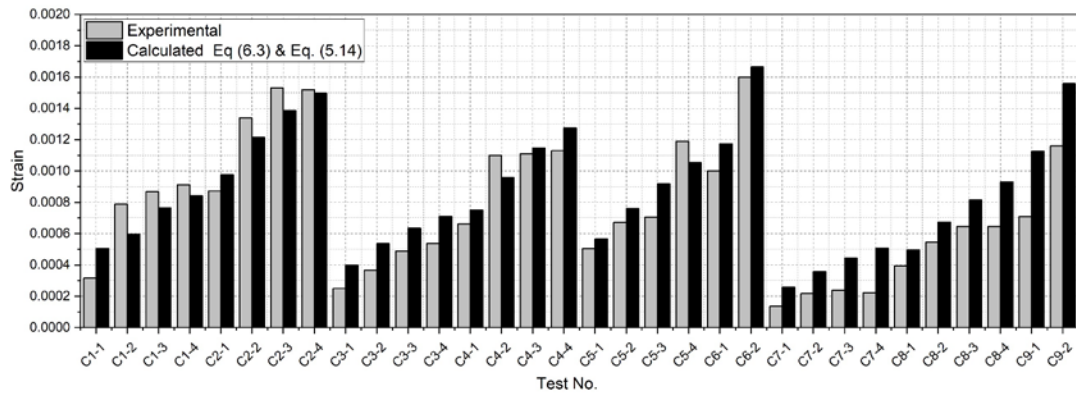


Figure 6.7 Strain comparison for Test Series C

In this chapter, a closed-form solution is proposed to use in conjunction with the design chart to estimate the deflection demand of the wall as well as the strain of reinforcement used. Results show that the presented analytical model is robust for the use of real life rockfall design problems. Following this, a design example has been documented in the next chapter to demonstrate step-by-step implementation of the proposed methodology. A method of calculating flexural demand with co-existence of lateral pressure from debris flow as well as simple design check for localised damage with the presence of a cushion layer are also presented for the completeness of the design.

Chapter 7: Industrial Application

In this chapter a new design method is stipulated for the design and illustrated with worked examples, to assess structural performance behaviour of a rigid barrier (having additional protection by gabion cushions) taking into considerations flexural actions and localised damage. Recommendations for introducing new design provisions are then made.

Design procedures that are related to the flexural action of the stem wall are based on findings presented in Chapter 3 to Chapter 6. Debris flow has been included in the proposed methodology (Section 7.1), and each section is aimed at presenting the analytical solutions to the problem of combining the actions of boulder impact and debris flow. A design procedure which incorporates the use of the derived expressions is then introduced in each section (Section 7.2). The design for localised damage to a barrier which is protected by gabion cushion is also presented in Section 7.3 for the completeness of the design. In section 7.4, design steps to be following the design are summarised and finally, in Section 7.5, a worked example is presented to illustrate the use of the proposed design methodology.

7.1 FORCE FROM DEBRIS FLOW

There are several different models exist for estimating the impact force of debris flows against barriers. A very common model based on hydrodynamic principals are considered in this study and have an appearance of Eq. 7.1 [147].

$$F_d = \alpha \rho_d v_0^2 h_d L \quad (7.1)$$

where α is empirical factor (dynamic pressure coefficient) and the value depends on the flow type, ρ_d is the density of the flow (kg/m^3), v_0 is frontal velocity (m/s), and h_d and L is the flow depth and barrier length respectively. A similar equation was used in GEO Report No. 270 [148] and shown in Eq. 7.2. The distinctive feature of Eq. 7.2 is the introduction of β_d which is the angle between the frontal face of the barrier and the direction of movement of the debris to the calculation of debris flow.

$$F_d = \alpha \rho_d v_0^2 \sin \beta_d h_d L \quad (7.2)$$

Similar hydro-dynamic model (as presented by Eq. 7.1) has also been recommended in guidelines published by other countries [149-151]. Values of the dynamic pressure coefficient α , ranging from 1.0 to 1.5 in the presented guidelines.

In assessing the potential performance of the stem wall which is subject to bending, the effective length (L_{eff}) as opposed to the total length (L) of the barrier should be used in order to be consistent with the wall stiffness (k_{cr}) considered. Effective length (L_{eff}) can be taken as twice the height of the stem wall (h_{stem}) for a RC barrier wall [74]. Eq. 7.2 is further modified into Eq. 7.3 by considering the effective length of the wall.

$$F_d = \alpha \rho_d v_0^2 \sin \beta_d h_d L_{eff} \quad (7.3)$$

In the proposed calculation model, the lateral load generated by debris flow (F) is taken to be quasi-static in nature (i.e. time-independent) over the course of the boulder impact. Given that bending action of the wall is very “short lived” (typically of the order of 0.1 to 0.3 s), the assumption of a time-independent lateral load over such a short duration would only result in minor modelling errors. Errors thus incurred would always be conservative because of Eq. 7.3 is based on the instance when the lateral pressure generated by the debris flow reaches the peak value. The design impact scenarios considered in this thesis have been illustrated in Figure 2.1 of GEO Report No. 270 [148] in which multiple surges of debris are considered.

7.2 CALCULATION OF BENDING PERFORMANCE OF THE WALL FOR COMBINED ACTIONS

The total amount of energy that is delivered to the stem wall of the barrier from the combined actions of boulder impact and debris flow is assumed to be transformed fully to the form of strain energy of the wall, as shown by Eq. 7.4. In this, Δ_b refers to deflection of wall when struck by boulder and $\Delta_d = F_d/k_{cr}$ refers to the amount deflection prior to being subjected to the impact action from a fallen boulder.

$$SE_2 = \frac{1}{2} \Delta_b (F_d + k_{cr} (\Delta_d + \Delta_b)) \quad (7.4)$$

The amount of energy delivered by the action of debris flow (E_d) can be estimated using Eq. 7.5.

$$E_d = F_d \Delta_b \quad (7.5)$$

As for analysis for bending action, the amount of kinetic energy delivered to the stem wall of the barrier by the impact of a boulder causing bending can be considered as KE_2 . By applying the principle of conservation of energy:

$$KE_2 + E_d = SE_2 \quad (7.6)$$

Substituting Eq. (7.4) and (7.5) into Eq. (7.6) results in Eq. (7.7).

$$\Delta_b = \sqrt{\frac{2KE_2}{k_{cr}}} \quad (7.7)$$

Note that wall stiffness k_{cr} should also be based on the effective length of $L_{eff} = 2h_{stem}$ (except for cases where $2h_{stem} > L$ in which case L_{eff} is taken to be equal to L). Similarly, calculation for the lateral load generated by debris flow can also be based on L_{eff} .

The total maximum deflection of the wall is given by $\Delta_b + \Delta_d$. By rearranging Eq. 7.4 to 7.7, the total maximum deflection (Δ) can be developed as shown by Eq. 7.8

$$\Delta = \frac{F_d + \sqrt{2k_{cr}KE_2}}{k_{cr}} \quad (7.8)$$

Meanwhile, the deflection demand of the impact action on a stem wall which is protected by a layer of gabion cushion can be estimated using Eq. 7.9.

$$\Delta_0 = \gamma \times \frac{mv_0}{\sqrt{mk_{cr}(1 + \lambda)}} \quad (7.9)$$

where Δ_0 is the deflection of stem wall (with protection by gabion cushion) due to boulder impact. The amount of energy delivered to the barrier (and gabions) by the impact of a boulder (KE_2) can be found using Eq. 7.10.

$$KE_2 = \frac{1}{2} k_{cr} \Delta_o^2 \quad (7.10)$$

7.3 DESIGN FOR LOCALISED DAMAGE

Although the focus of this thesis is purely on the global behavior of the structure it is worthy to have a simple check on the localised failure of the structure with the availability of a gabion cushion layer for the completeness of the calculation. Following design check is hence developed based on the experimental results of the large-scale test.

Nominal punching shear stress (v_u) of a thin slab panel when subject to a point force (from a circular cross-section column situated above the slab) can be calculated using Eq. 7.11 [152]. The mode of failure is as shown in Figure 7.1.

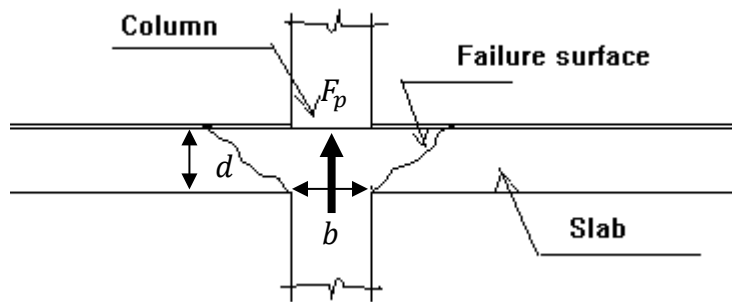


Figure 7.1 Punching shear failure of a flat slab panel

$$v_u = \frac{F_p}{\pi b d} \quad (7.11)$$

where, F_b is the point force acting on the column, b is the diameter of column and d is the depth of the slab panel. The localised damage to the wall when subject to the impact action was observed as punching shear. Therefore, Eq. 7.11 can be used for analysing the impact actions as well as for calculating the nominal punching shear stress using the assumptions of Figure 7.2. The contact force delivered by the boulder is actually applied to the gabions. However, a conservative assumption to adopt is that the contact force is applied directly to the bare surface of the concrete.

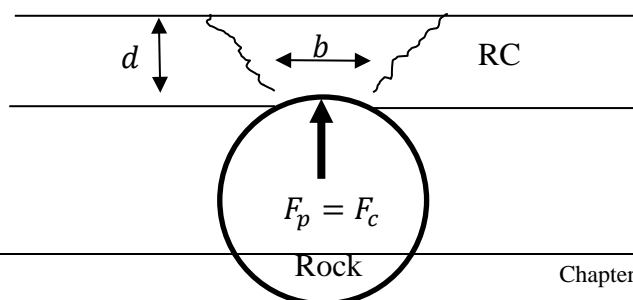


Figure 7.2 Punching shear failure of a boulder impact

Test Series A to C were conducted with some kind of protection at the contact surface and hence localised damage was not observed after any of these tests. At the end of the Test series C, all these protection measures (steel plate and gabion) were removed, and the bare wall was tested for localised damage (Test series D). Results from this test can be found in the Ref. [153] and some results are used for this study as presented in Table 7.1. The maximum amount of punching shear stress experienced by the specimen in Test series D was taken as the punching shear capacity when subject to the impact action of the boulder. The punching shear capacity was calculated with the use of Eq. 7.10. and shown in Table 7.1.

Table 7.1 Punching shear capacity calculated from Test series D

Test No.	b (mm)	d (mm)	F_c (kN)	v_u (MPa)
D1	20.5	230	250	16.9
D2	26.8	230	520	26.8
D3	47.6	230	680	19.8
D4	45.4	230	860	26.2
D7	56.9	230	890	21.7
D8	63.8	230	800	17.4

* F_c is the peak contact force recorded from full-scale impact experiments

It was observed from experimental results that the concrete wall could withstand localised damage when experiencing this amount of shear stress. Thus, the nominal shear capacity for large scale impact can be used for assessing the risk of localised damage; refer Eq. 7.12.

$$v_u = \frac{F_c}{\pi b d} < 25 \text{ MPa} \quad (7.12)$$

where, F_c is the contact force on the gabion cushion layer (= P), b is the diameter of contact surface (recommended to be $0.2 \times$ boulder diameter conservatively) and d is the thickness of the wall specimen.

7.4 DESIGN STEPS

The design procedure for checking the satisfactory performance of the stem wall in bending with gabion cushion cover is demonstrated herein.

1. Calculate cracked stiffness k_{cr} .

- a.
$$k_{cr} = \frac{3EI_{cr}}{h_{stem}^3}$$

- b.
$$EI_{cr} = \frac{M_y}{\phi_y}$$

- c.
$$M_y = 0.8A_{st}f_yd \left(1 - 0.6 \frac{A_{st}f_y}{Bdf'_c} \right)$$

- d.
$$\phi_y = \frac{1.7\varepsilon_{sy}}{D}$$

2. Determine generalised mass of stem wall with gabion cushion m_2 and calculate mass ratio $\lambda_2 = m_2/m$.
3. Determine the contact force (F_c) taking into account the mitigating effects of the gabion cushion.
4. Calculate value of k_n of the gabion cushion.
5. Use Excel spreadsheets to estimate the value of Δ_0 directly or perform calculations manually which involves the use of Figure 6.1 (for determining the γ factor) and Eq. 7.9.
6. Calculate KE_2 by use of Eq. 7.10
7. Calculate the value of the deflection demand Δ by use of Eq 7.8.
8. Calculate the value of Δ_y and check that $\Delta < \Delta_y$.

$$\Delta_y = \frac{\phi_y h_{stem}^2}{3}$$

9. Calculate the shear stress of the wall using Eq 7.11 and compare it with the nominal shear capacity of the wall.

$$v_u = \frac{F_c}{\pi bd} < 25 \text{ MPa}$$

7.5 WORKED EXAMPLE 1

The rigid barrier is designed to withstand a landslide event as specified in Table 7.2. Three debris surges are considered in this design for assessing the stability of the barrier, but final surge governs the flexural performance. The length of the barrier is 10 m. Reinforcement details of the rigid barrier and gabion cushion details are selected as specified in Table 7.3.

Table 7.2 Design data for rigid barrier

Input Parameters	Values
Boulder Diameter	1.5 m
Boulder and Debris Velocity, v_0	7 m/s
COR	0.3
Debris Density, ρ_d	1800 kg/m ³
Debris Thickness, h_d	1.5 m
Gabion thickness	0.5m
Gabon Density, ρ_g	1500 kg/m ³

Table 7.3 Reinforcement details

Parameters	Values
Compression strength of concrete (f'_c)	32 MPa
Bar diameter	40 mm
Spacing	200 mm
Cover thickness	80 mm
Tensile strength of reinforcement (f_y)	500 MPa
Elastic modulus of concrete (E_s)	200 GPa
Elastic modulus of gabion cushion (M_e)	4000 Pa
Friction angle of gabion fill rock particles	40°

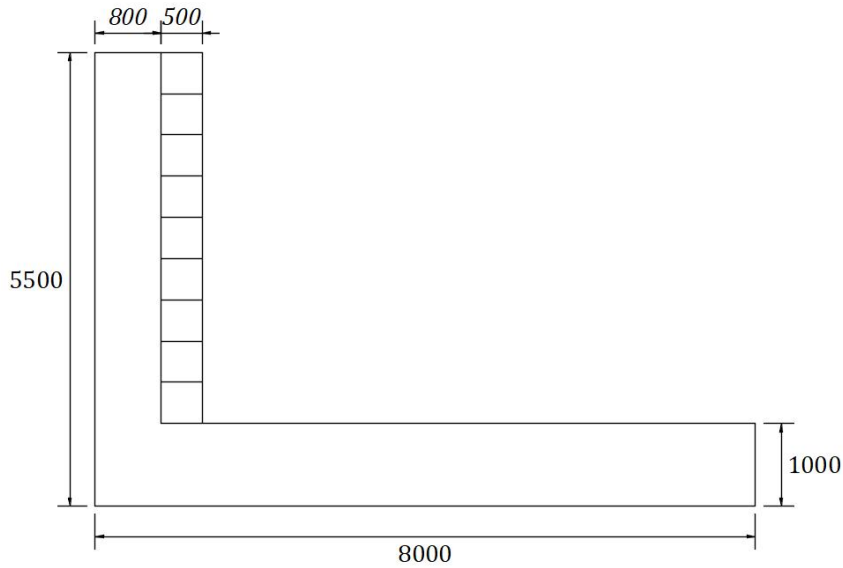


Figure 7.3 Dimensions of rigid barrier

Longitudinal reinforcement: 40 mm dia. high tensile bars at 200 mm spacing (T40-200). Calculation on per metre length of wall basis:

$$A_{st} = \frac{1000}{200} \times \pi \left(\frac{40}{2} \right)^2 = 6283.2 \text{ mm}^2/\text{m}$$

$$M_y = 0.8A_{st}f_yd \left(1 - 0.6 \frac{A_{st}f_y}{Bdf'_c} \right)$$

$$= 0.8 \times 6283.2 \times 500 \times 700 \times \left(1 - 0.6 \times \frac{6283.2 \times 500}{1000 \times 700 \times 32} \right) \times 10^{-6}$$

$$= 1611 \text{ kNm/m}$$

$$L_{eff} = 2(h) = 2 \times (5.5 - 1) = 9 \text{ m}$$

$$M_y = 1611 \times 9 = 14501 \text{ kNm}$$

$$\varepsilon_{sy} = \frac{f_y}{E_s} = \frac{500}{200000} = 0.0025; \phi_y = \frac{1.7\varepsilon_{sy}}{D} = \frac{1.7(0.0025)}{0.8} = 0.0053125 \text{ rad/m}$$

$$EI_{eff} = \frac{M_y}{\phi_y} = \frac{14501}{0.0053125} = 2729643 \text{ kNm}^2$$

$$k_{cr} = \frac{3EI_{cr}}{h^3} = \frac{3(2729643)}{4.5^3} = 89865 \text{ kN/m}$$

$$r_1 = r + e \times \tan(20^\circ) = 0.75 + 0.5 \times \tan(20^\circ) = 0.932 \text{ m}$$

$$m_{gabion} = \frac{1}{3} \pi (r_1^2 + r_1 r + r^2) e \rho_g$$

$$= \frac{1}{3} \pi (0.932^2 + 0.932 \times 0.75 + 0.75^2) 0.5 \times 1500$$

$$= 1672 \text{ kg}$$

$$m_{wall} = 0.25 \times 0.8 \times 9 \times 4.5 \times 2450 = 19845$$

$$m_2 = m_{wall} + m_{gabion} = 19845 + 1672 = 21517 \text{ kg}$$

$$m = 2650 \times \frac{4}{3} \pi \times \left(\frac{1.5}{2}\right)^3 = 4683 \text{ kg}$$

$$\lambda_2 = \frac{m_2}{m} = \frac{21517}{4683} = 4.59$$

$$F_c = 1.82 \times e^{-0.5} \times r^{0.7} \times M_E^{0.4} \times \tan \phi_k \times \left(\frac{mv_0^2}{2}\right)^{0.6}$$

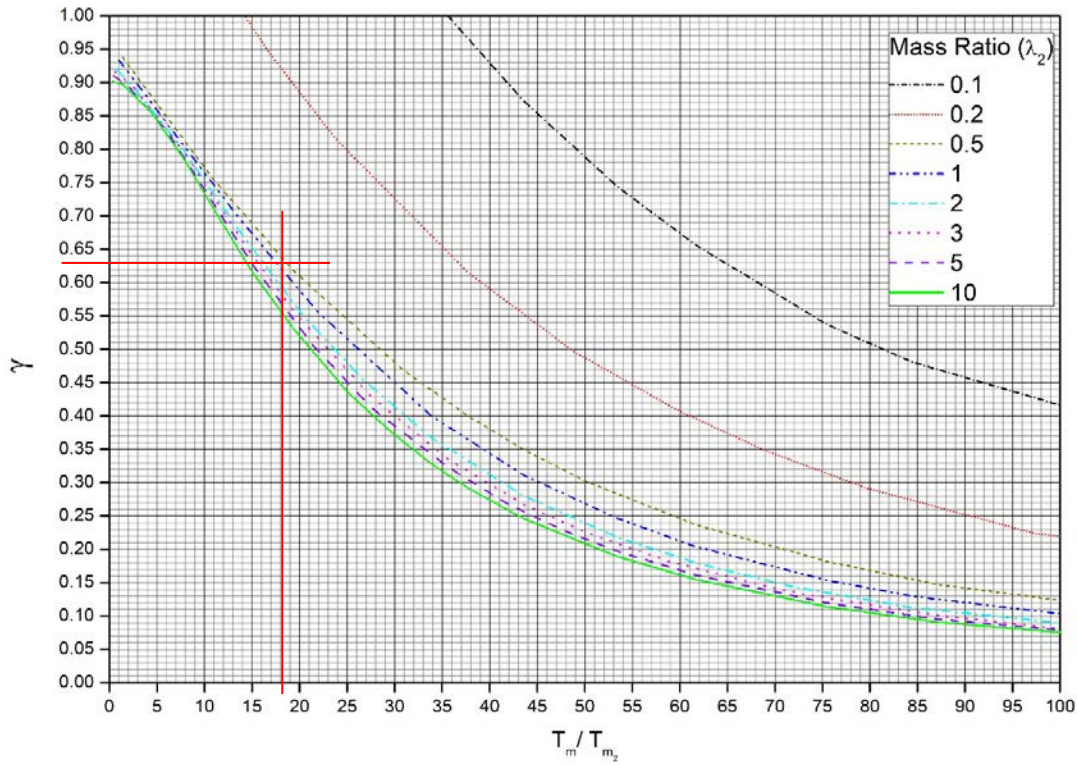
$$= 1.82 \times 0.5^{-0.5} \times 0.75^{0.7} \times 3000^{0.4} \times \tan 40^\circ \times \left(\frac{4.683 \times 7^2}{2}\right)^{0.6} = 747.49 \text{ kN}$$

$$k_n = \frac{F_c^2}{50mv_0^2} \times \left(\frac{1 + \lambda_2}{\lambda_2}\right) = \frac{747.49^2}{50 \times 4683 \times 7^2} \times \left(\frac{1 + 4.59}{4.59}\right) = 59298 \text{ N/m}$$

$$T_m = 2\pi \sqrt{\frac{m}{k_n}} = 2\pi \sqrt{\frac{4683}{59298}} = 1.77 \text{ s}$$

$$T_{m_2} = 2\pi \sqrt{\frac{m_2}{k_{cr}}} = 2\pi \sqrt{\frac{21517}{89865000}} = 0.097 \text{ s}$$

$$\frac{T_m}{T_{m_2}} = \frac{1.77}{0.097} = 18.16 ; \gamma = 0.63$$



$$\Delta = \gamma \times \frac{mv_0}{\sqrt{mk_{cr}(1 + \lambda_2)}} = 0.63 \times \frac{4683 \times 7}{\sqrt{4683 \times 89865000 \times (1 + 4.59)}}$$

$$= 13.46 \text{ mm}$$

$$\Delta_y = \frac{\phi_y h^2}{3} = \frac{0.0053125 \times 4.5^2}{3} = 36 \text{ mm}$$

It is concluded that:

$\Delta_y > \Delta$ meaning that the RC stem wall is predicted to respond within the limit of yield.

$$KE_2 = \frac{1}{2} k_{cr} \Delta_0^2 = 0.5 \times 117900000 \times 0.011^2 = 7114 \text{ J}$$

Given that the wall stiffness k_{cr} was calculated on the basis of wall length = L_{eff} (and not the entire wall length L), the lateral load from debris flow is also based on the same length:

$$F_d = \alpha \rho_d v_0^2 \sin \beta_d h_d L_{eff} = 2.5 \times 1800 \times 7^2 \times 1.5 \times 9 = 2977 \text{ kN}$$

$$\Delta = \frac{F_d + \sqrt{2k_{cr}KE_2}}{k_{cr}} = \frac{2976750 + \sqrt{2 \times 117900000 \times 7114}}{2 \times 117900000}$$

$$= 18.12 \text{ mm}$$

$\Delta_y > \Delta$ meaning that the RC stem wall is predicted to respond within the limit of yield.

$$v_u = \frac{F_c}{\pi b d} = \frac{747.49}{3.14 \times 0.8 \times 0.2 \times 1.5} = 442 \frac{kN}{m^2} = 0.442 MPa < 25 MPa$$

Chapter 8: Conclusions

This research project investigates global response behaviour of a rigid RC barrier which is protected by a layer of gabion cushion. The barrier is subjected to solid object impact using large scale pendulum style impact experiments. Experimental results show that the cushion layer was able to reduce the deflection demand on the RC stem wall by about 50% - 90%. A layer of gabion cushion also serves the purpose of distributing the contact force onto the wall surface thereby preventing the wall from being subjected to excessively high contact pressure. Based on these experimental findings a 2DOF model and hand calculation method are proposed to facilitate uptake in design practices. The ability of the proposed model for guiding the structural design of a RC rockfall protection barrier which has incorporated a layer of gabion cushion for additional protection is well demonstrated. The major findings that have been observed from each chapter are summarised and concluded in the following paragraphs.

8.1 SUMMARY AND CONCLUSIONS

8.1.1 Chapter 2

A critical review of the state of the art of experiments and predictive models available in the literature related to gabion and rockfall protection walls are presented in Chapter 2. It is shown that the gabion boxes are generally characterised by the unit characteristic strength. It was further clarified that size, roughness and durability characteristics of the fill material must comply with standards and, consequently the type of material used for filling the gabion does not vary significantly from place to place. It was also identified that the RC barriers are common in the area where land space availability is limited, and the amount of impact energy is moderate. Local and global response behaviour of the RC structure under impact load has been discussed. The difference between hard and soft impact has also been explained. A cushion layer can delay the transfer of momentum in an impact. The structural behaviour can become dynamic in nature. Therefore, it is considered that the importance of treating the problem dynamically in the design stage (instead of assuming as a quasi-static load).

State of the art of the design models is studied following the basic literature review on the theories behind impact loading. These models have been first categorised as forced-based (FB) or Displacement-based (DB) models. It has been found that the FB model ignores inertial effects of the impact as well as the dynamic response behaviour of the target. As a result, calculations based on the FB method could lead to either overdesigned (with or without cushion) or under designed (with cushion) structures. On the other hand, DB models consider the transfer of momentum and energy between the target and the impactor. However, the use of gabion can delay this momentum transfer and hence the assumption of instantaneous momentum transfer could lead to the over-design of the structure. Hence, the design of appropriate structure with a cushion layer should be based on the dynamic nature of the impact action. This could be achieved through single degree of freedom (SDOF) or two degrees of freedom (2DOF) systems modelling. However, employing a SDOF model in impact actions a predefined forcing function is required, and is difficult to achieve compared to modelling blast, wind and seismic actions. Alternatively, a 2DOF system can be used. Available forcing functions and their advantages and disadvantages are also discussed. From review of the literature it is considered that the Hunt and Crossley model is more accurate in simulating the contact force when experimentally measured COR values are known.

Some researchers have proposed analytical models for the design of impact resistance barriers and these models are single, two or multi-degree of freedom systems involving rigorous computational programs for calculations and cannot be used as simple design calculation method in the design office. Large-scale experiments are always performed in the field and without proper instrumentation. Small scale experiments can be performed in laboratories with proper instrumentation, but no one has performed a large-scale experiment in laboratory with proper instrumentation.

8.1.2 Chapter 3

In chapter 3, small scale experiments were carried out to study the behaviour of a gabion cushion under impact action. Force distribution through a cushion layer was studied using drop tests. Particles engaged in resisting the impact was found to be in a funnel shape with an angle of 20° . Moreover, stresses at the transmitted end are distributed in a radial manner. Small scale drop test results have proven that the equation proposed in the Swiss code [61] is accurate for the calculation of the contact

force of impact despite the fact that the original empirical equation was developed by employing three different soil materials without any confinement (gabion cage). The plate bearing test can be used for the prediction of the modulus of elasticity (ME) of the cushion layer in the original calculation model [61] but it is practically impossible to perform the test on a layer of gabion cushion that has been stacked vertically. Alternatively, static test performed on a single cage has been proven to be valid. More drop tests were performed in a consecutive manner. Empirical modification factors have been developed statistically to calculate ME values for multiple strikes which can be used in conjunction with the static test results. Small scale horizontal impact tests have shown that the empirical value used in the Swiss code is only valid for vertical impact scenario and hence that value would need to be modified for dealing with horizontal impact. A new equation has therefore been developed to be used for modelling horizontal impact of a boulder on the gabion cushion.

8.1.3 Chapter 4

In Chapter 4, pendulum style impact tests have been performed on a full-scale RC barrier specimen which had the protection of a layer of gabion cushion cover of two different filling materials, two different cushion strengths and three different thicknesses. Barrier specimen used in the test were 3 m wide, 1.5 m tall and 0.23 m thick with a base slab of 0.5 m in height and 1.23 m in length. Three impactors with mass of 280 kg, 435 kg and 1020 kg were employed to impact the gabion cushion layer (for up to four consecutive strikes) with three different impact energy levels. River pebbles and crushed gravel were used as filling materials to differentiate the performance of different filling materials. Gabion cages made of 3 mm and 5 mm wire meshes with 75 mm and 50 mm openings respectively were used to represent two different gabion designs. Three thicknesses: 300 mm 500 mm and 1000 mm gabions were used. Over 100 pieces of instruments were employed. A test series without cushioning has also been performed for comparison purposes.

It is shown in the time history of the contact force that the peak contact force has been reduced significantly by the extra gabion cushion protection whilst the duration of contact is prolonged. Contact force of the cushion layer depends on the confinement of the layer and the stiffness of the cushion could be increased following multiple strikes. Test results further show that the peak contact force would increase with reducing cushion thickness as well as increasing rigidity of the cage. Particles used to

fill the gabion has no significant influence on the contact force. Photographs of the damaged gabion cushion show that when confinement was high, the difference in permanent indentation in two consecutive strikes were low. If the confinement is high the contact force is high too. In contrast, a flexible cage is subject to higher permanent indentation compared to a rigid cage. This affects the contact force results as well. Deflection of the wall was measured using laser sensors attached to separate wooden frame. It was found that the use of gabion cushion has achieved some 50% to 90% reduction of the deflection of the wall. Reduction of the wall deflection was highest in the first strike in multiple impact scenarios. Similar to contact force, deflection demand were not affected by the fill material but decreased with decreasing rigidity of the gabion cage (flexible gabion). Increments in deflection with reducing cushion thickness was another important observation to make. Same observations were reflected in the strain measurements as well which is of interest to the design engineer.

8.1.4 Chapter 5

In chapter 5, it is shown that the forcing function of the impact action affecting the cantilevered wall (which was placed behind the cushion) could be simulated reasonably accurately by employing the non-linear viscoelastic model (also known as Hunt and Crossley model) for characterising the hysteretic properties of the frontal spring forming part of the two-degrees-of-freedom (2DOF) spring connected lumped mass system. The 2DOF system model so derived has been validated by comparison of the simulated deflection demand with experimental measurements. The ability of the proposed model for guiding the structural design of a RC rockfall protection barrier which has incorporated a layer of gabion cushion for additional protection is well demonstrated.

8.1.5 Chapter 6

In Chapter 6, a closed form expression which is used in conjunction with a design chart has been derived from the deflection demand data (that was generated from parametric studies employing the 2DOF system model) to facilitate uptake in design practices. Results presented in Chapter 4 have been compared with estimates from the simplified calculation method. Results so obtained from this method are shown to be in good agreement.

8.1.6 Chapter 7

Chapter 7 presents a simplified hand calculation method which takes into account co-existence lateral pressure from debris flow. A simple design check for localised damage with the presence of a cushion layer is also presented for the completeness of the design. A design example has been documented at the end to demonstrate step-by-step implementation of the proposed methodology.

8.2 LIMITATIONS AND RECOMMENDATIONS

This research project has studied the effect of gabion cushion layer in the design of a RC rockfall barrier. Experimental investigation was carried out with a large-scale wall specimen which was well instrumented. A 2DOF model and simplified calculation model are proposed for use in the design of the RC barrier which incorporates gabion cushion protection. These models have been validated with the experimental results. The project can be extended further by considering the following recommendations:

1. Proposed calculations are entirely based on the prediction model of the Swiss code [61] and could only be valid for a cushion layer made of geotechnical materials. Hence, the calculation method cannot be extended to other types of cushion materials (rubber). It is preferred to develop an equation to calculate the contact force which is general for any type of cushion materials.
2. Experiments have been carried out using steel impactors with a spherical contact interface. The contact force prediction of real rock with irregularities in the contact surface would be based on the original recommendations of ASTRA [61]. The legitimacy of this with irregularities of real rock and gabion cushion contact has not been validated experimentally.

3. It has been found from small scale experiments that the contact force is distributed radially through the cushion layer. However, in large scale experiments, no measurement devices were used to capture the reduction of stress distribution at the contact surface, and hence the effect of reduction of localised damage has not been quantified. The amount of localised damage reduction should be studied more rigorously to make sure that the cushion thickness is adequate with respect to protection from localised failure.
4. Sliding and overturning of the barrier are not within the scope of this study but those calculations would be affected by cushioning and initial resistance of the gabion cages. In practice, the barrier would need to be designed for bending, sliding and overturning actions.
5. Calculation methods proposed in this thesis involving either 2DOF or hand calculation method can be extended in the design of highway protection barriers. Impact on a highway protection barrier by a vehicle can be considered as a soft impact scenario as the frontal part of the vehicle would disintegrate gradually over the course of the impact, and hence there is cushioning inherent in the impactor (the vehicle).

Bibliography

1. Yin, Y., F. Wang, and P. Sun, *Landslide hazards triggered by the 2008 Wenchuan earthquake, Sichuan, China*. Landslides, 2009. **6**(2): p. 139-152.
2. Marzorati, S., L. Luzi, and M. De Amicis, *Rock falls induced by earthquakes: a statistical approach*. Soil Dynamics and Earthquake Engineering, 2002. **22**(7): p. 565-577.
3. Dorren, L.K., *A review of rockfall mechanics and modelling approaches*. Progress in Physical Geography, 2003. **27**(1): p. 69-87.
4. Matsuoka, N. and H. Sakai, *Rockfall activity from an alpine cliff during thawing periods*. Geomorphology, 1999. **28**(3): p. 309-328.
5. Stokes, A., et al., *Mechanical resistance of different tree species to rockfall in the French Alps*. Plant and soil, 2005. **278**(1-2): p. 107-117.
6. Haehnel, R.B. and S.F. Daly, *Maximum impact force of woody debris on floodplain structures*. Journal of Hydraulic Engineering, 2004. **130**(2): p. 112-120.
7. Lässig, R. *Flood and landslide damage hits a 10-year high in 2018*. 2019 [cited 2019 2019/08/05]; Available from: <https://www.wsl.ch/en/news/2019/03/flood-and-landslide-damage-hits-a-10-year-high-in-2018.html>.
8. Civil Engineering and Development Department, T.g.o.t.H.K.s.a.r. *Landslip Prevention and Mitigation Programme (LPMitP)*. 2019; Available from: <https://www.cedd.gov.hk/eng/our-projects/landslip/lpmitp/index.html>.
9. Lambert, S. and F. Bourrier, *Design of rockfall protection embankments: a review*. Engineering Geology, 2013. **154**: p. 77-88.
10. Peila, D., S. Pelizza, and F. Sassudelli, *Evaluation of behaviour of rockfall restraining nets by full scale tests*. Rock Mechanics and Rock Engineering, 1998. **31**(1): p. 1-24.
11. Calvetti, F., C. Di Prisco, and M. Vecchiotti, *Experimental and numerical study of rock-fall impacts on granular soils*. Rivista Italiana di Geotecnica, 2005. **4**: p. 95-109.
12. Gerber, W., et al. *Impact of rockfalls on reinforced foam glass cushion systems*. in *Proceedings of the Interdisciplinary Workshop on Rockfall Protection*. 2008.
13. Kishi, N., et al., *Prototype impact tests on ultimate impact resistance of PC rock-sheds*. International Journal of Impact Engineering, 2002. **27**(9): p. 969-985.

14. Labiouse, V., et al., *Experimental study of rock blocks falling down on a reinforced concrete slab covered by absorbing cushions*. *Revue française de géotechnique*, 1994. **69**: p. 41-61.
15. Roethlin, C., et al., *Numerical simulation of rockfall impact on a rigid reinforced concrete slab with a cushion layer*. 2013.
16. Schellenberg, K., et al. *Rockfall–Falling weight tests on galleries with special cushion layers*. in *Proceedings, 3rd international conference on protection of structures against hazards, September*. 2006.
17. Schellenberg, K., et al. *Large-scale impact tests on rock fall galleries*. in *7th Int. Conference on Shock & Impact Loads on Structures*. 2007.
18. Heymann, A., et al. *Use of external testing methods to assess damage on rockfall protection structures*. in *Applied Mechanics and Materials*. 2011. Trans Tech Publ.
19. Heymann, A., et al. *An experimental comparison of half-scale rockfall protection sandwich structures*. in *11th International Conference on Structures Under Shock and Impact (SUSI)*. 2010. WIT Press.
20. Lambert, S., et al., *Real-scale investigation of the kinematic response of a rockfall protection embankment*. *Natural Hazards and Earth System Sciences*, 2014. **14**(6): p. p. 1269-p. 1281.
21. Ng, C., et al., *Large-Scale Successive Boulder Impacts on a Rigid Barrier Shielded by Gabions*. *Canadian Geotechnical Journal*, 2016(ja).
22. Calvetti, F., *Distinct Element evaluation of the rock-fall design load for shelters*. *Rivista Italiana di geotecnica*, 1998. **3**: p. 63-83.
23. Kawahara, S. and T. Muro, *Effects of dry density and thickness of sandy soil on impact response due to rockfall*. *Journal of terramechanics*, 2006. **43**(3): p. 329-340.
24. Nicot, F., et al., *Multiscale approach to geo-composite cellular structures subjected to rock impacts*. *International journal for numerical and analytical methods in geomechanics*, 2007. **31**(13): p. 1477-1515.
25. Degago, S., R. Ebeltoft, and S. Nordal. *Effect of rock fall geometries impacting soil cushion: a numerical procedure*. in *proceedings of the 12th International Conference of International Association for Computer Methods and Advances in Geomechanics (IACMAG), Goa, India*. 2008.
26. Bourrier, F., et al. *A model for rockfall protection structures based on a multi-scale approach*. in *Conference Proceedings, Geoflorida, West Palm Beach, Florida*. 2010.
27. Gerber, W. and A. Volkwein. *Impact loads of falling rocks on granular material*. in *Proceedings of Third Euro Mediterranean Symposium on Advances in Geomaterials and Structures, AGS*. 2010.

28. Bhatti, A.Q. and N. Kishi, *Impact response analysis of prototype RC girders with sand cushion using equivalent fracture energy concept*. International Journal of Damage Mechanics, 2011: p. 1056789510397067.
29. Ali, M., et al., *Simple hand calculation method for estimating deflection generated by the low velocity impact of a solid object*. Australian Journal of Structural Engineering, 2014. **15**(3): p. 243-259.
30. Lam, N.T., et al., *Displacement-based approach for the assessment of overturning stability of rectangular rigid barriers subjected to point impact*. Journal of Engineering Mechanics, 2017. **144**(2): p. 04017161.
31. Agostini, R., *Flexible gabion structures in earth retaining works*. 1987: Officine Maccaferri.
32. Lin, D.-G., Y. Lin, and F. Yu, *Deformation analyses of gabion structures*. INTERPRAEVENT 2010, 2010: p. 512-526.
33. Yoshida, H. *Recent experimental studies on rockfall control in Japan*. in *Joint Japan-Swiss Scientific Seminar on Impact Load by Rock Falls and Design of Protection Structures, Kanazawa, Japan*. 1999.
34. Ranjan, R., et al., *Local impact effects on concrete target due to missile: An empirical and numerical approach*. Annals of Nuclear Energy, 2014. **68**: p. 262-275.
35. Sugano, T., et al., *Local damage to reinforced concrete structures caused by impact of aircraft engine missiles Part I. Test program, method and results*. Nuclear Engineering and Design, 1993. **140**(3): p. 387-405.
36. Itoh, Y., C. Liu, and R. Kusama, *Dynamic simulation of collisions of heavy high-speed trucks with concrete barriers*. Chaos, Solitons & Fractals, 2007. **34**(4): p. 1239-1244.
37. Bhatti, A.Q., et al., *Numerical study for impact resistant design of full scale arch type reinforced concrete structures under falling weight impact test*. Journal of Vibration and Control, 2011: p. 1077546311419176.
38. Miyamoto, A. and M. King, *Modeling of impact load characteristics for dynamic response analysis of concrete structures*. WIT Transactions on The Built Environment, 1970. **8**.
39. Miyamoto, A., M.W. King, and M. Fuji, *Nonlinear dynamic analysis of reinforced concrete slabs under impulsive loads*. Structural Journal, 1991. **88**(4): p. 411-419.
40. Miyamoto, A., M.W. King, and M. Fujii, *Analysis of failure modes for reinforced concrete slabs under impulsive loads*. Structural Journal, 1991. **88**(5): p. 538-545.
41. Roethlin, C., et al. *Numerical simulation of rockfall impact on a rigid reinforced concrete slab with a cushion layer*. 2013. Protect 2013, Fourth

- International Workshop on Performance, Protection and Strengthening of Structures.
42. Sawamoto, Y., et al., *Analytical studies on local damage to reinforced concrete structures under impact loading by discrete element method*. Nuclear Engineering and Design, 1998. **179**(2): p. 157-177.
 43. Fernández Ruiz, M., Y. Mirzaei, and A. Muttoni, *Post-punching behavior of flat slabs*. ACI Structural Journal, 2013. **110**(ARTICLE): p. 801-812.
 44. Sacramento, P.V.P., et al., *Punching strength of reinforced concrete flat slabs without shear reinforcement*. Revista IBRACON de Estruturas e Materiais, 2012. **5**(5): p. 659-691.
 45. Lambert, S., P. Gotteland, and F. Nicot, *Experimental study of the impact response of geocells as components of rockfall protection embankments*. Natural Hazards and Earth System Sciences, 2009. **9**: p. p. 459-p. 467.
 46. Plassiard, J.-P. and F.-V. Donzé, *Rockfall impact parameters on embankments: a discrete element method analysis*. Structural Engineering International, 2009. **19**(3): p. 333-341.
 47. Schellenberg, K., *On the design of rockfall protection galleries*. 2008, Diss., Eidgenössische Technische Hochschule ETH Zürich, Nr. 17924.
 48. Ngo, T., et al., *Blast loading and blast effects on structures—an overview*. Electronic Journal of Structural Engineering, 2007. **7**(S1): p. 76-91.
 49. Jones, N., *Recent studies on the dynamic plastic behavior of structures*. Applied Mechanics Reviews, 1989. **42**(4): p. 95-115.
 50. Rostasy, F., J. Scheuermann, and K. Sprenger, *Mechanical behaviour of some construction materials subjected to rapid loading and low temperature*. Betonwerk+ Fertigteil-Technik, 1984. **50**(6): p. 393-401.
 51. Schlüter, F.-H., *Dicke Stahlbetonplatten unter stossartiger Belastung-Flugzeugabsturz*. 1987: Institut für Massivbau und Baustofftechnologie.
 52. Schmidt-Hurtienne, B., *Ein dreiaxiales Schädigungsmodell für Beton unter Einschluss des Dehnrateneffekts bei Hochgeschwindigkeitsbelastung*. 2000: Inst. für Massivbau und Baustofftechnologie.
 53. Ho, T.S., H. Masuya, and N. Takashita, *Experimental study concerning impact characteristics by collision of weight on sand cushion over steel beam*. International Journal of GEOMATE, 2013. **14**(1 SERL 7): p. 471-477.
 54. Sun, J., et al., *Performance of Used Tire Cushion Layer under Rockfall Impact*. Shock and Vibration, 2016. **2016**.
 55. Johnson, K., *Contact Mechanics Cambridge University Press London*. UK, 1985.

56. Kwan, J.S.H., *Supplementary Technical Guidance on Design of Rigid Debris-resisting Barriers*. GEO Report No. 270, 2012.
57. Lam, C., *A pilot study of the use of cushioning materials for reducing dynamic impact loads on rigid debris-resisting barriers* Technical Note TN 5/2016, 2016.
58. Masuya, H. *history and highlights of rock fall research in Japan*. in *Interdisciplinary workshop on rockfall protection*. 2008.
59. Japan Road Association, *Manual for anti-impact structures against falling rocks (in Japanese)*. 1983.
60. Labiouse, V., F. Descoedres, and S. Montani, *Experimental study of rock sheds impacted by rock blocks*. *Structural Engineering International*, 1996. **6**(3): p. 171-176.
61. ASTRA, *Einwirkungen infolge Steinschlags auf Schutzgalerien, Richtlinie, Bundesamt für Strassen, Baudirektion SBB, Eidgenössische Drucksachen- und Materialzentrale, Bern*. 2008.
62. Sun, J., Lam, N., Zhang, L., Ruan, D. and Gad, E., *Contact forces generated by hailstone impact*. *International Journal of Impact Engineering*, 2015. **84**: p. 145-158.
63. Perera, S., Lam, N., Pathirana, M., Zhang, L., Ruan, D. and Gad, E., *Deterministic solutions for contact force generated by impact of windborne debris*. *International Journal of Impact Engineering*, 2016. **91**: p. 126-141.
64. Yang, Y., N. Lam, and L. Zhang, *Evaluation of simplified methods of estimating beam responses to impact*. *International Journal of Structural Stability and Dynamics*, 2012. **12**(03): p. 1250016.
65. Zhan, T., Z. Wang, and J. Ning, *Failure behaviors of reinforced concrete beams subjected to high impact loading*. *Engineering Failure Analysis*, 2015. **56**: p. 233-243.
66. Eurocode 1 - Actions on structures - Part 1-7: General actions - accidental actions (S.P. Committee, E., European Committee for Standardization: London., 2008.
67. Murthy, A.R.C., G. Palani, and N.R. Iyer, *Impact analysis of concrete structural components*. *Defence Science Journal*, 2010. **60**(3): p. 307-319.
68. Yong, A.C., et al., *Analytical solution for estimating sliding displacement of rigid barriers subjected to boulder impact*. *Journal of Engineering Mechanics*, 2019. **145**(3): p. 04019006.
69. Lam, N. and E. Gad. *The estimation of impact forces based on first principles*. in *Australasian Structural Engineering Conference: ASEC 2016*. 2016. Engineers Australia.

70. Wyllie, D.C., *Rock fall engineering*. 2014: CRC Press.
71. Chau, K., R. Wong, and C. Lee, *Rockfall problems in Hong Kong and some new experimental results for coefficients of restitution*. International Journal of Rock Mechanics and Mining Sciences, 1998.
72. Chau, K., R. Wong, and J. Wu, *Coefficient of restitution and rotational motions of rockfall impacts*. International Journal of Rock Mechanics and Mining Sciences, 2002. **39**(1): p. 69-77.
73. Yang, Y., *Modelling impact actions of spherical objects*. 2013.
74. Yong, A.C.Y., *Impact-resistance of Reinforced Concrete Structures*. 2019.
75. Lam, N., H. Tsang, and E. Gad, *Simulations of response to low velocity impact by spreadsheet*. International Journal of Structural Stability and Dynamics, 2010. **10**(03): p. 483-499.
76. Feraboli, P., *Modified SDOF models for improved representation of the impact response of composite plates*. Journal of composite materials, 2006. **40**(24): p. 2235-2255.
77. Schellenberg, K. and T. Vogel, *A dynamic design method for rockfall protection galleries*. Structural Engineering International, 2009. **19**(3): p. 321-326.
78. Hertz, H., *Über die Berührung fester elastischer Körper. On the contact of elastic solids, Reine und angewandte Mathematik*. London:(Instruction anglaise dans Miscellaneous papers by H. Hertz) Eds Jones et Schaott. 1896, Macmillan.
79. Sun, J., et al., *Contact forces generated by fallen debris*. Structural Engineering and Mechanics, 2014. **50**(5): p. 589-603.
80. Stoffel, S.M., *Sollicitation dynamique de la couverture des galeries de protection lors de chutes de blocs*. 1998, Thèse.
81. Bucher, K. *Dynamische Berechnung von Steinschlageinwirkungen*. in *Proceedings, Schweizerische Gesellschaft für Boden und Felsmechanik, Conference Paper Montreux*. 1997.
82. Khulief, Y. and A. Shabana, *A continuous force model for the impact analysis of flexible multibody systems*. Mechanism and Machine Theory, 1987. **22**(3): p. 213-224.
83. Hunt, K.H. and F.R.E. Crossley, *Coefficient of restitution interpreted as damping in vibroimpact*. 1975.
84. Herbert, R. and D. McWhannell, *Shape and frequency composition of pulses from an impact pair*. 1976.

85. Gilardi, G. and I. Sharf, *Literature survey of contact dynamics modelling*. Mechanism and machine theory, 2002. **37**(10): p. 1213-1239.
86. Lankarani, H.M. and P.E. Nikravesh. *Hertz contact force model with permanent indentation in impact analysis of solids*. in *18th Annual ASME Design Automation Conference*. 1992. Publ by ASME.
87. Sun, C. and J. Chen, *On the impact of initially stressed composite laminates*. Journal of Composite Materials, 1985. **19**(6): p. 490-504.
88. Cho, C. and G. Zhao, *Effects of geometric and material factors on mechanical response of laminated composites due to low velocity impact*. Journal of composite materials, 2002. **36**(12): p. 1403-1428.
89. Chung-Yue, W. and C.H. Yew, *Impact damage in composite laminates*. Computers & structures, 1990. **37**(6): p. 967-982.
90. Her, S.-C. and Y.-C. Liang, *The finite element analysis of composite laminates and shell structures subjected to low velocity impact*. Composite Structures, 2004. **66**(1-4): p. 277-285.
91. Herbert, R. and D. McWhannell, *Shape and frequency composition of pulses from an impact pair*. 1977.
92. Lee, T.W. and A. Wang, *On the dynamics of intermittent-motion mechanisms. Part 1: Dynamic model and response*. 1983.
93. Ye, K., L. Li, and H. Zhu, *A note on the Hertz contact model with nonlinear damping for pounding simulation*. Earthquake Engineering & Structural Dynamics, 2009. **38**(9): p. 1135-1142.
94. Sun, J., et al., *Computer Simulation of Contact Forces Generated by Impact*. International Journal of Structural Stability and Dynamics, 2016: p. 1750005.
95. Luo, L., *Development and validation of a geometry-based contact force model*. 2010, McGill University Library.
96. Sun, J., et al., *Contact forces generated by hailstone impact*. International Journal of Impact Engineering, 2015. **84**: p. 145-158.
97. Perera, S., *Modelling impact actions of flying and falling objects*. 2017.
98. di Prisco, C. and M. Vecchiotti, *Design charts for evaluating impact forces on dissipative granular soil cushions*. Journal of geotechnical and geoenvironmental engineering, 2010. **136**(11): p. 1529-1541.
99. Chikatamarla, R., *Optimisation of cushion materials for rockfall protection galleries*. Vol. 227. 2007: vdf Hochschulverlag AG.
100. Di Prisco, C. and M. Vecchiotti, *A rheological model for the description of boulder impacts on granular strata*. GEOTECHNIQUE-LONDON-, 2006. **56**(7): p. 469.

101. Bourrier, F., et al., *How multi-scale approaches can benefit the design of cellular rockfall protection structures*. Canadian Geotechnical Journal, 2011. **48**(12): p. 1803-1816.
102. Labiouse, V., F. Descoedres, and S. Montani, *Étude expérimentale de la chute de blocs rocheux sur une dalle en béton armé recouverte par des matériaux amortissants*. Revue française de Géotechnique, 1994(69).
103. Bourrier, F., F. Nicot, and F. Darve, *Evolution of the micromechanical properties of impacted granular materials*. Comptes Rendus Mécanique, 2010. **338**(10): p. 639-647.
104. Chikatamarla, R., J. Laue, and S. Springman. *Rockfall impact on protection galleries*. in *Second International Conference of Structural Engineering Mechanics and Computations, Balkema, Rotterdam, Cape Town, South Africa*. 2004.
105. Sy HO, T. and H. Masuya, *Finite element analysis of the dynamic behavior of sand-filled geocells subjected to impact load by rockfall*. International Journal of Erosion Control Engineering, 2013. **6**(1): p. 1-12.
106. Hallquist, J.O., *LS-DYNA keyword user's manual*. Livermore Software Technology Corporation, 2007. **970**: p. 299-800.
107. Johansson, A. and J. Fredberg, *Structural behaviour of prestressed concrete beams during impact loading*. 2015, M. Sc. Thesis Civil and Environmental Engineering Chalmers University Of
108. Cundall, P.A. and O.D. Strack, *A discrete numerical model for granular assemblies*. Geotechnique, 1979. **29**(1): p. 47-65.
109. Mahabadi, O., et al., *Y-Geo: new combined finite-discrete element numerical code for geomechanical applications*. International Journal of Geomechanics, 2012. **12**(6): p. 676-688.
110. Bertrand, D., et al., *Multi-scale modelling of cellular geo-composite structure under localized impact*. Revue européenne de génie civil, 2006. **10**(3): p. 309-322.
111. Liu, K., L. Gao, and S. Tanimura, *Application of discrete element method in impact problems*. JSME International Journal Series A, 2004. **47**(2): p. 138-145.
112. An, B. and D.D. Tannant, *Discrete element method contact model for dynamic simulation of inelastic rock impact*. Computers & geosciences, 2007. **33**(4): p. 513-521.
113. Salciarini, D., C. Tamagnini, and P. Conversini, *Discrete element modeling of debris-avalanche impact on earthfill barriers*. Physics and Chemistry of the Earth, Parts A/B/C, 2010. **35**(3): p. 172-181.

114. Plassiard, J.-P., N. Belheine, and F.-V. Donzé, *A spherical discrete element model: calibration procedure and incremental response*. Granular Matter, 2009. **11**(5): p. 293-306.
115. Kishi, N., et al. *Field test on shock-absorbing effect of three-layered absorbing system*. in *Transactions of the 12. international conference on Structural Mechanics in Reactor Technology (SMiRT). Volume J: Structural dynamics and extreme loads analysis*. 1993.
116. Kishi, N., *Absorbing performance of sand cushion and three-layered absorbing system*. Proceedings of Third SILOS, Singapore, 1999: p. 51-6.
117. Aminata, D., et al., *New protection wall against rockfall using a ductile cast iron panel*. Journal of Natural Disaster Science, 2008. **30**(1): p. 25-33.
118. Zhang, L., S. Lambert, and F. Nicot, *Discrete dynamic modelling of the mechanical behaviour of a granular soil*. International Journal of Impact Engineering, 2017. **103**: p. 76-89.
119. Nicks, J., T. Gebrenegus, and M. Adams, *Strength characterization of open-graded aggregates for structural backfills*. 2015.
120. Ghadimi Khasraghy, S., *Numerical simulation of rockfall protection galleries*. IBK Bericht, 2012. **334**.
121. Standards Australia, *AS 1379 Specification and supply of concrete*. 2007: New South Wales, Australia.
122. Standards Australia and Standards New Zealand, *AS/NZS 4671 Steel reinforcing materials*. 2001: New South Wales, Australia and Wellington, New Zealand.
123. Menegon, S.J., et al., *RC walls in Australia: seismic design and detailing to AS 1170.4 and AS 3600*. Australian Journal of Structural Engineering, 2017: p. 1-18.
124. Santamarina, J. and G. Cho. *Soil behaviour: the role of particle shape*. in *Advances in geotechnical engineering: The skempton conference*. 2004. Citeseer.
125. Beyer, K., A. Dazio, and M. Priestley, *Quasi-static cyclic tests of two U-shaped reinforced concrete walls*. Journal of earthquake engineering, 2008. **12**(7): p. 1023-1053.
126. Dazio, A., K. Beyer, and H. Bachmann, *Quasi-static cyclic tests and plastic hinge analysis of RC structural walls*. Engineering Structures, 2009. **31**(7): p. 1556-1571.
127. Alarcon, C., M.A. Hube, and J.C. de la Llera, *Effect of axial loads in the seismic behavior of reinforced concrete walls with unconfined wall boundaries*. Engineering Structures, 2014. **73**: p. 13-23.

128. Arthur, J. and B. Menzies, *Inherent anisotropy in a sand*. Geotechnique, 1972. **22**(1): p. 115-128.
129. Arthur, J. and A. Phillips, *Homogeneous and layered sand in triaxial compression*. Geotechnique, 1975. **25**(4): p. 799-815.
130. Oda, M., *Initial fabrics and their relations to mechanical properties of granular material*. Soils and foundations, 1972. **12**(1): p. 17-36.
131. Hunt, K.H. and F.R.E. Crossley, *Coefficient of Restitution Interpreted as Damping in Vibroimpact*. Journal of Applied Mechanics, 1975. **42**(2): p. 440.
132. Herbert, R.G. and D.C. McWhannell, *Shape and Frequency Composition of Pulses From an Impact Pair*. Journal of Manufacturing Science and Engineering, 1977. **99**(3): p. 513-518.
133. Lee, T.W. and A.C. Wang, *On The Dynamics of Intermittent-Motion Mechanisms. Part 1: Dynamic Model and Response*. Journal of Mechanical Design, 1983. **105**(3): p. 534-540.
134. Lankarani, H.M. and P.E. Nikravesh, *A contact force model with hysteresis damping for impact analysis of multibody systems*. Journal of Mechanical Design, 1990. **112**(3): p. 369-376.
135. Gonthier, Y., et al., *A regularized contact model with asymmetric damping and dwell-time dependent friction*. Multibody System Dynamics, 2004. **11**(3): p. 209-233.
136. Flores, P., et al., *On the continuous contact force models for soft materials in multibody dynamics*. Multibody System Dynamics, 2011. **25**(3): p. 357-375.
137. Hertz, H., *Über die Berührung fester elastischer Körper (On the contact of elastic solids)*. Journal für die reine und angewandte Mathematik, 1882. **92**: p. 156-171.
138. Perera, S., et al., *Deterministic solutions for contact force generated by impact of windborne debris*. International Journal of Impact Engineering, 2016. **91**: p. 126-141.
139. Perera, S., et al., *Use of static tests for predicting damage to cladding panels caused by storm debris*. Journal of Building Engineering, 2017. **12**: p. 109-117.
140. Thornton, C., *Coefficient of restitution for collinear collisions of elastic-perfectly plastic spheres*. Journal of Applied Mechanics, 1997. **64**(2): p. 383-386.
141. Bentz, E.C., *Sectional analysis of reinforced concrete members*. 2000: University of Toronto Toronto.
142. Lam, N., J. Wilson, and E. Lumantarna, *Force-deformation behaviour modelling of cracked reinforced concrete by EXCEL spreadsheets*. Computers and Concrete, 2011. **8**(1): p. 43-57.

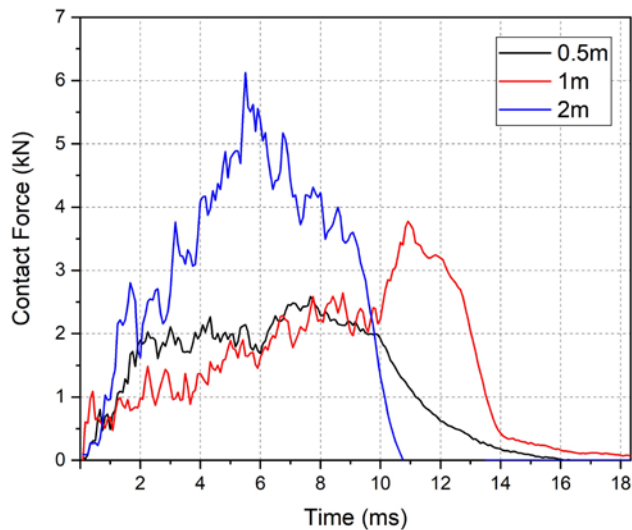
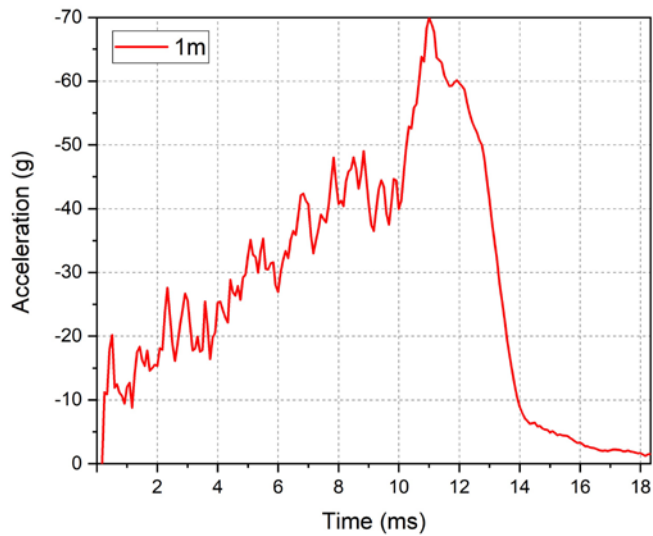
143. Park, R. and T. Paulay, *Reinforced concrete structures*. 1975: John Wiley & Sons.
144. Priestley, M.J.N., G.M. Calvi, and M.J. Kowalsky, *Displacement-Based Seismic Design of Structures*. 2007, Pavia, Italy: IUSS Press.
145. Lam, N.T.K., et al., *Displacement-based approach for the assessment of overturning stability of rectangular rigid barriers subjected to point impact*. *Journal of Engineering Mechanics*, 2018. **144**(2).
146. Yang, Y., N.T.K. Lam, and L. Zhang, *Evaluation of simplified methods of estimating beam responses to impact*. *International Journal of Structural Stability and Dynamics*, 2012. **12**(3): p. 1250016-1-1250016-24.
147. Hübl, J., et al. *Debris flow impact estimation*. in *Proceedings of the 11th international symposium on water management and hydraulic engineering, Ohrid, Macedonia*. 2009.
148. Kwan, J.S.H., *Supplementary technical guidance on design of rigid debris-resisting barriers (GEO Report No. 270)*. 2012: Geotechnical Engineering Office, the Government of the Hong Kong Special Administrative Region.
149. NILIM, *Manual of technical standards for designing sabo facilities against debris flow and Driftwood*. 2007, Natural Institute for Land and Infrastructure Management, Ministry of Land
150. VanDine, D., *Debris flow control structures for forest engineering*. Res. Br., BC Min. For., Victoria, BC, Work. Pap, 1996. **8**: p. 1996.
151. MLR, D.T.-. *Specification of geological investigation for debris flow stabilization*. National Land Resources Department, China (in Chinese). 2006.
152. Bažant, Z.P. and Z. Cao, *Size effect in punching shear failure of slabs*. *ACI Structural Journal*, 1987. **84**(1): p. 44-53.
153. Majeed, Z., et al., *Contact Force Generated by Impact of Boulder on Concrete Barriers*, in *ACMSM25*. 2020, Springer. p. 511-518.

Appendices

Appendix A - Calculation for Figure 3.8 (a) gravel

Acceleration measurements recorded from the accelerometer have been first filtered using a Butterworth filter and then applied the following calculation.

$$\text{Contact force (kN)} = (-\text{acceleration}) \times 9.81 \times (5\text{kg} / 1000)$$



Appendix B - Calculation for Figure 3.9 (a) – 1m drop height

Calculation for Figure 3.9

Impactor drop height = 1m

Experiment; $F_c = 3.76 \text{ kN}$

Swiss code; Employing Eq. (3.2),

$$\begin{aligned} F_c &= 2.8 \times e^{-0.5} \times r^{0.7} \times M_E^{0.4} \times \tan \phi_k \times \left(\frac{mv_0^2}{2} \right)^{0.6} \\ &= 2.8 \times 0.1^{-0.5} \times 0.05^{0.7} \times 3000^{0.4} \times \tan(40) \\ &\quad \times \left(\frac{0.005 \times 4.42^2}{2} \right)^{0.6} = 3.67 \text{ kN} \end{aligned}$$

Japanese code; Employing Eq. (3.3),

$$\begin{aligned} F_c &= 2.108(mg)^{\frac{2}{3}} \lambda^{\frac{2}{5}} H^{\frac{3}{5}} \left(\frac{e}{2r} \right)^{-0.5} \\ &= 2.108 \times (0.005 \times 9.81)^{\frac{2}{3}} \times 3000^{\frac{2}{5}} \times 1^{\frac{3}{5}} \left(\frac{0.1}{2 \times 0.05} \right)^{-0.5} \\ &= 6.94 \text{ kN} \end{aligned}$$

Labious et al; Employing Eq. (3.4),

$$F_c = 1.765 M_E^{\frac{2}{5}} r^{\frac{1}{5}} W^{\frac{3}{5}} H^{\frac{3}{5}} = 1.765 \times 3000^{\frac{2}{5}} \times 0.05^{\frac{1}{5}} \times 0.049^{\frac{3}{5}} \times 1^{\frac{3}{5}} = 3.90 \text{ kN}$$

Hertz; Employing Eq. (3.5),

$$F_c = 1.94 M_E^{\frac{2}{5}} r^{\frac{1}{5}} W^{\frac{3}{5}} H^{\frac{3}{5}} = 1.94 \times 3000^{\frac{2}{5}} \times 0.05^{\frac{1}{5}} \times 0.049^{\frac{3}{5}} \times 1^{\frac{3}{5}} = 4.29 \text{ kN}$$

Appendix C - Calculation for Figure 3.16 (a)

Experiment;

Impactor drop height = 0.05m

$$F_c = 0.338 \text{ kN}$$

Impactor drop height = 0.1m

$$F_c = 0.468 \text{ kN}$$

Impactor drop height = 0.2m

$$F_c = 0.687 \text{ kN}$$

Impactor drop height = 0.3m

$$F_c = 0.946 \text{ kN}$$

Impactor drop height = 0.5m

$$F_c = 1.07 \text{ kN}$$

Modified Swiss code; Employing Eq. 3.6,

Impactor drop height = 0.05m

$$\begin{aligned} F_c &= 1.82 \times 0.1^{-0.5} \times 0.05^{0.7} \times 2066^{0.4} \times \tan(40) \times \left(\frac{0.005 \times 0.99^2}{2} \right)^{0.6} \\ &= 0.341 \text{ kN} \end{aligned}$$

Impactor drop height = 0.1m

$$F_c = 1.82 \times 0.1^{-0.5} \times 0.05^{0.7} \times 2066^{0.4} \times \tan(40) \times \left(\frac{0.005 \times 1.4^2}{2} \right)^{0.6} = 0.52 \text{ kN}$$

Impactor drop height = 0.2m

$$\begin{aligned} F_c &= 1.82 \times 0.1^{-0.5} \times 0.05^{0.7} \times 2066^{0.4} \times \tan(40) \times \left(\frac{0.005 \times 1.98^2}{2} \right)^{0.6} \\ &= 0.78 \text{ kN} \end{aligned}$$

Impactor drop height = 0.3m

$$F_c = 1.82 \times 0.1^{-0.5} \times 0.05^{0.7} \times 2066^{0.4} \times \tan(40) \times \left(\frac{0.005 \times 2.42^2}{2} \right)^{0.6} = 1 \text{ kN}$$

Impactor drop height = 0.5m

$$F_c = 1.82 \times 0.1^{-0.5} \times 0.05^{0.7} \times 2066^{0.4} \times \tan(40) \times \left(\frac{0.005 \times 3.13^2}{2} \right)^{0.6} \\ = 1.36 \text{ kN}$$

Appendix D – Calculations of Cracked Stiffness k_{cr}

Wall specimen 1

Method no. 1 and 2

Wall height $h = 1.5 \text{ m}$

$$EI_{cr} = 16176 \text{ kNm}^2$$

Employing Eq. (5.7),

$$k_{cr} = \frac{3EI_{cr}}{h^3} = \frac{3(16176)}{1.5^3} = 14379 \text{ kN/m}$$

Method no. 3

For reinforcement arrangement of N20-200,

$$A_{st} = \frac{3000}{200} \times \pi \left(\frac{20}{2}\right)^2 = 4712 \text{ mm}^2$$

Employing Eq. 5.8 using values listed in Table 4.1,

$$\begin{aligned} M_y &= 0.8A_{st}f_yd \left(1 - 0.6 \frac{A_{st}f_y}{Bdf'_c}\right) \\ &= 0.8(4712)(543)(170) \left(1 - 0.6 \left(\frac{4712(543)}{3000(170)(47)}\right)\right) \times 10^{-6} \\ &= 326 \text{ kNm} \end{aligned}$$

Employing Eq. 5.9 using values listed in Table 4.1,

$$\phi_y = \frac{1.7\varepsilon_{sy}}{D} = \frac{1.7(0.0028)}{0.23} = 0.021 \text{ rad/m}$$

Employing Eq. 5.10 with the calculated values of M_y and ϕ_y ,

$$EI_{cr} = \frac{M_y}{\phi_y} = \frac{326}{0.021} = 15744 \text{ kNm}^2$$

Employing Eq. 5.7,

$$k_{cr} = \frac{3EI_{cr}}{h^3} = \frac{3(15744)}{1.5^3} = 14000 \text{ kN/m}$$

Wall specimen 2

Method no. 1 and 2

$$EI_{cr} = \frac{M_y}{\phi_y} = \frac{364}{0.023} = 15772 \text{ kNm}^2$$

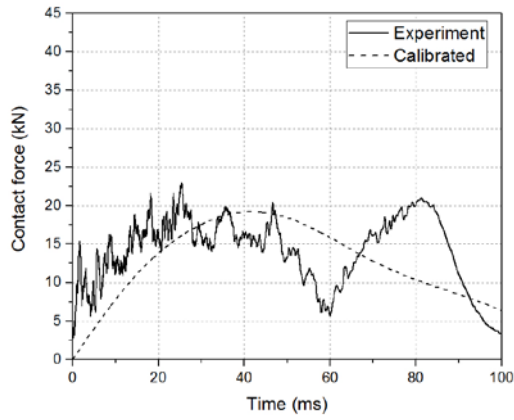
$$k_{cr} = \frac{3EI_{cr}}{h^3} = \frac{3(15772)}{1.5^3} = 14020 \text{ kN/m}$$

$$\Delta_{yi} = \frac{\phi_y h_i^2}{3} = \frac{0.023(1.25)^2}{3} \times 10^3 = 12 \text{ mm}$$

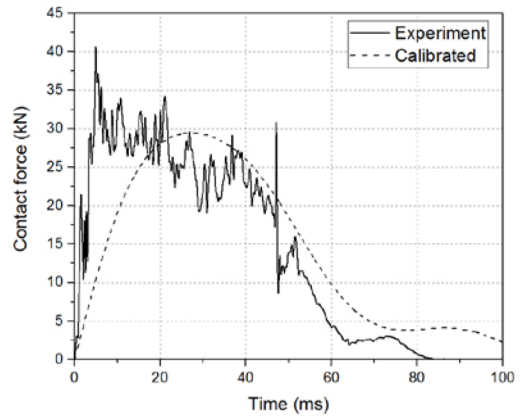
$$\Delta_y = \Delta_{yi} \left(\frac{3h - h_i}{2h_i} \right) = 12 \left(\frac{3(1.5) - 1.25}{2(1.25)} \right) = 15.6 \text{ mm}$$

Appendix E – Calibration of Contact Force

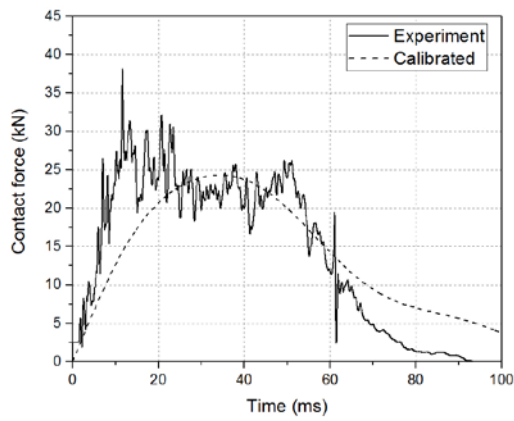
Test Series B - Calibration



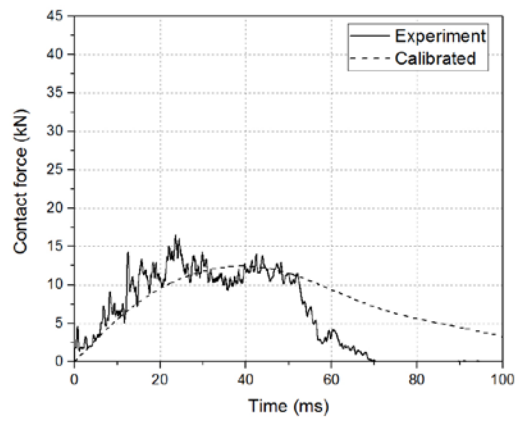
Test B1-1



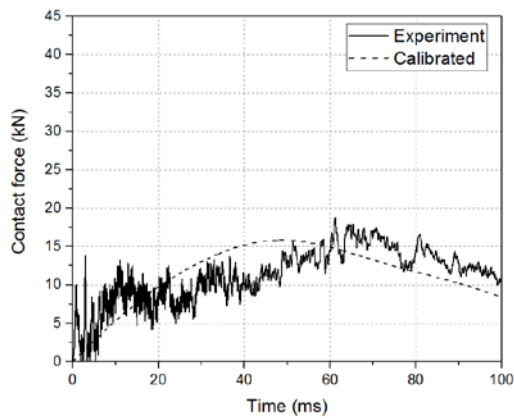
Test B1-2



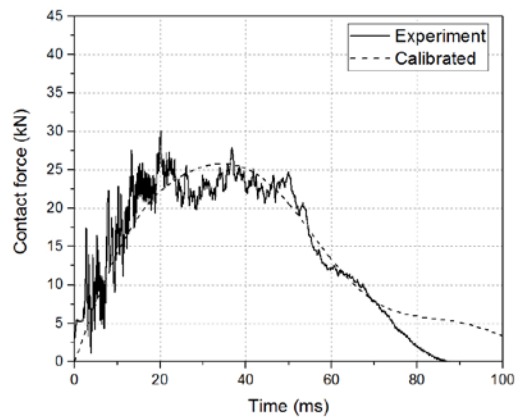
Test B1-3



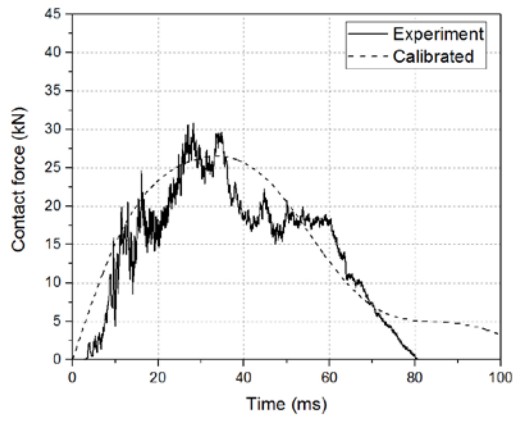
Test B1-4



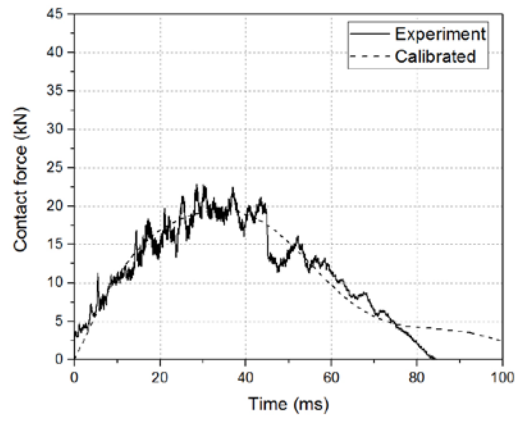
Test B2-1



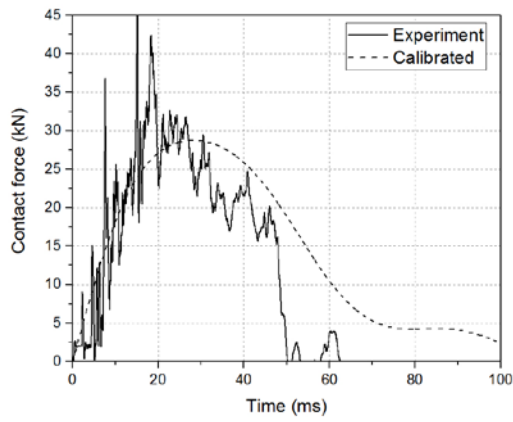
Test B2-2



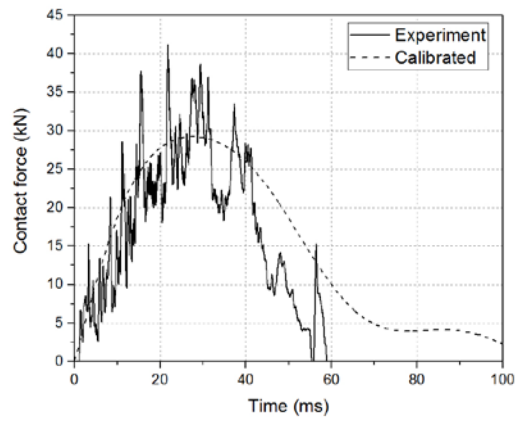
Test B2-3



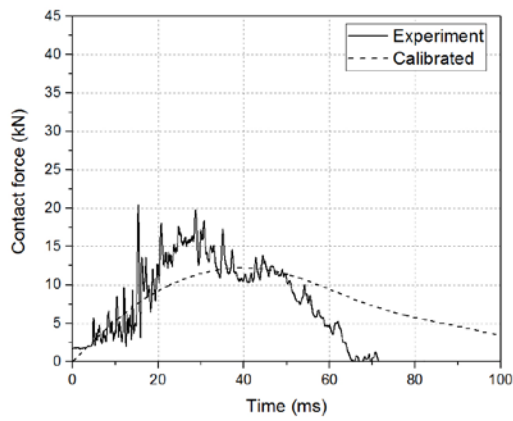
Test B2-4



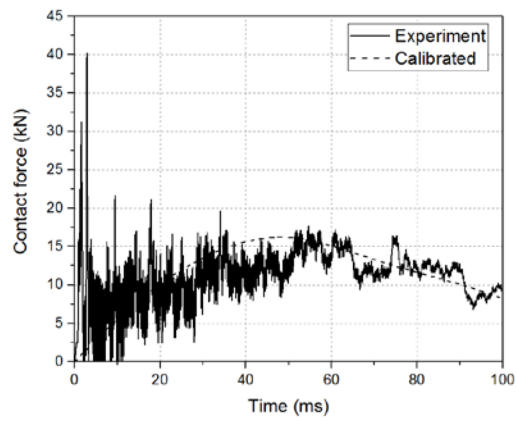
Test B3-2



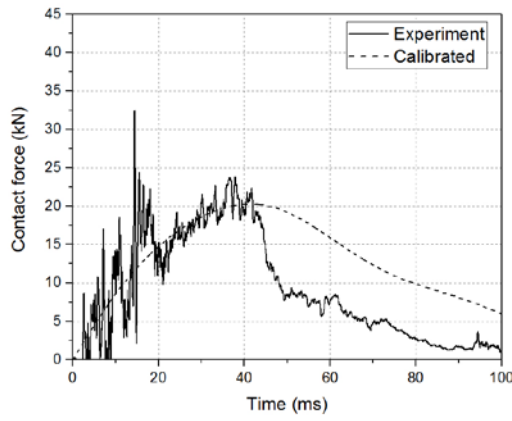
Test B3-3



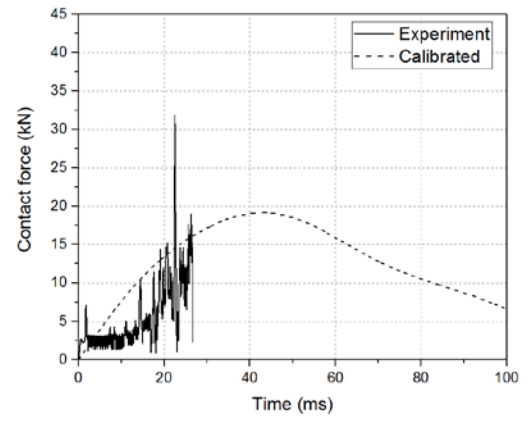
Test B3-4



Test B4-1

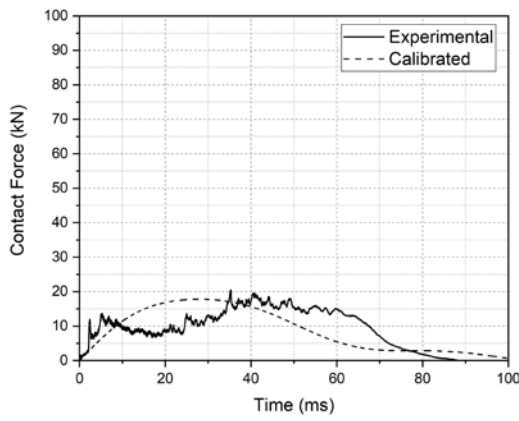


Test B4-2

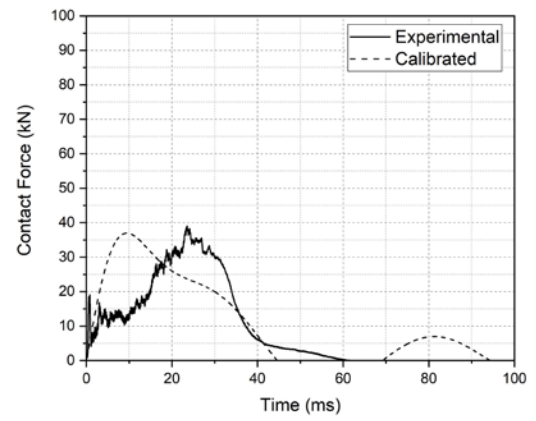


Test B4-3

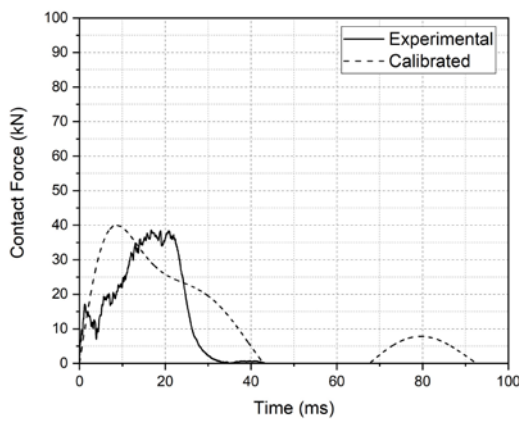
Test Series C - Calibration



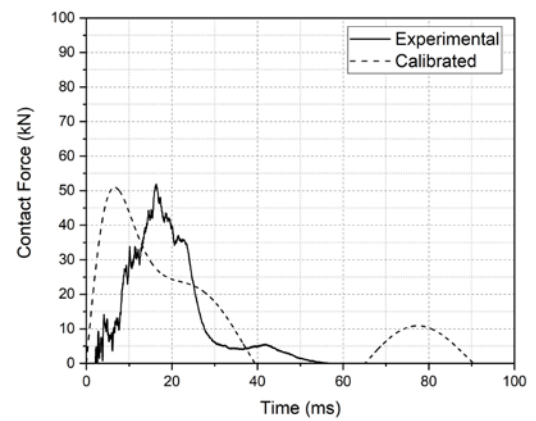
Test C1-1



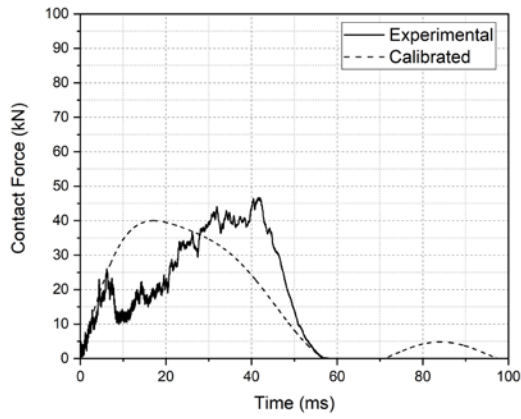
Test C1-2



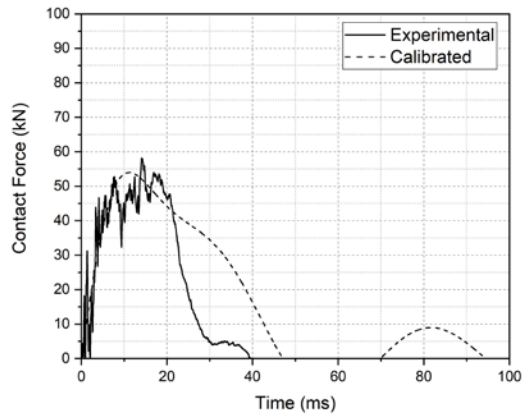
Test C1-3



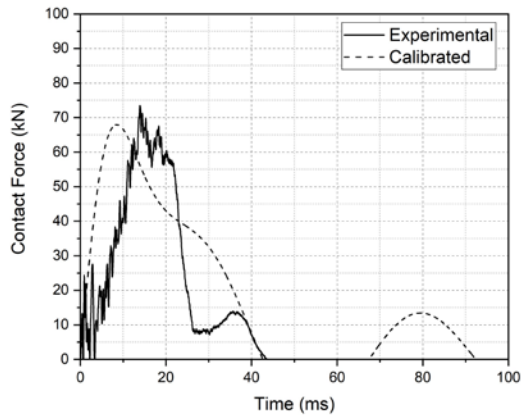
Test C1-4



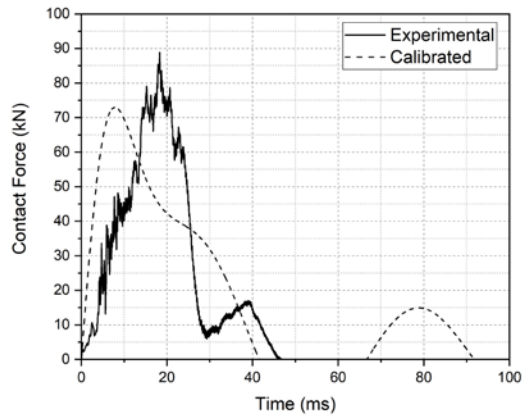
Test C2-1



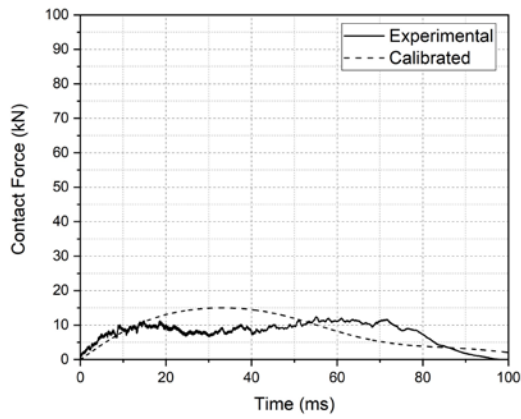
Test C2-2



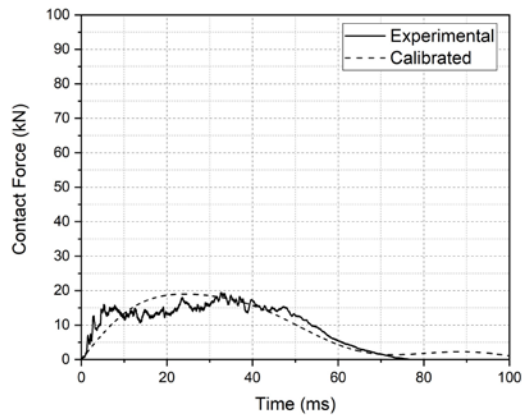
Test C2-3



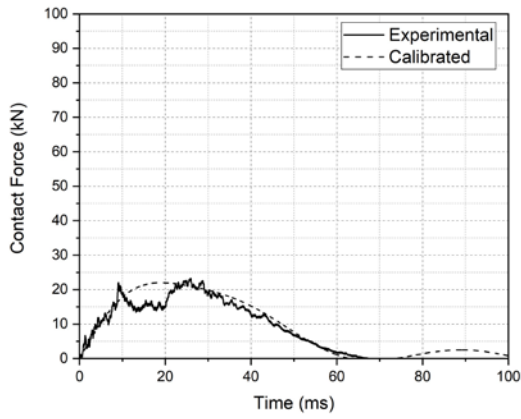
Test C2-4



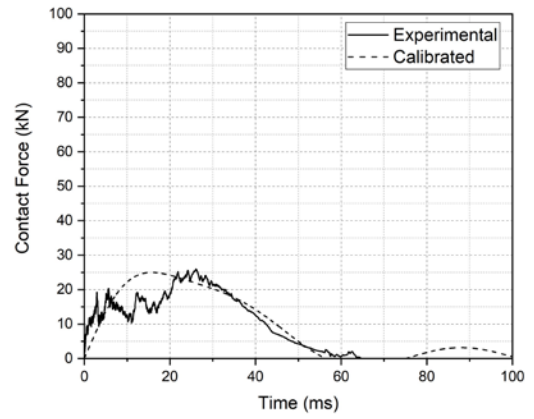
Test C3-1



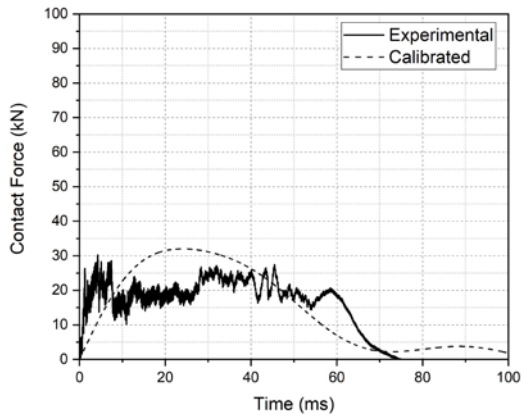
Test C3-2



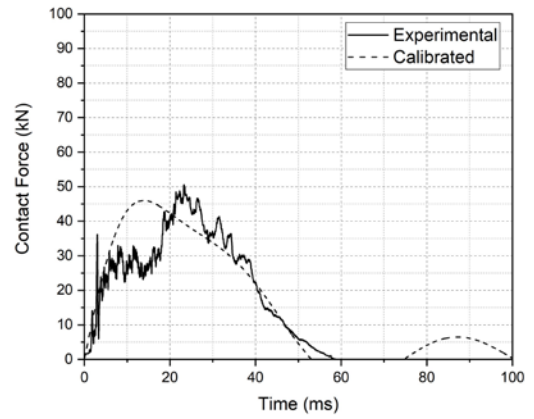
Test C3-3



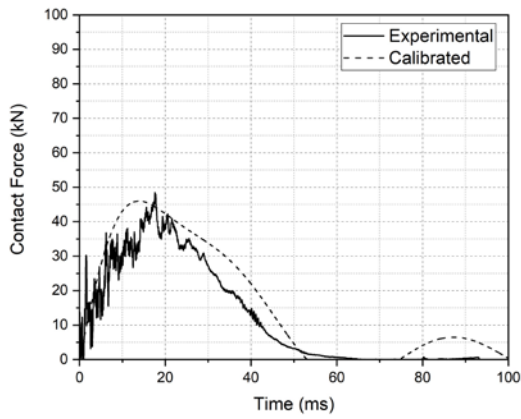
Test C3-4



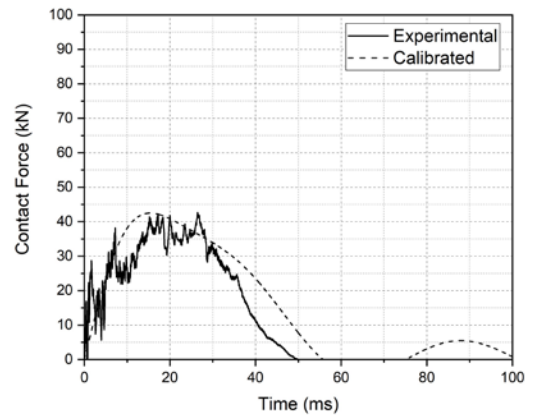
Test C4-1



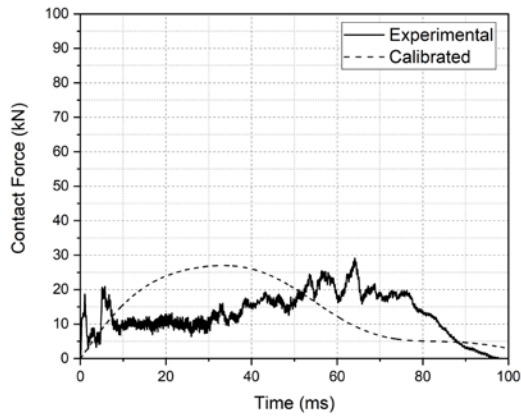
Test C4-2



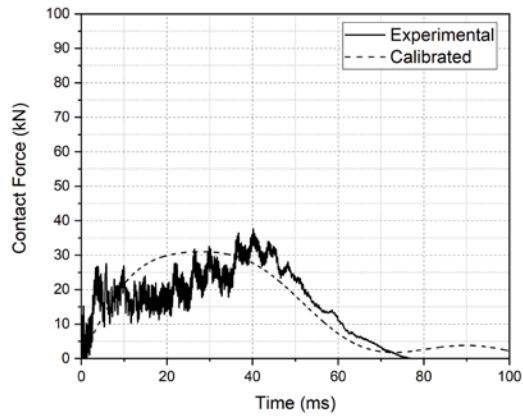
Test C4-3



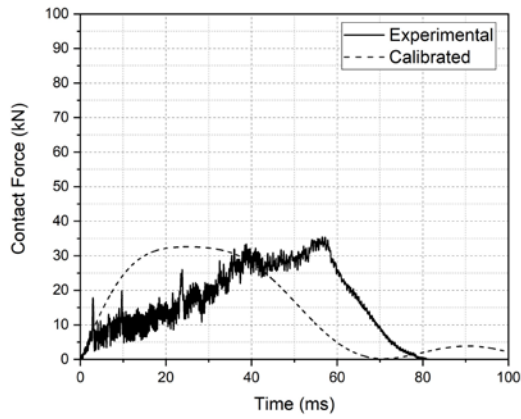
Test C4-4



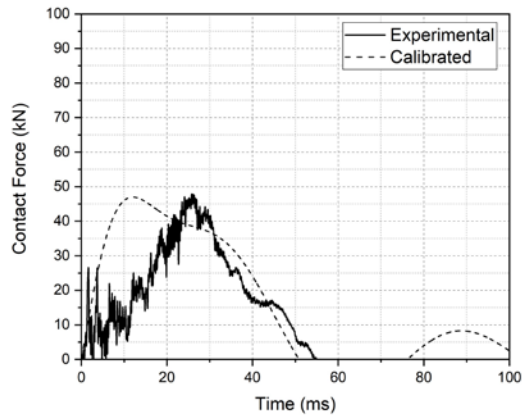
Test C5-1



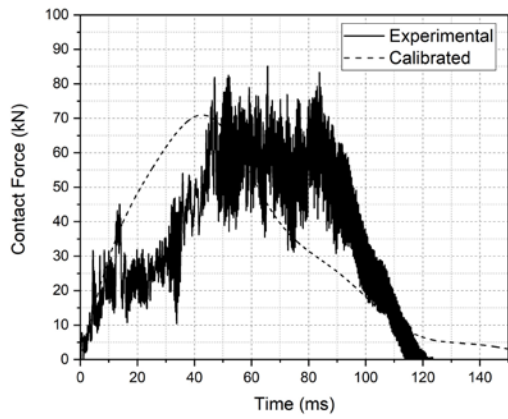
Test C5-2



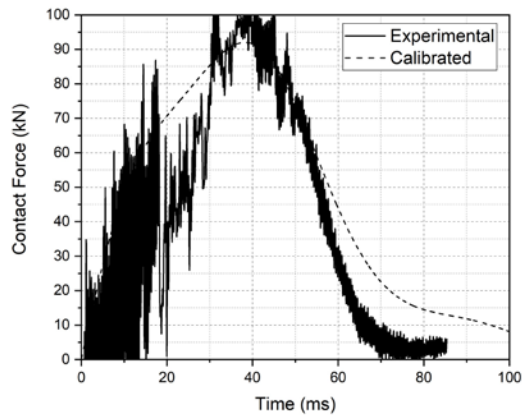
Test C5-3



Test C5-4

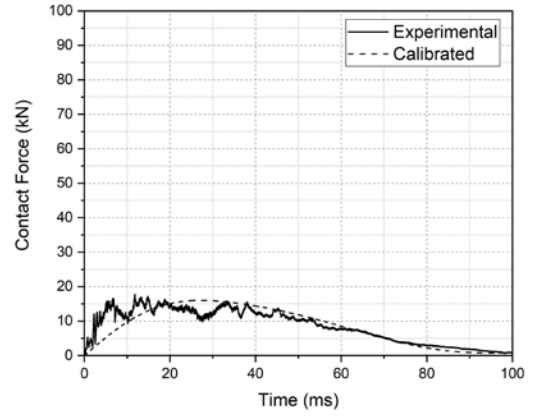


Test C6-1



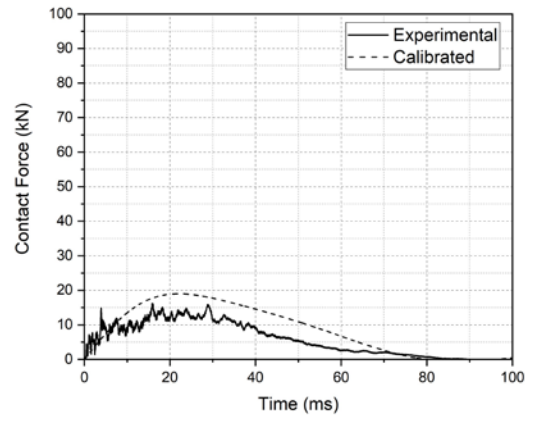
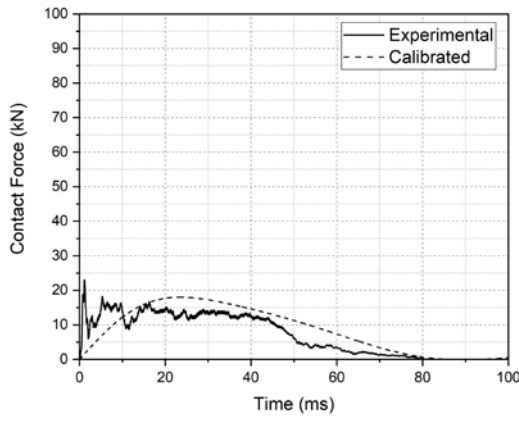
Test C6-2

Faulty Accelerometer



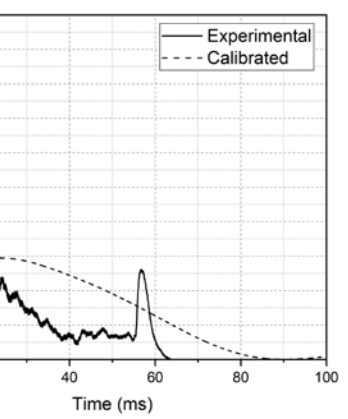
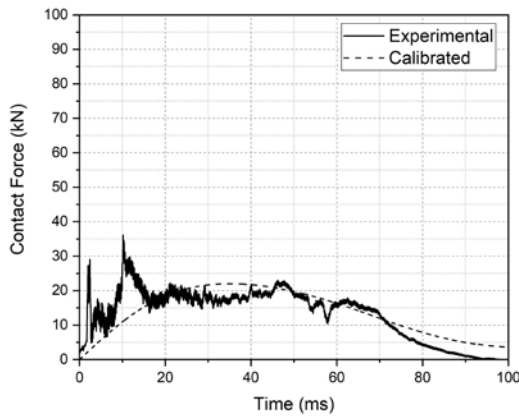
Test C7-2

Test C7-1



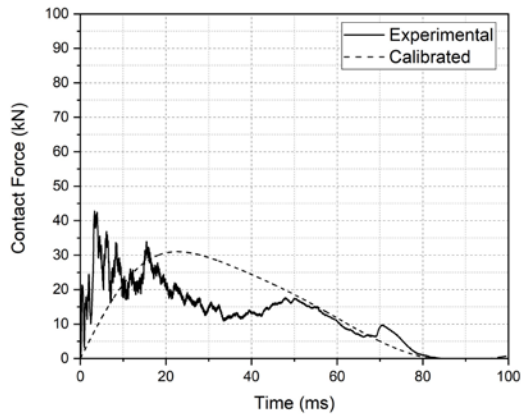
Test C7-4

Test C7-3

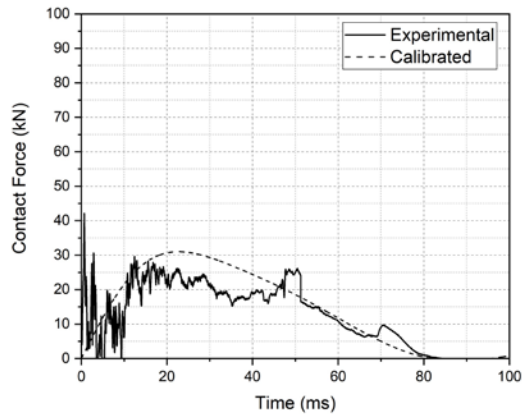


Test C8-2

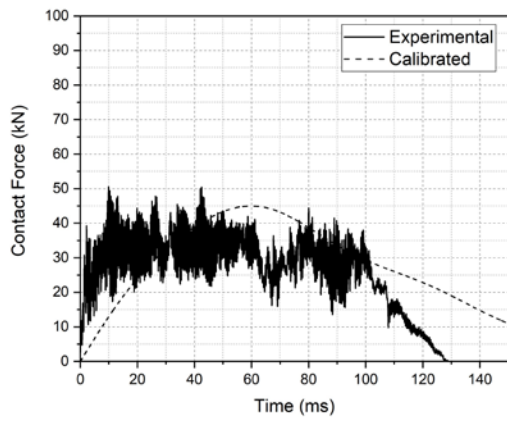
Test C8-1



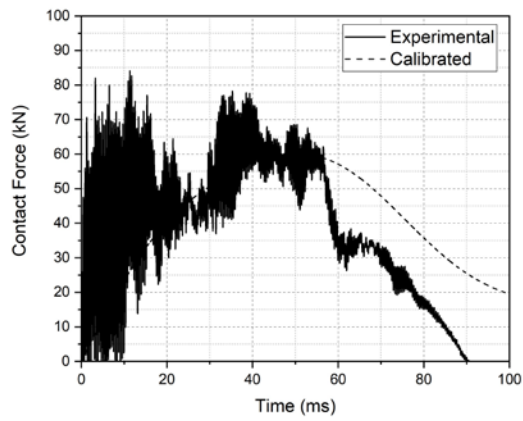
Test C8-3



Test C8-4



Test C9-1

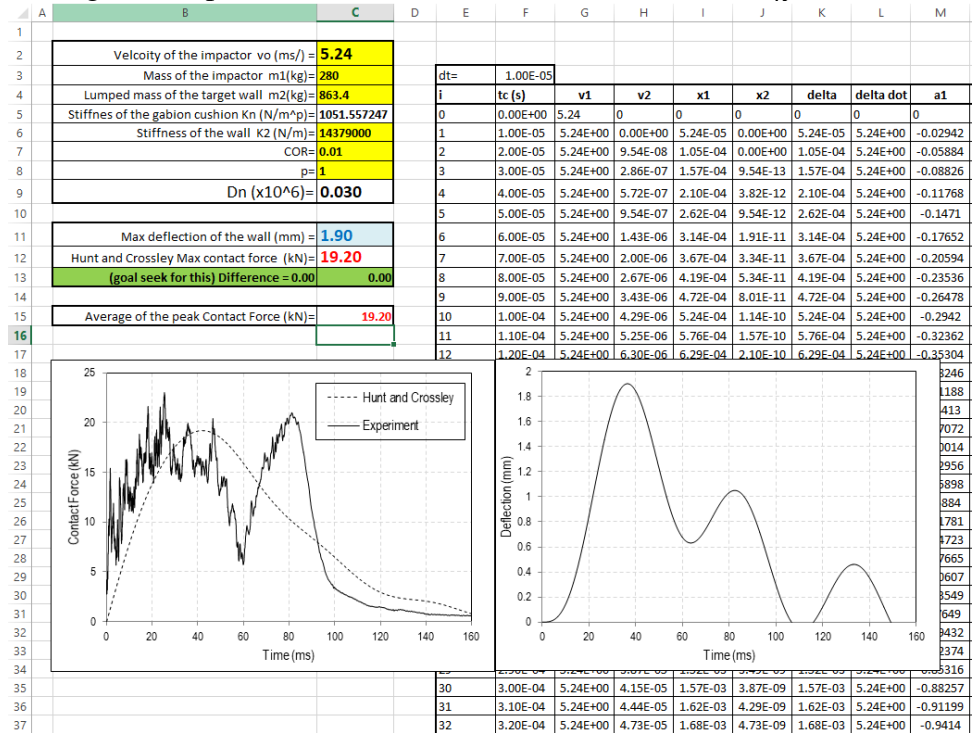


Test C9-2

Appendix F - Calibration of k_n with Experimental Contact Force Results

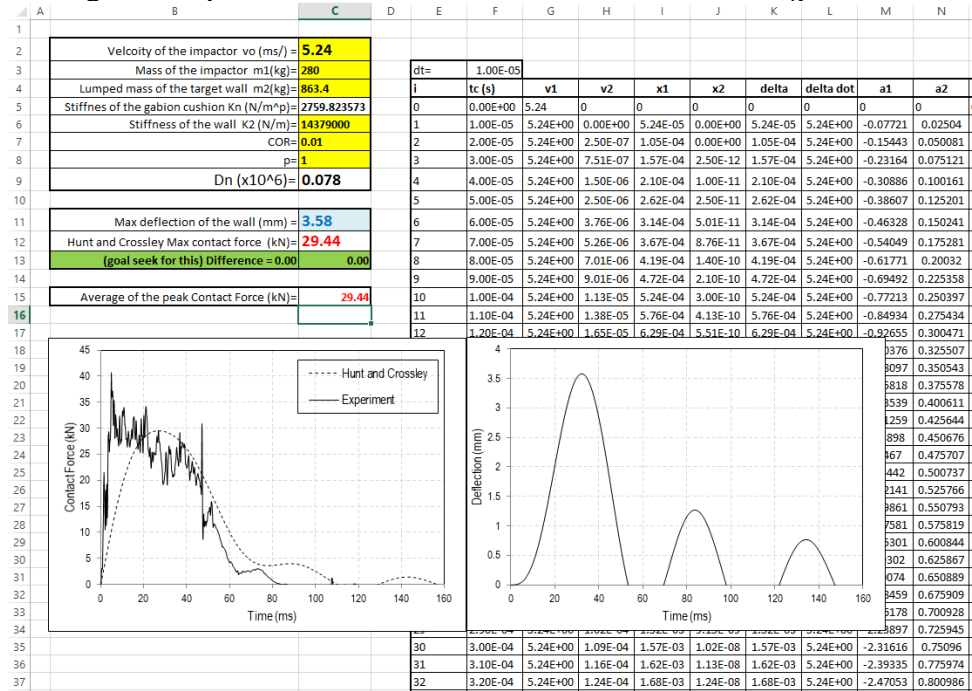
Test B1-1

Average of the peak contact forces = 19.2 kN , Calibrated $k_n = 1051.5$ N/m



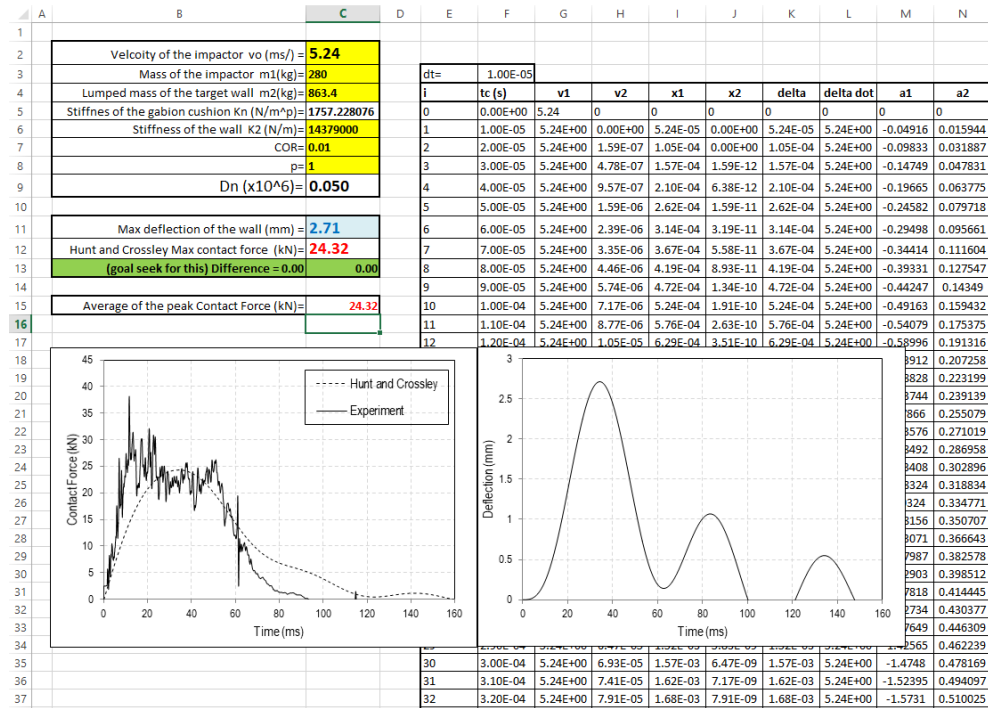
Test B1-2

Average of the peak contact forces = 29.44 kN , Calibrated $k_n = 2759.82$ N/m



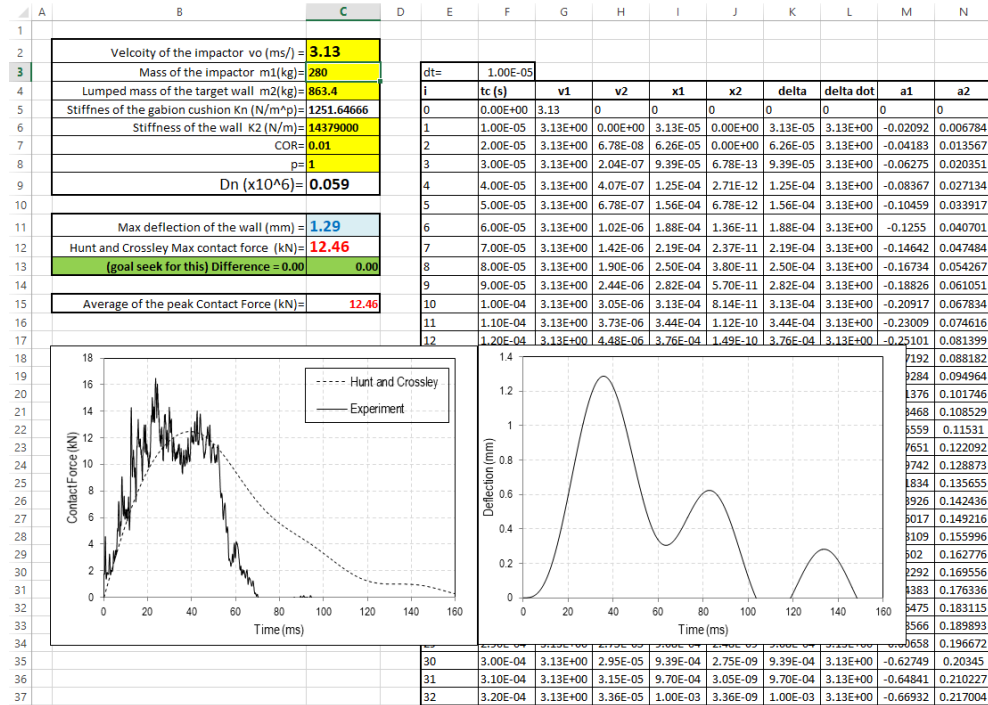
Test B1-3

Average of the peak contact forces = 24.32 kN, Calibrated $k_n = 1757.23 \text{ N/m}$



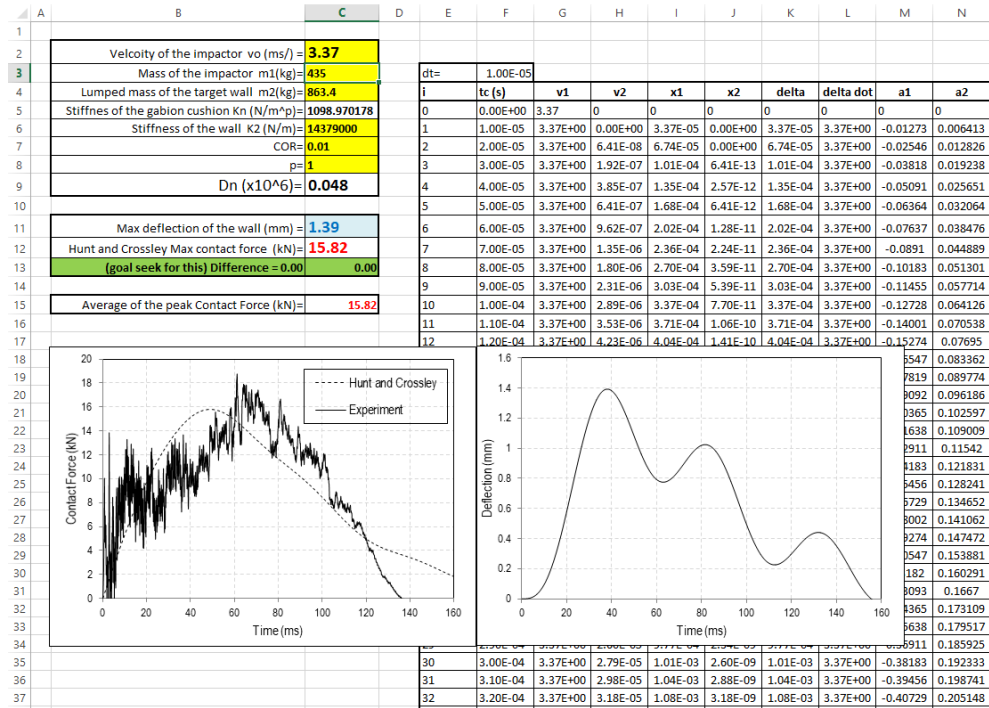
Test B1-4

Average of the peak contact forces = 12.46 kN, Calibrated $k_n = 1251.65 \text{ N/m}$



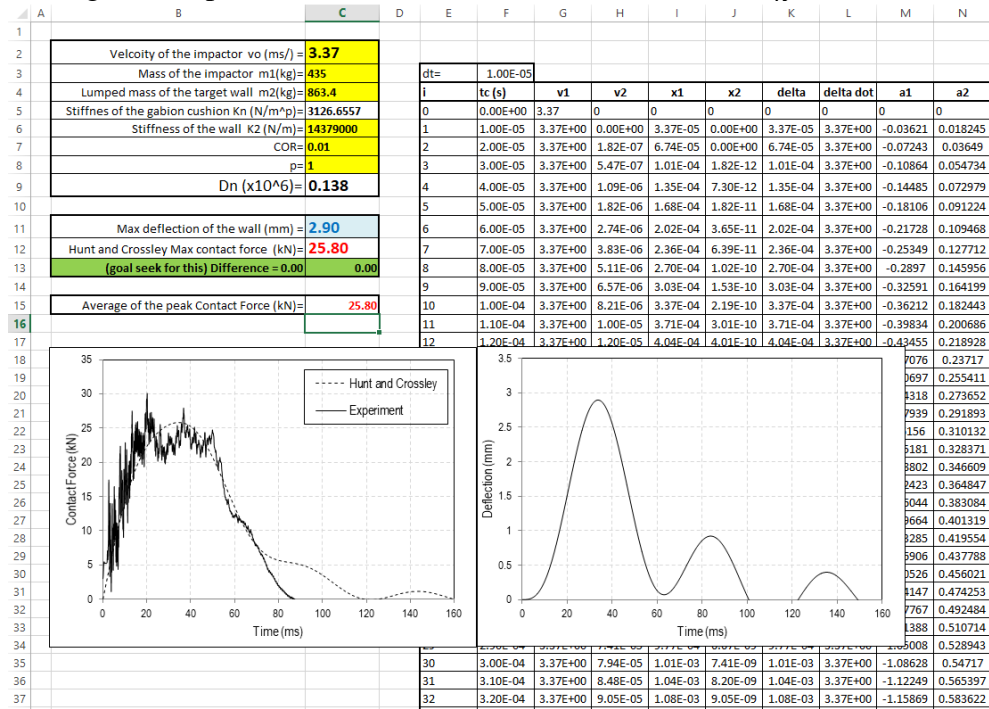
Test B2-1

Average of the peak contact forces = 15.82 kN , Calibrated $k_n = 1098.97 \text{ N/m}$



Test B2-2

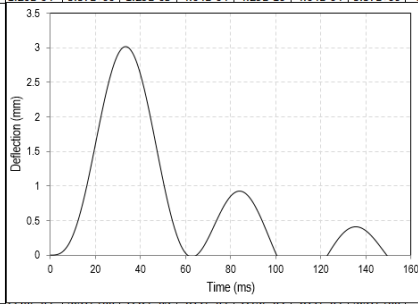
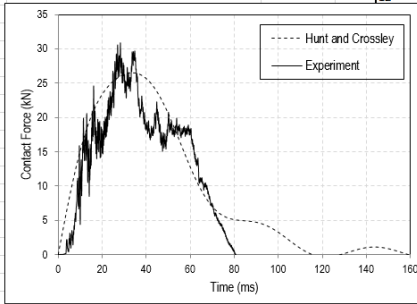
Average of the peak contact forces = 25.8 kN , Calibrated $k_n = 3126.66 \text{ N/m}$



Test B2-3

Average of the peak contact forces = 26.5 kN , Calibrated $k_n = 3344.4 \text{ N/m}$

	A	B	C	D	E	F	G	H	I	J	K	L	M	N	
1															
2		Velocity of the impactor v_0 (m/s) =	3.37			dt=	1.00E-05								
3		Mass of the impactor m_1 (kg)=	435			i	tc (s)	v1	v2	x1	x2	delta	delta dot	a1	a2
4		Lumped mass of the target wall m_2 (kg)=	863.4			0	0.00E+00	3.37	0	0	0	0	0	0	0
5		Stiffness of the gabion cushion K_n (N/m^p)=	3344.394842			1	1.00E-05	3.37E+00	0.00E+00	3.37E-05	0.00E+00	3.37E-05	3.37E+00	-0.03873	0.019515
6		Stiffness of the wall K_2 (N/m)	14379000			2	2.00E-05	3.37E+00	1.95E-07	6.74E-05	0.00E+00	6.74E-05	3.37E+00	-0.07747	0.039031
7		COR=	0.01			3	3.00E-05	3.37E+00	5.85E-07	1.01E-04	1.95E-12	1.01E-04	3.37E+00	-0.1162	0.058546
8		p=	1			4	4.00E-05	3.37E+00	1.17E-06	1.35E-04	7.81E-12	1.35E-04	3.37E+00	-0.15494	0.078061
9		D_n (x10^6)=	0.147			5	5.00E-05	3.37E+00	1.95E-06	1.68E-04	1.95E-11	1.68E-04	3.37E+00	-0.19367	0.097576
10						6	6.00E-05	3.37E+00	2.93E-06	2.02E-04	3.90E-11	2.02E-04	3.37E+00	-0.23241	0.117091
11		Max deflection of the wall (mm) =	3.02			7	7.00E-05	3.37E+00	4.10E-06	2.36E-04	6.83E-11	2.36E-04	3.37E+00	-0.27114	0.136606
12		Hunt and Crossley Max contact force (kN) =	26.50			8	8.00E-05	3.37E+00	5.46E-06	2.70E-04	1.09E-10	2.70E-04	3.37E+00	-0.30988	0.15612
13		[goal seek for this] Difference = 0.00	0.00			9	9.00E-05	3.37E+00	7.03E-06	3.03E-04	1.64E-10	3.03E-04	3.37E+00	-0.34861	0.175634
14						10	1.00E-04	3.37E+00	8.78E-06	3.37E-04	2.34E-10	3.37E-04	3.37E+00	-0.38734	0.195148
15		Average of the peak Contact Force (kN) =	26.50			11	1.10E-04	3.37E+00	1.07E-05	3.71E-04	3.22E-10	3.71E-04	3.37E+00	-0.42608	0.214661
16						12	1.20E-04	3.37E+00	1.29E-05	4.04E-04	4.29E-10	4.04E-04	3.37E+00	-0.46481	0.234174
17															
18															
19															
20															
21															
22															
23															
24															
25															
26															
27															
28															
29															
30															
31															
32															
33															
34															
35															
36															
37															
38															
39															
40															
41															
42															
43															
44															
45															
46															
47															
48															
49															
50															
51															
52															
53															
54															
55															
56															
57															
58															
59															
60															
61															
62															
63															
64															
65															
66															
67															
68															
69															
70															
71															
72															
73															
74															
75															
76															
77															
78															
79															
80															
81															
82															
83															
84															
85															
86															
87															
88															
89															
90															
91															
92															
93															
94															
95															
96															
97															
98															
99															
100															



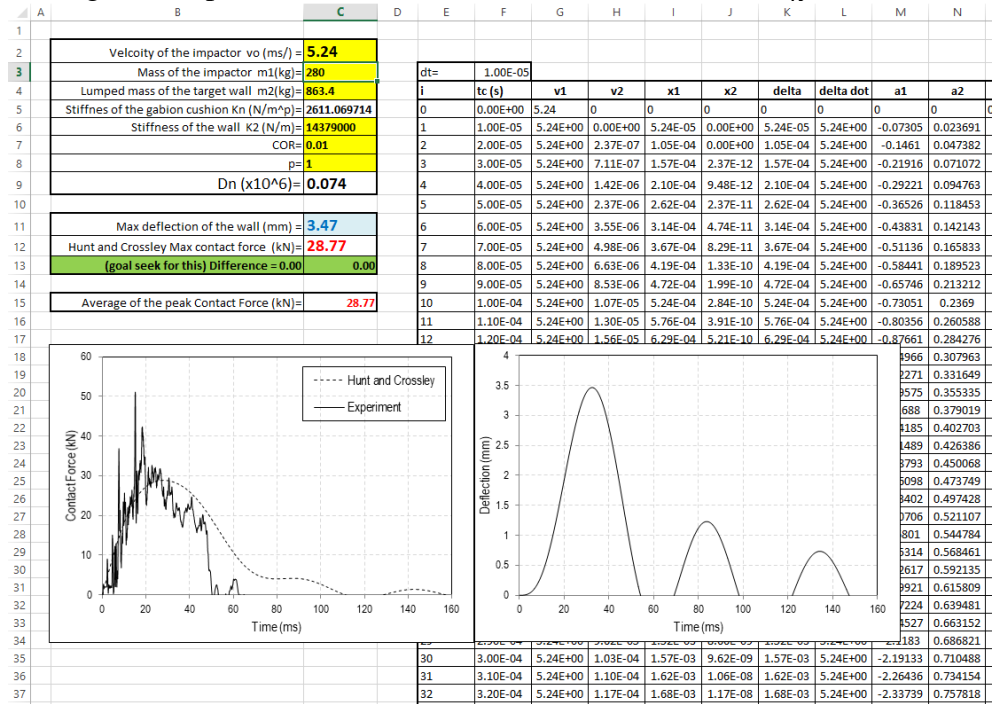
Test 2-4

Average of the peak contact forces = 19.46 kN , Calibrated $k_n = 3227.27 \text{ N/m}$

	A	B	C	D	E	F	G	H	I	J	K	L	M	N	
1															
2		Velocity of the impactor v_0 (m/s) =	2.51			dt=	1.00E-05								
3		Mass of the impactor m_1 (kg)=	435			i	tc (s)	v1	v2	x1	x2	delta	delta dot	a1	a2
4		Lumped mass of the target wall m_2 (kg)=	863.4			0	0.00E+00	2.51	0	0	0	0	0	0	0
5		Stiffness of the gabion cushion K_n (N/m^p)=	3227.268997			1	1.00E-05	2.51E+00	0.00E+00	2.51E-05	0.00E+00	2.51E-05	2.51E+00	-0.02784	0.014026
6		Stiffness of the wall K_2 (N/m)	14379000			2	2.00E-05	2.51E+00	1.40E-07	5.02E-05	0.00E+00	5.02E-05	2.51E+00	-0.05568	0.028052
7		COR=	0.01			3	3.00E-05	2.51E+00	4.21E-07	7.53E-05	1.40E-12	7.53E-05	2.51E+00	-0.08352	0.042078
8		p=	1			4	4.00E-05	2.51E+00	8.42E-07	1.00E-04	5.61E-12	1.00E-04	2.51E+00	-0.11336	0.056104
9		D_n (x10^6)=	0.191			5	5.00E-05	2.51E+00							

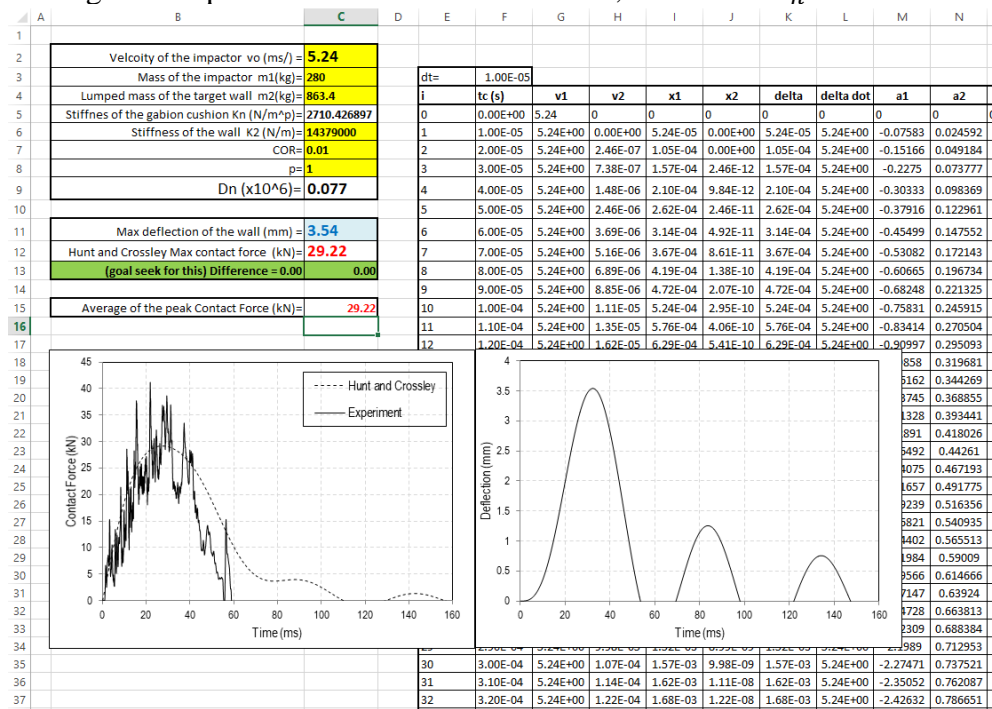
Test B3-2

Average of the peak contact forces = 28.77 kN , Calibrated $k_n = 2611.07 \text{ N/m}$



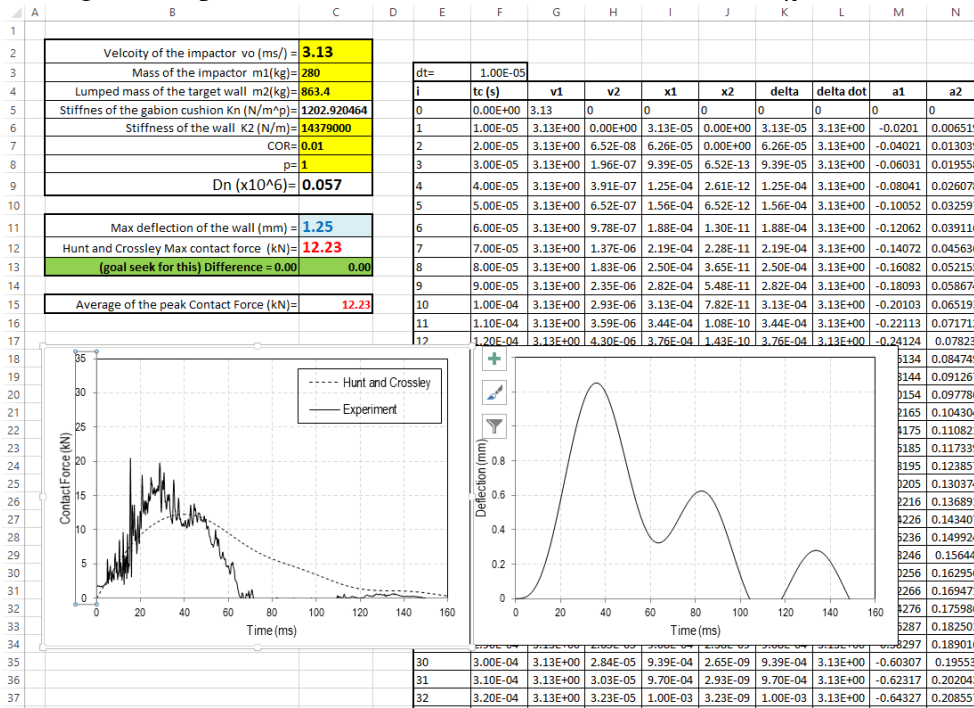
Test B3-3

Average of the peak contact forces = 29.22 kN , Calibrated $k_n = 2710.43 \text{ N/m}$



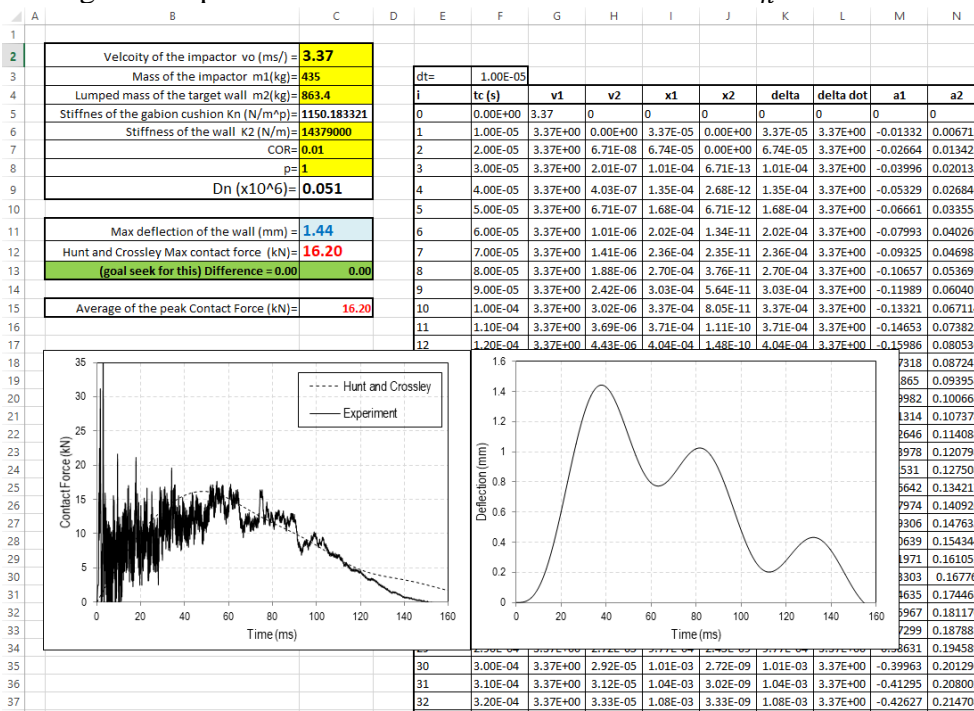
Test B3-4

Average of the peak contact forces = 12.23 kN , Calibrated $k_n = 1202.92 \text{ N/m}$



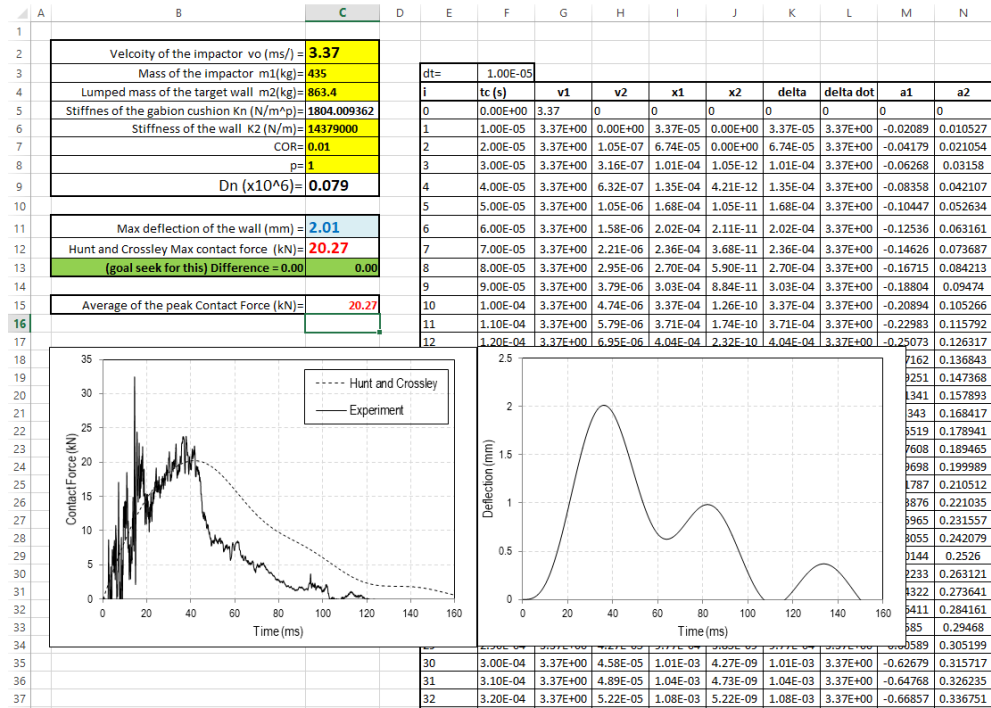
Test B4-1

Average of the peak contact forces = 16.2 kN Calibrated $k_n = 1150.18 \text{ N/m}$



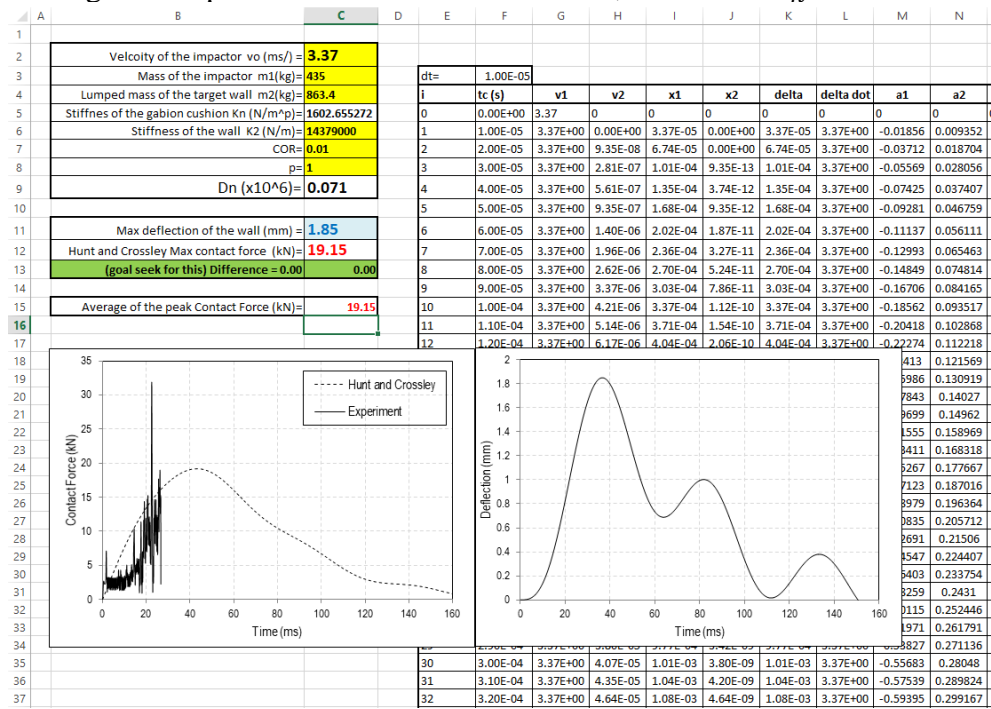
Test B4-2

Average of the peak contact forces = 20.27 kN , Calibrated $k_n = 1804.01$ N/m



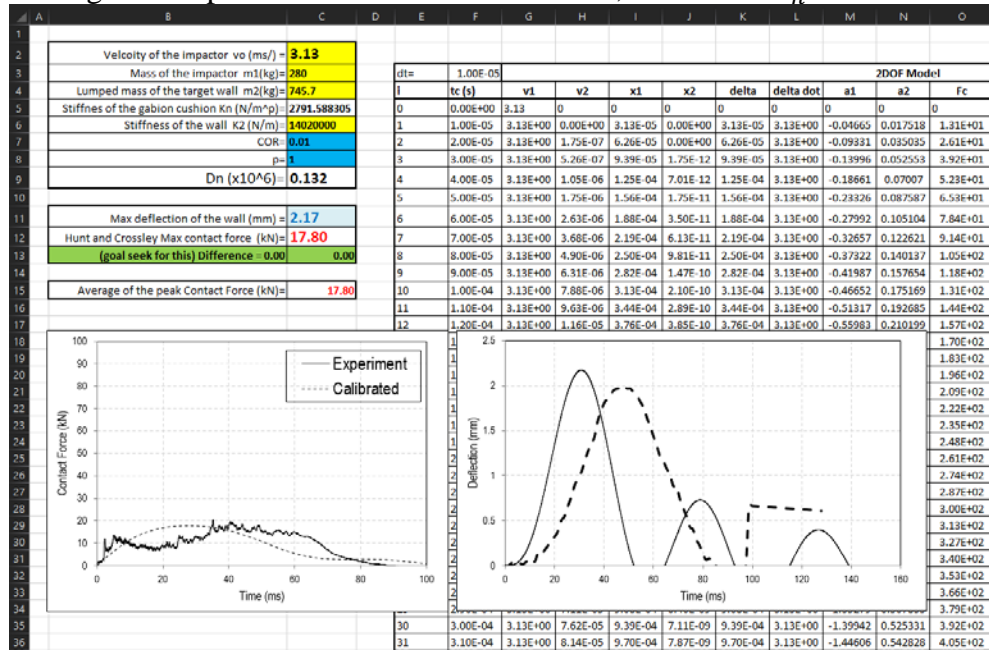
Test B4-3

Average of the peak contact forces = 19.15 kN , Calibrated $k_n = 1602.65$ N/m



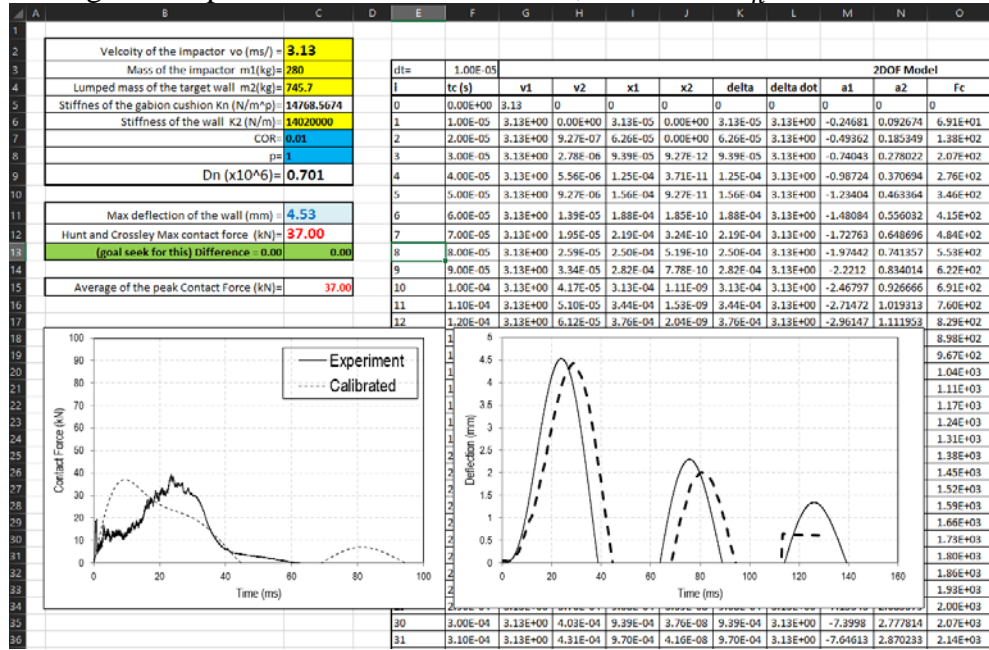
Test C1-1

Average of the peak contact forces = 17.80 kN , Calibrated $k_n = 2791.6$ N/m



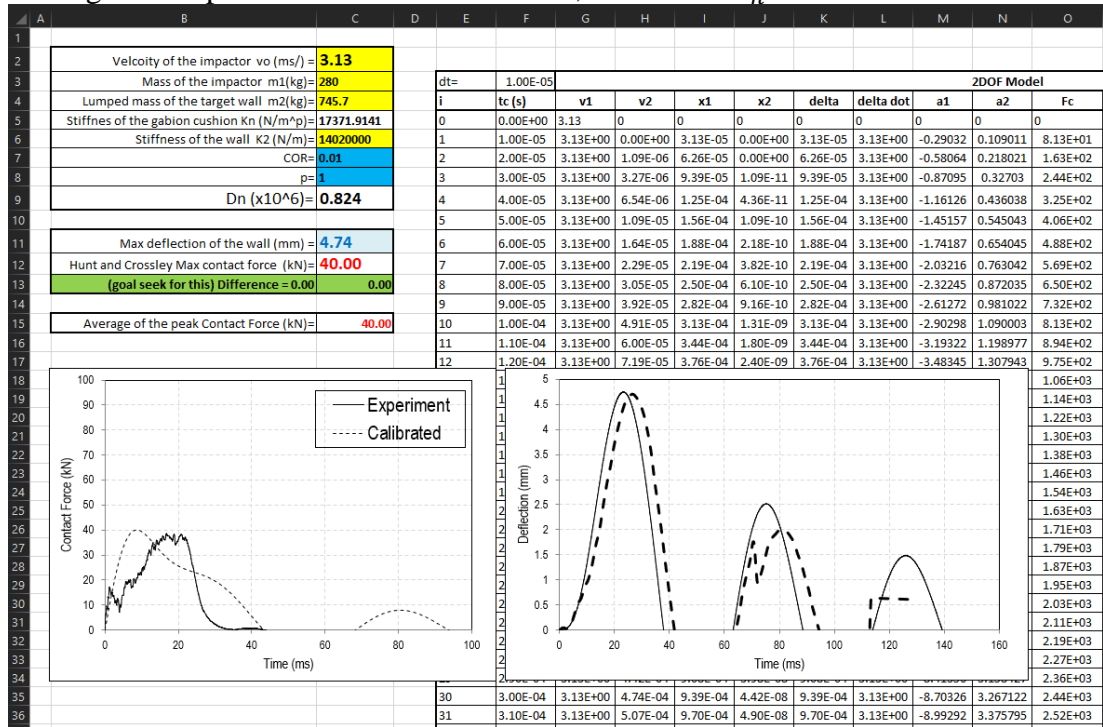
Test C1-2

Average of the peak contact forces = 37 kN , Calibrated $k_n = 14768.6$ N/m



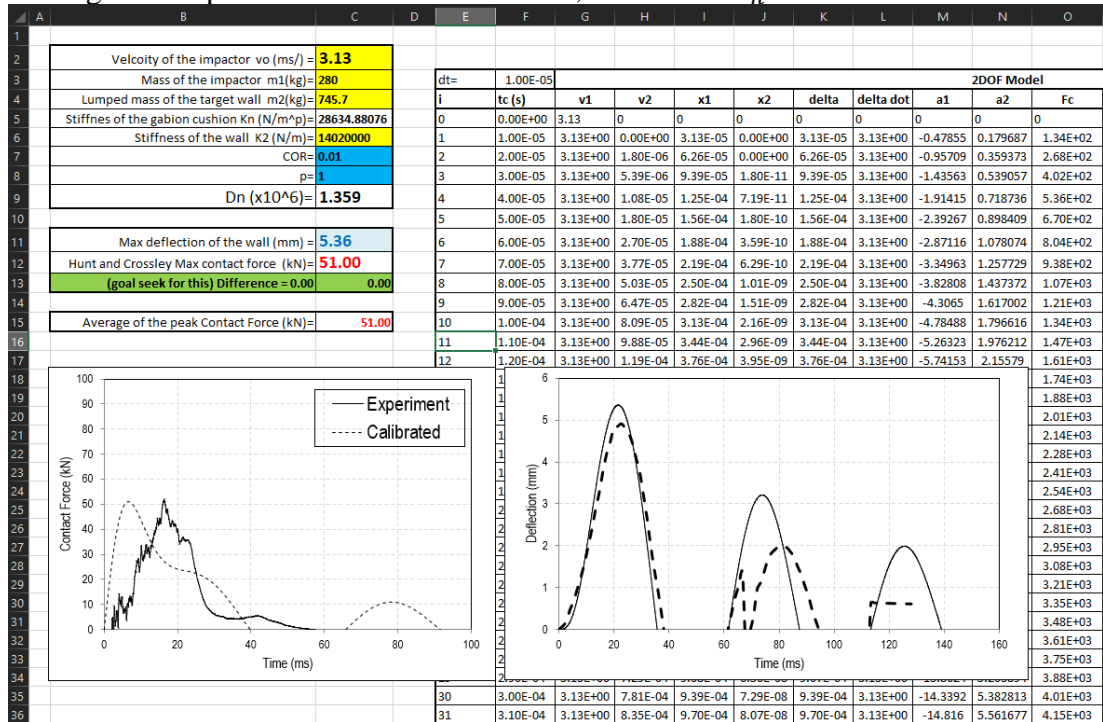
Test C1-3

Average of the peak contact forces = 40 kN , Calibrated $k_n = 17371.9$ N/m



Test C1-4

Average of the peak contact forces = 51 kN , Calibrated $k_n = 28634.9$ N/m



Test C2-3

Average of the peak contact forces = 68 kN , Calibrated $k_n = 17933.4$ N/m

	A	B	C	D	E	F	G	H	I	J	K	L	M	N
1														
2			Velocity of the impactor v_0 (m/s) = 5.24											
3			Mass of the impactor m_1 (kg) = 280											
4			Lumped mass of the target wall m_2 (kg) = 745.7											
5			Stiffnes of the gabion cushion K_n (N/m ²) = 17933.38287											
6			Stiffness of the wall K_2 (N/m) = 14020000											
7			COR = 0.01											
8			$p = 1$											
9			D_n (x10 ⁶) = 0.508											
10														
11			Max deflection of the wall (mm) = 8.01											
12			Hunt and Crossley Max contact force (kN) = 68.00											
13			(goal seek for this) Difference = 0.00 0.00											
14														
15			Average of the peak Contact Force (kN) = 68.00											
16														
17														
18														
19														
20														
21														
22														
23														
24														
25														
26														
27														
28														
29														
30														
31														
32														
33														
34														
35														
36														

		dt = 1.00E-05		2DOF Mod							
i	tc (s)	v1	v2	x1	x2	delta	delta dot	a1	a2		
0	0.00E+00	5.24	0	0	0	0	0	0	0		
1	1.00E-05	5.24E+00	0.00E+00	5.24E-05	0.00E+00	5.24E-05	5.24E+00	-0.50174	0.188396		
2	2.00E-05	5.24E+00	1.88E-06	1.05E-04	0.00E+00	1.05E-04	5.24E+00	-1.00347	0.376791		
3	3.00E-05	5.24E+00	5.65E-06	1.57E-04	1.88E-11	1.57E-04	5.24E+00	-1.50521	0.565184		
4	4.00E-05	5.24E+00	1.13E-05	2.10E-04	7.54E-11	2.10E-04	5.24E+00	-2.00693	0.753574		
5	5.00E-05	5.24E+00	1.88E-05	2.62E-04	1.88E-10	2.62E-04	5.24E+00	-2.50865	0.941959		
6	6.00E-05	5.24E+00	2.83E-05	3.14E-04	3.77E-10	3.14E-04	5.24E+00	-3.01035	1.130339		
7	7.00E-05	5.24E+00	3.96E-05	3.67E-04	6.59E-10	3.67E-04	5.24E+00	-3.51204	1.318711		
8	8.00E-05	5.24E+00	5.27E-05	4.19E-04	1.06E-09	4.19E-04	5.24E+00	-4.01372	1.507075		
9	9.00E-05	5.24E+00	6.78E-05	4.72E-04	1.58E-09	4.72E-04	5.24E+00	-4.51537	1.695429		
10	1.00E-04	5.24E+00	8.48E-05	5.24E-04	2.26E-09	5.24E-04	5.24E+00	-5.017	1.883772		
11	1.10E-04	5.24E+00	1.04E-04	5.76E-04	3.11E-09	5.76E-04	5.24E+00	-5.51861	2.072102		
12	1.20E-04	5.24E+00	1.24E-04	6.29E-04	4.14E-09	6.29E-04	5.24E+00	-6.02019	2.260418		
										1173	2.44872
										1325	2.637004
										1473	2.825271
										1617	3.013518
										1757	3.201744
										1893	3.389949
										2024	3.578131
										2151	3.766287
										2277	3.954418
										2399	4.142522
										2515	4.330597
										2626	4.518641
										2731	4.706655
										2831	4.894636
										2926	5.082583
										3016	5.270494
										3103	5.458369
30	3.00E-04	5.24E+00	8.19E-04	1.57E-03	7.65E-08	1.57E-03	5.24E+00	-15.0409	5.646206		
31	3.10E-04	5.24E+00	8.76E-04	1.62E-03	8.47E-08	1.62E-03	5.24E+00	-15.5414	5.834004		

Test C2-4

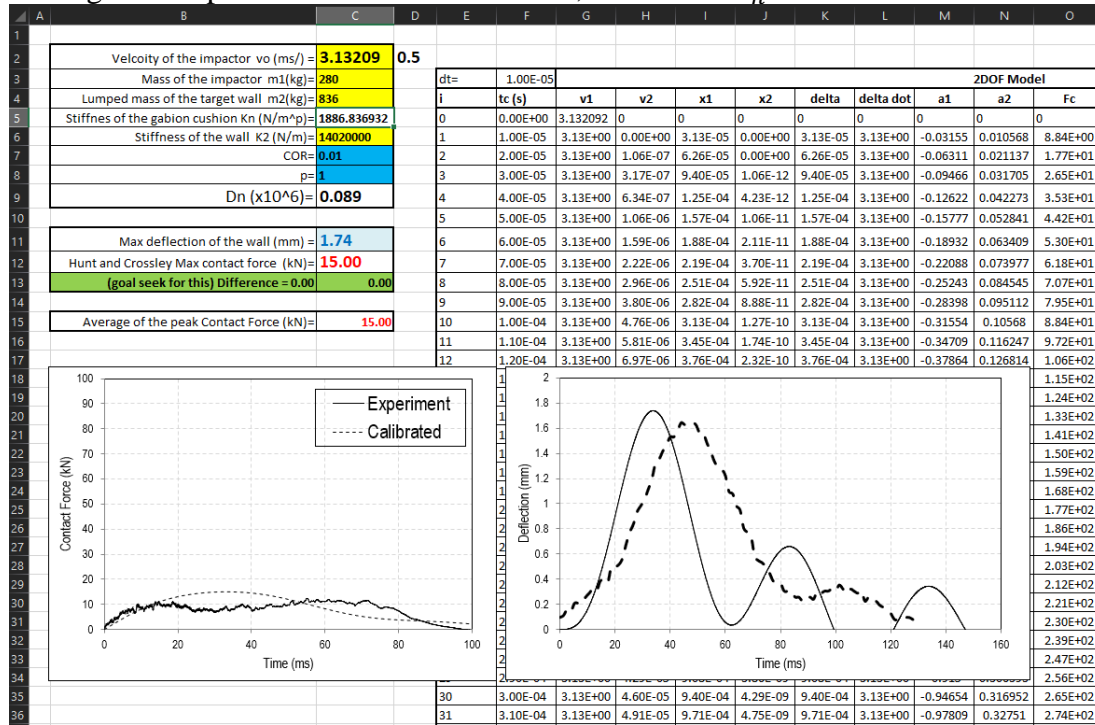
Average of the peak contact forces = 73 kN , Calibrated $k_n = 20765.4$ N/m

	A	B	C	D	E	F	G	H	I	J	K	L	M	N	O
1															
2			Velocity of the impactor v_0 (m/s) = 5.24												
3			Mass of the impactor m_1 (kg) = 280												
4			Lumped mass of the target wall m_2 (kg) = 745.7												
5			Stiffnes of the gabion cushion K_n (N/m ²) = 20765.43997												
6			Stiffness of the wall K_2 (N/m) = 14020000												
7			COR = 0.01												
8			$p = 1$												
9			D_n (x10 ⁶) = 0.588												
10															
11			Max deflection of the wall (mm) = 8.33												
12			Hunt and Crossley Max contact force (kN) = 73.00												
13			(goal seek for this) Difference = 0.00 0.00												
14															
15			Average of the peak Contact Force (kN) = 73.00												
16															
17															
18															
19															
20															
21															
22															
23															
24															
25															
26															
27															
28															
29															
30															
31															
32															
33															
34															
35															
36															

		dt = 1.00E-05		2DOF Model								
i	tc (s)	v1	v2	x1	x2	delta	delta dot	a1	a2	F_c		
0	0.00E+00	5.24	0	0	0	0	0	0	0			
1	1.00E-05	5.24E+00	0.00E+00	5.24E-05	0.00E+00	5.24E-05	5.24E+00	-0.58097	0.218147	1.63E+02		
2	2.00E-05	5.24E+00	2.18E-06	1.05E-04	0.00E+00	1.05E-04	5.24E+00	-1.16194	0.436294	3.25E+02		
3	3.00E-05	5.24E+00	6.54E-06	1.57E-04	2.18E-11	1.57E-04	5.24E+00	-1.74291	0.654438	4.88E+02		
4	4.00E-05	5.24E+00	1.31E-05	2.10E-04	8.73E-11	2.10E-04	5.24E+00	-2.32387	0.872578	6.51E+02		
5	5.00E-05	5.24E+00	2.18E-05	2.62E-04	2.18E-10	2.62E-04	5.24E+00	-2.90481	1.090712	8.13E+02		
6	6.00E-05	5.24E+00	3.27E-05	3.14E-04	4.36E-10	3.14E-04	5.24E+00	-3.48574	1.308838	9.76E+02		
7	7.00E-05	5.24E+00	4.58E-05	3.67E-04	7.64E-10	3.67E-04	5.24E+00	-4.06665	1.526955	1.14E+03		
8	8.00E-05	5.24E+00	6.11E-05	4.19E-04	1.22E-09	4.19E-04	5.24E+00	-4.64753	1.745061	1.30E+03		
9	9.00E-05	5.24E+00	7.85E-05	4.72E-04	1.83E-09	4.72E-04	5.24E+00	-5.22839	1.963155	1.46E+03		

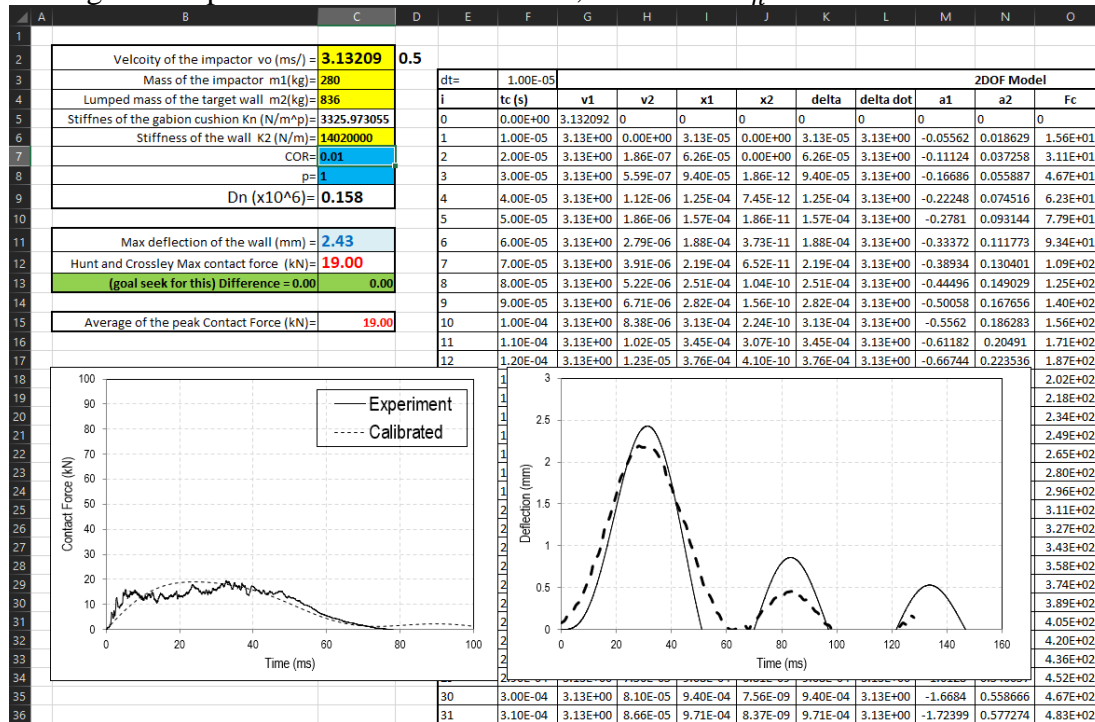
Test C3-1

Average of the peak contact forces = 15 kN , Calibrated $k_n = 1886.8$ N/m



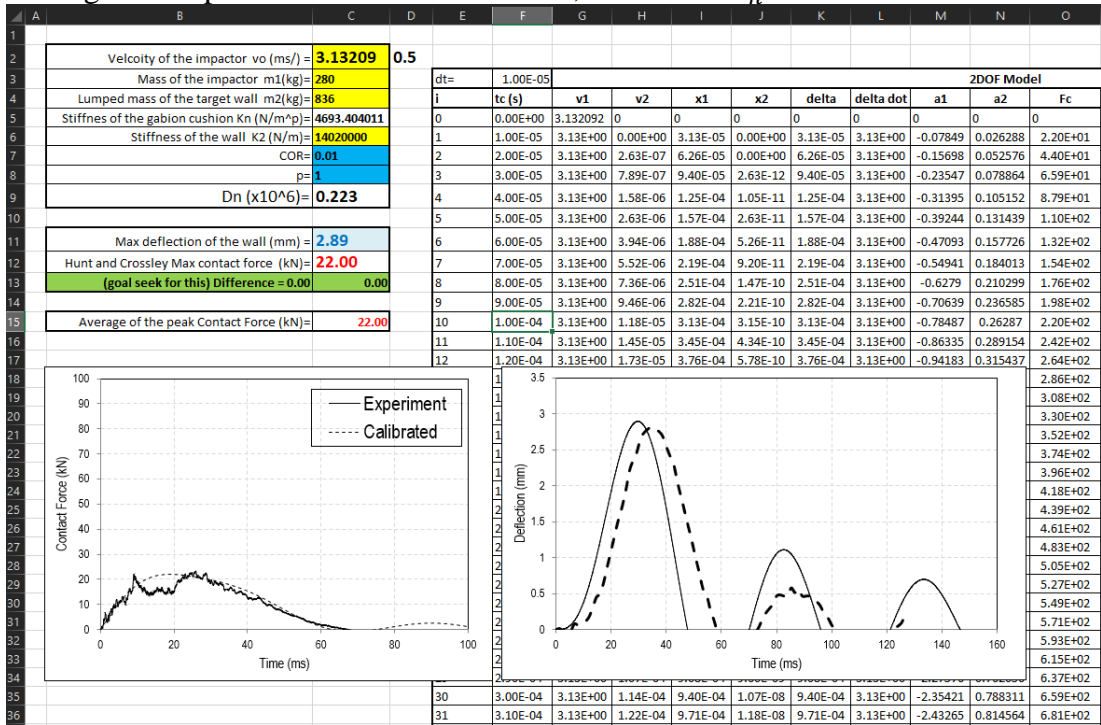
Test C3-2

Average of the peak contact forces = 19 kN , Calibrated $k_n = 3326$ N/m



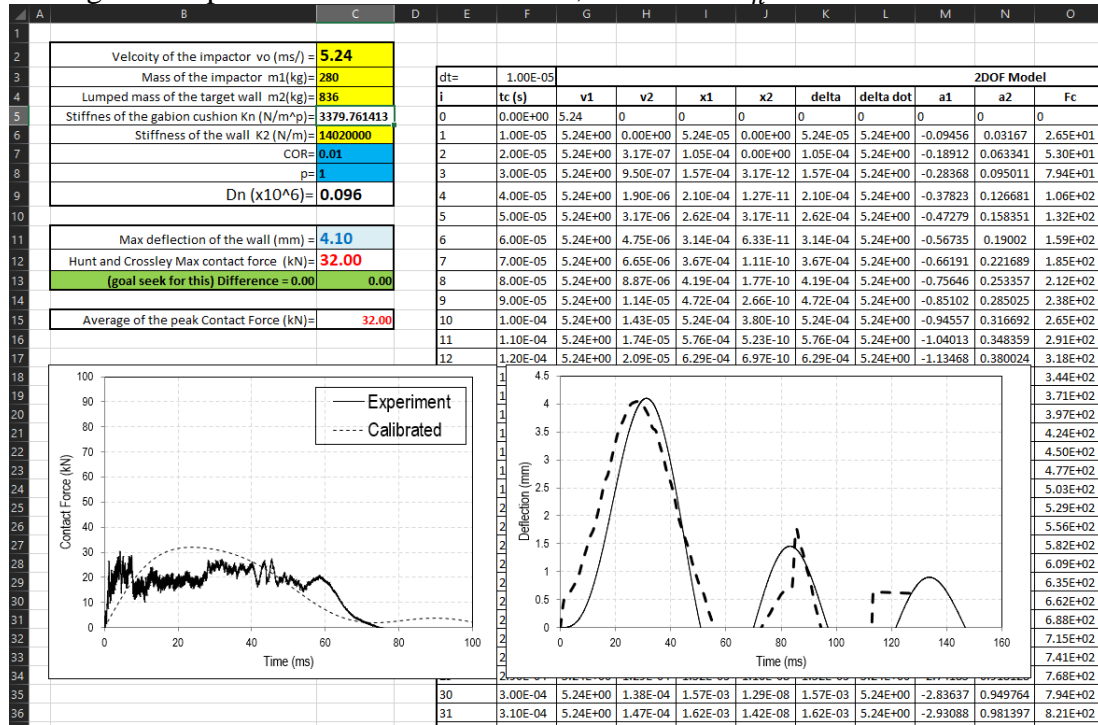
Test C3-3

Average of the peak contact forces = 22 kN , Calibrated $k_n = 4693.4 \text{ N/m}$



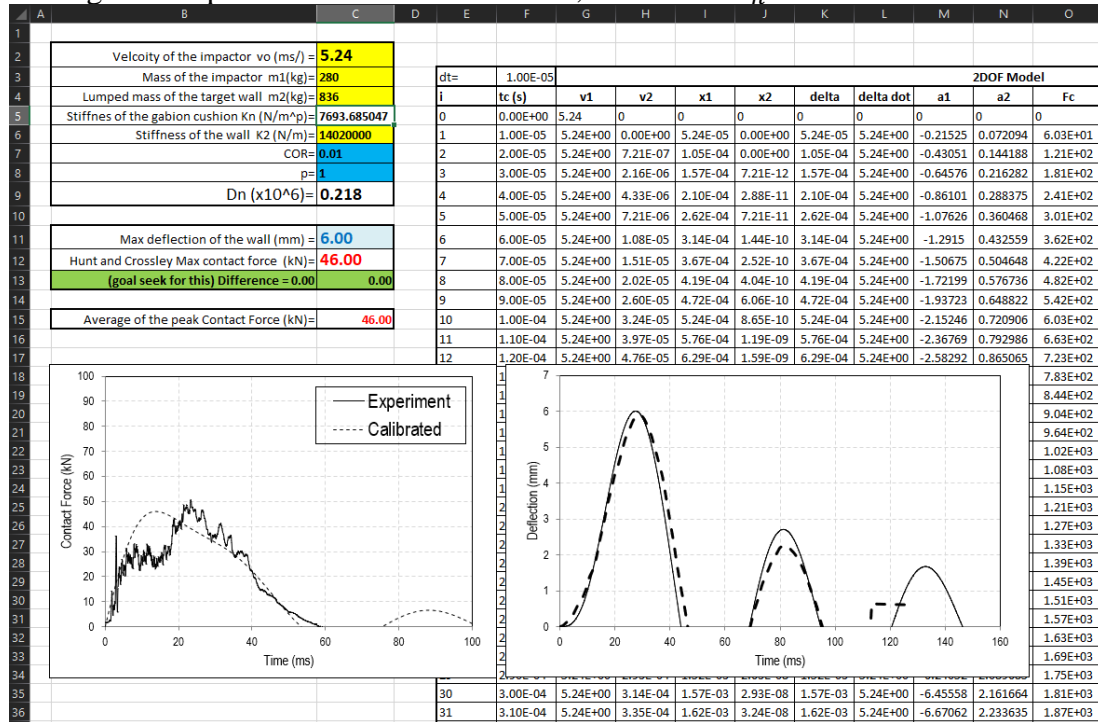
Test C4-1

Average of the peak contact forces = 32 kN , Calibrated $k_n = 3379.8 \text{ N/m}$



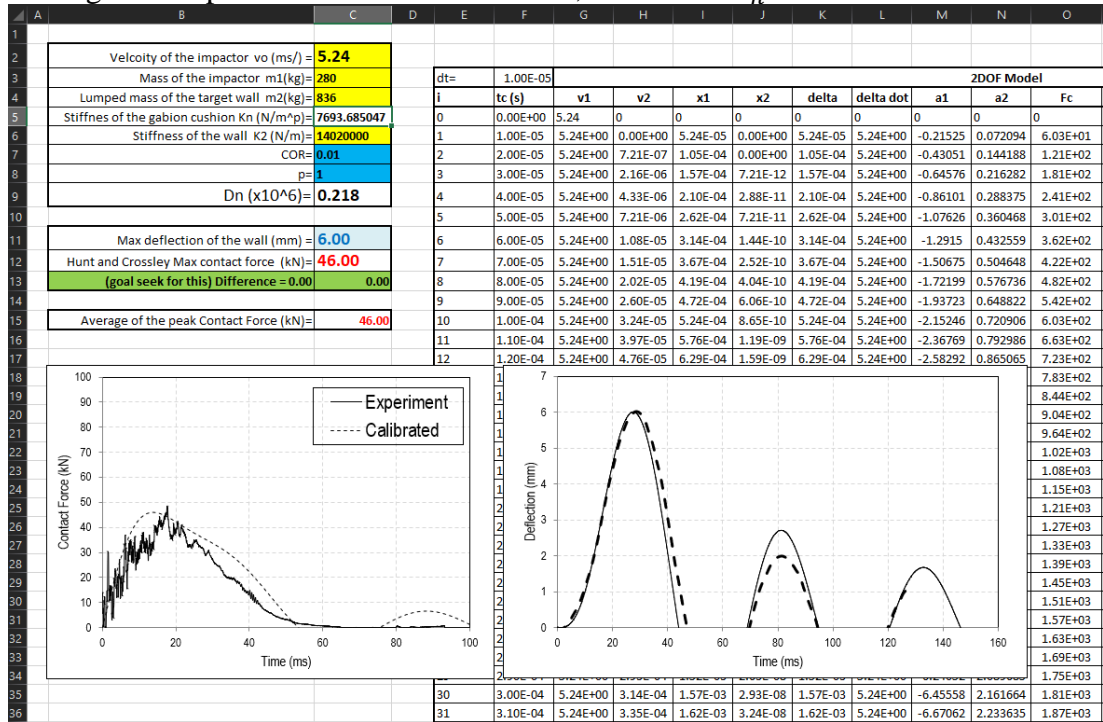
Test C4-2

Average of the peak contact forces = 46 kN , Calibrated $k_n = 7693.7 \text{ N/m}$



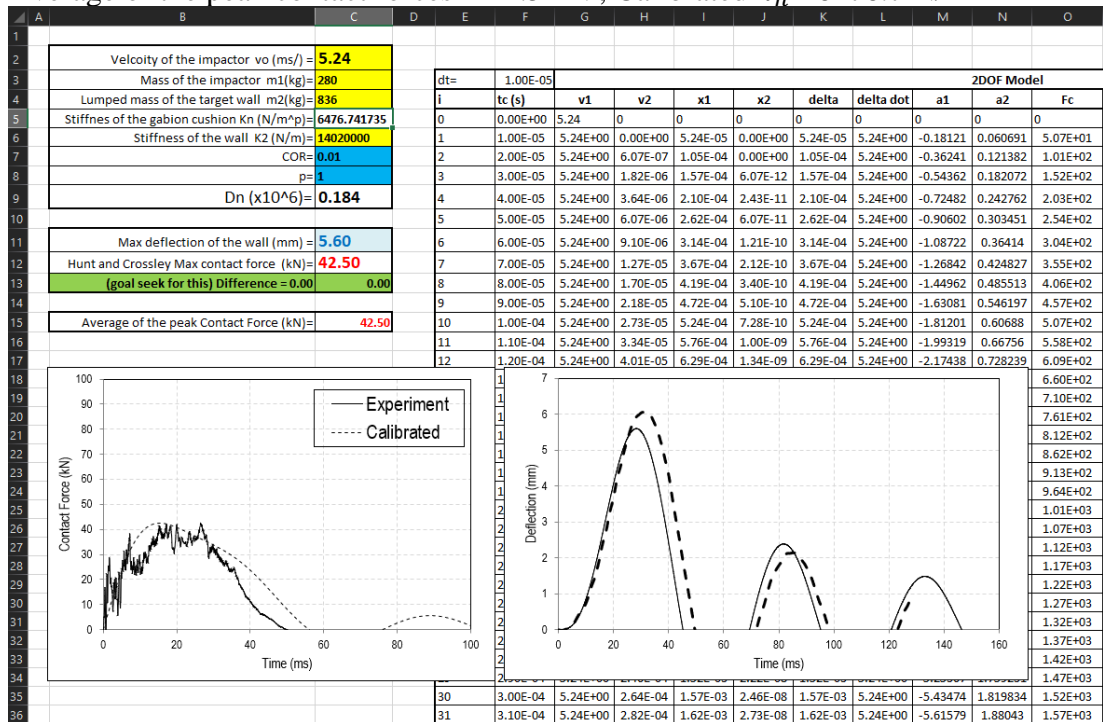
Test C4-3

Average of the peak contact forces = 46 kN , Calibrated $k_n = 7693.7 \text{ N/m}$



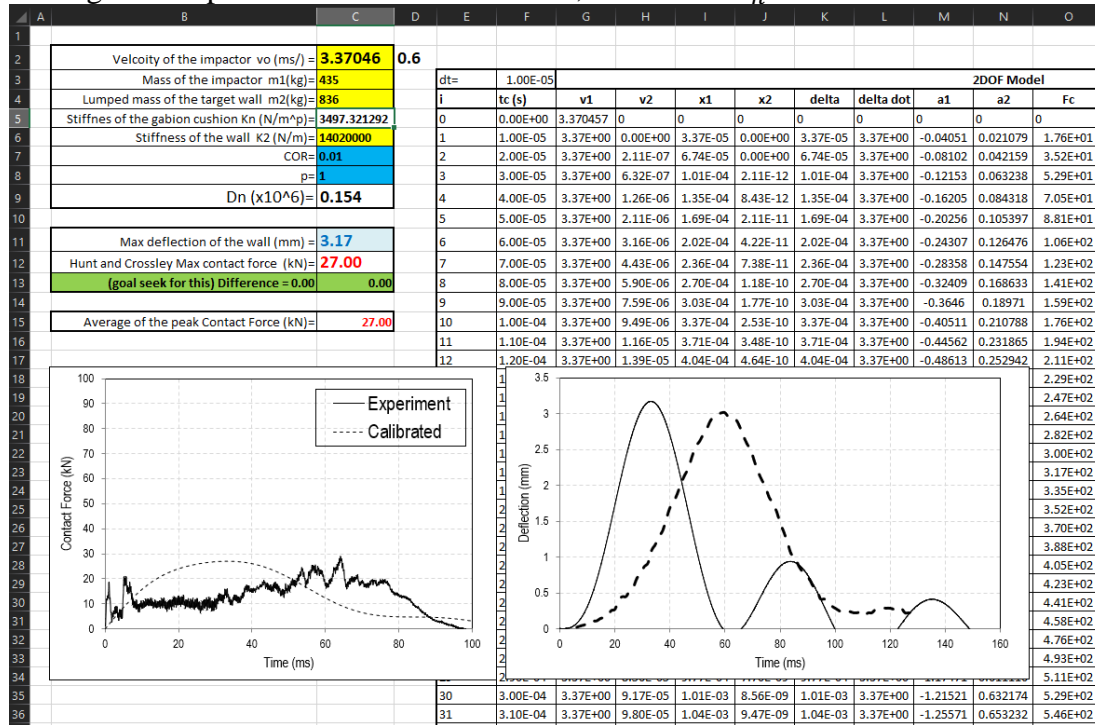
Test C4-4

Average of the peak contact forces = 42.5 kN , Calibrated $k_n = 6476.7 \text{ N/m}$



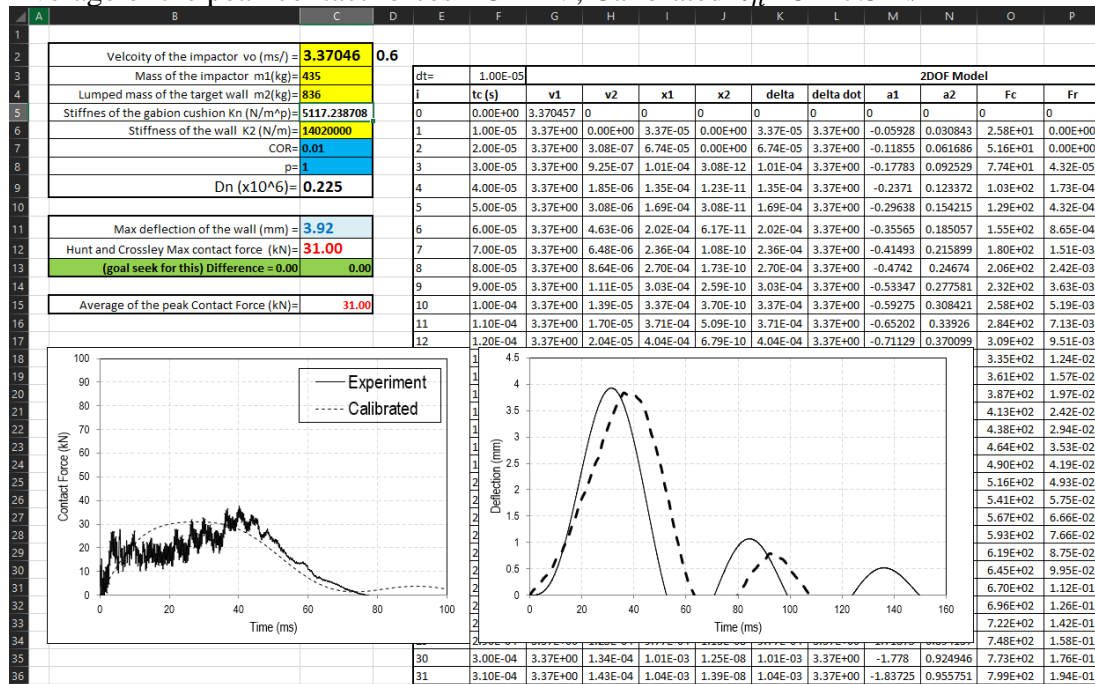
Test C5-1

Average of the peak contact forces = 27 kN , Calibrated $k_n = 3497.3$ N/m



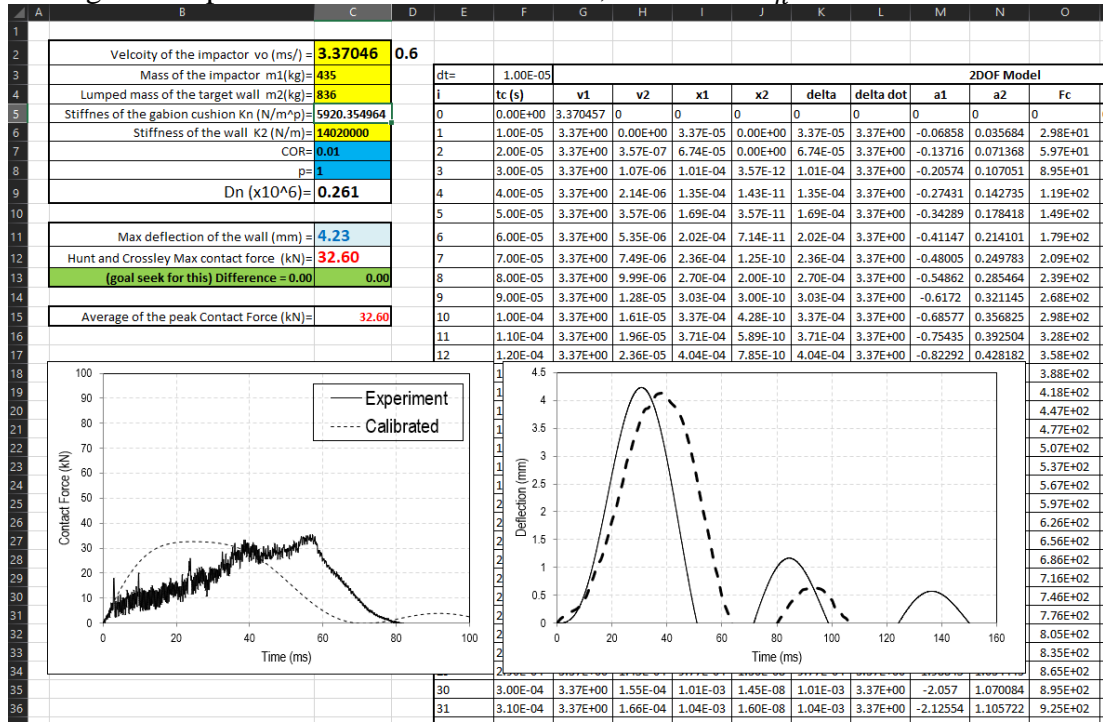
Test C5-2

Average of the peak contact forces = 31 kN , Calibrated $k_n = 5117.3$ N/m



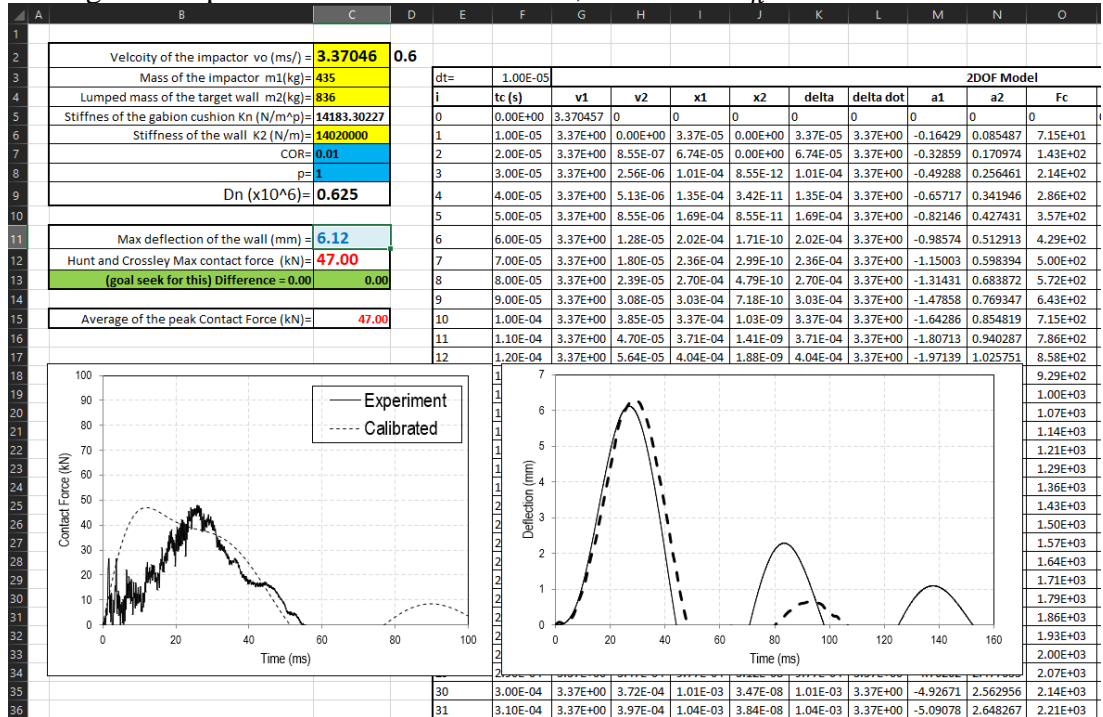
Test C5-3

Average of the peak contact forces = 32.6 kN , Calibrated $k_n = 5920.4$ N/m



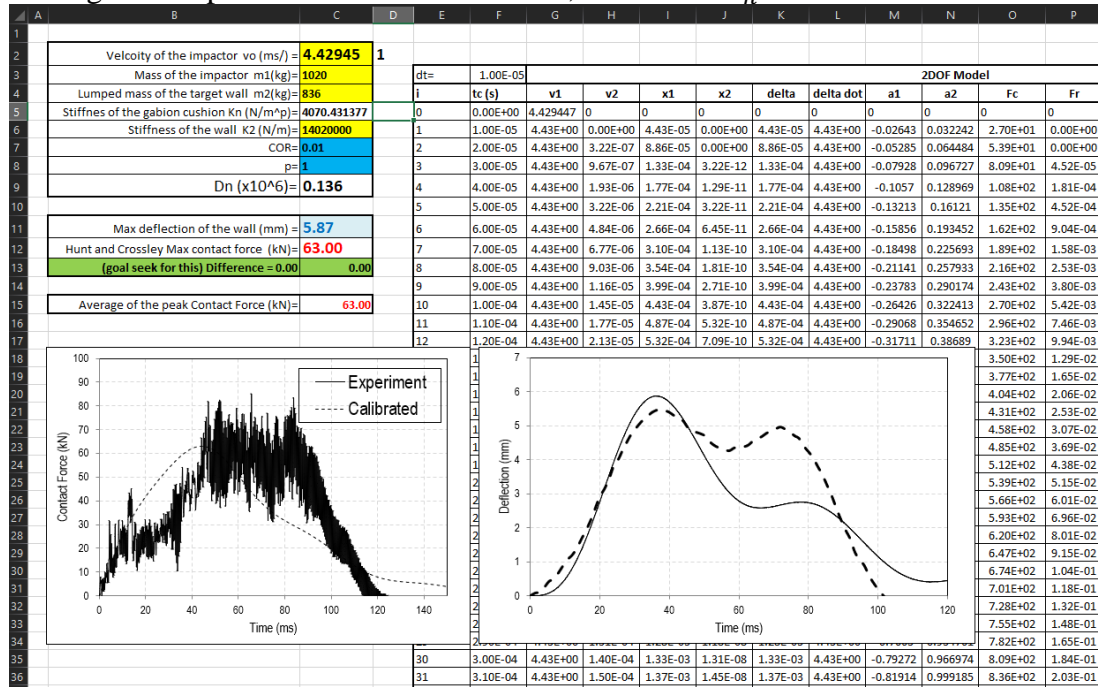
Test C5-4

Average of the peak contact forces = 47 kN , Calibrated $k_n = 14183.3$ N/m



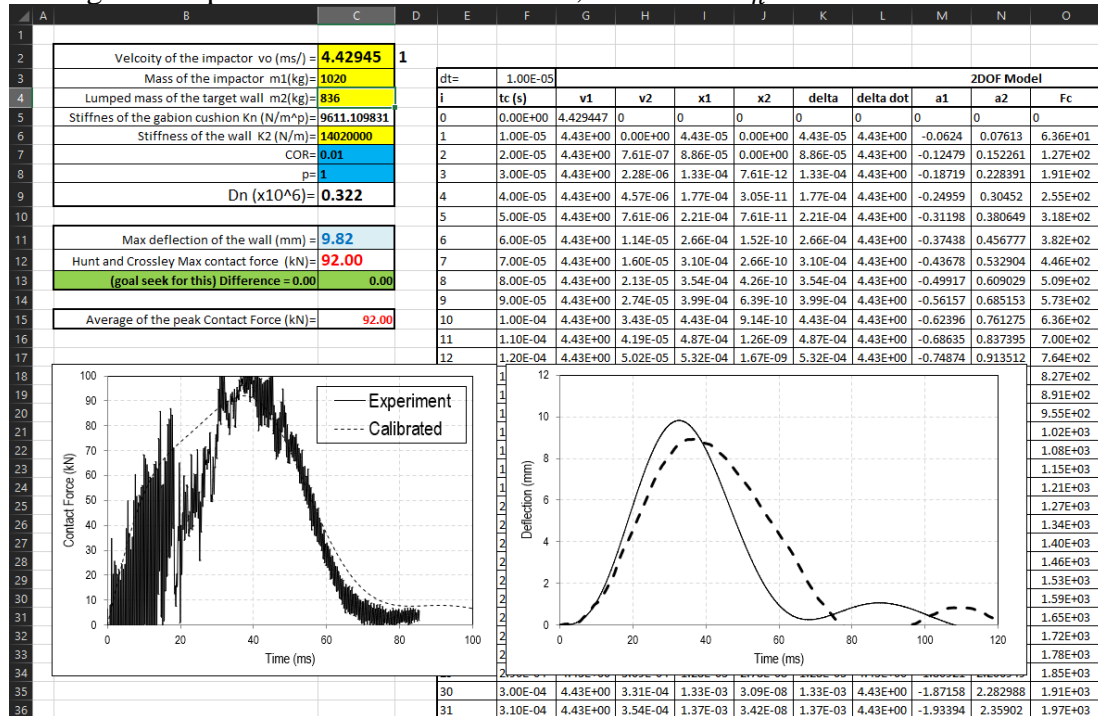
Test C6-1

Average of the peak contact forces = 65kN , Calibrated $k_n = 4070.4$ N/m



Test C6-2

Average of the peak contact forces = 92 kN , Calibrated $k_n = 9611.1$ N/m

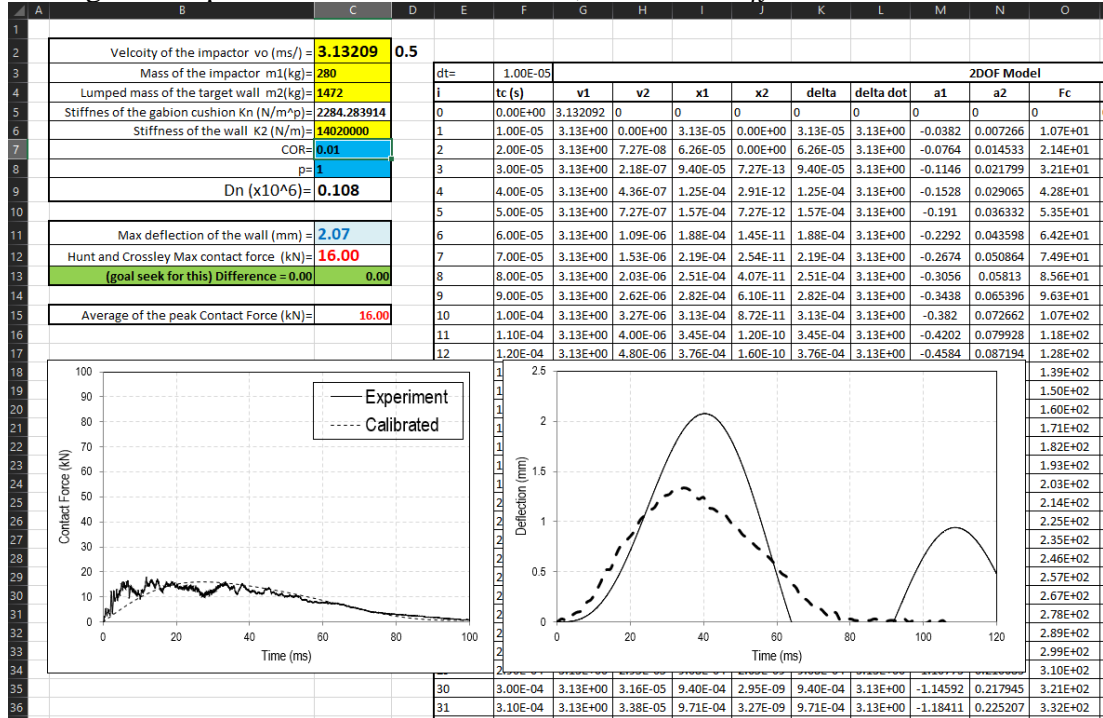


Test C7-1

Faulty accelerometer – no contact force results – no calibration

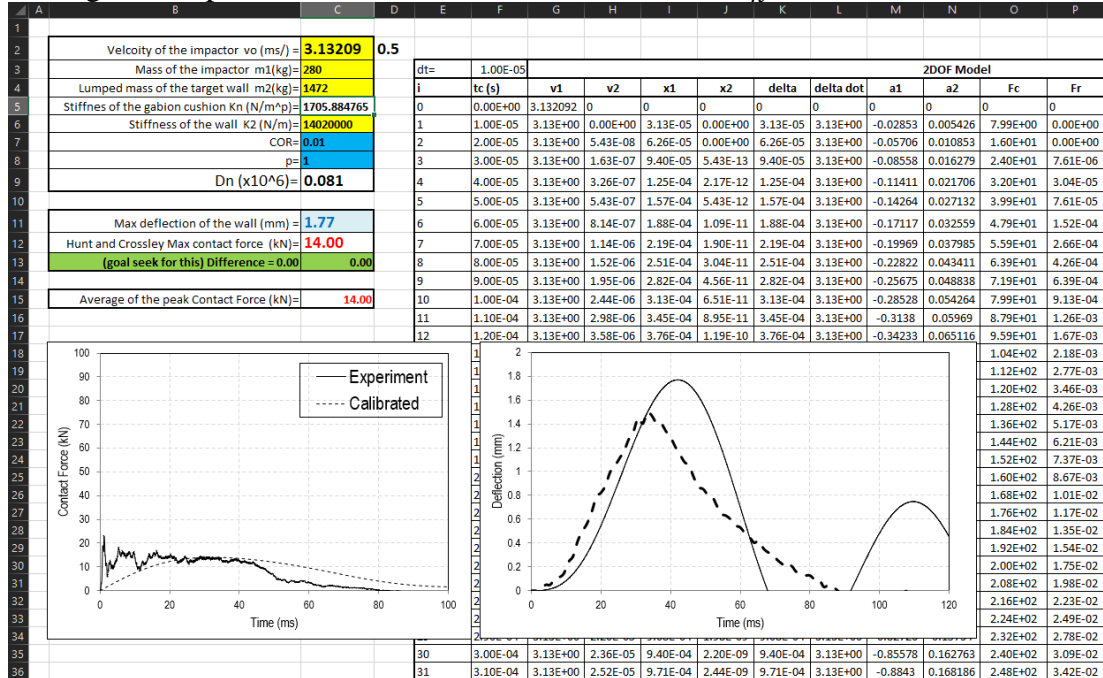
Test C7-2

Average of the peak contact forces = 16 kN , Calibrated $k_n = 2284.3 \text{ N/m}$



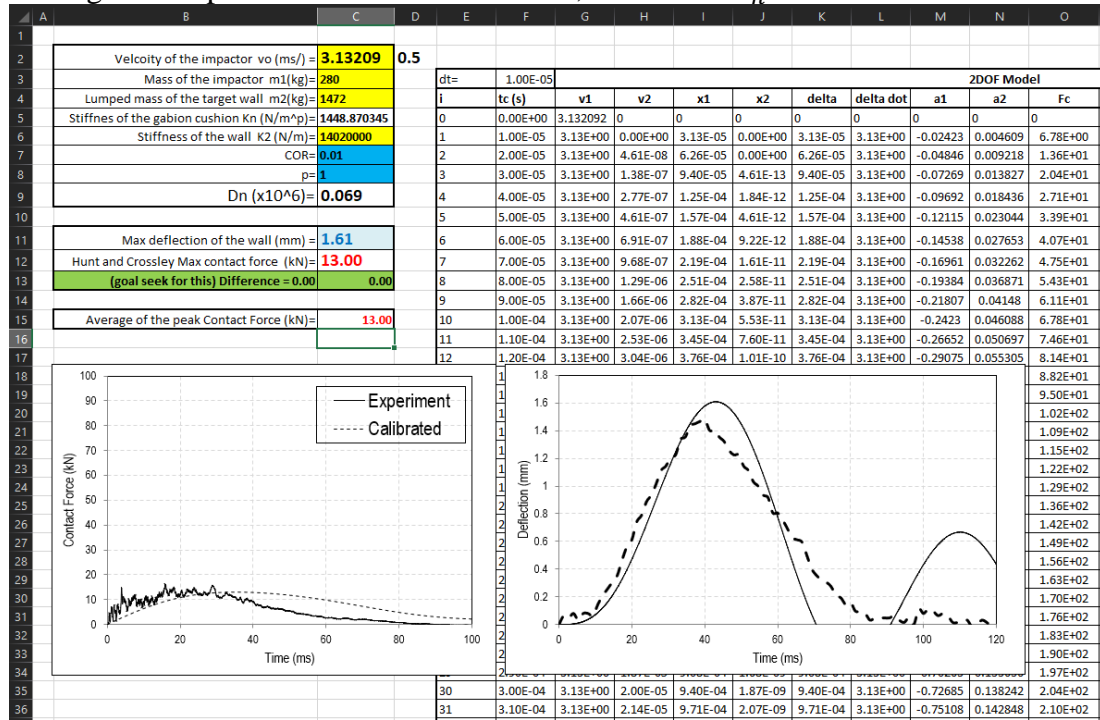
Test C7-3

Average of the peak contact forces = 14 kN , Calibrated $k_n = 1705.8 \text{ N/m}$



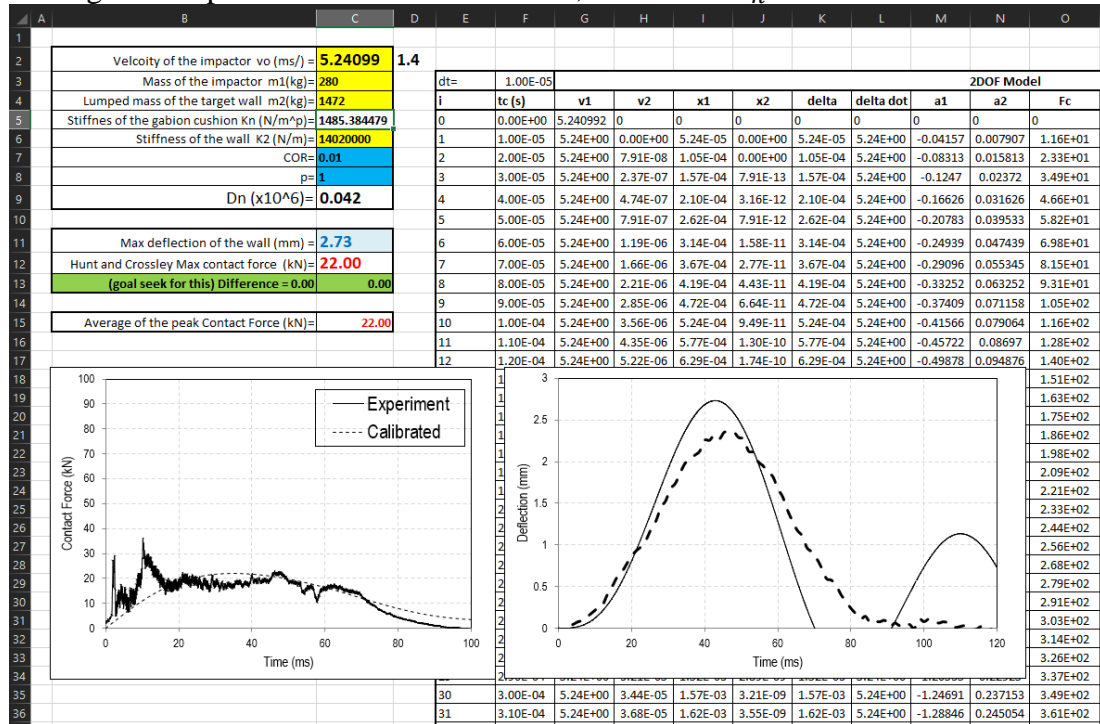
Test C7-4

Average of the peak contact forces = 13 kN , Calibrated $k_n = 1468.8 \text{ N/m}$



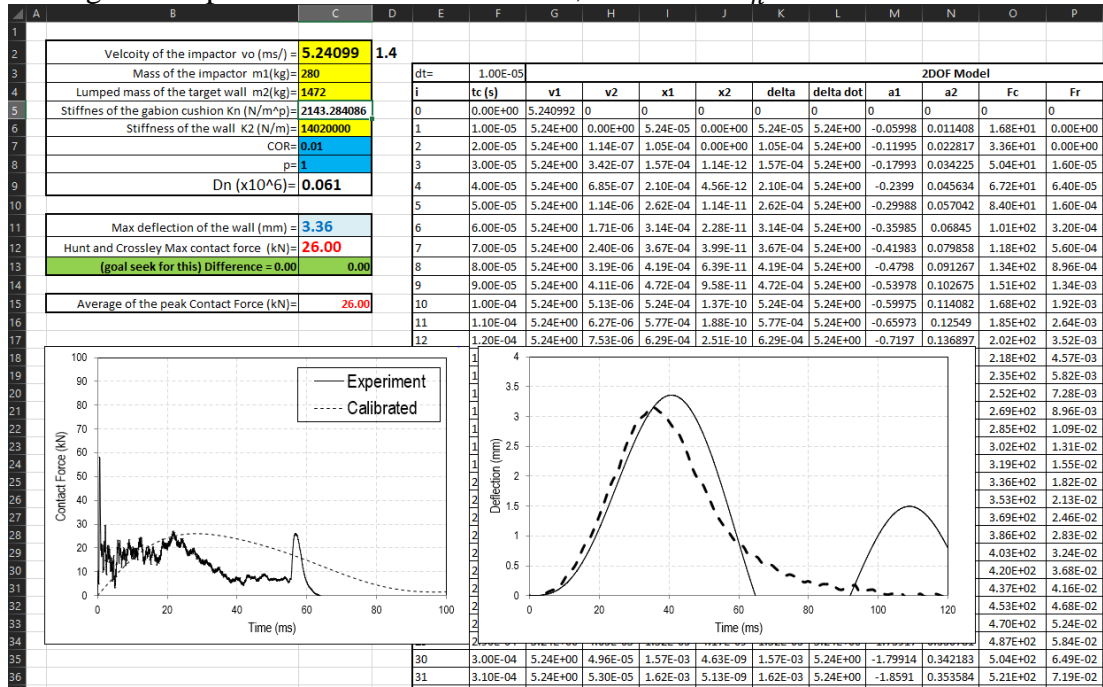
Test C8-1

Average of the peak contact forces = 22 kN , Calibrated $k_n = 1485.4 \text{ N/m}$



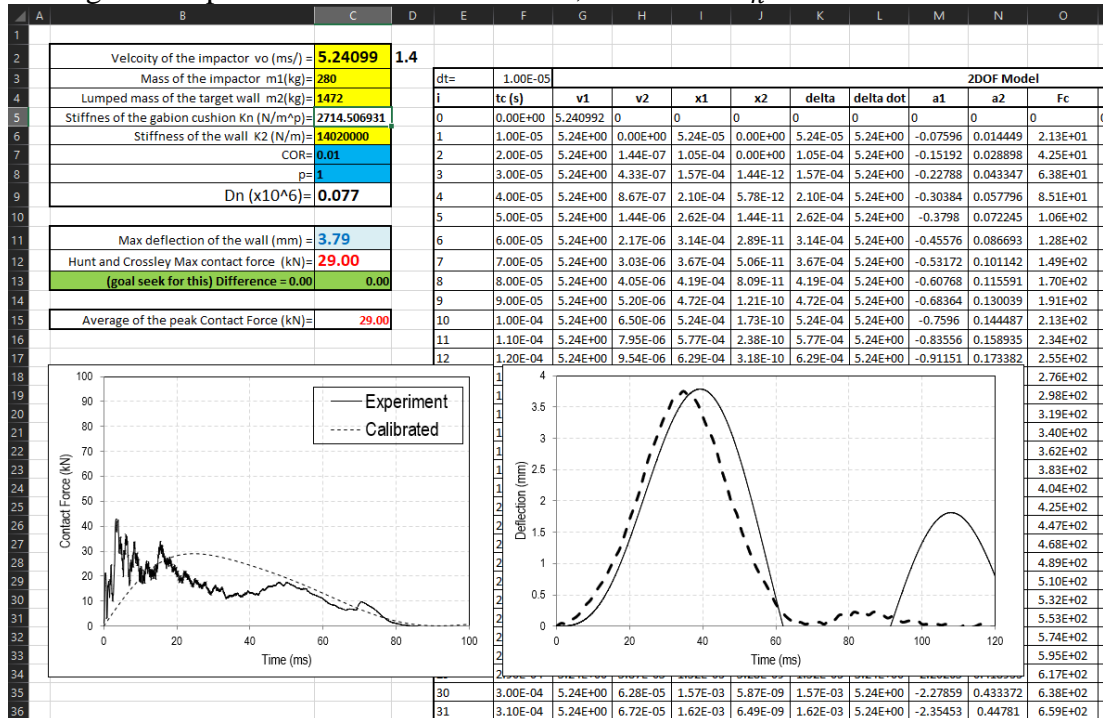
Test C8-2

Average of the peak contact forces = 26 kN , Calibrated $k_n = 2143.3 \text{ N/m}$



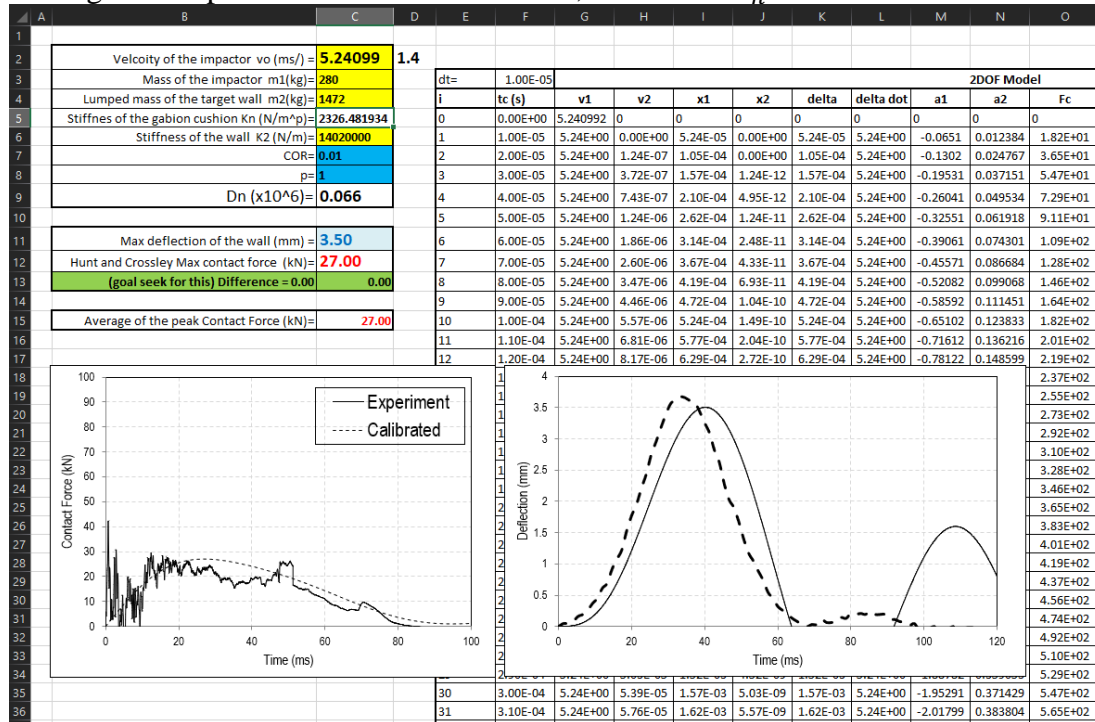
Test C8-3

Average of the peak contact forces = 29 kN , Calibrated $k_n = 2714.5 \text{ N/m}$



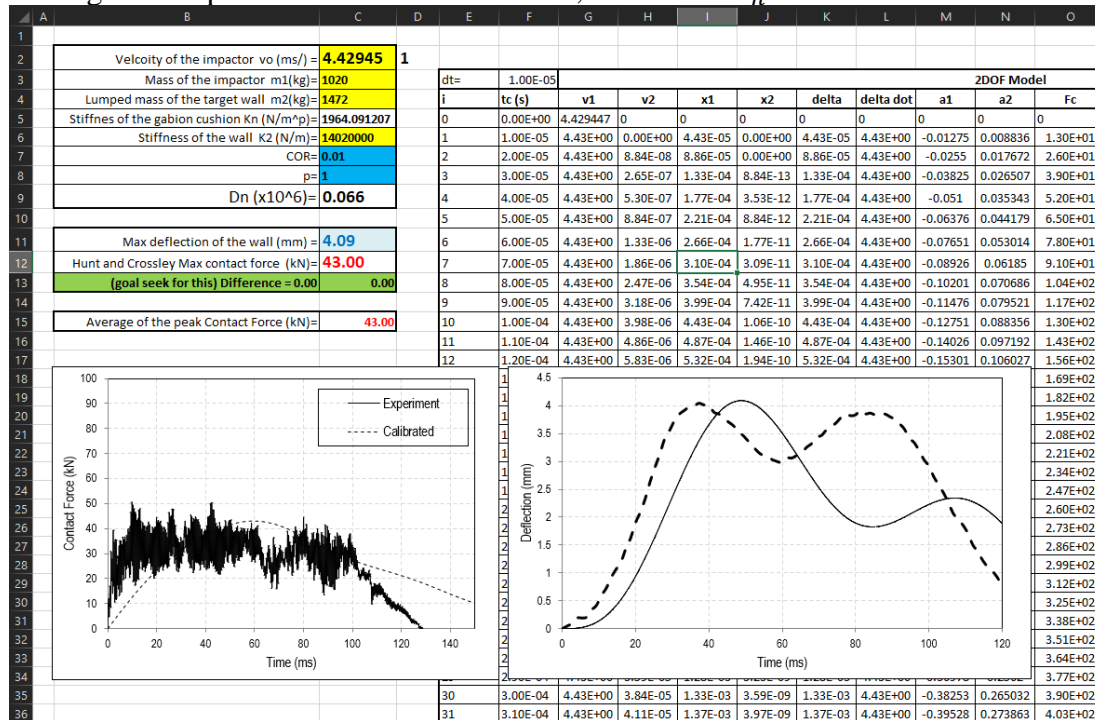
Test C8-4

Average of the peak contact forces = 27 kN , Calibrated $k_n = 2326.5$ N/m



Test C9-1

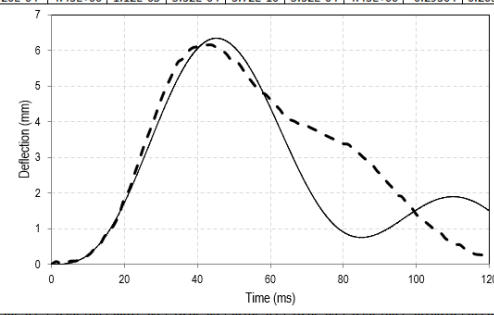
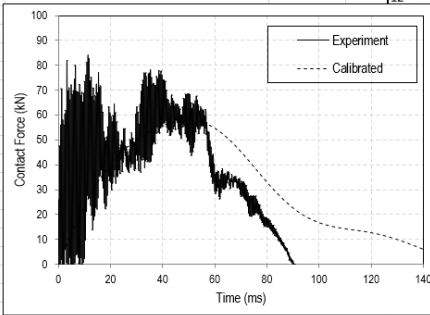
Average of the peak contact forces = 43 kN , Calibrated $k_n = 1964$ N/m



Test C9-2

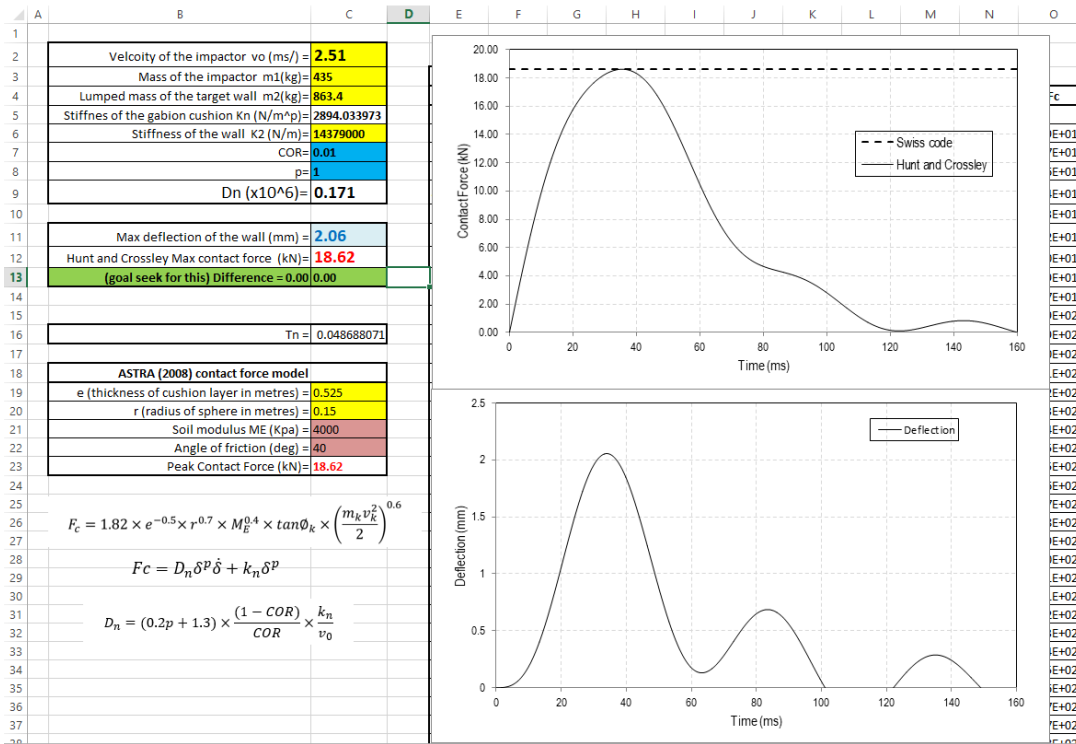
Average of the peak contact forces = 58 kN , Calibrated $k_n = 3761.5 \text{ N/m}$

	A	B	C	D	E	F	G	H	I	J	K	L	M	N	O		
1																	
2			Velocity of the impactor v_0 (m/s) =	4.42945	1												
3			Mass of the impactor m_1 (kg)=	1020		dt=	1.00E-03										
4			Lumped mass of the target wall m_2 (kg)=	1472		2DOF Model											
5			Stiffnes of the gabion cushion K_n (N/m ²)=	3761.50214		i	tc (s)	v1	v2	x1	x2	delta	delta dot	a1	a2	Fc	
6			Stiffness of the wall K_2 (N/m)=	14020000		0	0.00E+00	4.429447	0	0	0	0	0	0	0	0	
7			COR=	0.01		1	1.00E-05	4.43E+00	0.00E+00	4.43E-05	0.00E+00	4.43E-05	4.43E+00	-0.02442	0.016922	2.49E+01	
8			p=	1		2	2.00E-05	4.43E+00	1.69E-07	8.86E-05	0.00E+00	8.86E-05	4.43E+00	-0.04884	0.033843	4.98E+01	
9			Dn (x10 ⁶)=	0.126		3	3.00E-05	4.43E+00	5.08E-07	1.33E-04	1.69E-12	1.33E-04	4.43E+00	-0.07326	0.050765	7.47E+01	
10						4	4.00E-05	4.43E+00	1.02E-06	1.77E-04	6.77E-12	1.77E-04	4.43E+00	-0.09768	0.067687	9.96E+01	
11			Max deflection of the wall (mm) =	6.34		5	5.00E-05	4.43E+00	1.69E-06	2.21E-04	1.69E-11	2.21E-04	4.43E+00	-0.1221	0.084608	1.25E+02	
12			Hunt and Crossley Max contact force (kN) =	58.00		6	6.00E-05	4.43E+00	2.54E-06	2.66E-04	3.38E-11	2.66E-04	4.43E+00	-0.14652	0.10153	1.49E+02	
13			(goal seek for this) Difference =	0.00		7	7.00E-05	4.43E+00	3.55E-06	3.10E-04	5.92E-11	3.10E-04	4.43E+00	-0.17094	0.118451	1.74E+02	
14						8	8.00E-05	4.43E+00	4.74E-06	3.54E-04	9.48E-11	3.54E-04	4.43E+00	-0.19536	0.135372	1.99E+02	
15			Average of the peak Contact Force (kN) =	58.00		9	9.00E-05	4.43E+00	6.09E-06	3.99E-04	1.42E-10	3.99E-04	4.43E+00	-0.21978	0.152293	2.24E+02	
16						10	1.00E-04	4.43E+00	7.61E-06	4.43E-04	2.03E-10	4.43E-04	4.43E+00	-0.2442	0.169214	2.49E+02	
17						11	1.10E-04	4.43E+00	9.31E-06	4.87E-04	2.79E-10	4.87E-04	4.43E+00	-0.26862	0.186135	2.74E+02	
18						12	1.20E-04	4.43E+00	1.12E-05	5.32E-04	3.72E-10	5.32E-04	4.43E+00	-0.29304	0.203055	2.99E+02	
19																3.24E+02	
20																3.49E+02	
21																3.74E+02	
22																3.99E+02	
23																4.23E+02	
24																4.48E+02	
25																4.73E+02	
26																4.98E+02	
27																5.23E+02	
28																5.48E+02	
29																5.73E+02	
30																5.98E+02	
31																6.23E+02	
32																6.48E+02	
33																6.73E+02	
34																6.97E+02	
35																7.22E+02	
36																7.47E+02	
						30	3.00E-04	4.43E+00	7.36E-05	1.33E-03	6.87E-09	1.33E-03	4.43E+00	-0.73257	0.507559	7.47E+02	
						31	3.10E-04	4.43E+00	7.87E-05	1.37E-03	7.61E-09	1.37E-03	4.43E+00	-0.75699	0.524471	7.72E+02	



Appendix G - Using Excel Spreadsheet to Calculate k_n

Figure below shows a screenshot of the Excel spreadsheet developed to calculate simulate the 2DOF model explained in the Section 5.4.



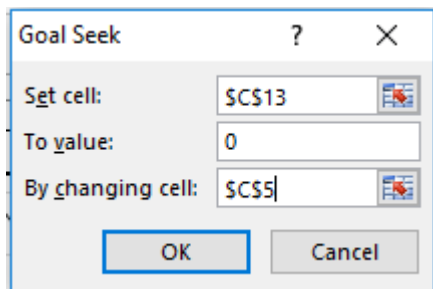
Input parameters into the 2DOF model are to be inserted into Cell C2, C3, C4 and C6 (highlighted in yellow colour). Values used in Cell C7 and C8 (highlighted in blue colour) are in accordance with Section 5.3.1 and Section 5.3.2.

Velocity of the impactor v_0 (ms/)	2.51
Mass of the impactor m_1 (kg)	435
Lumped mass of the target wall m_2 (kg)	863.4
Stiffness of the gabion cushion K_n (N/m ²)	2894.033973
Stiffness of the wall K_2 (N/m)	14379000
COR	0.01
p	1
D_n ($\times 10^6$)	0.171

In order to apply the GOAL SEEK function, the peak contact force will first need to be calculated with the use of Eq. 3.6. Two additional input parameters need to be inserted into Cell C19 and C20 (highlighted in yellow colour) for the operation of Eq. 3.6. Soil modulus (Cell C21) and angle of friction (Cell C22), both highlighted in pink, may be adjusted based on the properties of the cushion materials.

ASTRA (2008) contact force model	
e (thickness of cushion layer in metres) =	0.525
r (radius of sphere in metres) =	0.15
Soil modulus ME (Kpa) =	4000
Angle of friction (deg) =	40
Peak Contact Force (kN)=	18.62

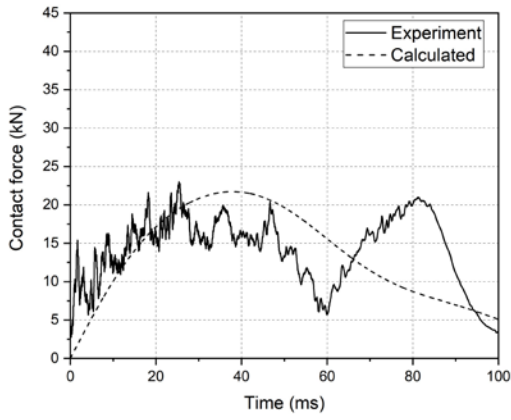
Finally, GOAL SEEK function can be employed. The “goal” is to be set as Cell C13 to value 0 by changing Cell C5.



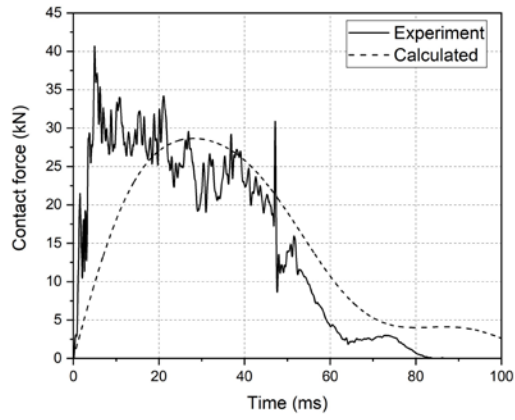
Once the GOAL SEEK operation is completed, both contact force and deflection time-histories will be produced in Cell E1 - O38.

Appendix H – Calculation of Contact Force Time History

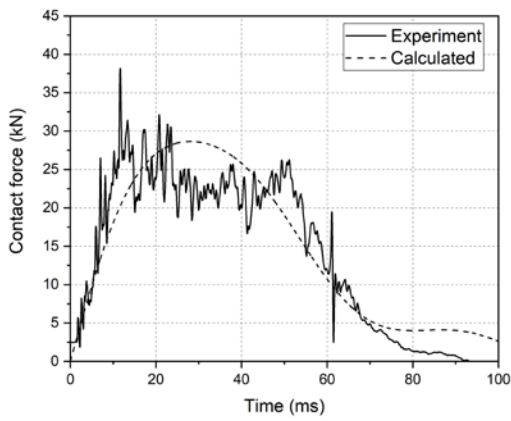
Test Series B - Calculated



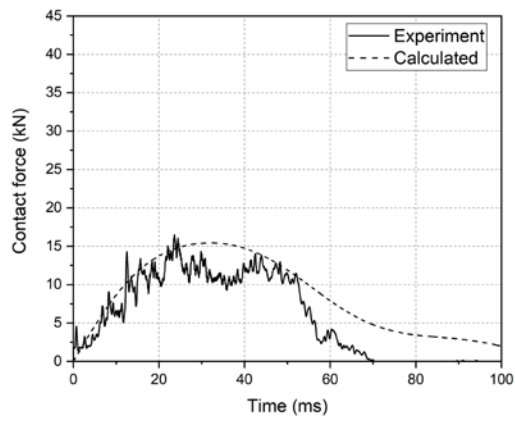
Test B1-1



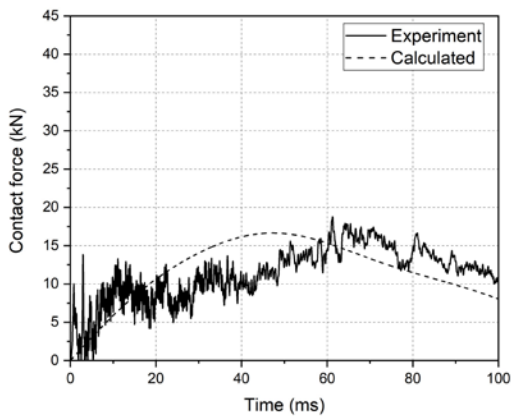
Test B1-2



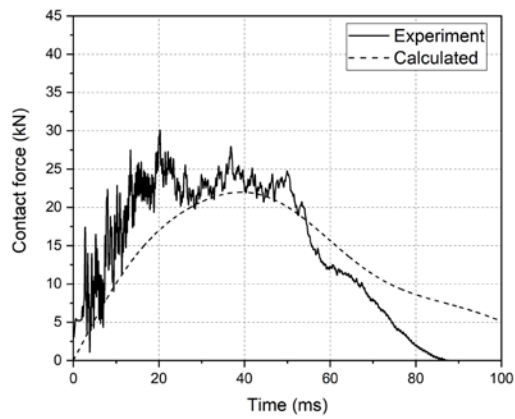
Test B1-3



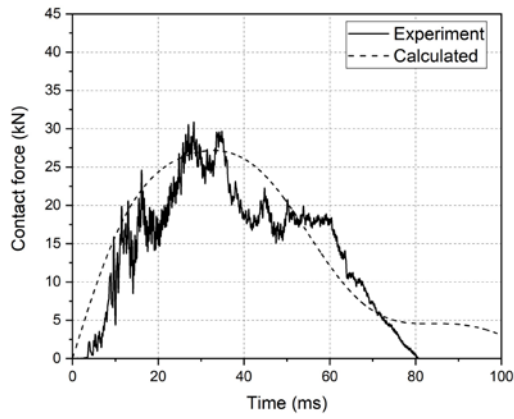
Test B1-4



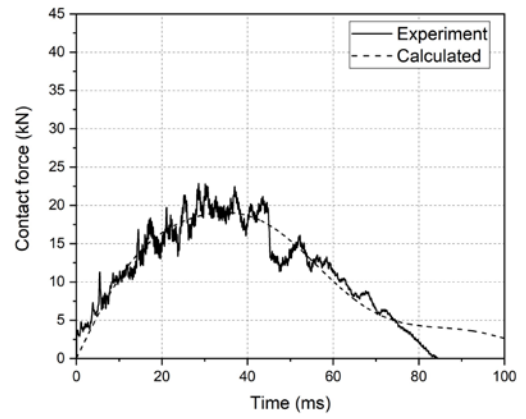
Test B2-1



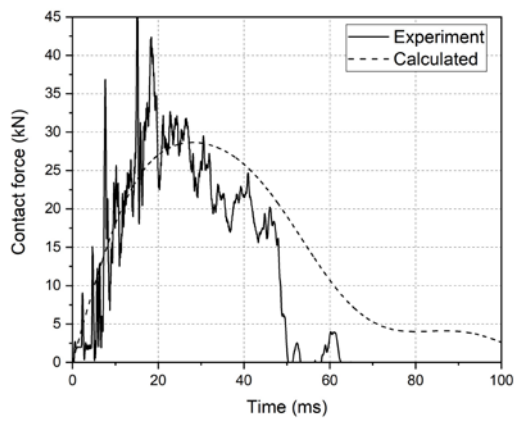
Test B2-2



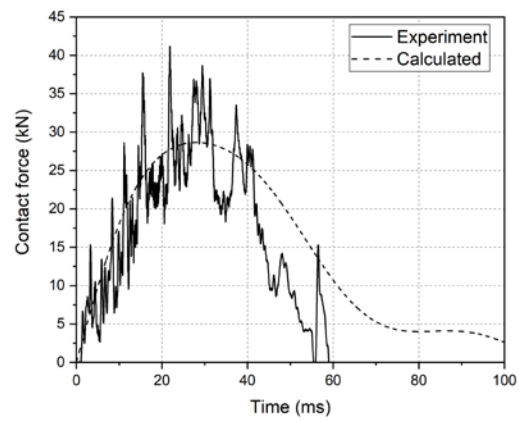
Test B2-3



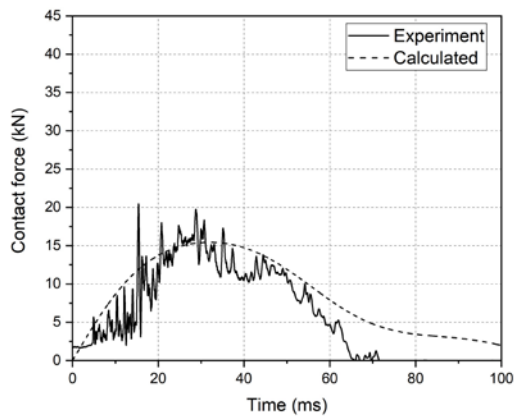
Test B2-4



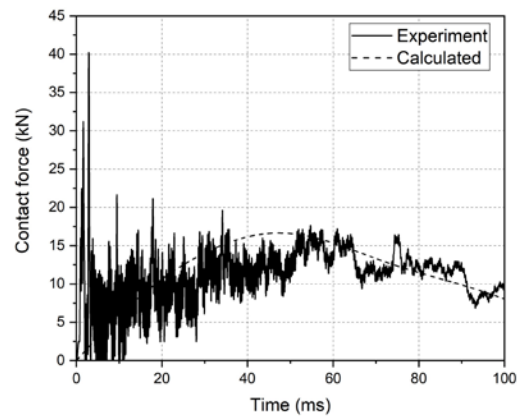
Test B3-2



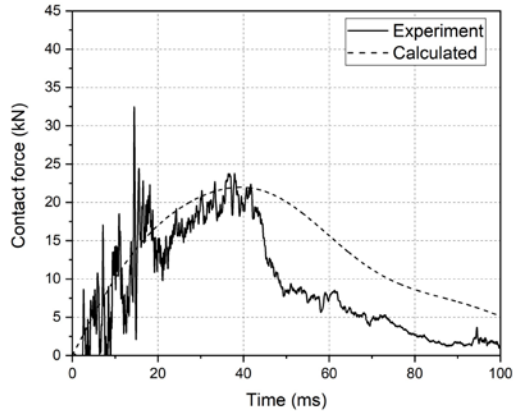
Test B3-3



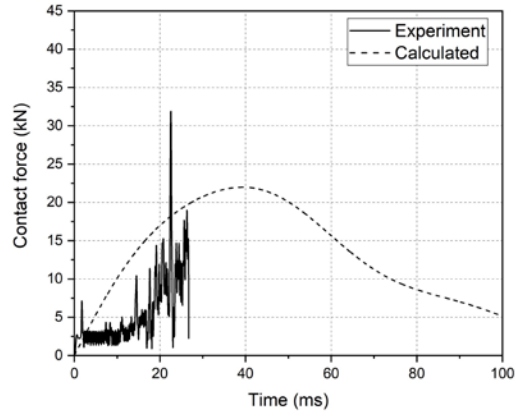
Test B3-4



Test B4-1

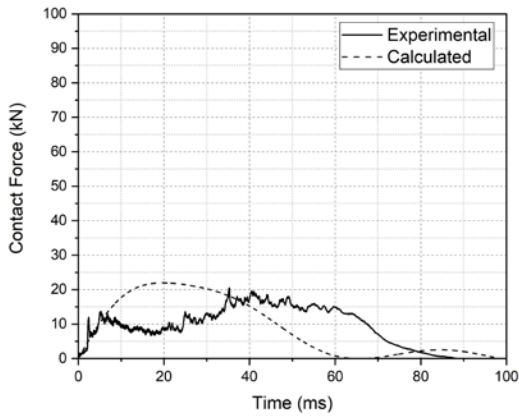


Test B4-2

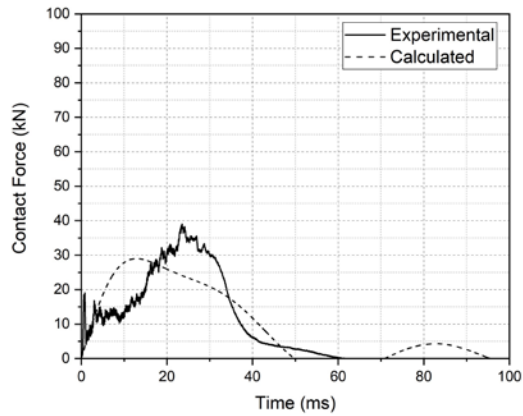


Test B4-3

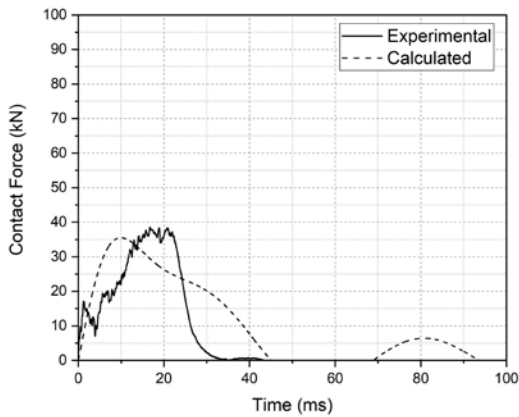
Test Series C - Calculated



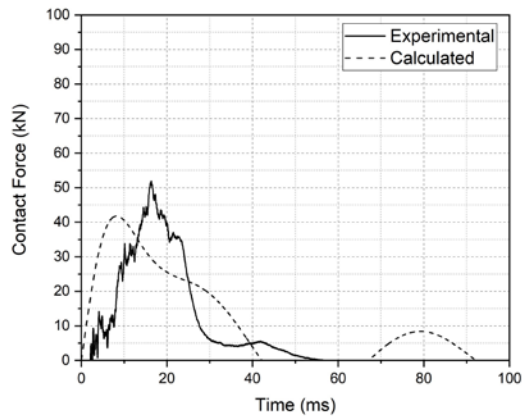
Test C1-1



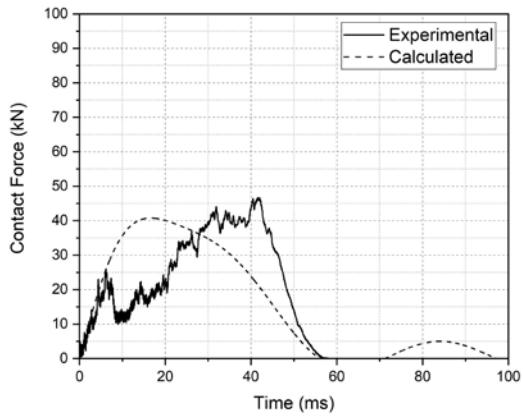
Test C1-2



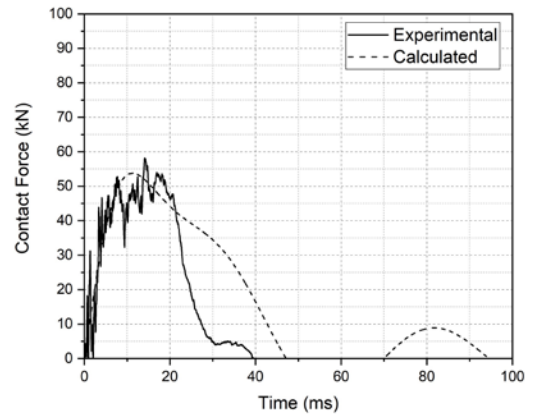
Test C1-3



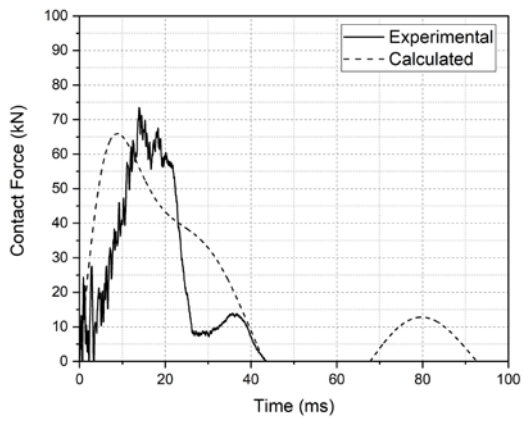
Test C1-4



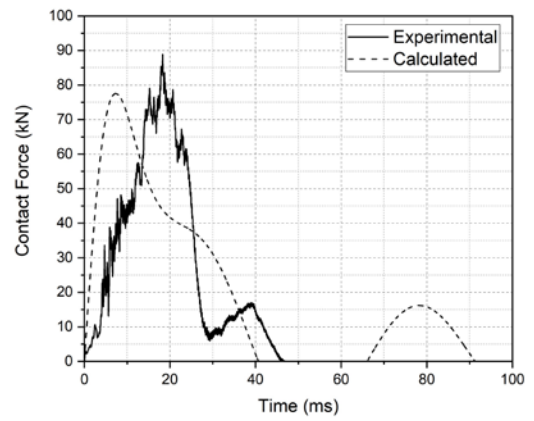
Test C2-1



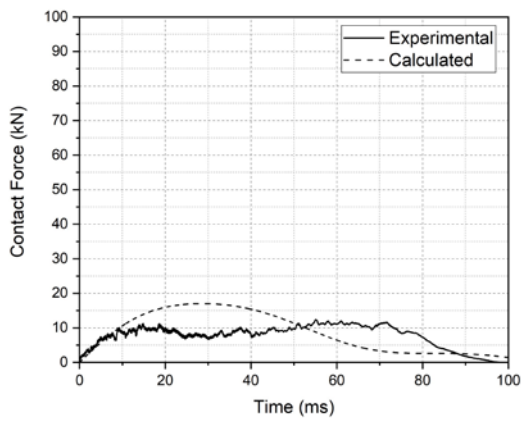
Test C2-2



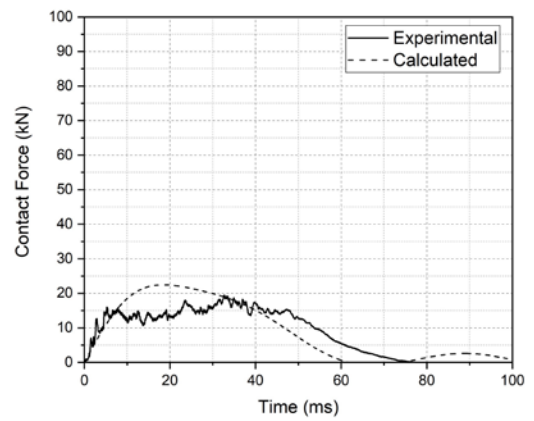
Test C2-3



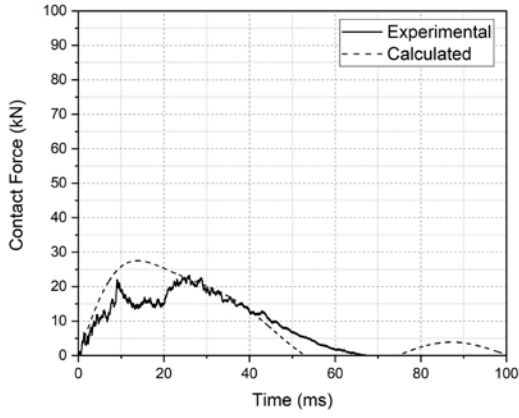
Test C2-4



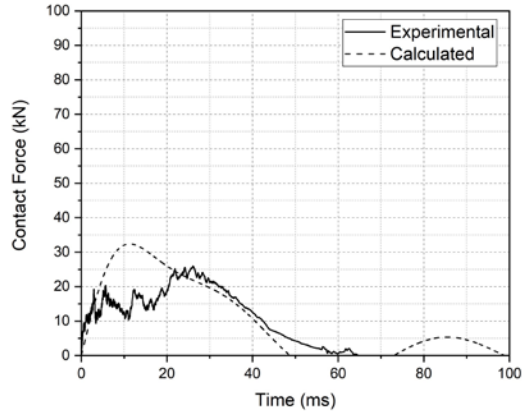
Test C3-1



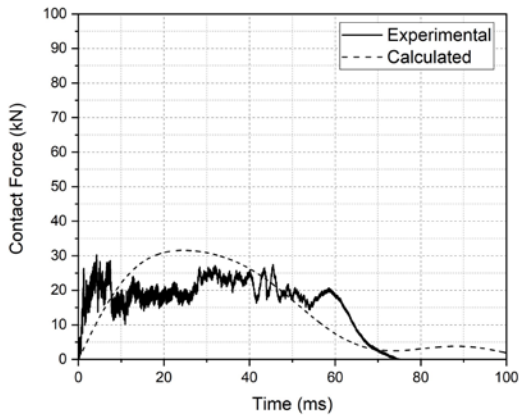
Test C3-2



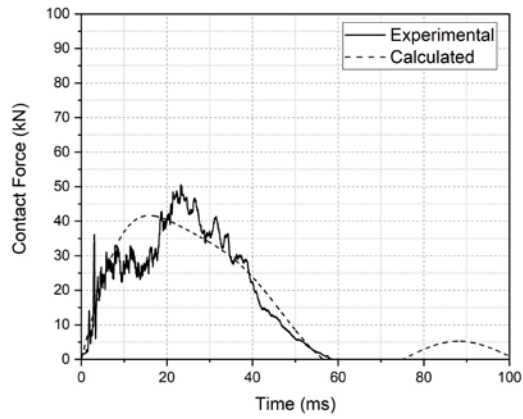
Test C3-3



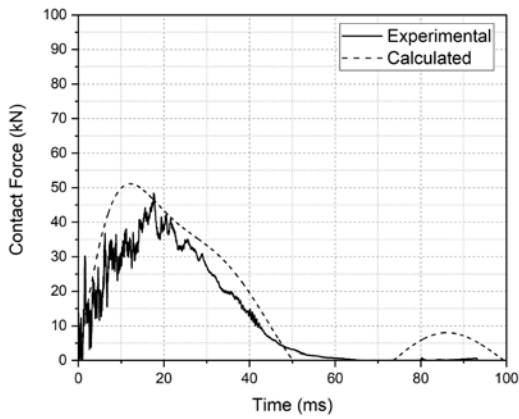
Test C3-4



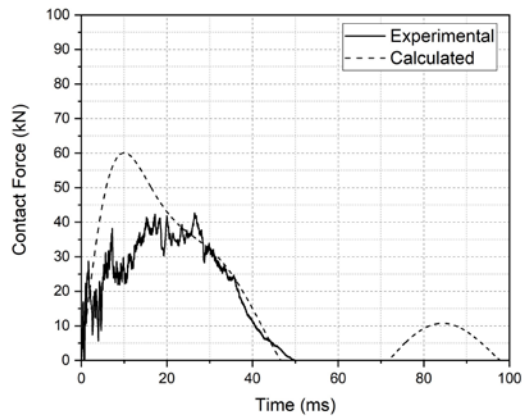
Test C4-1



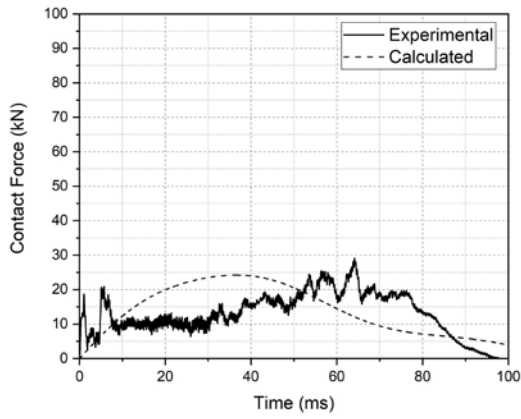
Test C4-2



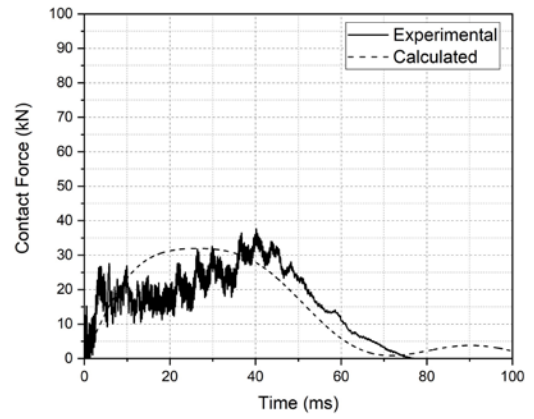
Test C4-3



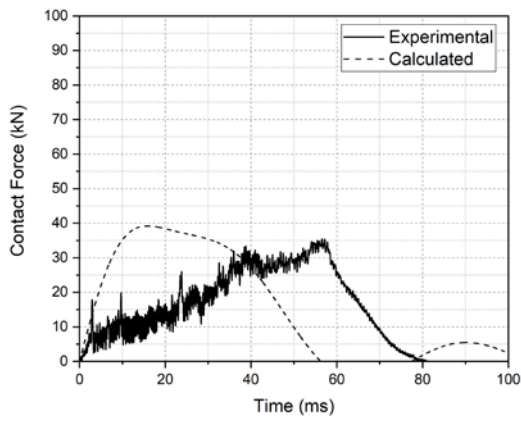
Test C4-4



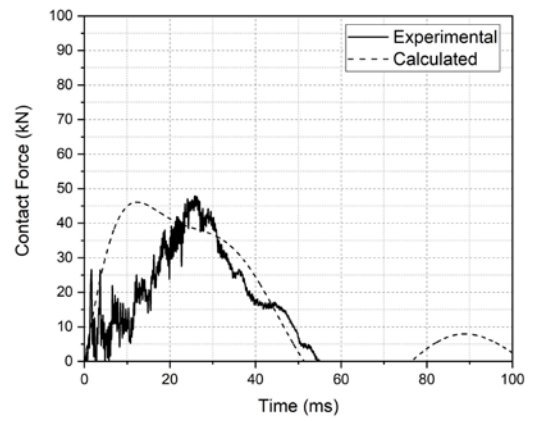
Test C5-1



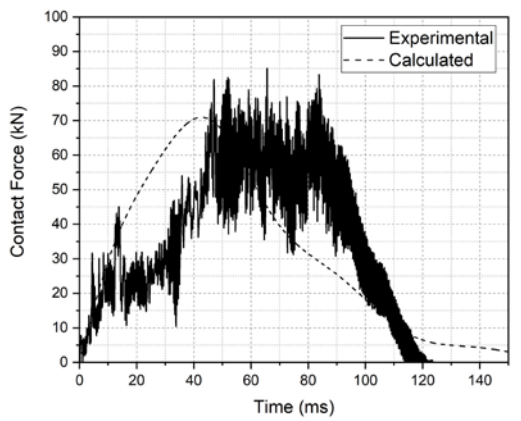
Test C5-2



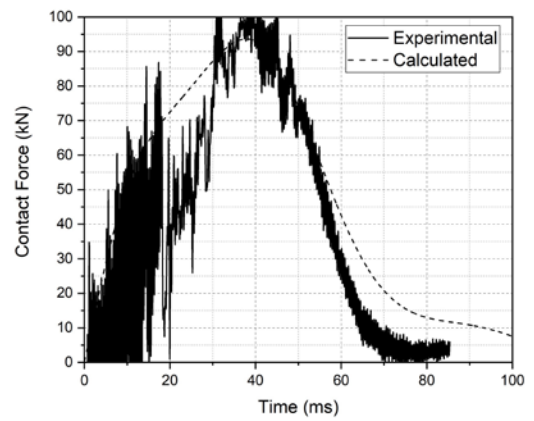
Test C5-3



Test C5-4

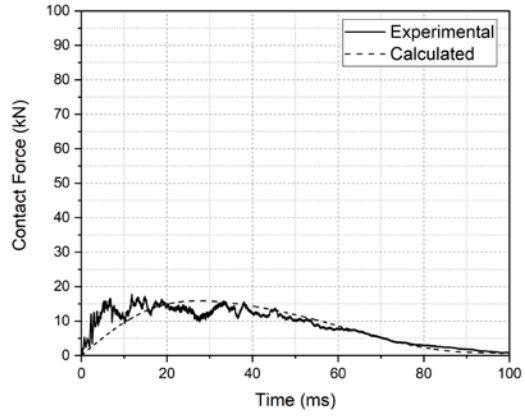


Test C6-1



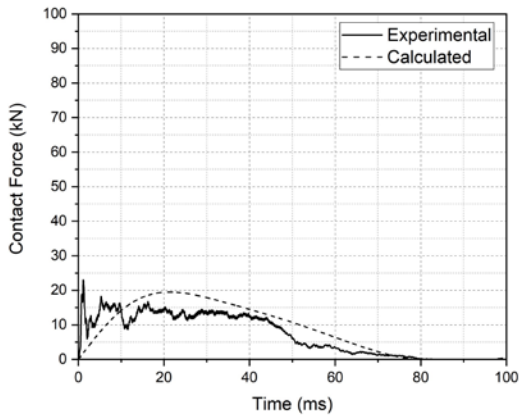
Test C6-2

Faulty Accelerometer

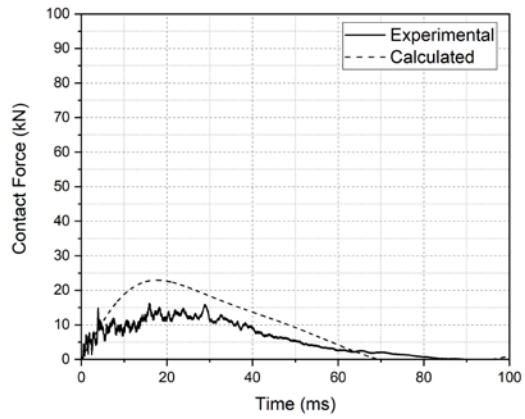


Test C7-1

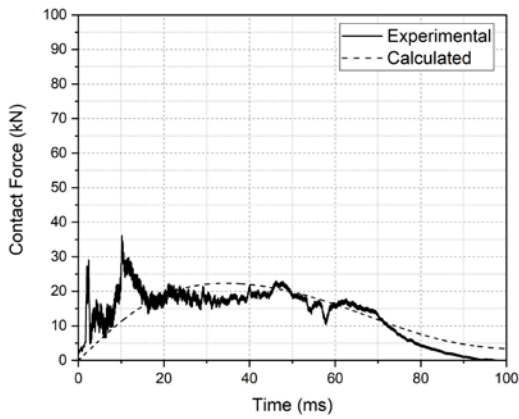
Test C7-2



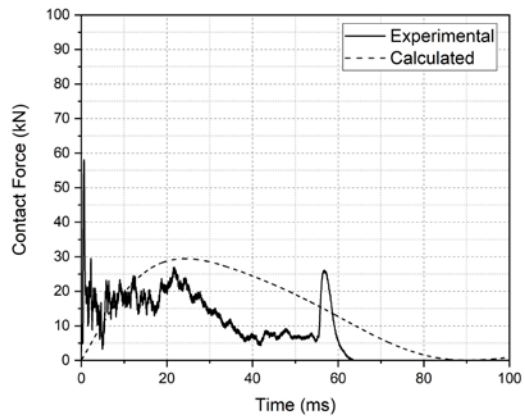
Test C7-3



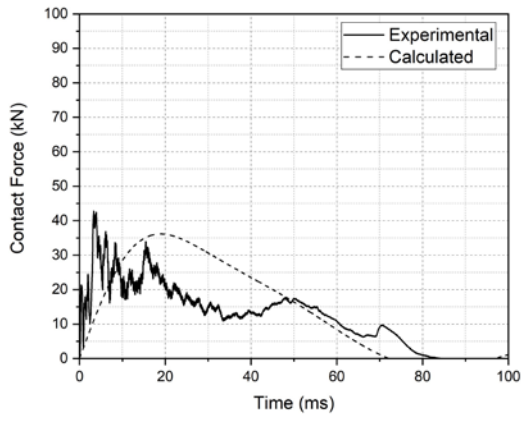
Test C7-4



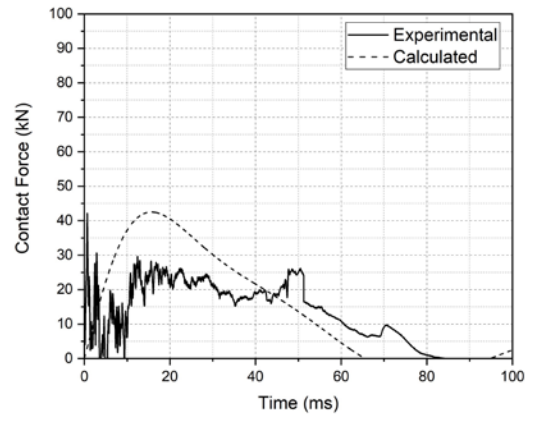
Test C8-1



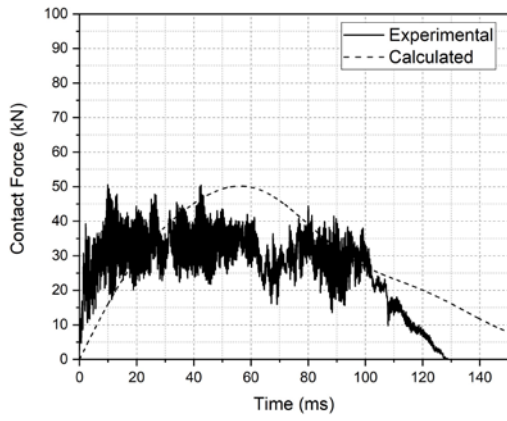
Test C8-2



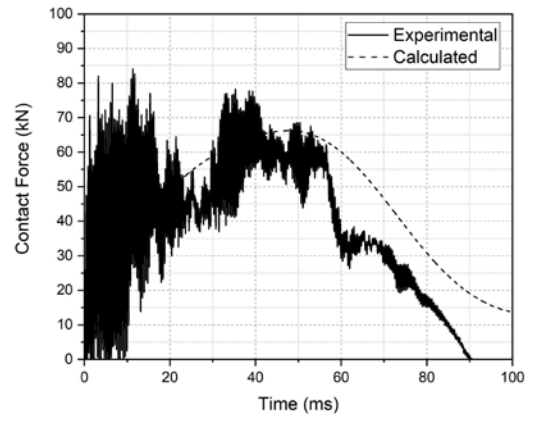
Test C8-3



Test C8-4



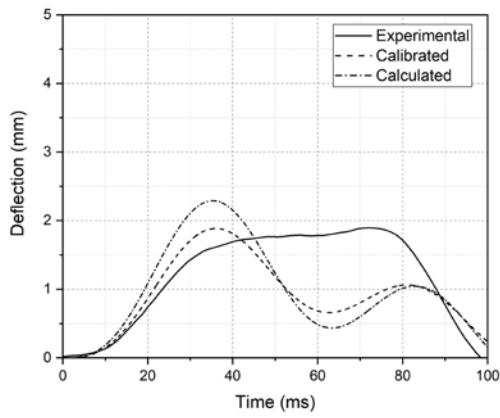
Test C9-1



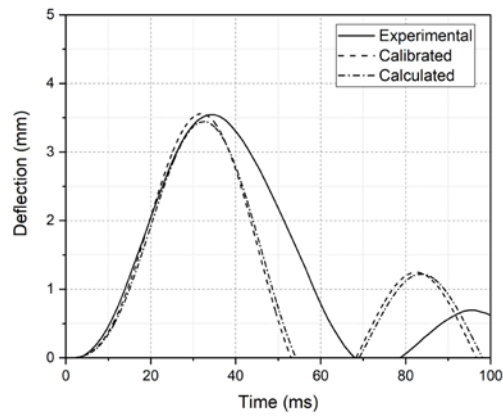
Test C9-2

Appendix I – Calculated & Calibrated Deflection Time history

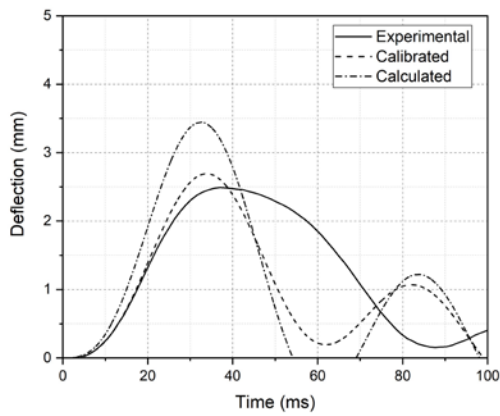
Test Series B – Calibration / Calculation



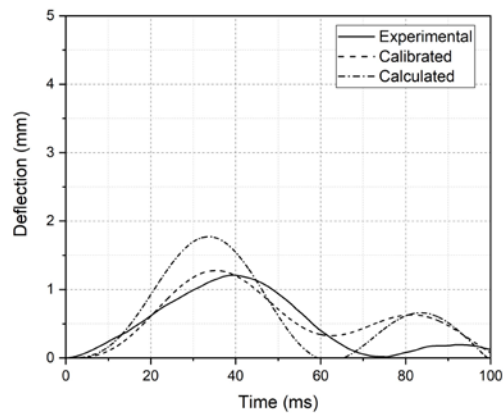
Test B1-1



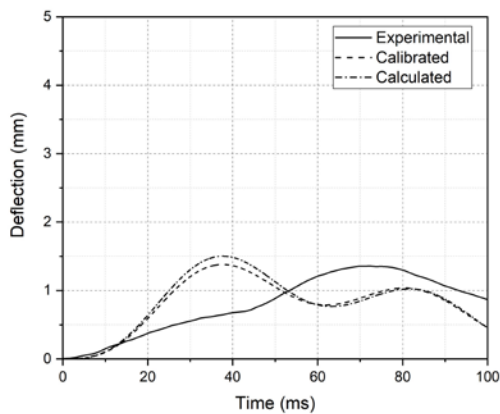
Test B1-2



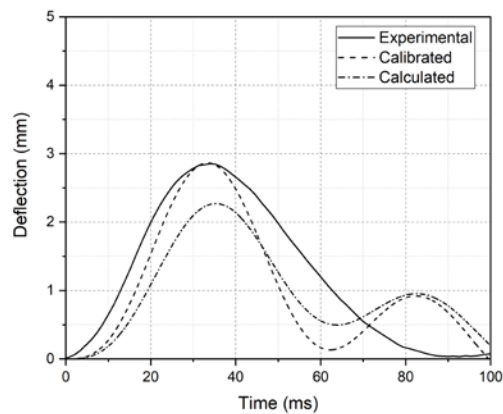
Test B1-3



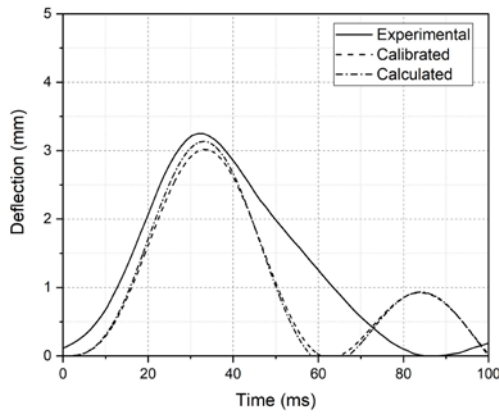
Test B1-4



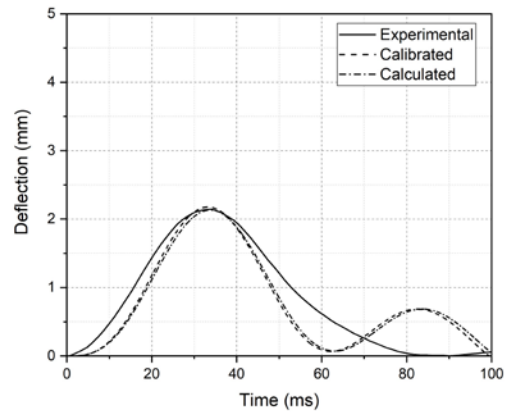
Test B2-1



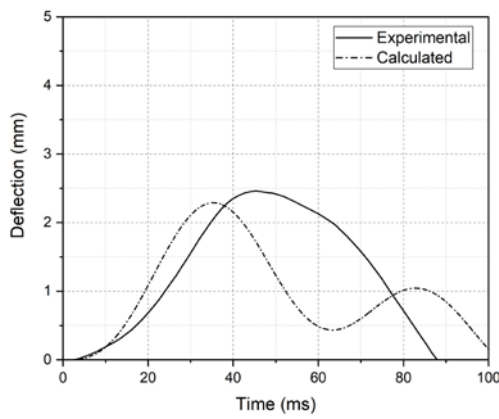
Test B2-2



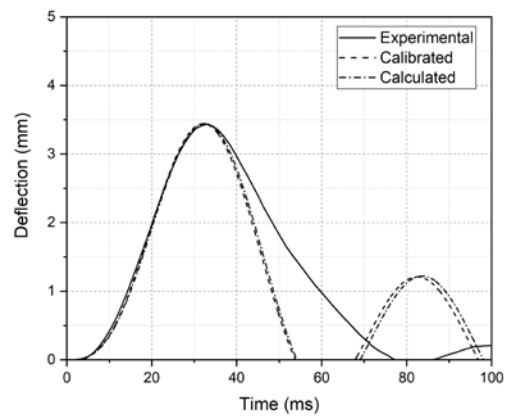
Test B2-3



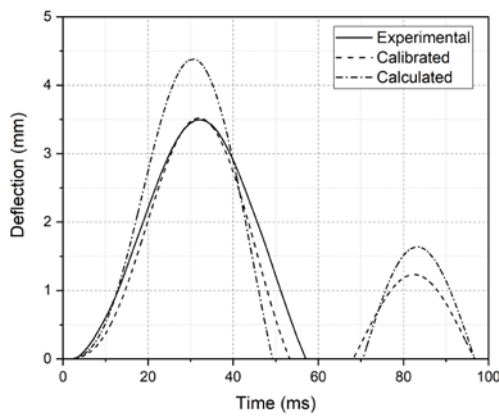
Test B2-4



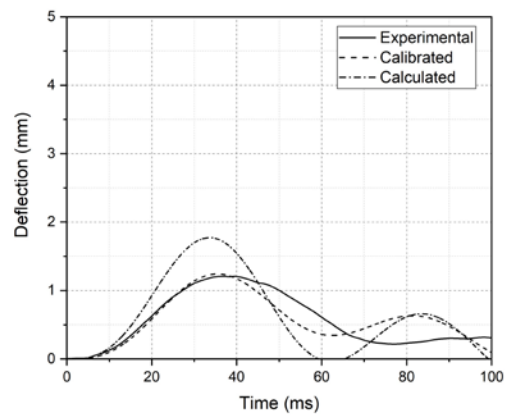
Test B3-1



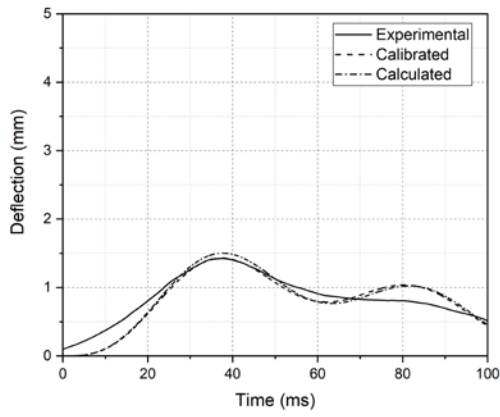
Test B3-2



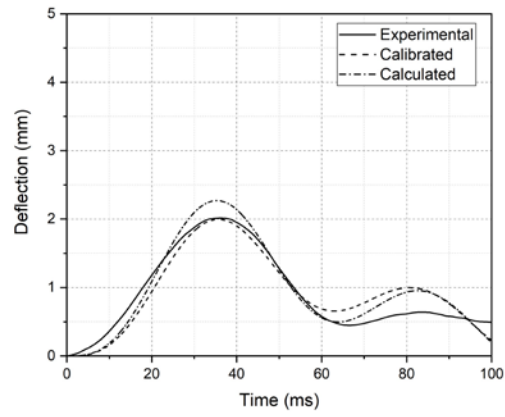
Test B3-3



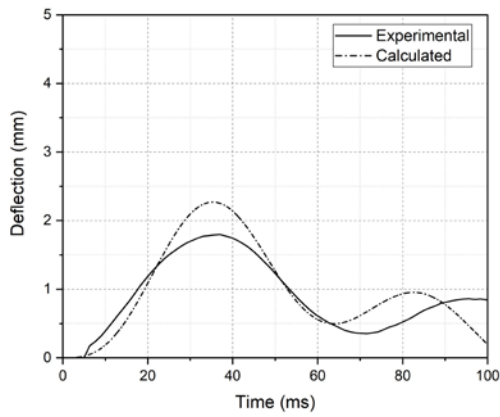
Test 3-4



Test B4-1

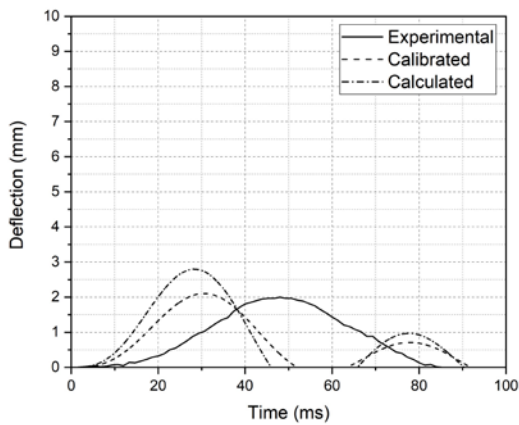


Test B4-2

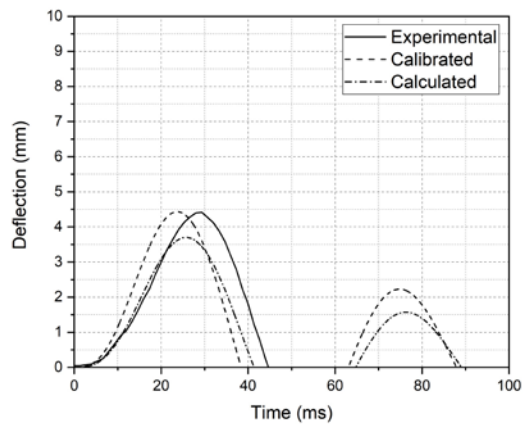


Test B4-3

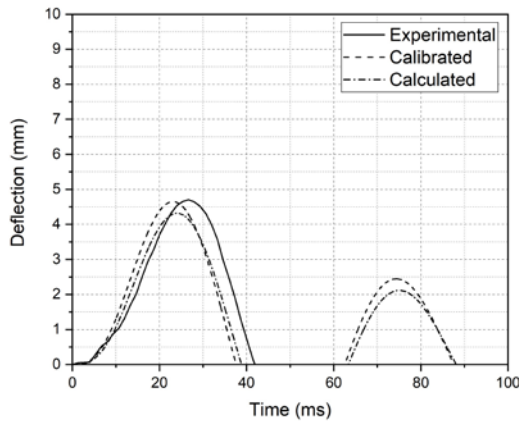
Test Series C - Calibration / Calculation



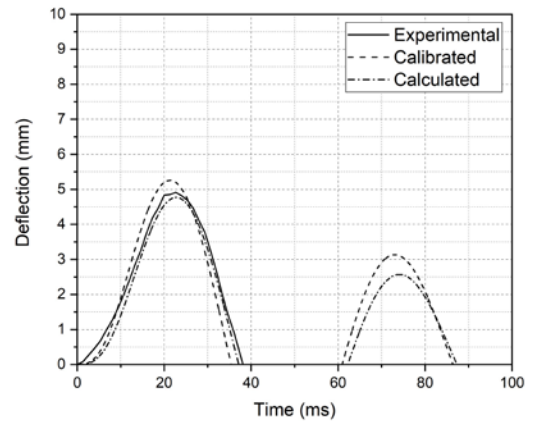
Test C1-1



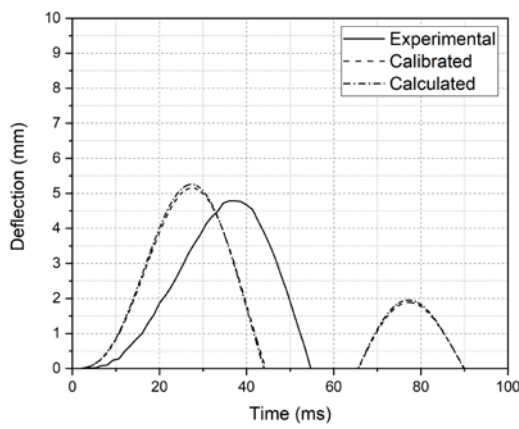
Test C1-2



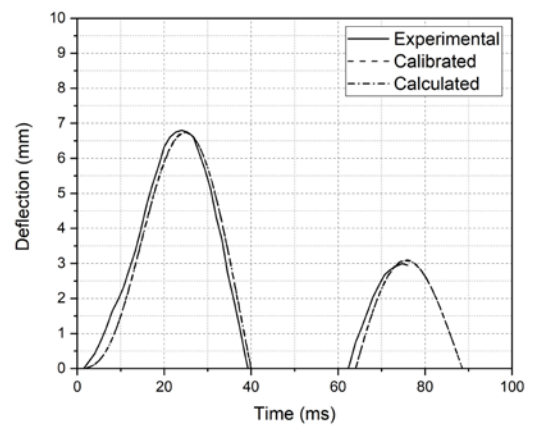
Test C1-3



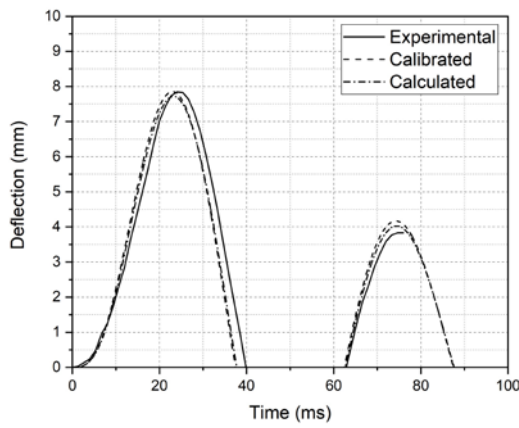
Test C1-4



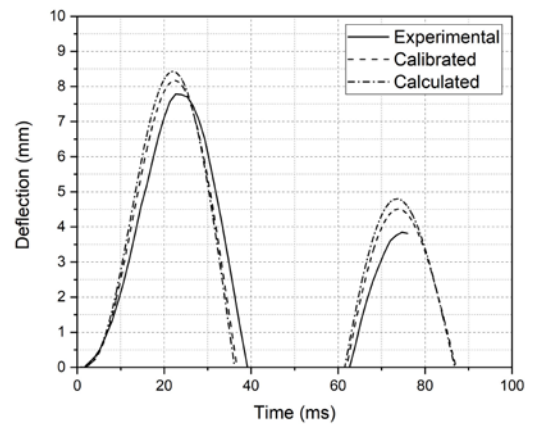
Test C2-1



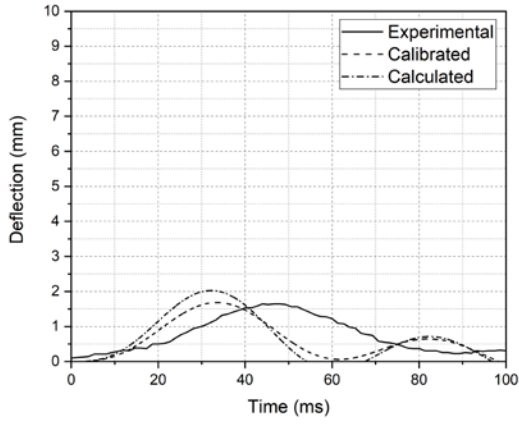
Test C2-2



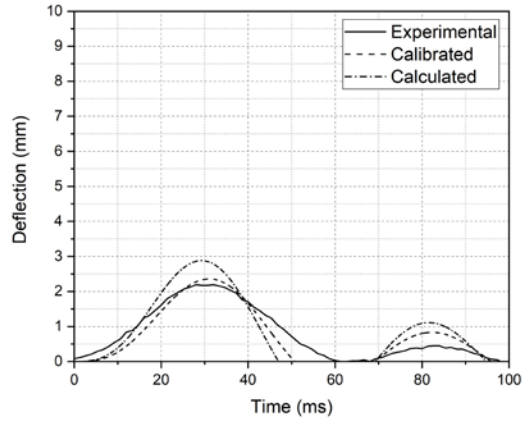
Test C2-3



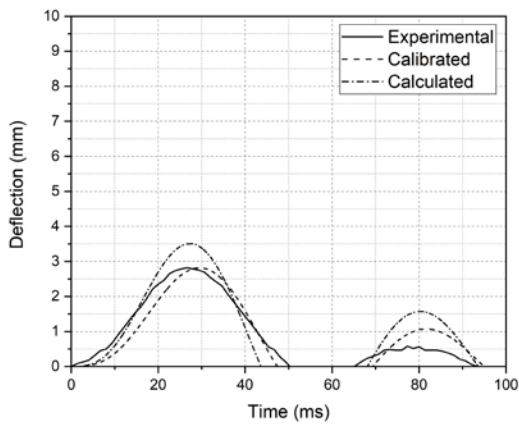
Test C2-4



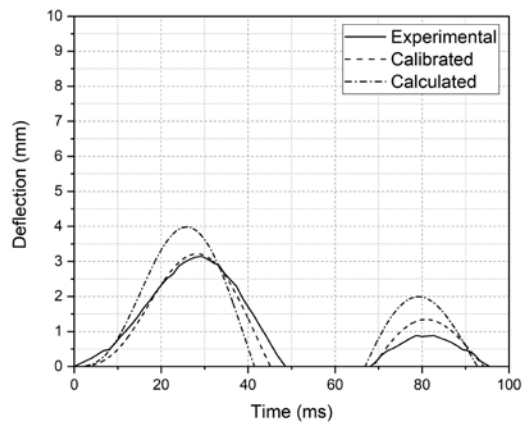
Test C3-1



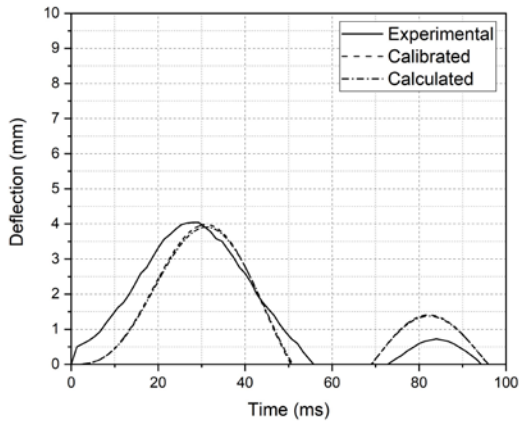
Test C3-2



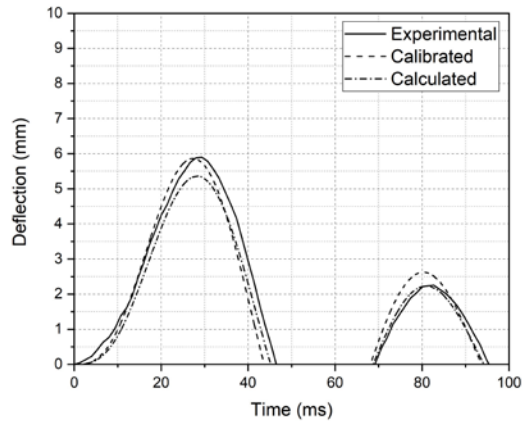
Test C3-3



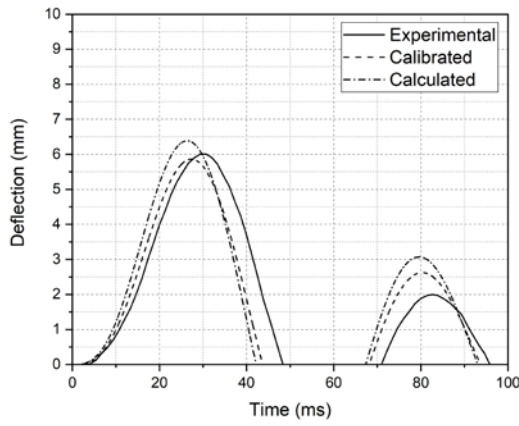
Test C3-4



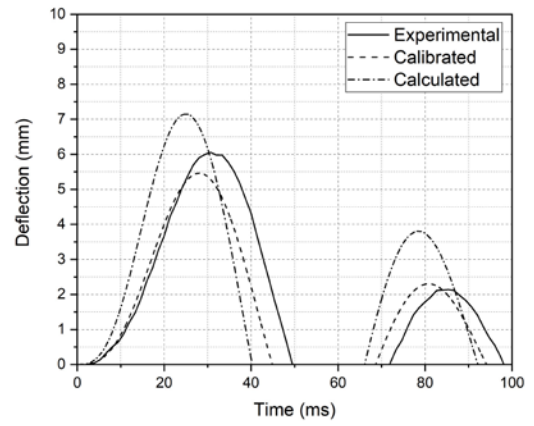
Test C4-1



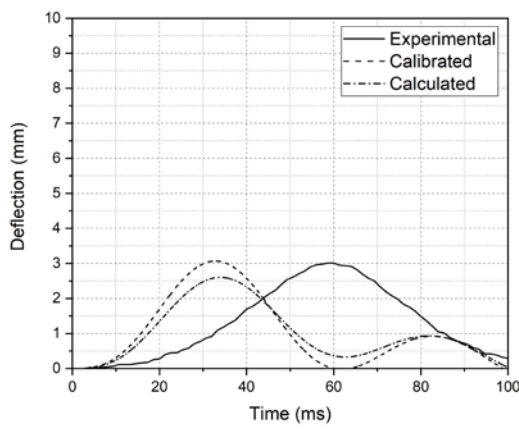
Test C4-2



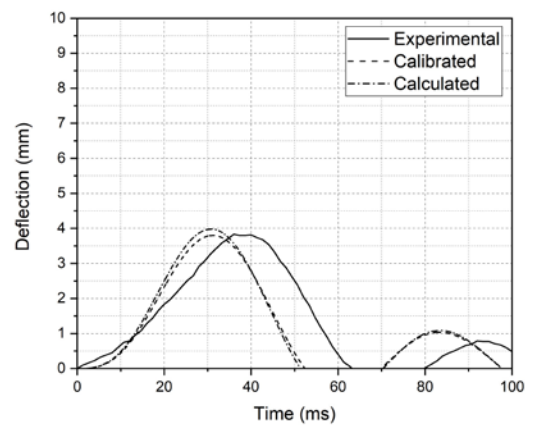
Test C4-3



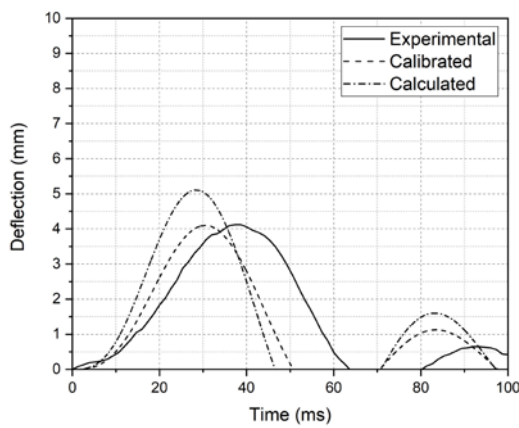
Test C4-4



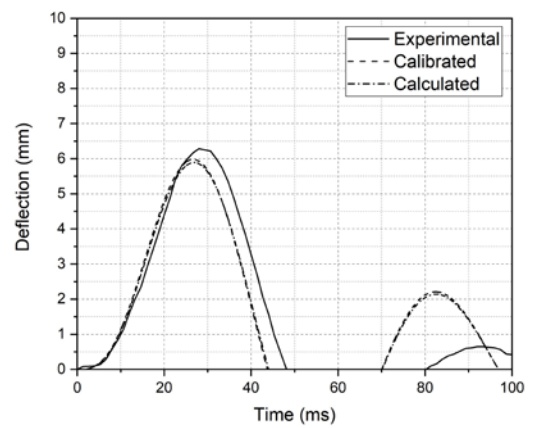
Test C5-1



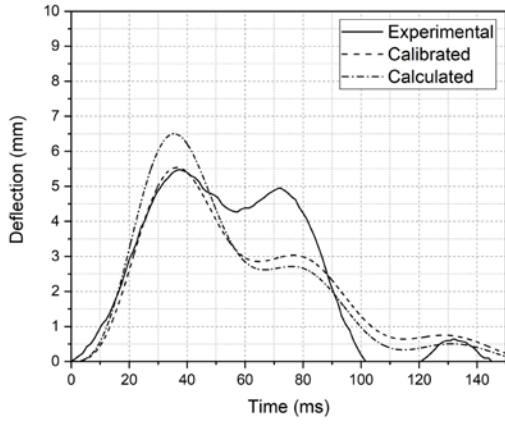
Test C5-2



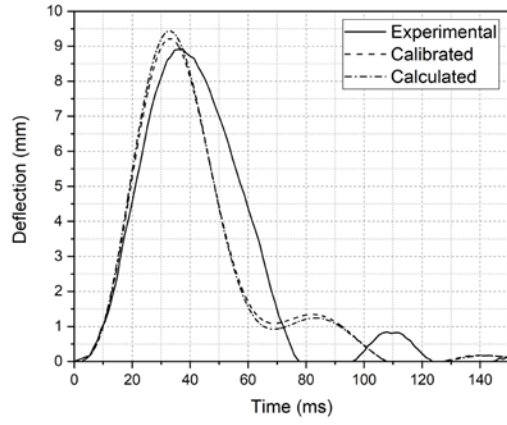
Test C5-3



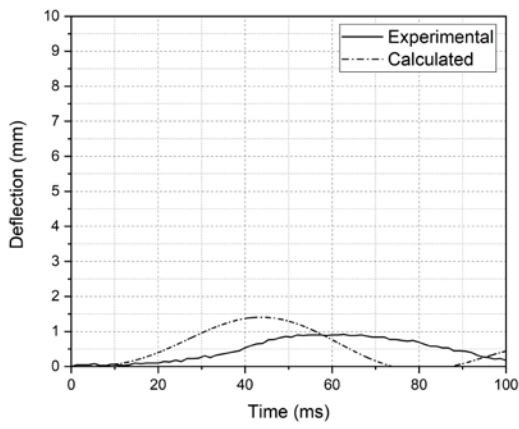
Test C5-4



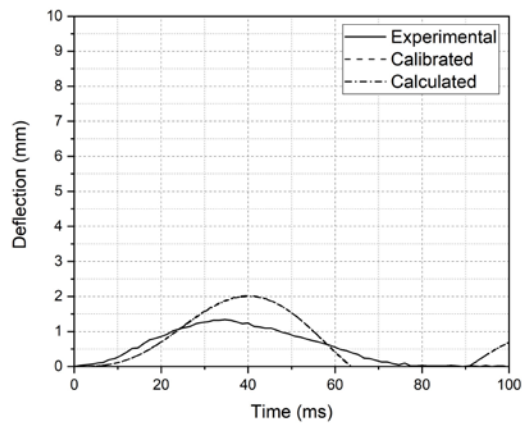
Test C6-1



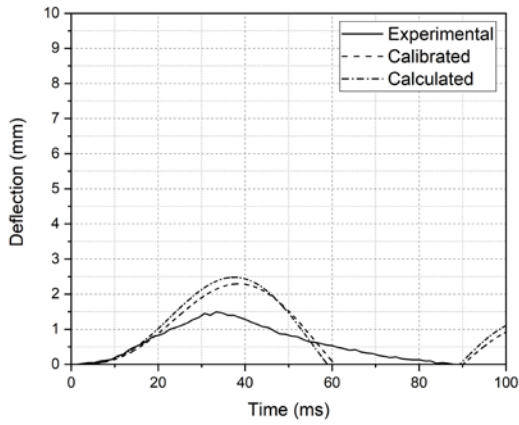
Test C6-2



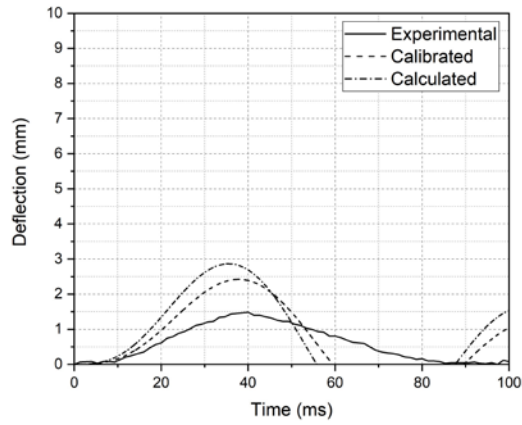
Test C7-1



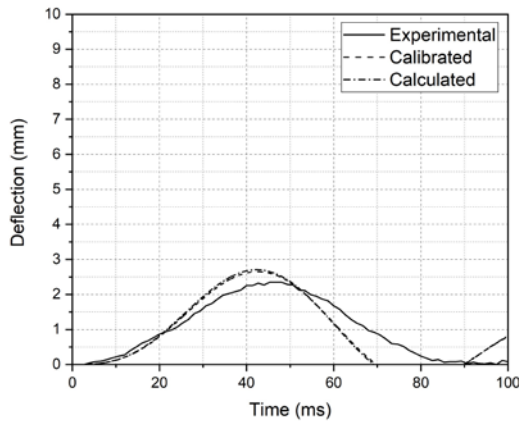
Test C7-2



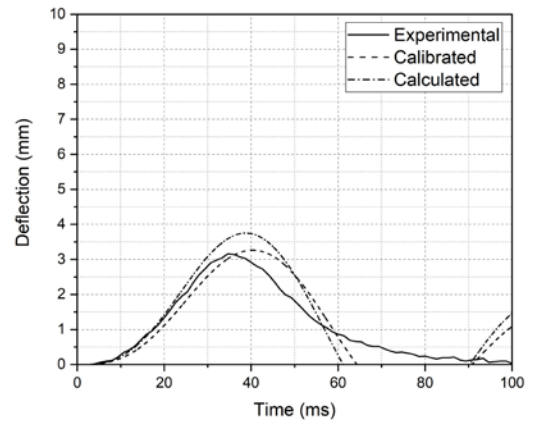
Test C7-3



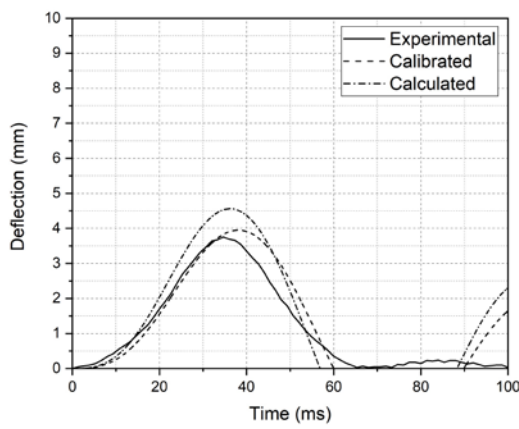
Test C7-4



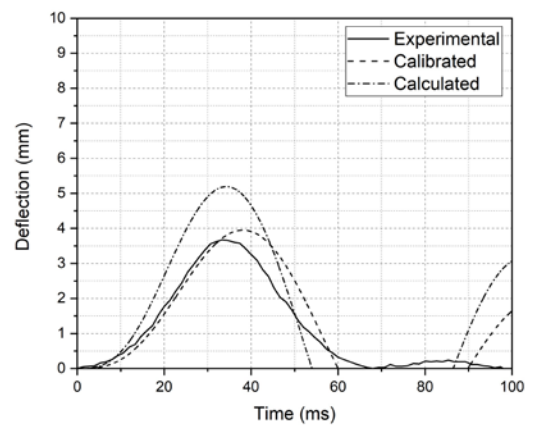
Test C8-1



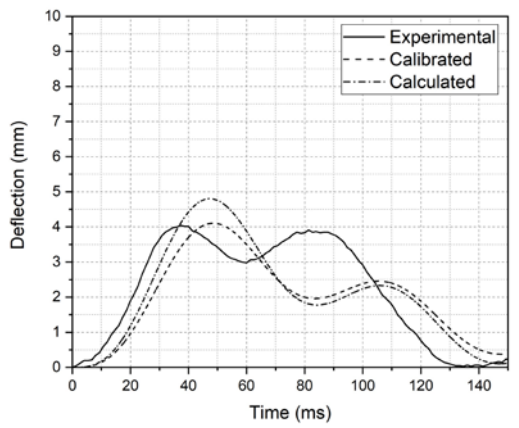
Test C8-2



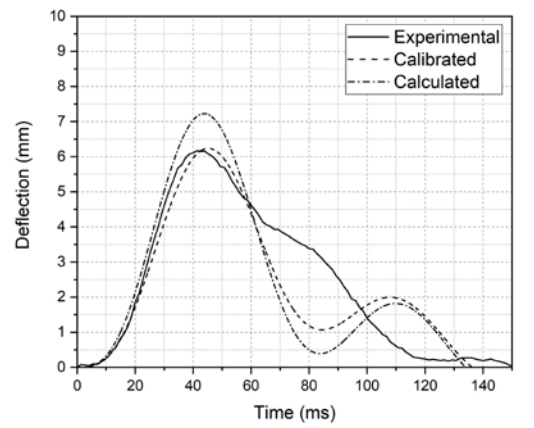
Test C8-3



Test C8-4



Test C9-1



Test C9-2

Appendix J

Test B1-1, B3-1:

$$F_c = 1.82 \times e^{-0.5} \times r^{0.7} \times M_E^{0.4} \times \tan \phi_k \times \left(\frac{mv_0^2}{2} \right)^{0.6}$$

$$F_c = 1.82 \times 0.525^{-0.5} \times 0.15^{0.7} \times 1250^{0.4} \times \tan(40^\circ) \times \left(\frac{0.28 \times 5.24^2}{2} \right)^{0.6}$$
$$= 21.71 \text{ kN}$$

$$\lambda_2 = \frac{m_2}{m} = \frac{864.2}{280} = 3.08$$

$$k_n = \frac{F_c^2}{50mv_0^2} \times \left(\frac{1 + \lambda_2}{\lambda_2} \right) = \frac{21712^2}{50 \times 280 \times 5.24^2} \times \left(\frac{1 + 3.08}{3.08} \right) = 1623.73 \text{ N/m}$$

$$T_m = 2\pi \sqrt{\frac{280}{1623.73}} = 2.61 \text{ s}$$

$$T_{m_2} = 2\pi \sqrt{\frac{863.4}{14379}} = 0.048738 \text{ s}$$

$$\frac{T_m}{T_{m_2}} = \frac{2.61}{0.04874} = 53.56$$

$$\lambda_2 = 3.08$$

By using the design chart,

$$\gamma = 0.23$$

By using Eq. 6.3,

$$\Delta = \gamma \times \frac{mv_0}{\sqrt{mk_{cr}(1 + \lambda)}} = 0.23 \times \frac{280 \times 5.24}{\sqrt{280 \times 14379 \times (1 + 3.08)}} = 2.63 \text{ mm}$$

$$\varepsilon_s = \varepsilon_{sy} \times \frac{\Delta}{\Delta_y} = 0.0028 \times \frac{2.63}{15.5} = 0.0004751$$

Test B1-2,B1-3, B3-2,B3-3:

$$F_c = 1.82 \times e^{-0.5} \times r^{0.7} \times M_E^{0.4} \times \tan\phi_k \times \left(\frac{mv_0^2}{2}\right)^{0.6}$$

$$F_c = 1.82 \times 0.525^{-0.5} \times 0.15^{0.7} \times 2500^{0.4} \times \tan(40^\circ) \times \left(\frac{0.28 \times 5.24^2}{2}\right)^{0.6}$$

$$= 15.43 \text{ kN}$$

$$\lambda_2 = \frac{m_2}{m} = \frac{864.2}{280} = 3.08$$

$$k_n = \frac{F_c^2}{50mv_0^2} \times \left(\frac{1 + \lambda_2}{\lambda_2}\right) = \frac{15437^2}{50 \times 280 \times 5.24^2} \times \left(\frac{1 + 3.08}{3.08}\right) = 2300.5 \text{ N/m}$$

$$T_m = 2\pi \sqrt{\frac{280}{2300.5}} = 2.19 \text{ s}$$

$$T_{m_2} = 2\pi \sqrt{\frac{863.4}{14379}} = 0.048738 \text{ s}$$

$$\frac{T_m}{T_{m_2}} = \frac{2.19}{0.04874} = 45$$

$$\lambda_2 = 3.08$$

By using the design chart,

$$\gamma = 0.28$$

By using Eq. 6.3,

$$\Delta = \gamma \times \frac{mv_0}{\sqrt{mk_{cr}(1 + \lambda)}} = 0.28 \times \frac{280 \times 5.24}{\sqrt{280 \times 14379 \times (1 + 3.08)}} = 1.91 \text{ mm}$$

$$\varepsilon_s = \varepsilon_{sy} \times \frac{\Delta}{\Delta_y} = 0.0028 \times \frac{1.91}{15.5} = 0.0003450$$

Test B1-4,B3-4:

$$F_c = 1.82 \times e^{-0.5} \times r^{0.7} \times M_E^{0.4} \times \tan\phi_k \times \left(\frac{mv_0^2}{2}\right)^{0.6}$$

$$F_c = 1.82 \times 0.525^{-0.5} \times 0.15^{0.7} \times 2500^{0.4} \times \tan(40^\circ) \times \left(\frac{0.28 \times 3.13^2}{2}\right)^{0.6}$$

$$= 15.43 \text{ kN}$$

$$\lambda_2 = \frac{m_2}{m} = \frac{864.2}{280} = 3.08$$

$$k_n = \frac{F_c^2}{50mv_0^2} \times \left(\frac{1 + \lambda_2}{\lambda_2} \right) = \frac{15437^2}{50 \times 280 \times 3.13^2} \times \left(\frac{1 + 3.08}{3.08} \right) = 2300 N/m$$

$$T_m = 2\pi \sqrt{\frac{280}{2300}} = 2.19 \text{ s}$$

$$T_{m_2} = 2\pi \sqrt{\frac{863.4}{14379}} = 0.048738 \text{ s}$$

$$\frac{T_m}{T_{m_2}} = \frac{2.19}{0.04874} = 45$$

By using the design chart,

$$\gamma = 0.28$$

By using Eq. 6.3,

$$\Delta = \gamma \times \frac{mv_0}{\sqrt{mk_{cr}(1 + \lambda)}} = 0.28 \times \frac{280 \times 3.13}{\sqrt{280 \times 14379 \times (1 + 3.08)}} = 1.91 \text{ mm}$$

$$\varepsilon_s = \varepsilon_{sy} \times \frac{\Delta}{\Delta_y} = 0.0028 \times \frac{1.91}{15.5} = 0.0003450$$

Test B2-1, B4-1:

$$F_c = 1.82 \times e^{-0.5} \times r^{0.7} \times M_E^{0.4} \times \tan \phi_k \times \left(\frac{mv_0^2}{2} \right)^{0.6}$$

$$F_c = 1.82 \times 0.525^{-0.5} \times 0.15^{0.7} \times 1250^{0.4} \times \tan(40^\circ) \times \left(\frac{0.435 \times 3.37^2}{2} \right)^{0.6} \\ = 16.65 \text{ kN}$$

$$k_n = \frac{F_c^2}{50mv_0^2} \times \left(\frac{1 + \lambda_2}{\lambda_2} \right) = \frac{16652^2}{50 \times 435 \times 3.37^2} \times \left(\frac{1 + 1.98}{1.98} \right) = 1687.6 N/m$$

$$T_m = 2\pi \sqrt{\frac{435}{1687.6}} = 3.19 \text{ s}$$

$$T_{m_2} = 2\pi \sqrt{\frac{863.4}{14379}} = 0.048738 \text{ s}$$

$$\frac{T_m}{T_{m_2}} = \frac{3.19}{0.04874} = 65.5$$

$$\lambda_2 = 1.98$$

By using the design chart,

$$\gamma = 0.18$$

By using Eq. 6.3,

$$\Delta = \gamma \times \frac{mv_0}{\sqrt{mk_{cr}(1+\lambda)}} = 0.18 \times \frac{435 \times 3.37}{\sqrt{280 \times 14379 \times (1+1.98)}} = 1.93 \text{ mm}$$

$$\varepsilon_s = \varepsilon_{sy} \times \frac{\Delta}{\Delta_y} = 0.0028 \times \frac{1.93}{15.5} = 0.00034865$$

Test B2-2, B7, B4-2, B4-3;

$$F_c = 1.82 \times e^{-0.5} \times r^{0.7} \times M_E^{0.4} \times \tan\phi_k \times \left(\frac{mv_0^2}{2}\right)^{0.6}$$

$$F_c = 1.82 \times 0.525^{-0.5} \times 0.15^{0.7} \times 2500^{0.4} \times \tan(40^\circ) \times \left(\frac{0.435 \times 3.37^2}{2}\right)^{0.6} \\ = 21.97 \text{ kN}$$

$$k_n = \frac{F_c^2}{50mv_0^2} \times \left(\frac{1+\lambda_2}{\lambda_2}\right) = \frac{21972^2}{50 \times 435 \times 3.37^2} \times \left(\frac{1+1.98}{1.98}\right) = 2938.3 \text{ N/m}$$

$$T_m = 2\pi \sqrt{\frac{435}{2938.3}} = 2.42 \text{ s}$$

$$T_{m_2} = 2\pi \sqrt{\frac{863.4}{14379}} = 0.048738 \text{ s}$$

$$\frac{T_m}{T_{m_2}} = \frac{2.42}{0.04874} = 49.63$$

$$\lambda_2 = 1.98$$

By using the design chart,

$$\gamma = 0.26$$

By using Eq. 6.3,

$$\Delta = \gamma \times \frac{mv_0}{\sqrt{mk_{cr}(1+\lambda)}} = 0.29 \times \frac{435 \times 3.37}{\sqrt{280 \times 14379 \times (1+1.98)}} = 2.78 \text{ mm}$$

$$\varepsilon_s = \varepsilon_{sy} \times \frac{\Delta}{\Delta_y} = 0.0028 \times \frac{3.02}{15.5} = 0.000547$$

Test B2-3

$$F_c = 1.82 \times e^{-0.5} \times r^{0.7} \times M_E^{0.4} \times \tan \phi_k \times \left(\frac{mv_0^2}{2} \right)^{0.6}$$

$$F_c = 1.82 \times 0.525^{-0.5} \times 0.15^{0.7} \times 4000^{0.4} \times \tan(40^\circ) \times \left(\frac{0.435 \times 3.37^2}{2} \right)^{0.6} \\ = 26.52 \text{ kN}$$

$$k_n = \frac{F_c^2}{50mv_0^2} \times \left(\frac{1 + \lambda_2}{\lambda_2} \right) = \frac{26520^2}{50 \times 435 \times 3.37^2} \times \left(\frac{1 + 1.98}{1.98} \right) = 4270.9 \text{ N/m}$$

$$T_m = 2\pi \sqrt{\frac{435}{4270.9}} = 2.01 \text{ s}$$

$$T_{m_2} = 2\pi \sqrt{\frac{863.4}{14379}} = 0.048738 \text{ s}$$

$$\frac{T_m}{T_{m_2}} = \frac{2.01}{0.04874} = 41.19$$

$$\lambda_2 = 1.98$$

By using the design chart,

$$\gamma = 0.3$$

By using Eq. 6.3,

$$\Delta = \gamma \times \frac{mv_0}{\sqrt{mk_{cr}(1 + \lambda)}} = 0.3 \times \frac{435 \times 3.37}{\sqrt{280 \times 14379 \times (1 + 1.57)}} = 3.47 \text{ mm}$$

$$\varepsilon_s = \varepsilon_{sy} \times \frac{\Delta}{\Delta_y} = 0.0028 \times \frac{3.02}{15.5} = 0.000547$$

Test B8:

$$F_c = 1.82 \times e^{-0.5} \times r^{0.7} \times M_E^{0.4} \times \tan \phi_k \times \left(\frac{mv_0^2}{2} \right)^{0.6}$$

$$F_c = 1.82 \times 0.525^{-0.5} \times 0.15^{0.7} \times 4000^{0.4} \times \tan(40^\circ) \times \left(\frac{0.435 \times 2.51^2}{2} \right)^{0.6} \\ = 18.62 \text{ kN}$$

$$k_n = \frac{F_c^2}{50mv_0^2} \times \left(\frac{1 + \lambda_2}{\lambda_2} \right) = \frac{18620^2}{50 \times 435 \times 2.51^2} \times \left(\frac{1 + 1.98}{1.98} \right) = 3795.3 \text{ N/m}$$

$$T_m = 2\pi \sqrt{\frac{435}{3795.3}} = 2.13 \text{ s}$$

$$T_{m_2} = 2\pi \sqrt{\frac{863.4}{14379}} = 0.048738 \text{ s}$$

$$\frac{T_m}{T_{m_2}} = \frac{2.13}{0.04874} = 43.7$$

$$\lambda_2 = 1.98$$

By using the design chart,

$$\gamma = 0.28$$

By using Eq. 6.3,

$$\Delta = \gamma \times \frac{mv_0}{\sqrt{mk_{cr}(1 + \lambda)}} = 0.28 \times \frac{435 \times 2.51}{\sqrt{280 \times 14379 \times (1 + 1.57)}} = 2.41 \text{ mm}$$

$$\varepsilon_s = \varepsilon_{sy} \times \frac{\Delta}{\Delta_y} = 0.0028 \times \frac{2.06}{15.5} = 0.0003641$$

Test C1-1

$$F_c = 1.82 \times 0.3^{-0.5} \times 0.15^{0.7} \times 3000^{0.4} \times \tan 40^\circ \times \left(\frac{0.28 \times 3.13^2}{2} \right)^{0.6} = 22 \text{ kN}$$

$$\lambda_2 = \frac{m_2}{m} = \frac{744.35}{280} = 2.66$$

$$k_n = \frac{22^2}{50 \times 280 \times 3.13^2} \times \left(\frac{1 + 2.66}{2.66} \right) = 4841.6 \text{ N/m}$$

$$\frac{T_m}{T_{m_2}} = \frac{1.511}{0.045} = 33.42 ; \gamma = 0.39$$

$$\Delta = 0.39 \times \frac{280 \times 3.13}{\sqrt{280 \times 14020 \times (1 + 2.66)}} = 2.85 \text{ mm}$$

$$\varepsilon_s = 0.00272 \times \frac{2.85}{15.6} = 0.0004969$$

Test C1-2

$$F_c = 1.82 \times 0.3^{-0.5} \times 0.15^{0.7} \times 6000^{0.4} \times \tan 40^\circ \times \left(\frac{0.28 \times 3.13^2}{2} \right)^{0.6}$$

$$= 28.98 \text{ kN}$$

$$\lambda_2 = \frac{m_2}{m} = \frac{744.35}{280} = 2.66$$

$$k_n = \frac{28.98^2}{50 \times 280 \times 3.13^2} \times \left(\frac{1 + 2.66}{2.66} \right) = 8429.7 \text{ N/m}$$

$$\frac{T_m}{T_{m_2}} = \frac{1.1451}{0.045} = 25.01 ; \gamma = 0.46$$

$$\Delta = 0.46 \times \frac{280 \times 3.13}{\sqrt{280 \times 14020 \times (1 + 2.66)}} = 3.36 \text{ mm}$$

$$\varepsilon_s = 0.00272 \times \frac{3.36}{15.6} = 0.0005858$$

Test C1-3

$$F_c = 1.82 \times 0.3^{-0.5} \times 0.15^{0.7} \times 10000^{0.4} \times \tan 40^\circ \times \left(\frac{0.28 \times 3.13^2}{2} \right)^{0.6}$$

$$= 35.56 \text{ kN}$$

$$\lambda_2 = \frac{m_2}{m} = \frac{744.35}{280} = 2.66$$

$$k_n = \frac{35.56^2}{50 \times 280 \times 3.13^2} \times \left(\frac{1 + 2.66}{2.66} \right) = 12685 \text{ N/m}$$

$$\frac{T_m}{T_{m_2}} = \frac{0.9335}{0.045} = 20.39 ; \gamma = 0.59$$

$$\Delta = 0.59 \times \frac{280 \times 3.13}{\sqrt{280 \times 14020 \times (1 + 2.66)}} = 4.31 \text{ mm}$$

$$\varepsilon_s = 0.00272 \times \frac{4.31}{15.6} = 0.0007515$$

Test C1-4

$$F_c = 1.82 \times 0.3^{-0.5} \times 0.15^{0.7} \times 15000^{0.4} \times \tan 40^\circ \times \left(\frac{0.28 \times 3.13^2}{2} \right)^{0.6}$$
$$= 41.81 \text{ kN}$$

$$\lambda_2 = \frac{m_2}{m} = \frac{744.35}{280} = 2.66$$

$$k_n = \frac{41.81^2}{50 \times 280 \times 3.13^2} \times \left(\frac{1 + 2.66}{2.66} \right) = 17545.42 \text{ N/m}$$

$$\frac{T_m}{T_{m_2}} = \frac{0.794}{0.045} = 17.33 ; \gamma = 0.65$$

$$\Delta = 0.65 \times \frac{280 \times 3.13}{\sqrt{280 \times 14020 \times (1 + 2.66)}} = 4.75 \text{ mm}$$

$$\varepsilon_s = 0.00272 \times \frac{4.75}{15.6} = 0.0008282$$

Test C2-1

$$F_c = 1.82 \times 0.3^{-0.5} \times 0.15^{0.7} \times 3000^{0.4} \times \tan 40^\circ \times \left(\frac{0.28 \times 5.24^2}{2} \right)^{0.6}$$
$$= 40.76 \text{ kN}$$

$$\lambda_2 = \frac{m_2}{m} = \frac{744.35}{280} = 2.66$$

$$k_n = \frac{40.76^2}{50 \times 280 \times 5.24^2} \times \left(\frac{1 + 2.66}{2.66} \right) = 5949.8 \text{ N/m}$$

$$\frac{T_m}{T_{m_2}} = \frac{1.363}{0.045} = 29.77 ; \gamma = 0.45$$

$$\Delta = 0.45 \times \frac{280 \times 5.24}{\sqrt{280 \times 14020 \times (1 + 2.66)}} = 5.51 \text{ mm}$$

$$\varepsilon_s = 0.00272 \times \frac{5.51}{15.6} = 0.00096071$$

Test C2-2

$$F_c = 1.82 \times 0.3^{-0.5} \times 0.15^{0.7} \times 6000^{0.4} \times \tan 40^\circ \times \left(\frac{0.28 \times 5.24^2}{2} \right)^{0.6}$$

$$= 53.79 \text{ kN}$$

$$\lambda_2 = \frac{m_2}{m} = \frac{744.35}{280} = 2.66$$

$$k_n = \frac{53.79^2}{50 \times 280 \times 5.24^2} \times \left(\frac{1 + 2.66}{2.66} \right) = 10359.21 \text{ N/m}$$

$$\frac{T_m}{T_{m_2}} = \frac{1.033}{0.045} = 22.56 ; \gamma = 0.56$$

$$\Delta = 0.56 \times \frac{280 \times 5.24}{\sqrt{280 \times 14020 \times (1 + 2.66)}} = 6.85 \text{ mm}$$

$$\varepsilon_s = 0.00272 \times \frac{6.85}{15.6} = 0.001194$$

Test C2-3

$$F_c = 1.82 \times 0.3^{-0.5} \times 0.15^{0.7} \times 10000^{0.4} \times \tan 40^\circ \times \left(\frac{0.28 \times 5.24^2}{2} \right)^{0.6}$$

$$= 65.99 \text{ kN}$$

$$\lambda_2 = \frac{m_2}{m} = \frac{744.35}{280} = 2.66$$

$$k_n = \frac{65.99^2}{50 \times 280 \times 5.24^2} \times \left(\frac{1 + 2.66}{2.66} \right) = 15588.54 \text{ N/m}$$

$$\frac{T_m}{T_{m_2}} = \frac{0.842}{0.045} = 18.39 ; \gamma = 0.64$$

$$\Delta = 0.64 \times \frac{280 \times 5.24}{\sqrt{280 \times 14020 \times (1 + 2.66)}} = 7.83 \text{ mm}$$

$$\varepsilon_s = 0.00272 \times \frac{7.83}{15.6} = 0.001365$$

Test C2-4

$$F_c = 1.82 \times 0.3^{-0.5} \times 0.15^{0.7} \times 15000^{0.4} \times \tan 40^\circ \times \left(\frac{0.28 \times 5.24^2}{2} \right)^{0.6}$$

$$= 77.61 \text{ kN}$$

$$\lambda_2 = \frac{m_2}{m} = \frac{744.35}{280} = 2.66$$

$$k_n = \frac{77.61^2}{50 \times 280 \times 5.24^2} \times \left(\frac{1 + 2.66}{2.66} \right) = 21561.48 \text{ N/m}$$

$$\frac{T_m}{T_{m_2}} = \frac{0.716}{0.045} = 15.64 ; \gamma = 0.69$$

$$\Delta = 0.69 \times \frac{280 \times 5.24}{\sqrt{280 \times 14020 \times (1 + 2.66)}} = 8.45 \text{ mm}$$

$$\varepsilon_s = 0.00272 \times \frac{8.45}{15.6} = 0.00147$$

Test C3-1

$$F_c = 1.82 \times 0.5^{-0.5} \times 0.15^{0.7} \times 3000^{0.4} \times \tan 40^\circ \times \left(\frac{0.28 \times 3.13^2}{2} \right)^{0.6}$$

$$= 17.01 \text{ kN}$$

$$\lambda_2 = \frac{m_2}{m} = \frac{827.07}{280} = 2.95$$

$$k_n = \frac{17.01^2}{50 \times 280 \times 3.13^2} \times \left(\frac{1 + 2.95}{2.95} \right) = 2825.53 \text{ N/m}$$

$$\frac{T_m}{T_{m_2}} = \frac{1.978}{0.045} = 40.98 ; \gamma = 0.32$$

$$\Delta = 0.32 \times \frac{280 \times 3.13}{\sqrt{280 \times 14020 \times (1 + 2.95)}} = 2.25 \text{ mm}$$

$$\varepsilon_s = 0.00272 \times \frac{2.25}{15.6} = 0.0003923$$

Test C3-2

$$F_c = 1.82 \times 0.5^{-0.5} \times 0.15^{0.7} \times 6000^{0.4} \times \tan 40^\circ \times \left(\frac{0.28 \times 3.13^2}{2} \right)^{0.6}$$

$$= 22.45 \text{ kN}$$

$$\lambda_2 = \frac{m_2}{m} = \frac{827.07}{280} = 2.95$$

$$k_n = \frac{22.45^2}{50 \times 280 \times 3.13^2} \times \left(\frac{1 + 2.95}{2.95} \right) = 4919.54 \text{ N/m}$$

$$\frac{T_m}{T_{m_2}} = \frac{1.5}{0.045} = 31.06 ; \gamma = 0.43$$

$$\Delta = 0.43 \times \frac{280 \times 3.13}{\sqrt{280 \times 14020 \times (1 + 2.95)}} = 3.02 \text{ mm}$$

$$\varepsilon_s = 0.00272 \times \frac{3.02}{15.6} = 0.00052656$$

Test C3-3

$$F_c = 1.82 \times 0.5^{-0.5} \times 0.15^{0.7} \times 10000^{0.4} \times \tan 40^\circ \times \left(\frac{0.28 \times 3.13^2}{2} \right)^{0.6}$$

$$= 27.54 \text{ kN}$$

$$\lambda_2 = \frac{m_2}{m} = \frac{827.07}{280} = 2.95$$

$$k_n = \frac{27.54^2}{50 \times 280 \times 3.13^2} \times \left(\frac{1 + 2.95}{2.95} \right) = 7402.93 \text{ N/m}$$

$$\frac{T_m}{T_{m_2}} = \frac{1.222}{0.045} = 25.32 ; \gamma = 0.51$$

$$\Delta = 0.51 \times \frac{280 \times 3.13}{\sqrt{280 \times 14020 \times (1 + 2.95)}} = 3.59 \text{ mm}$$

$$\varepsilon_s = 0.00272 \times \frac{3.59}{15.6} = 0.0006259$$

Test C3-4

$$F_c = 1.82 \times 0.5^{-0.5} \times 0.15^{0.7} \times 15000^{0.4} \times \tan 40^\circ \times \left(\frac{0.28 \times 3.13^2}{2} \right)^{0.6}$$

$$= 32.39 \text{ kN}$$

$$\lambda_2 = \frac{m_2}{m} = \frac{827.07}{280} = 2.95$$

$$k_n = \frac{32.39^2}{50 \times 280 \times 3.13^2} \times \left(\frac{1 + 2.95}{2.95} \right) = 10239.45 \text{ N/m}$$

$$\frac{T_m}{T_{m_2}} = \frac{1.039}{0.045} = 21.53 ; \gamma = 0.57$$

$$\Delta = 0.57 \times \frac{280 \times 3.13}{\sqrt{280 \times 14020 \times (1 + 2.95)}} = 4 \text{ mm}$$

$$\varepsilon_s = 0.00272 \times \frac{4}{15.6} = 0.0006974$$

Test C4-1

$$F_c = 1.82 \times 0.5^{-0.5} \times 0.15^{0.7} \times 3000^{0.4} \times \tan 40^\circ \times \left(\frac{0.28 \times 5.24^2}{2} \right)^{0.6}$$

$$= 31.58 \text{ kN}$$

$$\lambda_2 = \frac{m_2}{m} = \frac{827.07}{280} = 2.95$$

$$k_n = \frac{31.58^2}{50 \times 280 \times 5.24^2} \times \left(\frac{1 + 2.95}{2.95} \right) = 3472.28 \text{ N/m}$$

$$\frac{T_m}{T_{m_2}} = \frac{1.784}{0.045} = 37.44 ; \gamma = 0.36$$

$$\Delta = 0.36 \times \frac{280 \times 5.24}{\sqrt{280 \times 14020 \times (1 + 2.95)}} = 4.24 \text{ mm}$$

$$\varepsilon_s = 0.00272 \times \frac{4.24}{15.6} = 0.0007393$$

Test C4-2

$$F_c = 1.82 \times 0.5^{-0.5} \times 0.15^{0.7} \times 6000^{0.4} \times \tan 40^\circ \times \left(\frac{0.28 \times 5.24^2}{2} \right)^{0.6}$$

$$= 41.67 \text{ kN}$$

$$\lambda_2 = \frac{m_2}{m} = \frac{827.07}{280} = 2.95$$

$$k_n = \frac{41.67^2}{50 \times 280 \times 5.24^2} \times \left(\frac{1 + 2.95}{2.95} \right) = 6045.6 \text{ N/m}$$

$$\frac{T_m}{T_{m_2}} = \frac{1.352}{0.045} = 28.38 ; \gamma = 0.46$$

$$\Delta = 0.46 \times \frac{280 \times 5.24}{\sqrt{280 \times 14020 \times (1 + 2.95)}} = 5.41 \text{ mm}$$

$$\varepsilon_s = 0.00272 \times \frac{5.41}{15.6} = 0.0009433$$

Test C4-3

$$F_c = 1.82 \times 0.5^{-0.5} \times 0.15^{0.7} \times 10000^{0.4} \times \tan 40^\circ \times \left(\frac{0.28 \times 5.24^2}{2} \right)^{0.6}$$

$$= 51.11 \text{ kN}$$

$$\lambda_2 = \frac{m_2}{m} = \frac{827.07}{280} = 2.95$$

$$k_n = \frac{51.11^2}{50 \times 280 \times 5.24^2} \times \left(\frac{1 + 2.95}{2.95} \right) = 9097.42 \text{ N/m}$$

$$\frac{T_m}{T_{m_2}} = \frac{1.1023}{0.045} = 22.84 ; \gamma = 0.55$$

$$\Delta = 0.55 \times \frac{280 \times 5.24}{\sqrt{280 \times 14020 \times (1 + 2.95)}} = 6.48 \text{ mm}$$

$$\varepsilon_s = 0.00272 \times \frac{6.48}{15.6} = 0.00113$$

Test C4-4

$$F_c = 1.82 \times 0.5^{-0.5} \times 0.15^{0.7} \times 15000^{0.4} \times \tan 40^\circ \times \left(\frac{0.28 \times 5.24^2}{2} \right)^{0.6}$$

$$= 60.11 \text{ kN}$$

$$\lambda_2 = \frac{m_2}{m} = \frac{827.07}{280} = 2.95$$

$$k_n = \frac{60.11^2}{50 \times 280 \times 5.24^2} \times \left(\frac{1 + 2.95}{2.95} \right) = 12583.21 \text{ N/m}$$

$$\frac{T_m}{T_{m_2}} = \frac{0.9372}{0.045} = 19.42 ; \gamma = 0.61$$

$$\Delta = 0.61 \times \frac{280 \times 5.24}{\sqrt{280 \times 14020 \times (1 + 2.95)}} = 7.18 \text{ mm}$$

$$\varepsilon_s = 0.00272 \times \frac{7.18}{15.6} = 0.001252$$

Test C5-1

$$F_c = 1.82 \times 0.5^{-0.5} \times 0.15^{0.7} \times 3000^{0.4} \times \tan 40^\circ \times \left(\frac{0.435 \times 3.37^2}{2} \right)^{0.6}$$

$$= 24.21 \text{ kN}$$

$$\lambda_2 = \frac{m_2}{m} = \frac{827.07}{435} = 1.90$$

$$k_n = \frac{24.21^2}{50 \times 435 \times 3.37^2} \times \left(\frac{1 + 1.9}{1.9} \right) = 3623.34 \text{ N/m}$$

$$\frac{T_m}{T_{m_2}} = \frac{2.177}{0.046} = 45.11; \gamma = 0.29$$

$$\Delta = 0.29 \times \frac{435 \times 3.37}{\sqrt{435 \times 14020 \times (1 + 1.9)}} = 3.19 \text{ mm}$$

$$\varepsilon_s = 0.00272 \times \frac{3.19}{15.6} = 0.000562$$

Test C5-2

$$F_c = 1.82 \times 0.5^{-0.5} \times 0.15^{0.7} \times 6000^{0.4} \times \tan 40^\circ \times \left(\frac{0.435 \times 3.37^2}{2} \right)^{0.6}$$

$$= 31.96 \text{ kN}$$

$$\lambda_2 = \frac{m_2}{m} = \frac{827.07}{435} = 1.90$$

$$k_n = \frac{31.96^2}{50 \times 435 \times 3.37^2} \times \left(\frac{1 + 1.9}{1.9} \right) = 6308.6 \text{ N/m}$$

$$\frac{T_m}{T_{m_2}} = \frac{1.65}{0.046} = 34.19; \gamma = 0.39$$

$$\Delta = 0.39 \times \frac{435 \times 3.37}{\sqrt{435 \times 14020 \times (1 + 1.9)}} = 4.3 \text{ mm}$$

$$\varepsilon_s = 0.00272 \times \frac{4.3}{15.6} = 0.0007497$$

Test C5-3

$$F_c = 1.82 \times 0.5^{-0.5} \times 0.15^{0.7} \times 10000^{0.4} \times \tan 40^\circ \times \left(\frac{0.435 \times 3.37^2}{2} \right)^{0.6}$$

$$= 39.2 \text{ kN}$$

$$\lambda_2 = \frac{m_2}{m} = \frac{827.07}{435} = 1.90$$

$$k_n = \frac{39.2^2}{50 \times 435 \times 3.37^2} \times \left(\frac{1 + 1.9}{1.9} \right) = 9493.2 \text{ N/m}$$

$$\frac{T_m}{T_{m_2}} = \frac{1.345}{0.046} = 27.87; \gamma = 0.47$$

$$\Delta = 0.47 \times \frac{435 \times 3.37}{\sqrt{435 \times 14020 \times (1 + 1.9)}} = 5.18 \text{ mm}$$

$$\varepsilon_s = 0.00272 \times \frac{5.18}{15.6} = 0.00090318$$

Test C5-4

$$F_c = 1.82 \times 0.5^{-0.5} \times 0.15^{0.7} \times 15000^{0.4} \times \tan 40^\circ \times \left(\frac{0.435 \times 3.37^2}{2} \right)^{0.6}$$

$$= 46.1 \text{ kN}$$

$$\lambda_2 = \frac{m_2}{m} = \frac{827.07}{435} = 1.90$$

$$k_n = \frac{46.1^2}{50 \times 435 \times 3.37^2} \times \left(\frac{1 + 1.9}{1.9} \right) = 13130.62 \text{ N/m}$$

$$\frac{T_m}{T_{m_2}} = \frac{1.144}{0.046} = 23.7; \gamma = 0.54$$

$$\Delta = 0.54 \times \frac{435 \times 3.37}{\sqrt{435 \times 14020 \times (1 + 1.9)}} = 5.95 \text{ mm}$$

$$\varepsilon_s = 0.00272 \times \frac{5.95}{15.6} = 0.001037$$

Test C6-1

$$F_c = 1.82 \times 0.5^{-0.5} \times 0.2^{0.7} \times 3000^{0.4} \times \tan 40^\circ \times \left(\frac{1.02 \times 4.43^2}{2} \right)^{0.6} = 68.58 \text{ kN}$$

$$\lambda_2 = \frac{m_2}{m} = \frac{889.71}{1020} = 0.872 < 1$$

$$k_n = \frac{68.58^2}{50 \times 1020 \times 4.43^2} = 4699.1 \text{ N/m}$$

$$\frac{T_m}{T_{m_2}} = \frac{2.93}{0.049} = 58.48; \gamma = 0.24$$

$$\Delta = 0.24 \times \frac{1020 \times 4.43}{\sqrt{1020 \times 14020 \times (1 + 0.872)}} = 6.63 \text{ mm}$$

$$\varepsilon_s = 0.00272 \times \frac{6.63}{15.6} = 0.001156$$

Test C6-2

$$F_c = 1.82 \times 0.5^{-0.5} \times 0.2^{0.7} \times 6000^{0.4} \times \tan 40^\circ \times \left(\frac{1.02 \times 4.43^2}{2} \right)^{0.6} = 90.5 \text{ kN}$$

$$\lambda_2 = \frac{m_2}{m} = \frac{889.71}{1020} = 0.872 < 1$$

$$k_n = \frac{90.5^2}{50 \times 1020 \times 4.43^2} = 8181.6 \text{ N/m}$$

$$\frac{T_m}{T_{m_2}} = \frac{2.218}{0.049} = 44.32; \gamma = 0.34$$

$$\Delta = 0.34 \times \frac{1020 \times 4.43}{\sqrt{1020 \times 14020 \times (1 + 0.872)}} = 9.39 \text{ mm}$$

$$\varepsilon_s = 0.00272 \times \frac{9.39}{15.6} = 0.00164$$

Test C7-1

$$F_c = 1.82 \times 1^{-0.5} \times 0.15^{0.7} \times 3000^{0.4} \times \tan 40^\circ \times \left(\frac{0.28 \times 3.13^2}{2} \right)^{0.6} = 12.03 \text{ kN}$$

$$\lambda_2 = \frac{m_2}{m} = \frac{1254.9}{280} = 4.48$$

$$k_n = \frac{12.03^2}{50 \times 280 \times 3.13^2} \times \left(\frac{1 + 4.48}{4.48} \right) = 1290.95 \text{ N/m}$$

$$\frac{T_m}{T_{m_2}} = \frac{2.93}{0.059} = 49.23; \gamma = 0.245$$

$$\Delta = 0.245 \times \frac{280 \times 3.13}{\sqrt{280 \times 14020 \times (1 + 4.48)}} = 1.46 \text{ mm}$$

$$\varepsilon_s = 0.00272 \times \frac{1.46}{15.6} = 0.0002546$$

Test C7-2

$$F_c = 1.82 \times 1^{-0.5} \times 0.15^{0.7} \times 6000^{0.4} \times \tan 40^\circ \times \left(\frac{0.28 \times 3.13^2}{2} \right)^{0.6} = 15.88 \text{ kN}$$

$$\lambda_2 = \frac{m_2}{m} = \frac{1254.9}{280} = 4.48$$

$$k_n = \frac{15.88^2}{50 \times 280 \times 3.13^2} \times \left(\frac{1 + 4.48}{4.48} \right) = 2247.67 \text{ N/m}$$

$$\frac{T_m}{T_{m_2}} = \frac{2.22}{0.059} = 37.3 ; \gamma = 0.34$$

$$\Delta = 0.34 \times \frac{280 \times 3.13}{\sqrt{280 \times 14020 \times (1 + 4.48)}} = 2 \text{ mm}$$

$$\varepsilon_s = 0.00272 \times \frac{2}{15.6} = 0.000354$$

Test C7-3

$$F_c = 1.82 \times 1^{-0.5} \times 0.15^{0.7} \times 10000^{0.4} \times \tan 40^\circ \times \left(\frac{0.28 \times 3.13^2}{2} \right)^{0.6} \\ = 19.48 \text{ kN}$$

$$\lambda_2 = \frac{m_2}{m} = \frac{1254.9}{280} = 4.48$$

$$k_n = \frac{19.48^2}{50 \times 280 \times 3.13^2} \times \left(\frac{1 + 4.48}{4.48} \right) = 3382.3 \text{ N/m}$$

$$\frac{T_m}{T_{m_2}} = \frac{1.81}{0.059} = 30.4 ; \gamma = 0.42$$

$$\Delta = 0.42 \times \frac{280 \times 3.13}{\sqrt{280 \times 14020 \times (1 + 4.48)}} = 2.51 \text{ mm}$$

$$\varepsilon_s = 0.00272 \times \frac{2.51}{15.6} = 0.0004376$$

Test C7-4

$$F_c = 1.82 \times 1^{-0.5} \times 0.15^{0.7} \times 15000^{0.4} \times \tan 40^\circ \times \left(\frac{0.28 \times 3.13^2}{2} \right)^{0.6} = 22.9 \text{ kN}$$

$$\lambda_2 = \frac{m_2}{m} = \frac{1254.9}{280} = 4.48$$

$$k_n = \frac{22.9^2}{50 \times 280 \times 3.13^2} \times \left(\frac{1 + 4.48}{4.48} \right) = 4678.26 \text{ N/m}$$

$$\frac{T_m}{T_{m_2}} = \frac{1.54}{0.059} = 25.86 ; \gamma = 0.48$$

$$\Delta = 0.48 \times \frac{280 \times 3.13}{\sqrt{280 \times 14020 \times (1 + 4.48)}} = 2.87 \text{ mm}$$

$$\varepsilon_s = 0.00272 \times \frac{2.87}{15.6} = 0.0005004$$

Test C8-1

$$F_c = 1.82 \times 1^{-0.5} \times 0.15^{0.7} \times 3000^{0.4} \times \tan 40^\circ \times \left(\frac{0.28 \times 5.24^2}{2} \right)^{0.6} = 22.33 \text{ kN}$$

$$\lambda_2 = \frac{m_2}{m} = \frac{1254.9}{280} = 4.48$$

$$k_n = \frac{22.33^2}{50 \times 280 \times 5.24^2} \times \left(\frac{1 + 4.48}{4.48} \right) = 1586.44 \text{ N/m}$$

$$\frac{T_m}{T_{m_2}} = \frac{2.64}{0.059} = 44.4 ; \gamma = 0.28$$

$$\Delta = 0.28 \times \frac{280 \times 5.24}{\sqrt{280 \times 14020 \times (1 + 4.48)}} = 2.8 \text{ mm}$$

$$\varepsilon_s = 0.00272 \times \frac{2.8}{15.6} = 0.0004882$$

Test C8-2

$$F_c = 1.82 \times 1^{-0.5} \times 0.15^{0.7} \times 6000^{0.4} \times \tan 40^\circ \times \left(\frac{0.28 \times 5.24^2}{2} \right)^{0.6} = 29.46 \text{ kN}$$

$$\lambda_2 = \frac{m_2}{m} = \frac{1254.9}{280} = 4.48$$

$$k_n = \frac{29.46^2}{50 \times 280 \times 5.24^2} \times \left(\frac{1 + 4.48}{4.48} \right) = 2762.15 \text{ N/m}$$

$$\frac{T_m}{T_{m_2}} = \frac{2}{0.059} = 33.65 ; \gamma = 0.38$$

$$\Delta = 0.38 \times \frac{280 \times 5.24}{\sqrt{280 \times 14020 \times (1 + 4.48)}} = 3.8 \text{ mm}$$

$$\varepsilon_s = 0.00272 \times \frac{3.8}{15.6} = 0.0006625$$

Test C8-3

$$F_c = 1.82 \times 1^{-0.5} \times 0.15^{0.7} \times 10000^{0.4} \times \tan 40^\circ \times \left(\frac{0.28 \times 5.24^2}{2} \right)^{0.6}$$

$$= 36.14 \text{ kN}$$

$$\lambda_2 = \frac{m_2}{m} = \frac{1254.9}{280} = 4.48$$

$$k_n = \frac{36.14^2}{50 \times 280 \times 5.24^2} \times \left(\frac{1 + 4.48}{4.48} \right) = 4156.5 \text{ N/m}$$

$$\frac{T_m}{T_{m_2}} = \frac{1.63}{0.059} = 27.45 ; \gamma = 0.46$$

$$\Delta = 0.46 \times \frac{280 \times 5.24}{\sqrt{280 \times 14020 \times (1 + 4.48)}} = 4.59 \text{ mm}$$

$$\varepsilon_s = 0.00272 \times \frac{4.59}{15.6} = 0.0008$$

Test C8-4

$$F_c = 1.82 \times 1^{-0.5} \times 0.15^{0.7} \times 15000^{0.4} \times \tan 40^\circ \times \left(\frac{0.28 \times 5.24^2}{2} \right)^{0.6} = 42.5 \text{ kN}$$

$$\lambda_2 = \frac{m_2}{m} = \frac{1254.9}{280} = 4.48$$

$$k_n = \frac{42.5^2}{50 \times 280 \times 5.24^2} \times \left(\frac{1 + 4.48}{4.48} \right) = 5749.1 \text{ N/m}$$

$$\frac{T_m}{T_{m_2}} = \frac{1.387}{0.059} = 23.32 ; \gamma = 0.525$$

$$\Delta = 0.525 \times \frac{280 \times 5.24}{\sqrt{280 \times 14020 \times (1 + 4.48)}} = 5.25 \text{ mm}$$

$$\varepsilon_s = 0.00272 \times \frac{5.25}{15.6} = 0.0009153$$

Test C9-1

$$F_c = 1.82 \times 1^{-0.5} \times 0.2^{0.7} \times 3000^{0.4} \times \tan 40^\circ \times \left(\frac{1.02 \times 4.43^2}{2} \right)^{0.6} = 48.49 \text{ kN}$$

$$\lambda_2 = \frac{m_2}{m} = \frac{1423}{1020} = 1.395$$

$$k_n = \frac{48.49^2}{50 \times 1020 \times 4.43^2} \times \left(\frac{1 + 1.395}{1.395} \right) = 4033.64 \text{ N/m}$$

$$\frac{T_m}{T_{m_2}} = \frac{3.16}{0.062} = 49.91 ; \gamma = 0.26$$

$$\Delta = 0.26 \times \frac{1020 \times 4.43}{\sqrt{1020 \times 14020 \times (1 + 1.395)}} = 6.35 \text{ mm}$$

$$\varepsilon_s = 0.00272 \times \frac{6.35}{15.6} = 0.001107$$

Test C9-2

$$F_c = 1.82 \times 1^{-0.5} \times 0.2^{0.7} \times 6000^{0.4} \times \tan 40^\circ \times \left(\frac{1.02 \times 4.43^2}{2} \right)^{0.6} = 64 \text{ kN}$$

$$\lambda_2 = \frac{m_2}{m} = \frac{1423}{1020} = 1.395$$

$$k_n = \frac{64^2}{50 \times 1020 \times 4.43^2} \times \left(\frac{1 + 1.395}{1.395} \right) = 7022.98 \text{ N/m}$$

$$\frac{T_m}{T_{m_2}} = \frac{2.39}{0.062} = 37.83 ; \gamma = 0.36$$

$$\Delta = 0.36 \times \frac{1020 \times 4.43}{\sqrt{1020 \times 14020 \times (1 + 1.395)}} = 8.79 \text{ mm}$$

$$\varepsilon_s = 0.00272 \times \frac{8.79}{15.6} = 0.00153$$



Minerva Access is the Institutional Repository of The University of Melbourne

Author/s:

Pethati Mudiyanseelage Don, Jude Shalitha Perera

Title:

Rigid Barrier with a Gabion Cushion Subjected to Boulder Impact

Date:

2019

Persistent Link:

<http://hdl.handle.net/11343/240599>

File Description:

Final thesis file

Terms and Conditions:

Terms and Conditions: Copyright in works deposited in Minerva Access is retained by the copyright owner. The work may not be altered without permission from the copyright owner. Readers may only download, print and save electronic copies of whole works for their own personal non-commercial use. Any use that exceeds these limits requires permission from the copyright owner. Attribution is essential when quoting or paraphrasing from these works.